THE UNIVERSITY
of EDINBURGH

Earthquake Distributions at Volcanoes: Models and Field Observations

Nick S. Roberts

Thesis submitted for the degree of Doctor of Philosophy

The University of Edinburgh

2016

Acknowledgements

Firstly I would like to thank my supervisors Ian Main and Andy Bell. Ian has provided incredibly constructive feedback on all my work as it came together, and in particular has improved my writing style no-end allowing me to publish my work and get this thesis written up on time! Andy's enthusiasm behind the fieldwork on Rum, allowed me the rare opportunity for a geophysicist to get out and collect my own field data. I loved every second out on Rum (even in the wind, rain and hail) and in terms of my personal experience of my PhD, Rum was definitely the highlight. Also thanks to Andy for getting me up and running in Python with his original code. Making pretty figures certainly makes a thesis full of graphs more digestible (I hope). Thanks also to Mark Naylor for helping me early doors and contributing to my first paper, and to Florien Fusseis for his constructive criticism in year one that really made me knuckle down.

After spending six and a half years in Edinburgh there are a whole host of people who have made my time here very special. Firstly my 23 Melville Terrace flatties Kirsten, Gibbo and Wallsy; that flat has so many special memories and really defines my time here. My other flatmates, Qing, James, Rachel, Johannes, Jakob and Robyn; equally massive thanks for being such great company.

Squash is so important to me. Thanks to all my teammates and friends, especially Wardy, Noddy, DJ, Seigo, Iain and Elliot, who have made the matches and weekends away so enjoyable.

The motor sport crew. I never thought coming into university my best friends would be with EUMSC and going out the other end you are definitely all the reason I've been lucky enough to start a career in motor sport. Sean, Kirsten, Stephen, Finn, Callum, Scott, Stevie, Gary and James it's been an absolute pleasure. Here's hoping Poker on Tour becomes a permanent fixture in the F1 calendar.

All my officemates and fellow geoscientists. We've all taken a ride on the roller coaster, and you've all helped me pull through. Special thanks to Rachel, Sophie, Jamie, Claire and Yutong for making Rm 401 such an enjoyable place to work, and for allowing me and Jamie to practice our golf. Also thanks to Romesh, Gus, Joho, Rami, Maddy, Ed, Iain, Ben, Jakob and Robyn for all the various GradSchool, football and Hibee related fun through the years.

Finally and most importantly, thanks to my family for all their love and support throughout my PhD. It's certainly not been a walk in the park and I thoroughly appreciate all the support you have always and continue to show me.

Declaration

I declare that this thesis has been composed by myself and, except where otherwise acknowledged, is entirely my own work. It has not been submitted, either in whole or in part, in any previous application for a degree.

Nick Roberts

August 2016

Abstract

Volcanic earthquakes can provide significant insight into physical processes acting at volcanoes, such as magma accumulation and the mechanisms of deformation of the volcanic edifice. At the same time a statistical analyses of volcanic seismicity prior to an eruption (for example variations in the Gutenberg-Richter *b*-value – a measure of the proportion of large and small events) are a key component of the practical problem of forecasting eruptions. This thesis aims to tackle two key areas of research that are closely related to these important overall goals, by comparing seismic data obtained from currently-active volcanoes with direct field observation of faulting and fracturing from an exhumed extinct volcano.

First I introduce a new approach that improves the accuracy and reliability of calculating spatial and temporal variations of the seismic *b*-value for frequency-magnitude distributions at active volcanoes, and apply it to several test cases. An extensive literature review highlights a large variability and lack of standardisation of methodology used to analyse frequency-magnitude distributions in the past. Motivated by this, I introduce and test a new workflow to standardise calculating completeness magnitudes of seismic catalogues. The review also highlights the fact that uncertainties in estimating the threshold magnitude of complete reporting have been ignored to date. Here I use synthetic catalogues to quantify this previously unidentified source of error, and provide a template to estimate the total error in *b*-value. In standard analysis it is also common to sample time windows subjectively, although this can introduce bias. Here I develop a new objective, iterative sampling method that calculates the *b*-value as a full probability density function which need not have a Gaussian error structure. Application of this method reveals 'mode-

switching' behaviour for the first time in volcanic seismic catalogues. The results also show *b*-values often do have a value indistinguishable from that of tectonic seismicity (*b*=1 within error). Nevertheless there are also several robust examples of real high *b*-values, as high as 3.3.

The second part of the study is based on a field campaign to investigate the fracture zones from an exhumed volcanic setting on the Isle of Rum, NW Scotland. Lithological and structural mapping is used to collect structural data that is then used to quantify and explain complex fracture patterns and the underlying intra-magma chamber processes that occurred there in the geological past. In particular I identify a singular collapse event within the youngest volcanic unit, the Central Intrusion. This is responsible for forming the observed igneous breccias and the lineaments on satellite images that I interpret as contemporaneous faults. Using appropriate scaling relations, I infer the *b*-value for the Rum lineaments data. This would have been relatively high, at a value of approximately 1.9.

The final part of the study compares the fracture data on Rum to earthquake distributions at El Hierro volcano, Canary Islands. Here I show the level of fractal clustering is similar in both an extinct (60 Ma) and a currently active volcano. Both show similar high levels of clustering. However, in both cases there is a difference between the capacity and correlation dimensions ($D_0 \neq D_2$), implying the set of rupture sources or mapped fault traces form a multi-fractal set. Broadly, the scaling of fracture sets in an ancient volcano has similar properties to those observed in a modern volcano, except that the Rum data imply a greater absolute degree of spatial clustering of deformation than that for the recent unrest at El Hierro.

Lay Summary

Eruptions at volcanoes pose a very serious threat to human life. By measuring the behaviour of the volcano we hope to be able to better predict an eruption. One of the key behaviours we measure at volcanoes are earthquakes. These may be associated with magma movement at great depth surrounding a magma chamber, or may signify movement closer to the surface about to trigger an eruption. This thesis aims to improve two key areas of research associated with volcanic eruption forecasting.

Firstly, I have improved the methods used to calculate variations of a parameter, known as the '*b*-value', in both space and time. The *b*-value tells us the relative proportion of large to small earthquakes. In continental settings, such as the San-Andreas fault in California, *b*=1. At volcanoes *b* is often reported to be greater than 1, meaning there is a higher proportion of small to large earthquakes. These newly developed methods have revealed 'mode-switching' behaviour where the value changes quickly from one value the next. It has not previously been observed at volcanoes. The methods also show several cases where the *b*-value is indeed high, reaching up to a value of 3.3.

I have also performed geological mapping on the Island of Rum, NW Scotland. Rum is an ancient 60 million year old magma chamber that has been uplifted and exposed at the surface. By comparing the cracks that shows us where earthquakes occurred, to the distribution of real earthquakes at El Hierro volcano in the Canary Islands, we find both examples show very similar characteristics. This means we can use the observations on Rum to effectively, 'see into' the magma chamber at El Hierro.

Contents

Acknowledgements ..... **i**

Declaration ..... **iii**

Abstract ..... **v**

Lay Summary ..... **vii**

Contents ..... **ix**

Chapter 1 – Introduction **1**

1.1 The review 1

1.1.1 Seismological observations 1

1.1.2 Field observations 3

1.2 The claim 4

1.3 Thesis overview 5

Chapter 2 – Motivation and Literature Review **9**

2.1 Earthquake processes at volcanoes 9

2.2 Distribution of seismicity 12

2.2.1 Frequency-magnitude distributions 13

2.2.2 Current methods for identifying changes in frequency-magnitude distributions 14

2.3 Geological history of Rum 20

2.3.1 The British Palaeogene Igneous Province 20

2.3.2 Rum 23

2.3.3 The Central Intrusion 28

2.3.4 The Central Intrusion breccias 29

2.3.5 Glacial erosion 30

2.4 Fractal Dimensions 31
2.4.1 What is a fractal? 31
2.4.2 Methods for estimating fractal dimensions 33
2.4.3 Probability and clustering 34
2.4.4 Pair correlation 36
2.4.5 Fractal interpretation of the seismic *b*-value 38
2.4.6 Multifractal set 40
2.5 Summary 41
2.5.1 Research questions 41
Chapter 3 – Are Volcanic Seismic *b*-values High, and if so When? 43
3.1 Introduction to the paper 43
3.2 Abstract 45
3.3 Introduction 46
3.4 Review and synthesis of previous studies 49
3.5 Methods for analysis of Frequency-Magnitude Distributions 53
3.5.1 Gutenberg-Richter parameters 53
3.5.2 Calculating the completeness magnitude 55
3.6 Results for synthetic catalogues 57
3.6.1 Generating synthetic catalogues 57
3.6.2 Synthetic results 59
3.6.3 A proposed workflow for the calculation of Mc 67
3.6.4 Error introduced from the completeness magnitude 68
3.7 Application to volcanic catalogues 72
3.8 Conclusions 76
3.9 Acknowledgements 77
Chapter 4 – Mode-Switching in Volcanic Seismicity: El Hierro 2011-13 79
4.1 Abstract 80
4.2 Introduction 81
4.2.1 Mode-switching definition 82
4.3 Methods 83
4.3.1 *b*-value calculation 83
4.3.2 Iterative sampling methodology 83

4.3.3 Converting to a probability density function ... 86
4.3.4 Monte-Carlo simulation of error structure using moving windows ... 86
4.3.5 Choice of parameters ... 88
4.4 Results ... 89
4.5 Conclusions ... 97
4.6 Acknowledgements ... 97
Chapter 5 - A Systematic Study of Earthquake Scaling in a Range of Volcanic and Tectonic Settings ... 99
5.1 Introduction ... 99
5.2 Methodology ... 100
5.3 Data sets ... 101
5.4 Results ... 102
5.4.1 El Hierro ... 102
5.4.2 Mt. Etna ... 106
5.4.3 Kilauea ... 108
5.4.4 Tungurahua ... 109
5.4.5 Bárðarbunga ... 111
5.4.6 Grímsvötn ... 118
5.4.7 Eyjafallajökull ... 121
5.4.8 Katla ... 123
5.4.9 Tjörnes Fracture Zone ... 128
5.4.10 South Iceland Seismic Zone ... 134
5.4.11 Southern California ... 136
5.4.12 Summary ... 137
5.5 Conclusions ... 139
Chapter 6 – Fractures in a Magma Chamber: Isle of Rum ... 141
6.1 Introduction ... 141
6.1.1 Rationale ... 141
6.1.2 Structure of this chapter ... 142
6.2 Methodology ... 143
6.2.1 Study Area ... 143
6.2.2 Field mapping ... 145

6.2.3 Data collection 145
6.3 Results of field mapping 146
6.3.1 Units 146
6.3.2 History of the Central Intrusion 151
6.4 Fracture sampling 166
6.4.1 Quadrant sampling 166
6.4.2 Transects 169
6.4.3 Transect data 171
6.4.4 Observations from transect data 174
6.5 Lineaments on satellite imagery 179
6.5.1 Mattsson *et al.* 2014 study 180
6.5.2 Lineaments data 181
6.5.3 Observations from lineaments data 183
6.5.4 Strike-slip faulting 183
6.6 Summary and discussion of field data 187
6.6.1 West of Long Loch 188
6.6.2 East of Long Loch 190
6.7 Conclusions 190
6.8 Acknowledgements 192
Chapter 7 – Analysis of Fault Population Data in Comparison with Modern Volcanic Seismicity 193
7.1 Introduction 193
7.1.1 Rationale 193
7.1.2 Structure of this chapter 195
7.2 Rum frequency-magnitude distribution 195
7.3 Rum fractal dimensions 199
7.3.1 1D fractal dimension analysis 199
7.4 El Hierro fractal dimensions 208
7.4.1 2D ruler method sampling 208
7.4.2 1D analysis results 211
7.4.3 2D and 3D analysis results 216
7.5 Comparison of Rum and El Hierro fractal dimensions 219

7.5.1 Interpretation 221
7.6 Conclusions 223
Chapter 8 – Discussion 225
8.1 Introduction 225
8.2 Implications of results 226
8.3 Focal mechanisms 231
8.3.1 Rum 231
8.3.2 El Hierro 233
8.3.3 Mt. Etna 235
8.3.4 Summary 236
8.4 Gutenberg-Richter law assumption 237
8.5 Fieldwork resolution limitations 237
8.6 Spatial sampling of the *b*-value 238
8.7 Ideas for future work 241
Chapter 9 – Conclusions 245
9.1 New methodologies for calculating *b*-values 245
9.1 Application of methods to real catalogues 245
9.2 Field mapping on the Isle of Rum 246
9.3 Comparison of fault population data with modern volcanic seismic data 247
Bibliography 249
Appendix A – Glossary and a list of figures and tables 263
A.1 – Glossary of abbreviations and acronyms 263
A.1.1. Seismicity abbreviations 263
A.1.2. Fractal dimension abbreviations 264
A.1.3. Rum abbreviations 265
A.1.4. Acronyms associated with seismicity 265
A.1.5. Acronyms associated with fractal dimensions 266
A.1.6. Acronyms associated with Rum 266
A.2 – List of Figures 268
A.3 – List of Tables 278
Appendix B – Spatio-Temporal Evolution of Seismicity for Seismic Catalogues in Chapter 5 281

B.1 – El Hierro 281
B.2 – Mt. Etna 283
B.3 - Kilauea 284
B.4 - Tungurahua 285
B.5 - Bárðarbunga 286
B.6 - Grímsvötn 289
B.7 Eyjafallajökull 290
B.8 - Katla 291
B.9 - Tjörnes Fracture Zone 292
B.10 – South Iceland Seismic Zone 293
B.11 - Southern California 294
Appendix C – Rum transect data 295
C.1 – Transect 1 296
C.2 – Transect 2 301
C.3 – Transect 3 305
C.4 – Transect 4 309
C.5 – Transect 5 312
C.6 – Transect 6 315
Appendix D – Spatial sampling of the *b*-value using Voronoi polygons 321
D.1 Current literature 321
D.2 Iterative 2D Voronoi tessellation 324
D.2.1. El Hierro Voronoi interpretation 328
D.3 Further improvement of method 328
Appendix E - Code 331
E.1 Imported packages 331
E.2 Parameters 331
E.3 Importing the catalogue 332
E.4 Filtering the catalogue 333
E.5 Functions 334
E.5.1. Daily number of events rates 334
E.5.2. Frequency-magnitude distribution function 334
E.5.3. Maximum Curvature function – completeness magnitude 334

E.5.4. Goodness-of-Fit function – completeness magnitude 335
E.5.5. *b*-value stability function – completeness magnitude 336
E.5.6. Maximum-likelihood estimation of the Gutenberg-Richter distribution function 336
E.5.7. Estimated Gutenberg-Richter distribution function 337
E.5.8. Error modification 337
E.5.9. Iterative sampling method 338
E.6 Run analysis 341
E.7 Print outputs 343
E.8 Plotting figures 344
E.8.1. Frequency-magnitude related plots 344
E.8.2. *b*-value probability density related plots 348
E.9 Voronoi polygons 351
E.9.1. Description 351
E.9.2. Voronoi sampling code 352
E.9.3. Plotting figures 357

Chapter 1 – Introduction*

1.1 The review

1.1.1 Seismological observations

Earthquakes are one of the key tools used in volcano eruption forecasting. We cannot observe the processes occurring within the Earth's crust directly, so we rely heavily on indirect geophysical techniques to monitor the detectable signals associated with these processes such as: size, rate, location and nature of events. Then it is possible to infer what may be happening physically in the sub-surface before, during, and after an eruption.

One of the most fundamental properties of a seismic catalogue is the frequency-magnitude distribution. This is commonly described by the Gutenberg-Richter relationship (Gutenberg and Richter, 1954):

$$\log(N) = a - bM, \qquad [\,1.1\,]$$

where N is the total number of earthquakes of magnitude equal to or greater than M, and a and b are real, positive constants characteristic of the specific catalogue. The 'b-value' represents the relative proportion of large and small events in the catalogue, and has been used after calibration with controlled experiments to gain insight into

* *with acknowledgement to Jon Claerbout*

the role physical variables such as the stress play in controlling the distribution within the catalogue.

The *b*-value has been widely studied using real seismic catalogues. A major study by Frolich and Davis (1993) found that in tectonic settings globally $b \approx 1.0$. Main (1996) found that the Gutenberg-Richter relationship holds for at least small and intermediate events across a vast range of sizes and loading conditions, from laboratory experiment to tectonic earthquakes. McNutt (2005) collated results from 13 volcanoes to date for which the frequency-magnitude distribution had been analysed. While some regions had a 'normal' *b*-value of 1.0, many had anomalously high values of up to $b=3.0$ using the techniques then available. In subsequent work it became almost axiomatic that volcanic earthquakes were associated with a high *b*-value. The question remains, is this true, and if so when, and why?

Marzocchi and Sandri (2003) reviewed the different methods of estimating the *b*-value and its uncertainty. The original maximum likelihood estimate of *b* had been defined by Aki in 1965, and is still the least biased estimate. Further improvements on the uncertainty in *b* were developed by Shi and Bolt (1982) along with an estimate of *b* including binned magnitudes by Bender (1983). Using synthetic catalogues with known *b*-values, Marzocchi and Sandri tested the validity of various estimates, including those of Bender (1983), to calculate *b* and its uncertainty for complete catalogue sizes ranging between 25 and 10,000 events, concluding that the bias in the estimation of *b* is significantly reduced when binned magnitudes are accounted for.

It is assumed the Gutenberg-Richter relationship applies to a complete seismic catalogue where every event in a space-time volume is recorded. In reality not all events are recorded. Small events may simply not register on the seismometer, or they may be masked by larger events; or there may be a limitation on the number of events that can be processed, including times where there are many events and the operator's time is limited. Therefore a pre-requisite to calculating an accurate *b*-value is to successfully calculate the completeness magnitude, *Mc*, above which the

catalogue is assumed to be complete (Rydelek and Sacks, 1989; Woessner and Wiemer, 2005; Mignan and Woessner, 2012). Mignan and Woessner (2012) tested six techniques for calculating *Mc*, five of which were based on the Gutenberg-Richer law. They tested each method on various real catalogues, presenting the results and summarising the pros and cons of each method without stipulating a preferred method of the six.

1.1.2 Field observations

Making observations of deformation and fracturing in the field allows us to observe processes that occurred in geological history millions of years ago in greater detail. By looking at ancient, no longer active, exhumed systems we have the opportunity to directly witness processes that were occurring when the volcano was active, and hence to interpret or place constraints on some of the processes we may be observing the effects of in seismological data today.

Wells and Coppersmith (1994) devised the ground-breaking empirical formula among magnitude, rupture length, rupture width, rupture area and surface displacement from 244 earthquakes with observable surface ruptures. This calibration can be used to infer the magnitude of the earthquake associated with the rupture of the causative fault. Conversely, if we know the magnitude of an earthquake from seismological data, it is possible to estimate the above parameters of the deformation it would had generated.

The Isle of Rum in north-west Scotland is an exhumed, extinct magma chamber well studied in terms of its petrology (Emeleus, 1994; Emeleus et al., 1996; Emeleus, 1997; Troll et al., 2000; Emeleus, 2005a; O'Driscoll et al., 2007; Troll et al., 2008; Holohan et al., 2012; Upton et al., 2012; Emeleus and Troll, 2014; Mattsson et al., 2014) and is known to have had active faulting concurrent with volcanism. The Long Loch fault is a right-lateral strike-slip fault that might have acted as a feeder for the Central Intrusion series of magmatic rocks (McClurg, 1982; Volker and Upton, 1990; Emeleus *et al.*, 1996). The surrounding fracture pattern is believed to be related to a trans-

tensional strike-slip basin, however, to date only orientations of the faults have been analysed (Mattsson *et al.*, 2014). There has been no structural data gathered to constrain potential focal mechanisms or statistical measures of potential attributes of its past earthquake sources such as the distribution of rupture length and spatial correlations in the population.

1.2 The claim

In this thesis I make some fundamental improvements of the methodologies used to analyse completeness magnitudes and *b*-values associated with seismic frequency-magnitude distributions. The methods are general and can be applied to any type of seismicity. I update and extend the summary of volcanic *b*-values studies by McNutt (2005) and identify a problem with consistency of approach. Accordingly, I produce a standardised workflow for estimating *Mc*; and quantify the resulting additional source of error in the *b*-value. I then address the problem of the subjective choice of time window in *b*-value analysis by introducing a new iterative Monte-Carlo sampling method. This results in a full *b*-value probability density function as a function of time, with greatly increased resolution compared to current studies. This methodology is applied to nine volcanic seismic catalogues, and two tectonic seismic catalogues as a 'control' for comparison. The results confirm that b=1 in tectonic settings and that b is often greater than 1.0 at volcanoes with values as high as 3.3. However, b is also often equal to 1.0 at volcanoes and the seismicity for each volcano has a unique character. There is no consistent underlying mechanism for locations or times when *b*-values are high. I also identify 'mode-switching' behaviour in the *b*-value for the first time in real seismic catalogues. This phenomena had previously only been seen in experimental results (Main, 1996).

I use Rum as a case study of an exhumed extinct magma chamber. I improve on the current known geological history of the Central Intrusion series and associated intrusive breccias, and collect extensive quantitative fracture data to aid in the understanding of the extensional tectonics as well as creating a datasets that can be

compared to a real seismic catalogue. The fracture data reveals predominantly left-lateral extensional offset, directly contradicting the right-lateral offset observed on the main strike-slip fault, thus we attribute the observed fracture patterns to intra-magma chamber deformation rather than more regional slip on the Long Loch Fault.

Finally, in order to compare the Rum fracture data to the El Hierro seismic catalogue, I model each earthquake using the Wells and Coppersmith (1994) laws to estimate the length of each rupture. I then compare the one-dimensional fractal distributions of both datasets using three different methods, concluding that within error both distributions have a similar fractal dimension, implying high levels of clustering between small events, or jointly with a single major phase of deformation.

1.3 Thesis overview

- Chapter 2 is a literature review of the three key topics in this thesis: frequency-magnitude distributions, the geological history of Rum, and fractal dimensions associated with populations of faults, fractures and earthquakes. This gives motivations for the seven key research questions stated at the end of the chapter.
- Chapter 3 extends the review of McNutt (2005) from 13 to 21 studies, and increases the number of parameters and attributes recorded for the different volcanoes and periods of unrest. A standardised workflow for calculating *Mc* is presented, based on analysis of incomplete synthetic catalogues and a new source of error introduced by calculating *Mc* is quantified. Finally the methodology is applied to the El Hierro and Mount Etna catalogues.
- Chapter 4 introduces a methodology that eliminates the bias introduced by sampling discrete time windows, using iterative sampling to create a cloud of data points. Each point is the converted to a Gaussian distribution, and points are then summed within a window to generate a full probability density profile that can have a non-Gaussian or multi-modal character. This methodology is then applied to the El Hierro catalogue and then compared to

the results in Chapter 2. The results show a much greater resolution in *b*-value variability, including mode-switching behaviour that has not been seen before in volcanic seismicity.

- In Chapter 5 the iterative sampling methodology developed in Chapter 4 is applied to nine volcanic and two tectonic seismic catalogues, in order to test the null hypothesis that b=1.0 globally and the general hypothesis that b>1.0 at volcanoes. For each catalogue the probability distribution is presented and used to identify the modal and maximum *b*-values, and if necessary look at specific spatial and/or temporal zones where *b* is anomalous, and to infer why this is the case. The *b*-values at volcanos are sometimes significantly greater than 1.0 although a baseline value of b=1.0 is still very common, and some examples also show of mode-switching behaviour in *b*.
- Chapter 6 presents the results from the field mapping campaign, including fracture sampling and satellite image analysis on Rum. By mapping the intrusive breccia a new process that has not been recorded in the literature at Rum to date is identified: a breccia flow, associated with a singular chamber-wide deformation event. The chapter includes data on approximately 1000 fractures, measured along six transects. Some 405 lineaments associated with faulting were identified on satellite images as a pre-requisite for the quantitative analysis in Chapter 7. Together they form a broad bandwidth data set spanning over four orders of magnitude, from 10^{-2} to 10^{2}m.
- Chapter 7 compares the fractal dimensions of the Rum fracture data with those of the El Hierro seismic catalogue. In order to make a direct comparison each event is assigned an inferred magnitude related to the surface rupture length, after which one-dimensional fractal analysis could be applied. As the minimum magnitude threshold decreases, the number of events increases, and so does the intensity of clustering. The results are consistent with the hypothesis that smaller magnitude events are more likely to be correlated with each other, and/or associated with a single geological event.

- Chapter 8 discusses the implications of the results in response to the seven research questions stated in Chapter 1. It then provides a general discussion on how the models of fracture distributions at both Rum and more generally at active volcanoes could be improved by implementing known focal mechanisms. The limitations of resolution in the field study are discussed. Preliminary results for a further improvement on the iterative sampling method devised in Chapter 4 for analysing *b*-values in 2D and 3D space are shown. Finally ideas for future work are presented.
- Chapter 9 concludes the thesis.

A glossary of all the abbreviations and acronyms used in this thesis is provided in Appendix A.1.

Chapters 3 and 4 contain two published papers, preceded by additional text that sets the context within this thesis. The details of each paper, in chapter order, are as follows:

- N. S. Roberts, A. F. Bell, and I. G. Main. Are volcanic *b*-values high, and if so when? *Journal of Volcanology and Geothermal Research*, 308, p127-141, (2015).
- N. S. Roberts, A. F. Bell, and I. G. Main. Mode-Switching in volcanic seismicity: El Hierro 2011-13. *Geophysical Research Letters,* 43, 2016.

Chapter 2 – Motivation and Literature Review

This chapter presents an introduction to the current literature and conceptual framework underpinning the three main areas of research described within this thesis and outlines the motivation behind the subsequent research. A more extensive and targeted literature review is presented in both Chapters 3 and 4, i.e. for the work presented in the form of scientific papers. The underpinning areas and their research applications reviewed in this chapter are: (i) the distribution of seismicity, in particular the frequency magnitude distribution for active volcanoes (Chapter 3-5); (ii) the geological history of Rum as an analogue of a formerly active volcano (Chapter 6); and (iii) the concept of a fractal dimension, used here as a basis for an integrative analysis of seismicity and faulting associated with volcanoes using (Chapter 7). These are reviewed in turn below. Finally the key research questions obtained from this review are listed.

2.1 Earthquake processes at volcanoes

An earthquake is the release of energy caused by the sudden breaking of rocks along a surface/fault plane. There are three ideal forms of displacement that can occur: mode I, mode II, and mode III (Figure 2.1). In mode I displacement, referred to as opening or tensile mode, the crack surfaces or walls move directly apart. In mode II displacement, referred to as sliding, in-plane or forward shear mode, the fracture surfaces or walls slide over one another in a direction perpendicular to the leading edge (tip) of the crack. In mode III displacement, referred to as tearing, anti-plane or traverse shear mode, the crack surfaces or walls move relative to one another in a

direction that is parallel with the leading edge of the crack (Gudmundsson, 2011a). In nature, fractures are typically best modelled as a combination of two of the modes.

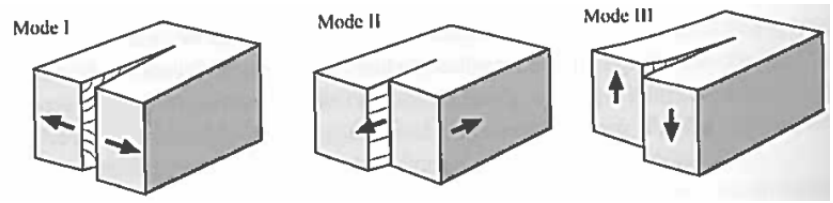

Figure 2.1 – Ideal wall or surface displacements of a fracture are denoted by mode I, mode II, and mode III (Gudmundsson, 2011a).

Volcanoes have a wide range of both magmatic and tectonic processes creating earthquakes with varying types of displacement. Figure 2.2 shows two examples of magma chamber and collapsed caldera complexes exhibiting mode I and mode III cracks. Dykes cause mode I opening as the magma pushes through the rock. Whilst mode III is occurring along the ring fault in both examples. There is also an example of compressive stresses closing the fractures around the ring fault in Figure 2.2b.

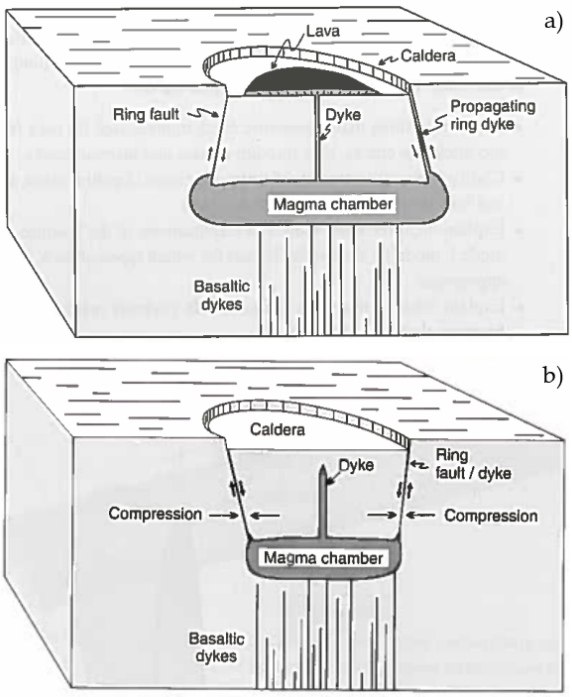

Figure 2.2 – Two examples of a magma chamber, dyke and collapsed caldera. a) A feeder dyke (Mode I) in the centre of a collapsed caldera and the ring dyke/fault

(Mode III) are best modelled as through cracks. All ring faults are dip-slip faults, here it is a reverse fault. b) A non-feeder dyke in the centre of a collapsed caldera. The dyke originates at the top of a shallow, fluid magma chamber and then extends partly up into the host rock. Here the ring fault of the collapsed caldera is a normal fault (Gudmundsson, 2011a).

Figure 2.3 shows a schematic cross-section through a layered stratovolcano (Gudmundsson, 2011b). It introduces a sill structure defined as the lateral migration of magma between two layers of rock. A dyke is a vertical intrusion cross-cutting the layers of rock. The tip of the intrusion is where the rock is fracturing, and therefore where the earthquakes will be generated. Here a conduit is a sill or dyke that has reached the surface.

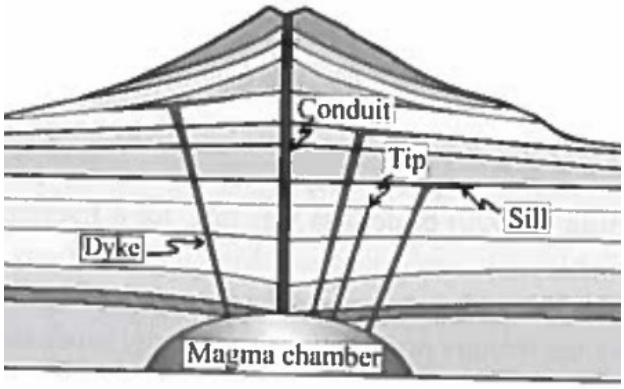

Figure 2.3 – Schematic diagram of a stratovolcano showing the difference between a conduit, dyke, sill, and tip (Gudmundsson, 2011b).

There are three ideal geometries of cracks that can occur (Gudmundsson, 2011a), as shown in Figure 2.4. These can be directly related to volcanic processes. A 'through' crack (Figure 2.4a) is an appropriate model for a conduit dyke and a ring fault. The dyke extend from one free surface to another (magma chamber to the surface). A 'part-through' crack (Figure 2.4b) is an appropriate model for a non-feeder dyke and sills that have not breached the surface. An 'interior' crack (Figure 2.4c) is contained entirely within an elastic body. An example would be a small joint located within, and far from the surface of a large pluton.

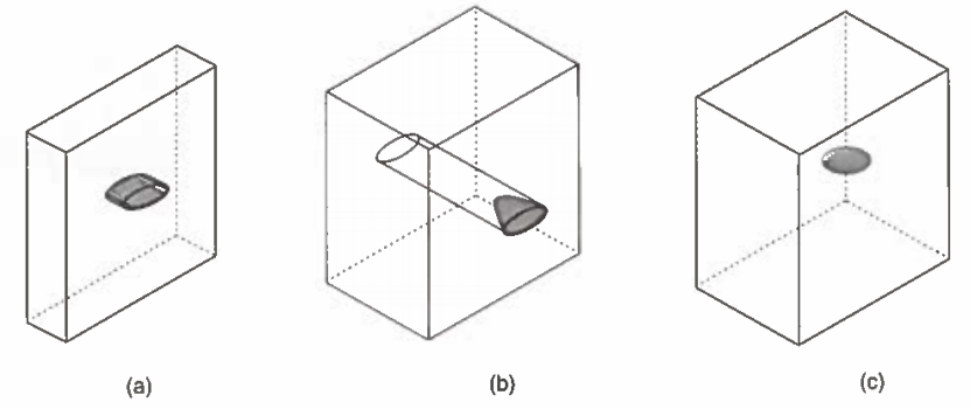

Figure 2.4 – Ideal crack geometries for modelling fractures: a) a 'through' crack, b) a 'part-through' crack, and c) an' interior' crack (Gudmundsson, 2011a).

A further source of deformation is the inflation and deflation of a magma chamber (Thatcher and Savage, 1982; Savage and Cockerham, 1984; Marti *et al.*, 2013b). As the magma chamber fills it pressurizes until the surrounding rock reaches a peak level of stress and then fractures. Conversely, during a period of expulsion from the magma chamber the pressure on the surrounding rock drops and subsidence may occur in the roof of the magma chamber, again causing the rocks to fracture.

All of these processes can generate earthquakes of different natures at volcanoes. By monitoring and studying the distribution in space and in magnitude we can gain insight into the processes creating them.

2.2 Distribution of seismicity

Earthquakes are one of many processes that can be monitored in near-real-time at active volcanoes, in order to identify unrest and aid with eruption forecasting. Typically a network of seismometers records all seismic disturbances in the region of the volcano. A single component seismometer can detect ground-movement in just one plane of motion, therefore three seismometers, or one three-component instrument, are required to detect every possible orientation of motion or polarization in three dimensions. Many modern seismometers are broadband, meaning they detect a wide range of frequencies. The recorded seismograms are then processed to

calculate a local magnitude (M_L) (Gutenberg and Richter, 1956) or now more widely used in literature, the moment magnitude (M_W) (Hanks and Kanamori, 1979), because it is more directly connected to the deformation and slip than M_L. Using a minimum of three stations the location and origin time of an event can be estimated. A collection of events with their relevant calculated parameters is then known as a seismic catalogue.

2.2.1 Frequency-magnitude distributions

Seismic catalogues typically contain data for some or all of the following parameters for each individual seismic event: Date & time, magnitude (local and/or moment), longitude, latitude, depth and type of event. These parameters are the basis for our understanding and forecasting of volcanic processes. Frequency-magnitude distributions (FMD) are the binned discrete/cumulative magnitudes of events within the catalogue. Where the catalogue is completely reported, the FMD commonly takes the form of a Gutenberg-Richter (GR) relation (Gutenberg and Richter, 1954):

$$\log(N) = a - bM, \qquad [\ 2.1\ ]$$

where N is the total number of earthquakes of magnitude equal to or greater than M, and a and b are real, positive constants characteristic of the specific catalogue. The parameter a is the logarithm of the number of earthquakes with $M \geq 0$, and is thus a measure of the seismicity rate of the region. From this, Bender (1983) calculated the maximum likelihood-estimation of b using binned magnitudes, (Equation [3.4]) and with the associated uncertainty estimate (Equation [3.5]) (Shi and Bolt, 1982; Marzocchi and Sandri, 2003):

$$\tilde{b} = \frac{1}{\ln 10[\hat{\mu} - (M_c - \Delta M)]} \qquad [\ 2.2\ ]$$

$$\sigma_{\tilde{b}} = 2.30\tilde{b}^2 \sqrt{\frac{\sum_{i=1}^{N}(M_i - \hat{\mu})^2}{N_c(N_c - 1)}} \qquad [\ 2.3\ ]$$

where M_c is the completeness magnitude, ΔM is the binned magnitude width, $\hat{\mu}$ is the average magnitude of the sample, and N_c is the number of events in the complete catalogue.

The *b*-value represents the relative proportion of large and small events in the catalogue. Equation [2.1] was originally defined for cumulative data, but a discrete probability density function (PDF) may be more informative. As part of the paper in Chapter 3, I present a full review of previous studies of *b*-values for volcanic seismic catalogues.

The work presented in this thesis develops our core-understanding of FMD's. Using synthetic catalogues I first address the need to correctly calculate the completeness magnitude, *Mc*, defining the complete catalogue to which we then apply Equation [2.1]. I look at the effect of under-sampling of the FMD due to under-estimation of *Mc* can have on the *b*-value. I then study FMD's of active volcanoes, specifically looking at temporal variations in the *b*-value, and whether the anomalous results are real or an artefact of the FMD not following the Gutenberg-Richter relationship. Using field data from the extinct volcanic centre at the Isle of Rum, I then investigate how FMD's might be generated by fault populations. Then finally I discuss the implications for monitoring and forecasting that these improvements in analysing FMD's can make.

2.2.2 Current methods for identifying changes in frequency-magnitude distributions

Studying spatial and temporal variations in the *b*-value is a common form of analysis of seismic catalogues. Two frequently used ways with dealing with a large seismic catalogue are to either divide it into phases (either as clusters of events or by changes in event rate) or to apply a moving window in space/time to attempt to identify small *b*-value variations over time. Here I discuss the disadvantages of using these methods in preparation for proposing a new workflow in Chapter 3.

2.2.2.1 *Visual selection of phase boundaries*

Selecting phase boundaries by eye involves subjectively deciding where is a change in event rate or completeness magnitude that warrants a new 'phase' of data. This introduces inherent bias into how the $\tilde{b}$-value evolves. A phase may inadvertently be created that is too small therefore it may be incomplete, or too large, so that the resultant $\tilde{b}$-value may be an average of several clusters of independent catalogues. This method tends to pick up large scale trends rather than small variations in $\tilde{b}$. This is because there is a tendency to select clear major divisions in the catalogues rather than attempting to pick out more subtle variations, for example changes in the completeness magnitude. It can also lead to long periods of time being represented by just one data point, when there may be significant variation in $\tilde{b}$ within this period.

2.2.2.2 *Moving windows*

A commonly used method for evaluating $\tilde{b}$-value evolution in seismic catalogues is to apply a moving window that selects a discrete volume/number of events to define overlapping phases. This can be in 1D (time) or in 2D/3D in space, typically either focusing on $\tilde{b}$-value anomalies with depth, or over an entire volume through time. This method can be an improvement on selecting phase boundaries by eye, in that it eradicates the introduction of bias due to human preference and produces more data points allowing clearer identification of changes in the $\tilde{b}$-value. It can however introduce many other sources of bias or error as detailed below.

The moving window method calculates the $\tilde{b}$-value for a window with a fixed number of events/duration within the whole catalogue. The window is moved by the fixed number of events to form a new phase. This is repeated through the entire catalogue to generate $\tilde{b}$-value evolution through space/time. Figure 2.5 demonstrates an example of a synthetic catalogue with a known completeness magnitude and b-value of 1.0. It highlights several problems with this method of sampling catalogues.

Here using a synthetic catalogue with known parameters allows an assessment of validity of the technique in recovering a known result.

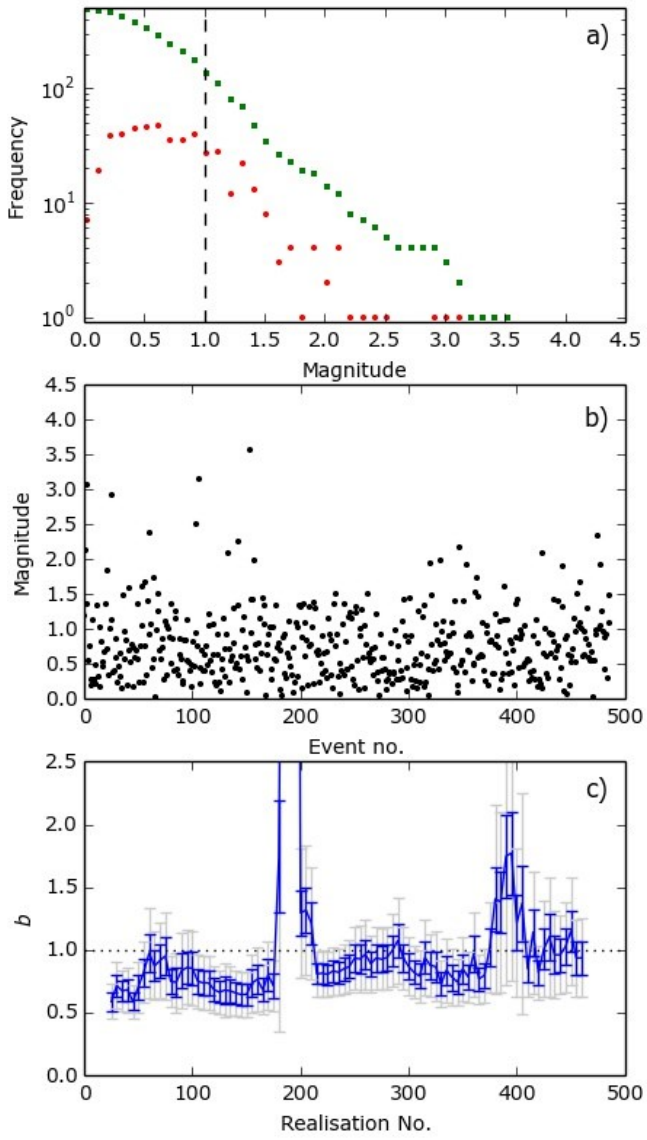

Figure 2.5 – a) A filtered synthetic frequency-magnitude distribution containing 500 events. The synthetic data have a known completeness magnitude of 1.0 and a known b-value of 1.0. The discrete frequency is shown by red circles and the cumulative frequency by green squares. b) Event magnitudes plotted in the order they were generated. The magnitude range is 0.0 to 3.6. c) A moving window containing 50 events moving in increments of 5 events is applied to the catalogue to generate a varying $\tilde{b}$-value against realisation number (which could be time or depth). The blue error bars show one standard deviation calculated using a best fit Equation [2.3]. The grey error bars are calculated using the modified error distribution proposed by Roberts *et al.* (2015) and in this thesis.

Firstly the original catalogue size controls how well defined the discrete cumulative frequency distribution is. The greater the number of events that are generated, the greater the bandwidth of the complete catalogue will be. Full detail on how the synthetic catalogues are generated is given later in Section 3.6.1. Figure 2.5a shows results from a synthetic catalogue with a total of 500 events with a magnitude range of 0.0-3.4. Even with 500 events the sampled discrete distribution does not follow the GR trend above M2.0 events due insufficient catalogue size. This means any of these high magnitude events will affect a small moving window by lowering the resultant $\tilde{b}$-value. In Figure 2.5c the baseline $\tilde{b}$-value appears to be approximately 0.6-0.8 with a few spikes in the data.

The effect of having a small window size relative to the total catalogue size is also visible. In Figure 2.5 the moving window contains 50 events. If the total catalogue of 500 events does not follow a perfect GR distribution then a catalogue ten times smaller is even more likely to have a poor fit. This is demonstrated by the two spikes in the $\tilde{b}$-value in Figure 2.5c. Between realisation number 100-120 $\tilde{b}$ reaches 1.4 and at approximately 340, $\tilde{b}$>2.0. Both anomalies follow a period in Figure 2.5b where no events greater than M2.0 are recorded throughout the 50 event window. This demonstrates how a high $\tilde{b}$-value anomaly can be generated for a catalogue that is known to be 1.0 purely through under-sampling.

Thirdly, by moving the window through a small number of events relative to the window size a false correlation is introduced into the resultant $\tilde{b}$-value evolution with so much overlapping data. In Figure 2.5c a 50 event window is moved through increments of 5 events, this means any given window will be correlated to the 10 previous windows as they will have included a proportion of the same events. This means, in this example, one high magnitude event can lower the $\tilde{b}$-value for 10 successive windows, thus explaining why the typical $\tilde{b}$-value in Figure 2.5 is less than the known value of 1.0.

Overall these factors introduce a significant bias to the conventional estimates of *b*-value and its uncertainty in Figure 2.5c. Here only 27% of the error bars obtained using the standard method to estimate uncertainty (blue) capture the known b=1, whereas 64% of the modified errors using the method described in Chapter 3 successfully capture the known b within one standard deviation error or 67% confidence.

The latter is a significant validation of the new method presented here for the case of a constant value of b and a constant event rate throughout the catalogue. In reality both will vary with time (variable b is examined explicitly in Section 3.7). A high event rate may raise the completeness magnitude, as smaller events will be masked by larger events. Increasing depth of a series of earthquakes may also raise the completeness magnitude as energy from smaller earthquakes will be attenuated before they can be recorded at the surface. Although these are not variables that will be considered in this study it is worth stating that they are not negligible in real catalogues.

2.2.2.3 ZMAP

The most commonly used open source software for evaluating seismic catalogues is ZMAP (Wiemer, 2001). As well as using moving window analysis, this software uses overlapping circles (2D) and spheres (3D) of fixed area/volume or number of events to create a dense spatial grid of data points (Wiemer and Benoit, 1996). This methodology removes the bias of visual inspection, however the recommend sample size is quite small at only 100 events (Wiemer and McNutt, 1997; Sanchez *et al.*, 2004; Jacobs and McNutt, 2010). The analysis presented in Chapter 3 and in Roberts *et al.* (2015) suggests a larger recommended minimum of $N_c \geq 200$.

2.2.2.4 Penalized-likelihood method for spatial Voronoi tessellation

A new approach has recently been developed to assess the spatial variation of *b*-values. Kamer and Hiemer (2015) use multi-model Voronoi tessellation to calculate the *b*-value in each Voronoi polygon. They then estimate the overall likelihood for each model and rank them using the Bayesian Information Criterion (Schwarz, 1978). The best models are then stacked to obtain an ensemble solution. Their results suggest previously reported *b*-value variations obtained using classical fixed radius of nearest neighbour methods (i.e. done in ZMAP) are likely to have been overestimated, mainly due to subjective parameter choice (Kamer and Hiemer, 2015). This is an improvement on current practice, but one issue remains with their results. They used the sub-optimal 'maximum curvature' method (MaxC) to estimate the completeness threshold. In Chapter 3 I show that this method severely underestimates *Mc* (in their Figure 8) and consequently underestimates *b*.

In Chapter 4 I propose a variation on the moving window method that aims to eliminate subjective bias by iterative random sampling of non-overlapping catalogue windows. This is similar to the method used by Kamer and Hiemer (2015) except that I use all of the samples to find the underlying trend, and I apply a minimum threshold for the number of events in a sample. I also show results as a full probability density function of $\tilde{b}$, rather than single finite value with an associated error. This allows exploration of the full (potentially non-Gaussian) error structure.

2.3 Geological history of Rum

This thesis is motivated by a need to understand and correctly model seismic frequency-magnitude distributions, and to assess their potential as a key tool in eruption forecasting. However it is also important that we attempt to study and quantify the processes that may be causing volcanic earthquakes. It is not possible to do this directly with a modern volcano at the resolution required. Accordingly I carried out a field mapping campaign to investigate such potential seismic sources in their geological context on the Isle of Rum in the North West Scottish Highlands. Part of the British Palaeogene Igneous Province, Rum contains an exhumed ancient volcanic magma chamber and its associated structures. Studying the outcrops here allows for the opportunity to study the fossilised remains of an active magma chamber and associated deformation features. The excellent exposure in the Central Intrusion allows for very detailed studies and robust data to be collected and is described in Chapter 6. The following sections detail the geological setting of Rum, focussing on the youngest least-deformed volcanic suite, the Central Intrusion.

2.3.1 The British Palaeogene Igneous Province

The British Palaeogene Igneous Province (BPIP) contains a number of exhumed extinct ancient volcanos (Thompson, 1982; Mussett *et al.*, 1988) that are accessible along the west coast of Scotland making them ideal field localities. The BPIP runs all the way down the west coast of Great Britain; however we can consider the centres of the North West coast to be more specifically part of the Hebridean Igneous Province (HIP) (Emeleus, 2005a). The Palaeogene lava fields, dyke swarms, sill complexes and central complexes of the HIP are part of a much larger North Atlantic Igneous Super-province that extends to east and west Greenland. It was formed as a consequence of a large mantle plume that initiated the opening of the North Atlantic Ocean in the early Cenozoic (Jolley *et al.*, 2003), and continues today along the mid-Atlantic ridge and under Iceland; however it is much smaller and less productive that

at its formation. The HIP extends from Arran in the South, to Skye and St Kilda, off the northwest coast of the Outer Hebrides (Figure 2.6).

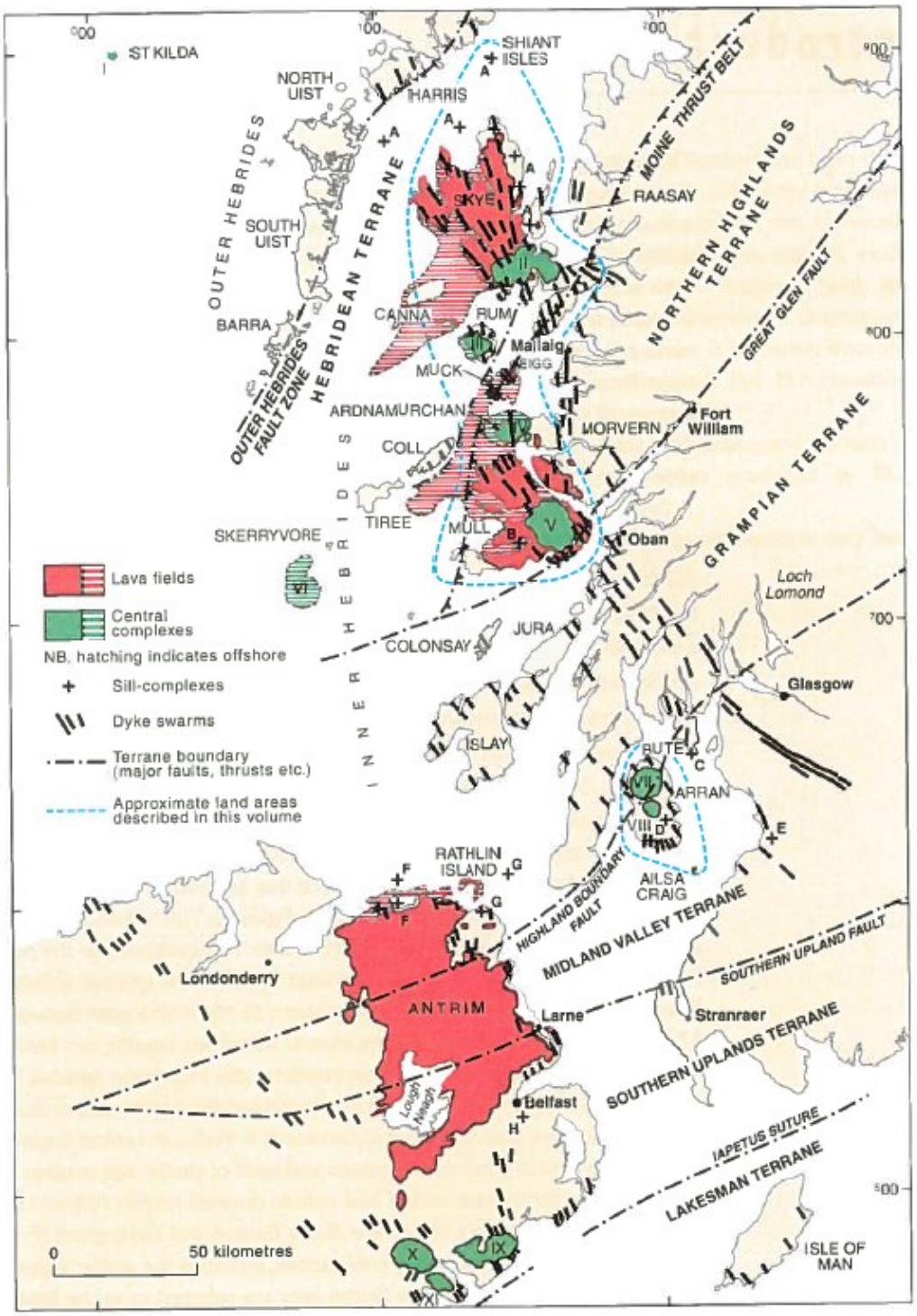

Figure 2.6 - Map showing the positions of the Palaeogene central complexes, lava fields, sill-complexes and dyke swarms in the BPIP (Emeleus, 2005a)

The majority of the lava fields exposed today, both onshore and offshore, were originally erupted sub-aerially, predominantly from fissure-type feeders, now represented as laterally continuous near linear dyke swarms. The NW-SE trending dyke swarms associated with the Skye and Mull lava fields have formed at right angles to the rift margin showing NE-SW extension along the northwest European margin. The central complexes are deeply eroded roots of ancient volcanoes. They mark an important change in the character of igneous activity, from widespread feeders of lava fields to much more localised and intense magmatism. They were formed when magma emplacement in the upper continental crust along the rift margin reached anomalously large proportions. The BPIP can be traced along an approximately 40 km wide zone from Lundy in the Bristol Channel, through northeast Ireland and along the west coast of Scotland (Emeleus, 2005b). There are five central complexes exposed in the HIP; Skye, Rum, Ardnamurchan, Mull and Arran.

Typically the central complexes occur within basement rocks exposed in elevated footwalls of Mesozoic faults (Figure 2.7). They have been elevated to their current topographically high positions by syn-extensional footwall uplift (Roberts and Holdsworth, 1999). Rum and Skye are both situated on a west-dipping half graben in the hanging wall of the Minch Fault. The cross-section in Figure 2.7 shows how the basement rocks on Rum have been uplifted above sea level, and how a series of easterly dipping extensional normal fault has formed the numerous Islands off the West Coast of Scotland. The Camasunary Fault bounds Rum to the east (Roberts and Holdsworth, 1999) and has been identified as a submarine escarpment in bathymetry images of the seafloor (Smith, 2012).

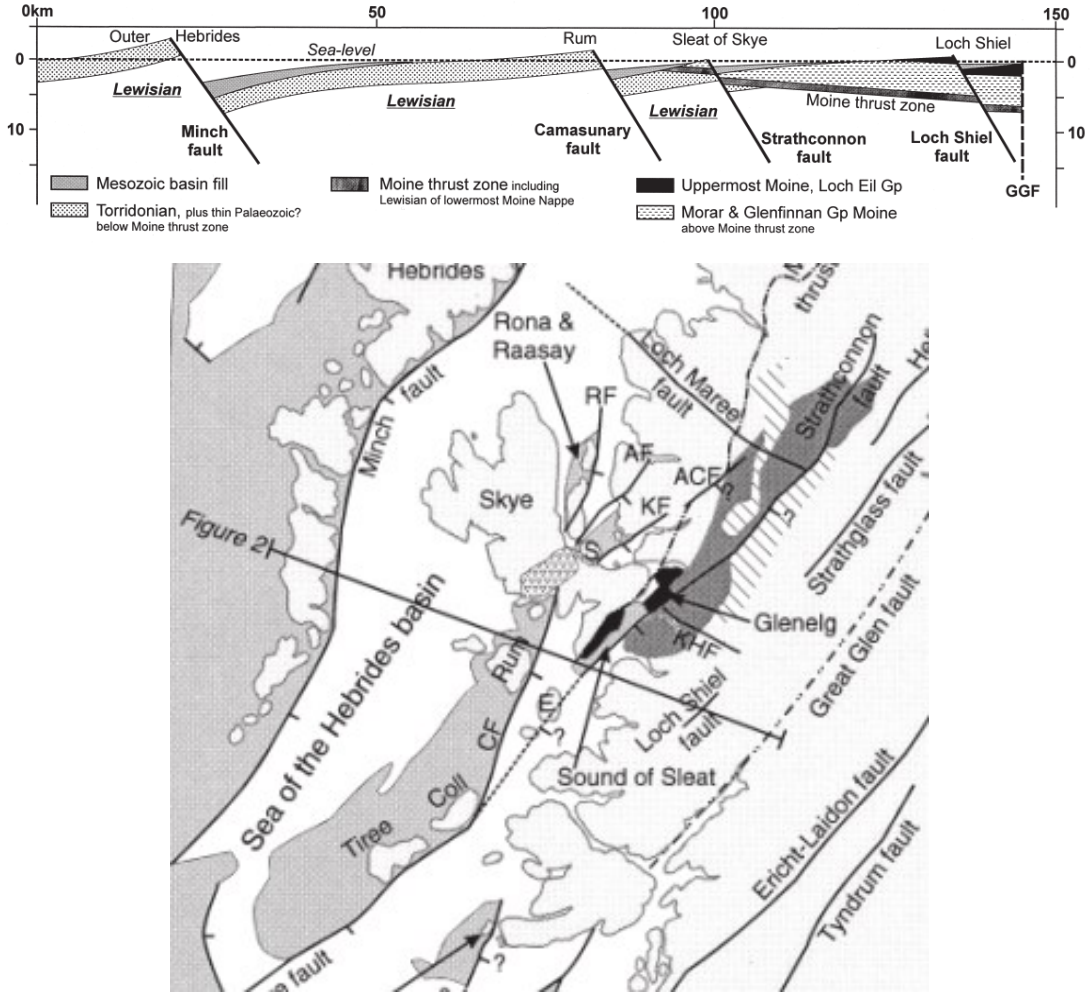

Figure 2.7 - Top: Schematic section from the Outer Hebrides to the Great Glen Fault showing how the elevated footwalls of Mesozoic faults are exposed above sea level (Roberts and Holdsworth, 1999) Bottom: Orientation of the section.

2.3.2 Rum

Rum is a small island situated approximately 25 km off the northwest coast of Scotland. It is located on a NE-SW trending ridge of Lewisian and Torridonian basement, bound on either side by south-easterly dipping normal faults (Roberts and Holdsworth, 1999). It was intruded by one of the central complexes associated with the early Palaeogene HIP and has been uplifted to its current topographical high above sea level by rotation due to the late Mesozoic extensional faulting. There are two key phases in the formation of the volcanic centre on Rum; the first is the activation of the Main Ring Fault (MRF) and the formation of the Northern Marginal

Zone (NMZ), the Western Granite and the Southern Mountains Zone (SMZ), and the second being the emplacement of the basic and ultrabasic layered suites (Emeleus, 2005a).

During the first phase the Lewisian Gneiss and Torridonian Sandstone were tilted to give them their westerly dip direction. There was also early movement of the Long Loch fault (LLF), a dextral strike-slip fault running north-south through the centre of the island (Figure 2.8). In the early Paleogene there was doming of the Torridonian to the west of Rum due to emplacement of the Western Granite. The Western Granite is bound by the MRF, therefore initial displacement on the fault must be synchronous with emplacement.

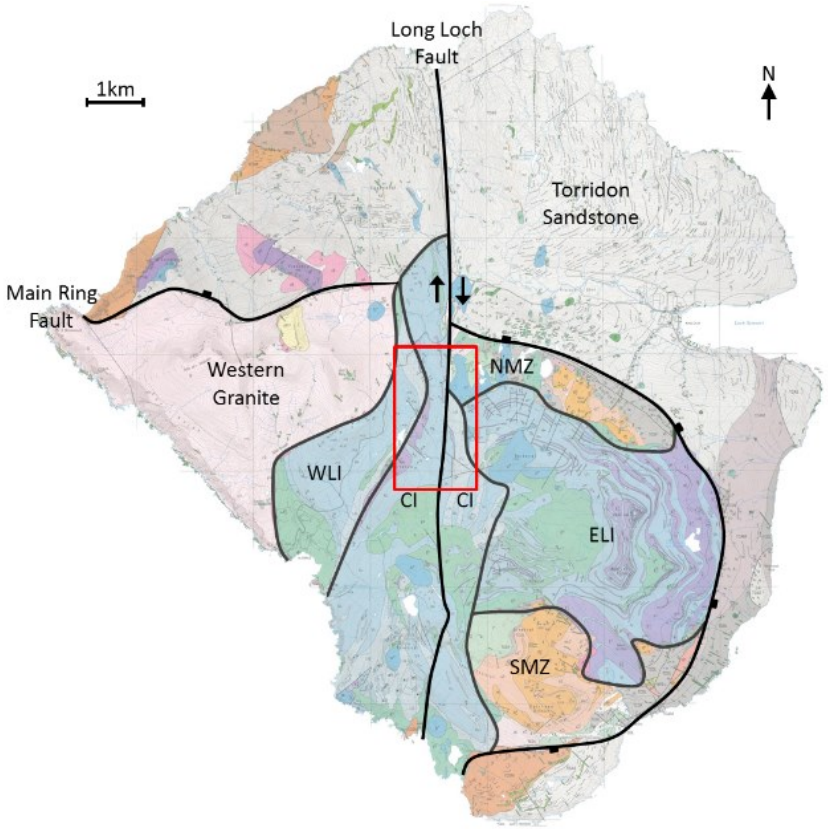

Figure 2.8 - Geological map of Rum (Emeleus, 1994) with key faults and units highlighted. The volcanic units forming the central complex are the Western Granite, Northern Marginal zone (NMZ), Southern Mountains zone (SMZ), Eastern Layered Intrusion (ELI), Western Layered Intrusion (WLI) and the Central Intrusion (CI). The study area is marked by the red box.

Next was the main phase of uplift along the MRF of approximately 1-1.5km (Troll *et al.*, 2000). Within the NMZ the Diabeg Formation of the Lower Torridonian Sandstone has been uplifted to be topographically higher than the younger Applecross Formation seen to the north. A period of subsidence within the MRF followed, forming the Rum caldera. As the caldera walls steepened blocks of Torridonian sandstone collapsed into the basin forming the Corie Dubh Breccia's in the NMZ. These breccia's lack igneous clasts indicating the onset of volcanism had not yet occurred.

The rhyodacite intrusions found in the NMZ are the first evidence of active volcanism. Ar/Ar dating of feldspars in the Meall Brec and Am Màm intrusions (Figure 2.8) dates them at 60.33 ± 0.21 Ma (Troll *et al.*, 2008). The entire sequence of events on the Isle of Rum, from violent ignimbrite eruptions, intrusion of granite and the ultrabasic layered suite, to the rapid erosion of 0.7–2 km of overburden down to the heart of the Rum volcano. A minimum estimate of the time through which this sequence of events could have occurred is as little as 500k years.

In terms of driving mechanisms for the formation of the caldera, the classical view of collapse of the magma chamber due to evacuation of the underlying magma chamber is widely accepted. However it cannot be the only mechanism responsible (Troll *et al.*, 2000). During the first phase (Figure 2.9) the collapse was preceded by doming. There were no volcanics found in the collapse-breccia, and the structure and orientation of the MRF zone have all been identified in laboratory and theoretical modelling of caldera formation due to tumescence for various other volcanoes (Komuro *et al.*, 1984; Komuro, 1987; Gudmundsson, 1988; Marti *et al.*, 1994; Gudmundsson *et al.*, 1997; Gudmundsson, 1998). During the second phase (Figure 2.9) the rhyodacite feeders initiated during resurgence as a result of extensional strain. The reason for the small localised nature of the rhyodacite is that the initial ring fractures during doming are inward-dipping thrust faults; therefore it is very difficult for the magma to escape. After partial evacuation of the magma chamber, subsidence occurred altering the

faults to inward-dipping normal faults. In places there are several ring faults seen on Rum due to the imperfect nature of the subsidence.

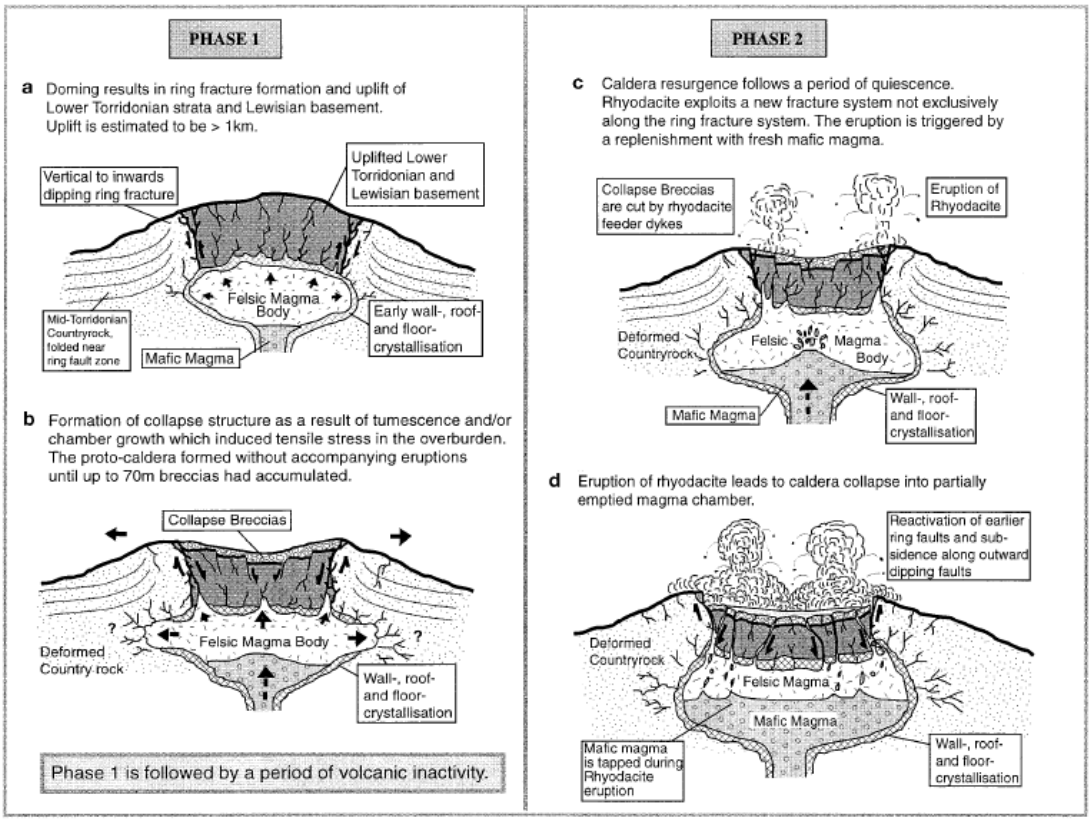

Figure 2.9 - Diagrams showing the possible evolution of the Rum caldera (Troll *et al.*, 2000).

The reason for the caldera collapse may have been due to a change in the underlying magma chamber preceding the first eruption (Troll *et al.*, 2000). Palaeocene basalts, dated at 60.65 ± 0.07 Ma (Chambers *et al.*, 2005), found within the MRF and SMZ are thought to be representative of the Eigg lava formation. These predate the first activity by as little as 40 k years or as much as 600 k years, however it is thought to be more likely to be closer to 40 k. A final major period of uplift on the MRF completed the first phase of activity on Rum.

Figure 2.10 summarises the ages of the second phases of magmatism dominated by the emplacement of various igneous bodies. The cone sheets, radial dykes and

regional dykes found across Rum are believed to be an early phase of volcanism. However the exact age and relationship to the major igneous units is undefined. The Eastern Layered Ultrabasic suite forming the central mountains zone on the island has been dated at 60.53 ± 0.04 Ma (Hamilton, 1998), which must be incorrect as this predates the initiation of the formation of the caldera. Troll *et al.* (2008) give a mean age of magmatism as 60.33 ± 0.21Ma.

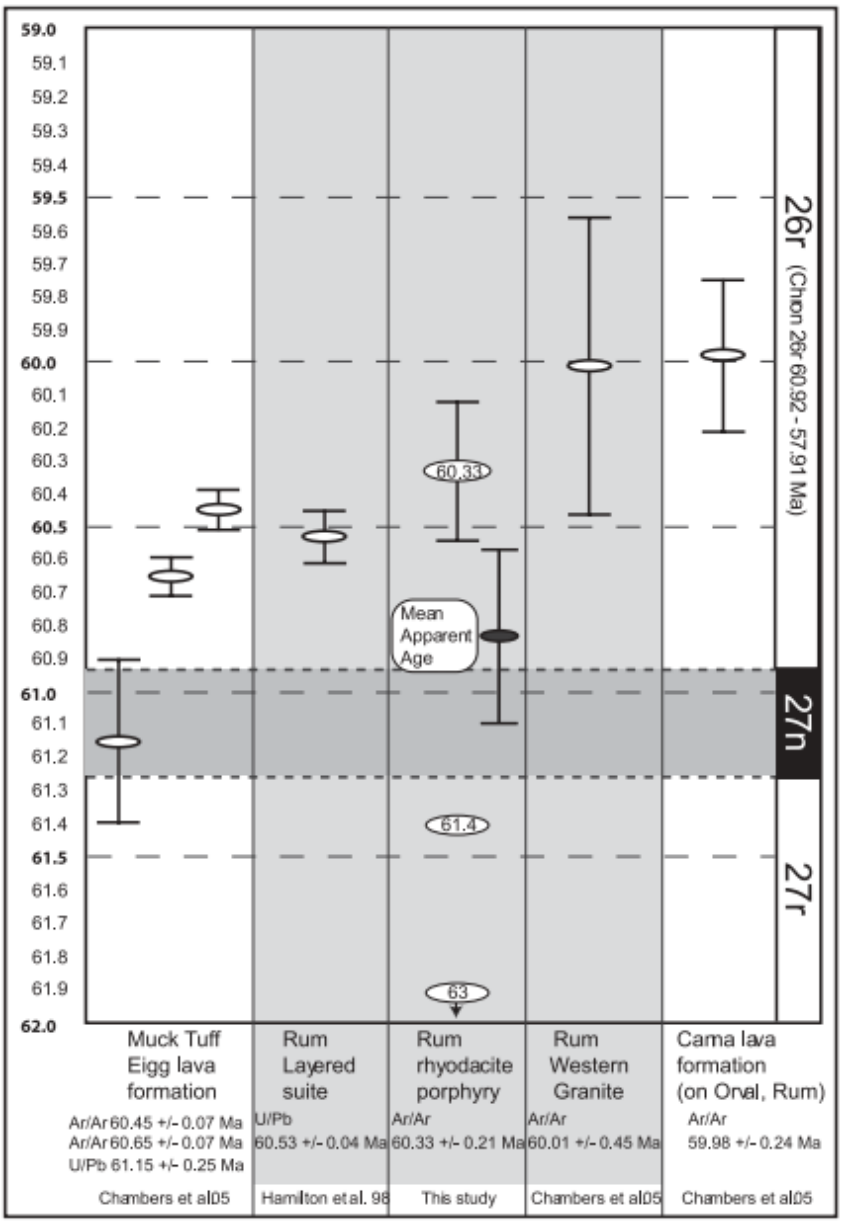

Figure 2.10 – Taken from Figure 7 in Troll *et al.* (2008). The timeline shows the age of the Rum volcanic suites.

The layered suite cross-cuts the rhyodacite in the field, so this age cannot be accurate. To address this Hamilton *et al.* used independent U/PB dating which generally yields ages ~1% older than Ar/Ar dating used by Troll *et al.* (2008), thereby explaining this discrepancy. The WLI is thought to have formed at a similar time to the ELI; however there is no field evidence to suggest which is younger. The CI cuts all previous volcanism and the MRF at both the northern and southern side of the island, therefore uplift must have completely finished. Ductile deformation within the western intrusion breccias suggests there was reactivation along the Long Loch Fault at the time the CI was being emplaced. Accordingly, the Long Loch Fault is thought to have acted as a conduit for the CI (McClurg, 1982; Emeleus et al., 1996; Emeleus, 2005a; Troll et al., 2008; Emeleus and Troll, 2014; Mattsson et al., 2014). There are approximately 40 volcanic plugs on Rum, ranging from 210 m to 610 m in diameter, most of which are peridotitic (Volker and Upton, 1990). They vary in age but have generally been interpreted as volcanic conduits though which olivine-rich magmas flowed for substantial periods (Holness *et al.*, 2011).

The Western Granite is overlain by the Canna lava formation, which has an estimated age of 59.98 ± 0.24 Ma (Chambers *et al.*, 2005). From this structural relation, the granite must have been emplaced at depth at a time between the ultrabasic suite and the Canna lava flow (Figure 2.10). Conglomerates from the ultrabasic suite, the western granite and the rhyodacites are inter-bedded in the Canna lavas, indicating igneous activity had ceased, and unroofing began prior to the lava flows. With the onset of volcanism dated at 60.33 ± 0.21 Ma, this means the lifetime for igneous activity could be as short as 500 ka years.

2.3.3 The Central Intrusion

The CI is a distinct series situated between the Eastern and Western Layered Suites (McClurg, 1982). Like the ELI and WLI it has layered units, however there are many fewer cycles of deposition, and their sources have been widely debated (Wadsworth, 1961; Volker, 1983; Wadsworth, 1992; Emeleus *et al.*, 1996). A prominent feature in the

CI are the extensive igneous breccias on either side of the LLF, striking roughly north-south. The outcrops are approximately linear and strike parallel to the LLF. The CI peridotites are divided into three major members: the Ruinsival, the Long Loch, and the An Dornabac members. However, these division are probably superfluous as the CI is likely to be a set of collapsed members of the ELI and WLI (Emeleus *et al.*, 1996; Emeleus, 1997). The relationship between the ELI and WLI is complex as they are not simply cumulate layered sequences; they have undergone tectonic deformation associated with the LLF. Also, as the units are separated spatially there is no way of confining the relative timing.

2.3.4 The Central Intrusion breccias

There are several zones of breccias within the CI likely originating from different processes, however this study is focussed on the breccia forming the contact with the WLI. The breccias typically have a grey feldspathic matrix containing angular peridotite blocks ranging in size from centimetre to metre scale. Mattsson *et al.* (2014) summarises the results of the previous studies. It was originally proposed that the breccias were of intrusive origin due to lack of sorting and the intrusion showing varying degrees of force in different areas (Donaldson *et al.*, 1973). McClurg (1982) furthered this observation by suggesting the CI was all of intrusive origin, acting as a principal feeder system to the ultrabasic layered complex of Rum. Wadsworth (1992) found the breccia matrix to be of the same composition as the feldspathic peridotite of the WLI and ELI, and thus concluded there must be some cumulate residual magma, not all associated with the central Long Loch feeder zone. This was additionally supported by outcrops showing collapse breccia with no upwards migration. A conceptual model for the mechanisms of brecciation is based on the extension and sliding of blocks forcing evolved magma to migrate upwards along block boundaries (Volker and Upton, 1990; Mattsson *et al.*, 2014). At the northern end of the CI, both easterly and westerly dip-directions within the cumulates were found, while to the east of the LLF, the dips steepen closer to the fault, from 20°-60°

(McClurg, 1982; Wadsworth, 1992). Outcrops within the CI show examples of all the mechanisms sketched in Figure 2.11.

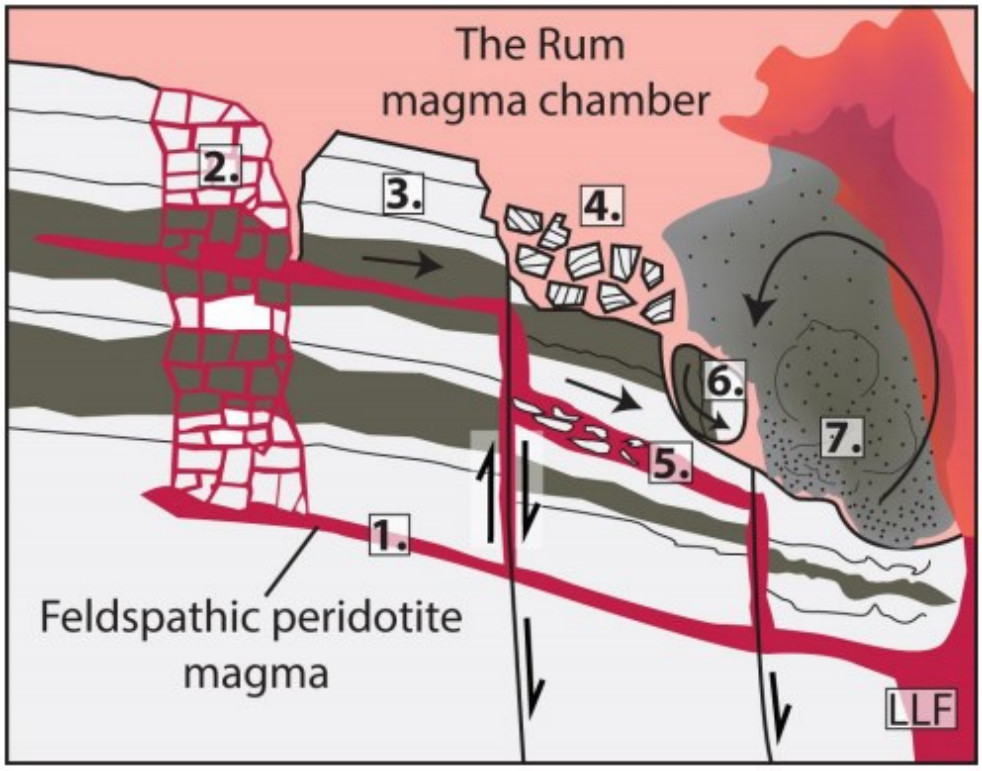

Figure 2.11 - Conceptual model of breccia formation from Mattsson et. al. (Figure 69, 2014) 1) Intrusion along cumulate bedding. 2) Hydraulic fracturing forming clasts supported braccia. 3) Megablocks sliding along planes lubricated by intrusive material. 4) Talus breccia forming at the base of faults. 5) Shearing occurs in intrusive planes. 6) Rotational collapse of clasts. 7) Large convection clouds of magma settling to form pebbly peridotite. Photos of hese units are described in Section 6.3.

2.3.5 Glacial erosion

The current landscape is a result of glaciation in the most recent Ice Age ~20 ka, with movement of the ice sheet generally being north to south across the island (Clark *et al.*, 2012) leaving near 100% exposure of the underlying rock across the large parts of the field area. This level of exposure, and the resulting potential for a broad-band study of the scaling properties of the faults and fractures, makes the field area ideal for the type of study described in Chapter 6.

2.4 Fractal Dimensions

In Chapter 6, I present a comparison of fracture data collected in the field on Rum with seismic data from El Hierro. El Hierro provides a direct analogue of a currently active, well-monitored and recently interpreted volcano in terms of volcanic deformation processes; with an ancient exhumed volcano in Rum, where the outcrops of similar deformation can be directly observed and quantified.

This is achieved by comparing the fractal dimensions of each data set. Fractal dimensions are important because the localisation of deformation of the population of faults, fracture and the clustering of earthquake hypocentres is a key control on the potential to generate larger events, and in turn to develop pathways for subsurface fluid flow, including magma. Critically, fractal dimensions can be obtained both for structural and seismic data, presenting a unified framework for making a comparison between an exposed former volcano system and a modern one accessible only by seismic observation. The methodology proposed in this section is largely summarised from the textbook by Turcotte (1997).

2.4.1 What is a fractal?

A fractal is a scale-invariant rough or fragmented geometric shape that can be subdivided into parts, each of which is similar to the whole in some way (Feder, 1988). Fractal structures are common in mathematics, and can either be self-similar (i.e. isotropic scale invariance) or self-affine (i.e. orientation-dependent scale-invariance). Many geophysical and geological phenomena, such as rock fragmentations, faulting, earthquakes, volcanic eruptions, mineral deposits and oil fields, etc. exhibit self-similar properties characterised by power-law scaling relations. For example the frequency-magnitude distributions of these systems exhibit a power-law dependence on source rupture length or area, directly equivalent to the Gutenberg-Richter distribution for earthquake magnitude. In terms of object size, a fractal set can be defined as:

$$N_i = \frac{C}{r_i{}^D} \qquad [\ 2.4\ ]$$

Where N_i is the number of objects (i.e. fragments) with a characteristic linear dimension r_i in the i^{th} order, C is the constant of proportionality, and D is the fractal dimension. When the fractal dimension is an integer it is a Euclidean Dimension. For D=0 is the Euclidean dimension of a point, D=1 is a line, D=2 a square, and D=3 a cube. In the general case the dimension is not an integer but is instead fractional, or 'fractal' for short (Turcotte, 1997). In order to determine D we rearrange [2.4] to give:

$$D = \frac{\log N_{i+1}/N_i}{\log r_i/r_{i+1}} \qquad [\ 2.5\ ]$$

It is possible to construct mathematical fractal structures deterministically; their initial conditions are fully specific and not random or stochastic (Turcotte, 1997). Two examples of mathematical fractal structures are the Cantor Set and the Sierpinski Carpet. Figure 2.12a shows the construction of a Cantor Set. A line of unit length is divided into 3 parts at first order so that $r_1 = \frac{1}{3}$; the two end segments are retained and the central segment is discarded so that $N_1 = 2$. This process is repeated at second order so that $r_2 = \frac{1}{9}$ and $N_2 = 4$. From Equation [2.5] we find that $D = \log 2/\log 3 = 0.6039$. This similarity of appearance in a cascade of different scales is one of the hallmarks of a fractal set.

The Sierpinski Carpet (Figure 2.12b) is constructed by using the same methods in two dimensions. A square with sides of unit length is divided into nine equal sizes squares. At each order the central square is removed and the eight external squares are retained. At first order, $r_2 = \frac{1}{9}$ and $N_2 = 4$. At second order $r_2 = \frac{1}{9}$ and $N_2 = 4$. Thus applying Equation [2.5], $D = \log 8/\log 3 = 1.8928$. These values are useful references for estimated fractal dimensions of real data sets to be examined for real data in Chapter 7.

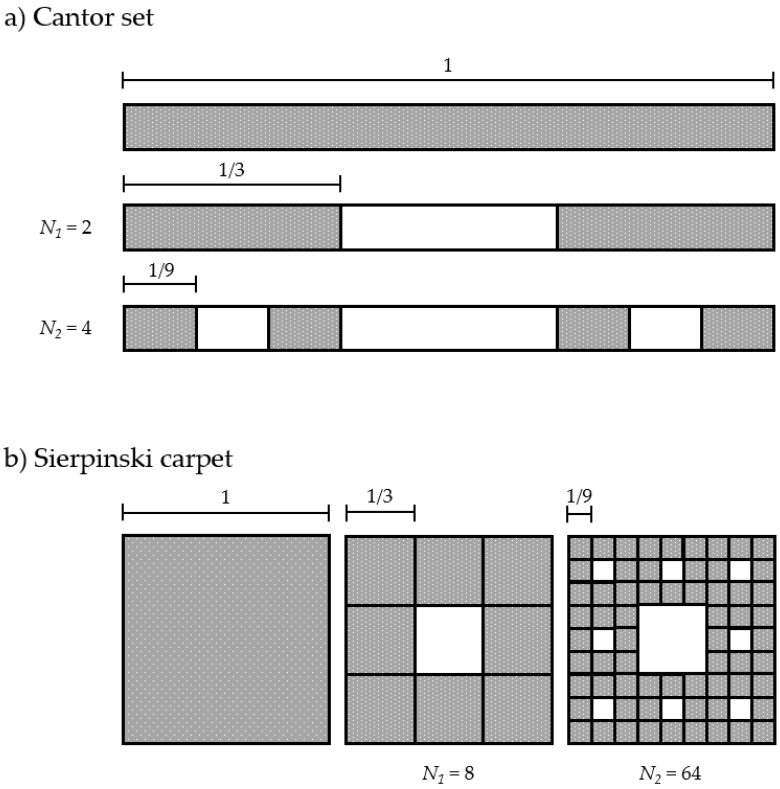

Figure 2.12 – Illustration of a 1st and 2nd order a) Cantor Set, and b) Sierpinski Carpet.

2.4.2 Methods for estimating fractal dimensions

2.4.2.1 The ruler and box-counting methods

The 'ruler' and 'box-counting' methods are simple geometric methods for estimating the fractal dimension of an object in 1D and 2D respectively. For the ruler method, a ruler of fixed length r_i, is used to measure the length of the object perimeter P_i. The process is repeated for varing fixed lengths. The length of the perimeter is given by:

$$P_i = r_i N_i \qquad [\ 2.6\ ]$$

Where N_i is the number of lengths required to measure the length of the perimeter at order i. Substituting in N_i from Equation [2.4] gives:

$$P_i = \frac{C}{r_i^{D-1}} \qquad [\ 2.7\ ]$$

Therefore, the gradient of a linear log-log plot of perimeter against ruler length, is equal to 1-*D*, where *D* is the fractal dimension. For example the ruler method can be used to measure the fractal dimension and contours of coastlines and lava flows (Mandelbrot, 1967; Bruno *et al.*, 1992; Gaonach *et al.*, 1992; Bruno *et al.*, 1994).

The box-counting method should be performed over as wide a range of box sizes as is feasible, however these should be between the largest and smallest fragments or fracture spacing. Beyond these limits the slope of the curve tends asymptotically to -2.0 and -1.0 due to finite size sampling effects. It is not advisable to decide these limits in advance. Instead the initial analysis should be over the widest possible range of box sizes to define the valid range objectively (Walsh and Watterson, 1993). The box-counting method has a wider range of applicability (Pfeiffer and Obert, 1989) than the ruler method. For example it can be applied to a distribution of points as well as a continuous curve. In this method a regular grid of square boxes with length r_i is laid over the data set. N_i is the number of boxes requires to completely overlay the data. In the case of a point distribution this is the number of boxes containing at least one data point. The fractal dimension found using the box-counting method is known as the capacity dimension, D_0, as it measures the ability of a fractal set to fill space.

2.4.3 Probability and clustering

In the ruler method the fractal dimension of a set of lines in two dimensions (for example an outcrop of a set of faults or fractures) depends on the probability p_i, that a step of length r_i, will include a line segment. For example consider the Cantor Set in Figure 2.12a. At zero order $r_0 = 1$ and $p_0 = 1$; at first order $r_1 = \frac{1}{3}$ and $p_1 = \frac{2}{3}$; and at second order $r_2 = \frac{1}{9}$ and $p_2 = \frac{4}{9}$. The probability that a step r_i along a 1D transect (where the Euclidean sampling dimension *d*=1), will include a line segment is then:

$$p_i = r_i^1 N_i \qquad [\,2.8\,]$$

where N_i is the number of line segments of length r_i. Taking $C = 1$ and substituting for N_i in Equation [2.4]we obtain:

$$p_i = r_i^{1-D} \qquad [\ 2.9\ ]$$

In the case of a Cantor Set (Figure 2.12a) the probability that a step length $r_i = \left(\frac{1}{3}\right)^i$ encounters a line segment is $p_i = \left(\frac{2}{3}\right)^i$ so that $D = \log 2/\log 3 = 0.6039$ in this case, as previously obtained. For a linear log-log plot of step length against probability, it follows that the gradient is equal to 1-*D*, where *D* is the fractal dimension. Figure 2.13 gives an example of the ruler method applied to fracture data from the Isle of Rum.

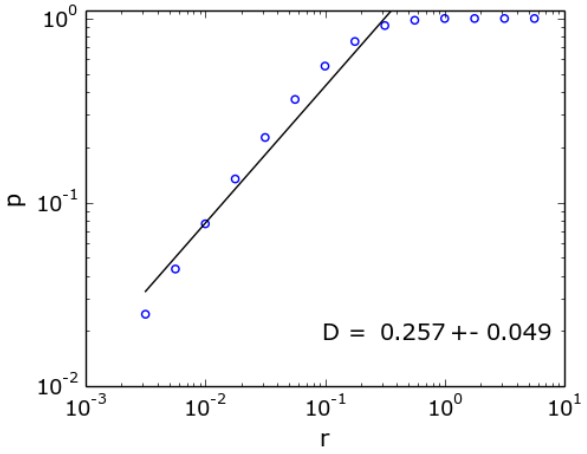

Figure 2.13 – Example of fractal clustering and the calculation of fractal dimension, *D*, for 234 fractures on the Isle of Rum, Scotland, taken from Chapter 7. The circles gives the fraction of intervals *p*, of length *r*, that include a fracture. The solid line represents the best-fit Equation [2.9] with *D*=0.257.

Fractal clustering has been applied to numerous seismic catalogues. In one early example the seismicity around Etafe Island, New Hebrides arc from 1978-84 was examined. Some 49 earthquakes exceeded the minimum magnitude for detection here, producing a relatively low fractal dimension of *D*=0.255 (Smalley *et al.*, 1987). The well-studied San Andreas Fault zone was found to have *D*=0.67, and the San Gabriel Fault *D*=0.43-0.46 (Lee and Schwarz, 1995), implying distinct spatial variability of clustering properties.

In the 2D box-counting method we are trying to determine the probability that a square box of size r_i contains an object (data point, line or line segment). For the

Sierpinski Carpet (Figure 2.12b) at zero-th order $r_0 = 1$ and $p_0 = 1$; at first order $r_1 = \frac{1}{3}$ and $p_1 = \frac{8}{9}$; and at second order $r_2 = \frac{1}{9}$ and $p_2 = \frac{64}{81}$. The probability that a square box of size r_i in two dimensions (d=2) will contain an object is then:

$$p_i = r_i^2 N_i \qquad [\ 2.10\ ]$$

And substituting N_i from Equation [2.4] gives:

$$p_i = r_i^{2-D} \qquad [\ 2.11\ ]$$

In 3D the probability generalises to:

$$p_i = r_i^{3-D} \qquad [\ 2.12\ ]$$

Therefore further generalisation to working in any given sampling dimension d, gives:

$$p_i = r_i^{d-D} \qquad [\ 2.13\ ]$$

2.4.4 Pair correlation

The pair-correlation distribution $C(r)$, is defined as the number of pairs of points whose separation is between $r - \frac{1}{2}\Delta r$ and $r + \frac{1}{2}\Delta r$ per unit are (Vicsek, 1992). First a point is selected, and the distances to all other points is determined. This is then completed recursively for all the other points. This produces a set of $N(N-1)$ data points, where N is the original number of points. In 1D sampling the number of pairs within each bin $(r - \frac{1}{2}\Delta r, r + \frac{1}{2}\Delta r)$ is divided by Δr to obtain a density $\rho(r)$. For a two-dimensional (2D) distribution the number in each bin is divided by $r\Delta r$, and for a three-dimensional (3D) distribution $r^2\Delta r$. The pair-correlation distribution is then defined as (Vicsek, 1992):

$$C(r) = \frac{1}{N}\sum_{r'} \rho(r + r')\rho(r') \qquad [\ 2.14\ ]$$

where N is the number of particles in the cluster/data set. This gives the probability of finding a particle at the position $r + r'$, if there is one a r'. If the points are randomly distributed in space the pair-correlation distribution is exponential:

$$C(r) \sim e^{-r/r_0} \qquad [\ 2.15\ ]$$

This highlights the fact that even random distributions are clustered, albeit at short range r_0. The same is true of random processes in time – a Poisson process likewise has an exponential distribution of inter-event times (Touati *et al.*, 2011). In the case of scale-invariant spatial clustering, a power-law dependence is obtained instead:

$$C(r) \sim r^{\alpha} \qquad [\ 2.16\ ]$$

where α is related to the fractal dimension of the distribution in the general case by:

$$\alpha = d - D \qquad [\ 2.17\ ]$$

For a linear log-log plot of r against $C(r)$, the gradient is equal to the modulus of α. Therefore:

$$D = d - |gradient| \qquad [\ 2.18\ ]$$

For shallow worldwide seismicity the pair correlation function exhibits a power law with $D \approx 1$ (Kagan and Knopff, 1980). The level of clustering is consistent with the spatial distribution of aftershocks in California where $D \approx 2$ (Robertson *et al.*, 1995). The fractal dimension found using the box pair-correlation method is known as the correlation dimension, D_2, as it takes into account the way one element in the fractal set is correlated to all the others.

This technique is equivalent to the box-counting technique for point events. Both methods give the same fractal dimension in the case of scale-invariant distributions. Figure 2.14 gives an example of the pair-correlation distribution for fracture data from the Isle of Rum.

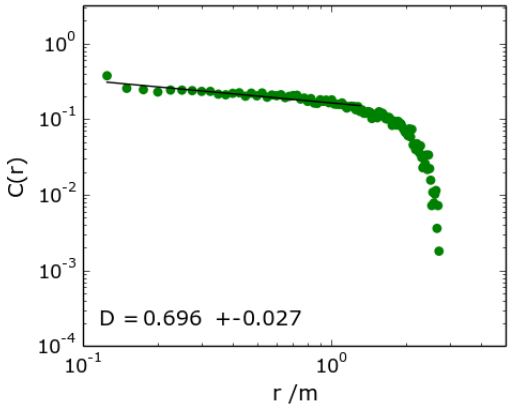

Figure 2.14 - Example of the pair-correlation, *C(r)*, as a function of spacing, *r*, for a transect containing 238 fractures on the Isle of Rum, Scotland. The solid line is the best-fit correlation, described in Equation [2.14], for *r*, up to half the total transect length.

2.4.4.1 Nearest neighbour correlation

An abbreviation of the pair-correlation method is to reduce $C(r)$ to only use the minimum value between each point. This method will simply produce n data points.

2.4.5 Fractal interpretation of the seismic *b*-value

The Gutenberg-Richter law (Equation [2.1]) states there is an exponential relationship between the frequency of earthquakes and their magnitudes. However, it has been suggested that the *b*-value itself is fundamentally related to the fractal dimension of the source rupture length, here denoted D_{mag} (Aki, 1984; Turcotte, 1997). The relationship between b and D_{mag} can be derived by expressing the Gutenberg-Richter equation in terms of seismic moment, *M*, and rupture area, *A*. The relationship between *M* and *A* is (Kanamori and Anderson, 1975):

$$M = \alpha A^{3/2} \qquad [\ 2.19\ ]$$

where α is a constant. Earthquake magnitude *m* is related to *M* by:

$$\log M = cm + d \qquad [\ 2.20\ ]$$

where c and d are constants. Combining Equations [2.19] and [2.20] gives:

$$\log N = -\frac{3b}{2c}\log A + \log\beta \qquad [\ 2.21\ ]$$

$$\text{with} \quad \log\beta = \frac{bd}{c} + \log\alpha - \frac{b}{c}\log\alpha \qquad [\ 2.22\ ]$$

[2.21] can then be written as:

$$N = \beta A^{-3b/2c} \qquad [\ 2.1\ ]$$

A comparison with the definition of a fractal given in Equation [2.4], assuming $A \sim r^2$, shows the fractal dimension of distributed seismicity is:

$$D = \frac{3b}{c} \qquad [\ 2.23\ ]$$

Taking the theoretical relation of c=1.5 (Turcotte, 1997) leaves:

$$D = 2b \qquad [\ 2.24\ ]$$

Thus the fractal dimension of regional seismicity is simply twice the seismic b-value.

Legrand (2002) relaxed the common assumption that c is constant, based on empirical observation. Using the relationship between the scalar seismic moment and surface magnitude (Equation [2.20]) Legrand (2002) calculated c for small, intermediate and large earthquakes. The results are summarised in the Table 2.1.

Table 2.1 – The relationship between seismic moment M, and earthquake magnitude m, (Equation [2.20]) to calculate the constant, c, in order to relate the fractal dimension D, and seismic b-value b, using Equation [2.24] (Legrand, 2002).

	Small events	Intermediate events	Large events
M and m relation	$\log M_0 \propto m$	$\log M_0 \propto \frac{3}{2}m$	$\log M_0 \propto 2m$
c	1	1.5	2
Fractal dimension	$D = 3b$	$D = 2b$	$D = 1.5b$

2.4.6 Multifractal set

A multifractal set is a generalisation of a fractal set in which a single exponent (fractal dimension) is not enough to describe its dynamics. Higher-order dimensions can be calculated by weighting an object by an attribute, such as length or recorded slip D_i, and compared with the capacity dimension D_0. Such analysis in particular has been applied to fault populations. For example Cowie *et al.* (1995) modelled the evolution of a synthetic fault population using a resistor network analogue (Cowie *et al.*, 1993). They reproduced realistic patterns of faulting despite the model simplicity. In the initial stages fracture is dominated by random nucleation. In this phase they found that $D_0 \approx D_1 \approx D_2$, indicating the fault pattern approximates a homogeneous fractal and is (uniformly-random) space filling. However, as faults grow and coalesce in the model and deformation concentrates on one or more dominant faults, a multifractal pattern gradually emerges where $D_0 > D_1 > D_2$ (Cowie *et al.*, 1995). The progressive decrease in D_1 and D_2 through time is indicative of progressive strain localisation, meaning the relative strain contribution of the smallest faults decreases as the total strain increases.

Many real fault/seismic populations have been shown to have multifractal properties:

- Analysis of fault trace maps in the Tayma province of Arabia gave $D_0 = 2.00, D_1 = 1.94$ and $D_2 = 1.85$ for scales ranging from 12km to 100 km (Ouillon *et al.*, 1995). A second study of the same data produced $D_1 = 1.70$ and $D_2 = 1.55$ (Poliakov and Herrmann, 1994).
- A study of the spatial distribution of earthquake epicentres in the Zagros and Alboraz-Kopeh Dagh regions of Iran revealed $D_0 = 1.83, D_1 = 1.63$ and $D_2 = 1.50$, and $D_0 = 1.82, D_1 = 1.53$ and $D_2 = 1.40$ respectively (Zamani and Agh-Atabi, 2011).
- Likewise a study of epicentre distributions in southern Italy showed $D_0 > D_1 > D_2$ for five sampled sectors, with ranges of $D_0 = 1.39 - 1.80$, $D_1 = 1.17 - 1.49$ and $D_2 = 1.03 - 1.28$ (Godano *et al.*, 1996).

- At Mount St. Helens during the eruptive period of 1980-86, D_q varied from 1.0 to 0.36 as $-\infty \leftarrow q \rightarrow \infty$. During the non-eruptive period of 1987-2002 D_q varied from 1.0-0.7 (Caruso *et al.*, 2006).
- A seismic cluster of in the Canary Islands, from 1989 to 1996, has a varying spatial fractal dimension of 1.3 to 0.4. An initial decrease is the result of consistent activation of seismogenic volumes/faults. A later increase in D is thought to be due to an increase in the sensitivity of the monitoring network (Vinciguerra and Day, 2013).

2.5 Summary

In Sections 2.1 to 2.3 the current literature for the three main areas of research within this thesis has been reviewed. Chapters 3-7 take this literature as a starting point in order to answer the following research questions, from which the standard practice is improved and new methods are developed, allowing for new conclusions to be drawn across all three topics.

2.5.1 Research questions

1) To what extent can we infer physical volcanic processes around edifaces from properties of volcanic earthquakes?
2) Is the currently methodology for calculating completeness magnitudes and *b*-values adequate, and if not how can it be improved upon?
3) Are volcanic seismic *b*-values 'high', and if so when?
4) How do volcanic *b*-values vary through time?
5) Can studies of structural aspects of ancient volcanic systems provide insights into the processes controlling patterns of seismicity at active volcanoes?
6) Is it possible to compare fracture distributions at an ancient volcano to seismic frequency-magnitude distributions at an active volcano, using *b*-values and fractal dimensions?
7) Can improved understanding and analysis of FMDs lead to improved eruption forecasting?

Chapter 3 – Are Volcanic Seismic *b*-values High, and if so When?

3.1 Introduction to the paper

This paper takes the form of a published paper, re-formatted for the thesis style, without further edits. It addresses research questions 1), 2) and 3) from Section 2.5.1. I first assess the current state-of-play with regards to volcanic seismic *b*-values, including an extensive targeted literature review, then I propose a standardised workflow for calculating accurate and reliable *b*-values; show statistically that a minimum complete catalogue size of 200 events should be adhered to; as well as quantifying a previously unidentified source of error when calculating the completeness magnitude of a seismic catalogue. Finally this methodology is applied to the recent El Hierro and Mount Etna catalogue to compare the results to the current literature.

The results from previous literature, summarised in Table 3.1 and Figure 3.1 show that there is currently no consistent implementation of methodology to compute the completeness magnitude of a seismic catalogue. I tested the three most commonly used methods by iteratively generating synthetic catalogues and assessing the spread of results. The original code defining the three methods was written by Andy Bell, all further coding was done myself.

The key outcomes of this paper are the workflow in Figure 3.9 and contour plot of Figure 3.11c defining the modified error in *b* in terms of complete catalogue size and

the *b*-value; as these allow for consistent calculation of *b*-values and their errors for any seismic catalogue, not just specifically for volcanics.

Paper

Nick. S. Roberts[1], Andrew F. Bell[1], Ian G. Main[1]

[1]School of Geosciences, University of Edinburgh, James Hutton Road, Edinburgh, UK. EH9 3FE

Submitted to the Journal of Volcanology and Geothermal Research, April 2015

Accepted October 2015

Published December 2015

3.2 Abstract

The Gutenberg-Richter exponent *b* is a measure of the relative proportion of large and small earthquakes. It is commonly used to infer material properties such as heterogeneity, or mechanical properties such as the state of stress from earthquake populations. It is 'well known' that the *b*-value tends to be high or very high for volcanic earthquake populations relative to *b*=1 for those of tectonic earthquakes, and that *b* varies significantly with time during periods of unrest. We first review the supporting evidence from of 34 case studies, and identify weaknesses in this argument due predominantly to small sample size, the narrow bandwidth of magnitude scales available, variability in the methods used to assess the minimum or cut-off magnitude *Mc*, and to infer *b*. Informed by this, we use synthetic realisations to quantify the effect of choice of the cut-off magnitude on maximum likelihood estimates of *b*, and suggest a new work flow for this choice. We present the first quantitative estimate of the error in *b* introduced by uncertainties in estimating *Mc*, as a function of the number of events and the *b*-value itself. This error can significantly

exceed the commonly-quoted statistical error in the estimated *b*-value, especially for the case that the underlying *b*-value is high. We apply the new methods to data sets from recent periods of unrest in El Hierro and Mount Etna. For El Hierro we confirm significantly high *b*-values of 1.5-2.5 prior to the 10 October 2011 eruption. For Mount Etna the *b*-values are indistinguishable from *b*=1 within error, except during the flank eruptions at Mount Etna in 2001-2003, when $1.5<b<2.0$. For the time period analysed, they are rarely lower than *b*=1. Our results confirm that these volcano-tectonic earthquake populations can have systematically high *b*-values, especially when associated with eruptions. At other times they can be indistinguishable from those of tectonic earthquakes within the total error. The results have significant implications for operational forecasting informed by *b*-value variability, in particular in assessing the significance of *b*-value variations identified by sample sizes with fewer than 200 events above the completeness threshold.

3.3 Introduction

Volcanic earthquakes provide insight into physical processes acting at volcanoes, such as the mechanisms of deformation of the volcanic edifice and magma accumulation, and statistical analysis of earthquake catalogues are a key component of eruption forecasting methods (McNutt, 1996). Increased rates of earthquakes are a primary indicator of volcanic unrest, and changing locations of earthquake hypocentres can be used to map magma migration (Wiemer and Wyss, 2002). The frequency-magnitude distribution (FMD) of volcanic earthquakes can provide insight into the state of stress or material properties, and are a key component of most studies of volcanic seismicity.

Where the catalogue is completely reported, the FMD, commonly takes the form of a Gutenberg-Richter (GR) relation (Gutenberg and Richter, 1954):

$$\log(N) = a - bM, \qquad [\,3.1\,]$$

where N is the total number of earthquakes of magnitude equal to or greater than M, and a and b are real, positive constants characteristic of the specific catalogue. The parameter a is the logarithm of the number of earthquakes with $M \geq 0$, and is thus a measure of the seismicity rate of the region. The b-value represents the relative proportion of large and small events in the catalogue. It is best calculated or inferred using the maximum likelihood method (Aki, 1965), now used almost universally in earthquake seismology (Mignan and Woessner, 2012). Other methods such as a least squares fit of the data to Equation [3.1] are known to produce a biased estimate (Naylor *et al.*, 2010). In addition, if the bandwidth of data is narrow, or equivalently the sample is small, then it is easy to overestimate the underlying b-value (Main, 2000). Finally, the b-value may also be biased due to incorrect identification of the threshold for complete reporting, denoted Mc here (Mignan and Woessner, 2012). These and other sources of bias introduce an epistemic error to any inference from the data. In principle this should be accounted for in addition to the aleatory uncertainties inferred from the random error associated with measurement or statistical fluctuation in the data, but it is often neglected in studies of volcanic earthquake populations.

The Gutenberg-Richter form of the distribution holds, at least for small and intermediate events across a remarkable range of sizes and loading conditions, from laboratory experiments to volcanic and tectonic earthquakes (Main, 1996). In controlled laboratory tests, seismic b-values commonly change systematically with respect to a variety of controlling factors. These include the degree of material heterogeneity (Mogi, 1962), the level of applied stress (Scholz, 1968), the degree of stress concentration, i.e. the stress intensity normalised to the fracture toughness (Meredith and Atkinson, 1983), the chemical reactivity of the pore fluid (Meredith and Atkinson, 1983), and the pore fluid pressure (Sammonds *et al.*, 1992). In nature other factors that affect the b-value systematically include the earthquake focal mechanism (Schorlemmer *et al.*, 2005), the depth (Mori and Abercrombie, 1997), and

the degree of coupling or strain partition between seismic and aseismic deformation at plate boundaries (Mazzotti *et al.*, 2011).

The b-value for tectonic earthquakes, using best practice and large regional or global data sets, is commonly reported as taking values near unity (Frolich and Davis, 1993). In contrast the reported b-values from published studies of earthquake populations associated with volcanic unrest are commonly reported as being significantly higher than this, allowing for the random error expected for a b-value of unity (described in more detail below). The main question we address here is whether this difference is real or, at least to some extent, an artefact of the known sources of bias described above.

To examine this question we first use synthetic data to explore the effect of various factors on the estimated b-value, denoted $\tilde{b}$, and the underlying b-value, henceforth denoted b. Uncertainties in $\tilde{b}$ at one standard deviation, denoted $\sigma_{\tilde{b}}$, are estimated using the method of Shi & Bolt (1982), which correctly reflects the (approximately) Poisson 'counting errors' expected from sampling a whole number of events (Greenhough and Main, 2008). The advantage of using synthetic data is that we can distinguish between the random error $\sigma_{\tilde{b}}$, and the systematic error or bias $\tilde{b} - b$, or equivalently to errors of precision and accuracy respectively. We show how both depend intrinsically on the sample size. First we determine an optimised method of estimating the cut-off magnitude of complete reporting of events, *Mc,* for catalogues of different sizes, and then propose a formal workflow for the estimation of *Mc*. The proposed workflow is then applied to two volcanic seismic catalogues at Mount Etna and El Hierro as important examples of recently-active volcanic systems to address the questions: (a) are the b-values higher than 1? And (b) do they vary with time significantly outside the estimated margins of error? For these examples, b is remarkably stationary and similar to (~1) or only somewhat larger (1-1.5) than to those of tectonic earthquakes, except for specific transients where the b-value can be significantly greater than background at 95% confidence. The results presented here

will provide greater confidence in identifying statistically-significant variations in *b*-value, and in identifying physical causes for this variability.

3.4 Review and synthesis of previous studies

In this section we extend the review of McNutt (2005), who summarised reported *b*-values and associated parameters such as source depth from 13 different volcanoes around the world. This review includes *b*-values as high as 3 in one case (McNutt, 2005). In Table 3.1 we extend this study to 21 volcanoes, and include a wider range of associated parameters, including: the number of events; the range of magnitudes used in the analysed catalogues; the methods used to calculate the completeness magnitude and fit the *b*-value; and the range of *b*-values reported in each study, including a typical value. Multiple studies use several methods for analysing *b*-value variations and thus the results are reported separately in Table 3.1, giving 38 separate results for comparison in this new synthesis. Information on all the different fields of data could not be found in all cases, e.g. how the threshold magnitude was estimated, resulting in some blank entries in Table 1.

The maximum reported *b*-values range between 1.4 and 3.5, with a peak at b=1.7 (Figure 3.1c). From Figures 1b there is no clear dependence on the magnitude and *b*-value. Bonnet *et al.* (2001) also found there was no direct dependence of the scaling exponent for fracture length on the scale of observation and that no significant trends could be determined in the type of faulting (Bonnet *et al.*, 2001).

Table 3.1 - Compilation of *b*-values and range of magnitudes for volcanic seismic catalogues.

Reference	Volcano	Dates	Depth, km	*N*
(Jacobs and McNutt, 2010)	Augustine	2000 - 2006	-2-0	100
(Jacobs and McNutt, 2010)	Augustine	17/11/05 - 10/12/05	-2-0	~250
M. Wyss (written comm.)	Coso		0.8-3	
(Ibanez *et al.*, 2012)	El Hierro	19/7/11 - 16/9/11	8-16	7000+
(Ibanez *et al.*, 2012)	El Hierro	19/07/2011	8-16	200
(Marti *et al.*, 2013b)	El Hierro	14/8/11 - 18/8/11	8-16	-
(Ibanez *et al.*, 2012)	El Hierro	19/7/11 - 28/7/11	8-16	-
(Patane *et al.*, 1992)	Etna	1984	-	200
(Patane *et al.*, 1992)	Etna	29/3/1983 - 6/8/1983	-	-
(Murru *et al.*, 1999)	Etna	-	9-15	50
(Centamore *et al.*, 1999)	Etna	1/1/1990 - 31/12/92	-	100
(Centamore *et al.*, 1999)	Etna	1/1/1990- 31/12/92	-	100
(Murru *et al.*, 2007).	Etna	July - Aug 2001	0-2	50
(Murru *et al.*, 2005)	Etna	July - Aug 2001	0-12	50
(Murru *et al.*, 2007)	Etna	Aug 1999 - Dec 2005	1-3	100
*(Vinciguerra et al., 2001)**	*Etna*	*1983-1988*	*-3-7*	*374*
*(Vinciguerra et al., 2001)**	*Etna*	*1993-1996*	*-3-7*	*27*
*(Vinciguerra et al., 2001)**	*Etna*	*1983-1988*	*7-30*	*345*
*(Vinciguerra et al., 2001)**	*Etna*	*1993-1196*	*7-30*	*84*
(Sanchez *et al.*, 2005)	Galeras	Sep 1995 - Jun 2002	0-2	300
(Jolly and McNutt, 1999)	Katmai	-	6-8	-
(Wyss *et al.*, 2001)	Kilauea	-	4-7,20	-
(Wyss *et al.*, 2001)	Kilauea	1979 - 1997	4-7	50
(Wiemer *et al.*, 1998)	Long Valley	1989 - 1998	1-11	150
(Jolly and McNutt, 1999)	Mageik	Sep 1996 - April 1997	0-5	-
(Bridges and Gao, 2006)	Makushin	July 1996 - April 05	0-8	50
(Wiemer *et al.*, 1998)	Mammoth Mtn.	1989 - 1990.5	3-4,7-9	150
(Jolly and McNutt, 1999)	Martin/Mageik	Sep 1996 - April 1997	-2-10	-
(Wiemer and McNutt, 1997)	Mount Spurr	1991 - 1995	2.3-4.5	100
(Main, 1987)	Mount St Helens	20 Mar - 18May 1980	na	~300
(Wiemer and McNutt, 1997)	Mount St. Helens	1988 - Jan 1996	2.7-3.8	100
(Wyss *et al.*, 1997)	Off-Ito	1982 - 1996	7-15	100
M. Wyss (written comm.)	Oshima		4	
(Sanchez *et al.*, 2004)	Pinatubo	29 June - 19 Aug 1999	0-4,8-13	100
(Novelo-Casanova *et al.*, 2006)	Popocatepetl	Dec 2000 - Jan 2001	2-7	20
S. Wiemer (written. comm.)	Redoubt		3-4,6-8	
(Power *et al.*, 1998)	Soufriere Hills	Aug 1995 - Mar 1996	2.0-2.5	100
(Farrell *et al.*, 2009)	Yellowstone	1984 - 2006	4-18	>10

Values for *N* are the number of events analysed in each catalogue. These figures are either given or estimated from figures. The methods for calculating the completeness magnitude, *Mc*, are; using ZMAP software; the Goodness-of-Fit method (GFT) with given percentage threshold (e.g. 90GFT is 90% fit); the Maximum Curvature method (MaxC); Inspection is choosing a *Mc* by eye; and using the Entire Magnitude Range method (EMR). The methods for approximating the *b*-value are the Maximum Likelihood Estimation (MLE) and the Least Squares and Weighted Least Squares fit (LS & WLS). The *b*-value ranges in each study are described by the minimum (b_{min}) and maximum (b_{max}) quoted values in the study, with a typical value (b_{typ}) being estimated by eye. **Data added post-publication.*

Continuation of Table 1.

Volcano	Method *Mc*	Mag. range	Method *b*	b_{min}	b_{typ}	b_{max}
Augustine	ZMAP	-	MLE	0.8	1.4	2.1
Augustine	ZMAP	-0.1-0.7	MLE	-	-	1.85
Coso				-	-	1.7
El Hierro	90GFT	1.3-2.7	LS	1.12	1.57	2.25
El Hierro	90GFT	-	LS	0.75	1.25	2.55
El Hierro	-	-	MLE	0.8	1.1	2.3
El Hierro	90GFT	1.5-2.6	LS	0.81	1.2	3.01
Etna	-	2.8-	MLE	0.8	1.1	1.7
Etna	-	2.5-	MLE	0.7	1.0	2.1
Etna	MaxC	2.5-	MLE	1.4	1.5	3.5
Etna	-	2.3-5.1	LS	0.5	1.2	1.9
Etna	-	2.3-5.1	MLE	0.9	1.1	1.7
Etna	GFT	2.6-3.5	MLE	0.7	1	2.6
Etna	90GFT	2.6	MLE	0.8	1.5	2.50
Etna	90GFT	2.5	MLE	0.7	1.0	1.86
Etna	*(Tinti and Mulargia, 1985)*	*-*	*MLE*	*1.00*	*1.08*	*1.16*
Etna	*(Tinti and Mulargia, 1985)*	*-*	*MLE*	*1.30*	*1.59*	*1.88*
Etna	*(Tinti and Mulargia, 1985)*	*-*	*MLE*	*0.8*	*0.9*	*1.0*
Etna	*(Tinti and Mulargia, 1985)*	*-*	*MLE*	*1.3*	*1.6*	*1.9*
Galeras	-	1.2-2.8	MLE	0.65	1.0	1.4
Katmai	-	-	-	1.0	1.3	1.6
Kilauea	-	-	-	-	-	1.9
Kilauea	-	1.8-2.6	MLE & LS	0.6	1.0	1.73
Long Valley	MaxC	1.3-	MLE	1.1	1.4	2.0
Mageik	-	-	WLS	1.0	1.5	2.0
Makushin	74GFT	0.9-3.9	MLE	0.73	1.21	2.03
Mammoth Mtn.	MaxC	1.3-	MLE	0.95	1.2	1.6
Martin/Mageik	-	0.7-4.5	WLS	-	-	1.56
Mount Spurr	Inspection	0.1-2.2	MLE & LS	0.6	1.1	1.8
Mount St Helens	Inspection	3.5-5	MLE	0.5	1.0	1.5
Mount St. Helens	Inspection	0.4-2.8	MLE & LS	0.8	1.2	1.6
Off-Ito	MaxC	1.6-2.5	MLE	0.44	1.0	1.54
Oshima				-	-	1.5
Pinatubo	ZMAP	0.73-	MLE	1.0	1.3	1.7
Popocatepetl	Inspection	1.9-3.3	MLE	1.0	1.7	2.70
Redoubt				-	-	1.7
Soufriere Hills	-	1.7-2.4	MLE	0.9	1	3.07
Yellowstone	EMR	1.5-	MLE	0.5	1.0	1.5

Figure 3.1 shows the distribution of *b*-values compared to the other variables in the study. There are no clear trends with depth (Figure 3.1a) or magnitude range or size (Figure 3.1b). However, there is a weak decreasing trend in the *b*-value as the number of events in the sample, *N*, increases (Figure 3.1c). The data only spans from 10 to 300 events covering just over one magnitude unit, with over half, (16 of 25) of the studies using catalogues with either 50 or 100 events. One further study (Ibanez *et al.*, 2012) containing 7000 events reports a relatively high *b*-value of 1.57 that does not follow this trend. However, this study - and many others cited in Table 1 - use the Least Squares method to fit *b* or to check the results of the maximum likelihood estimation, introducing a known source of potential bias outlined in the introduction.

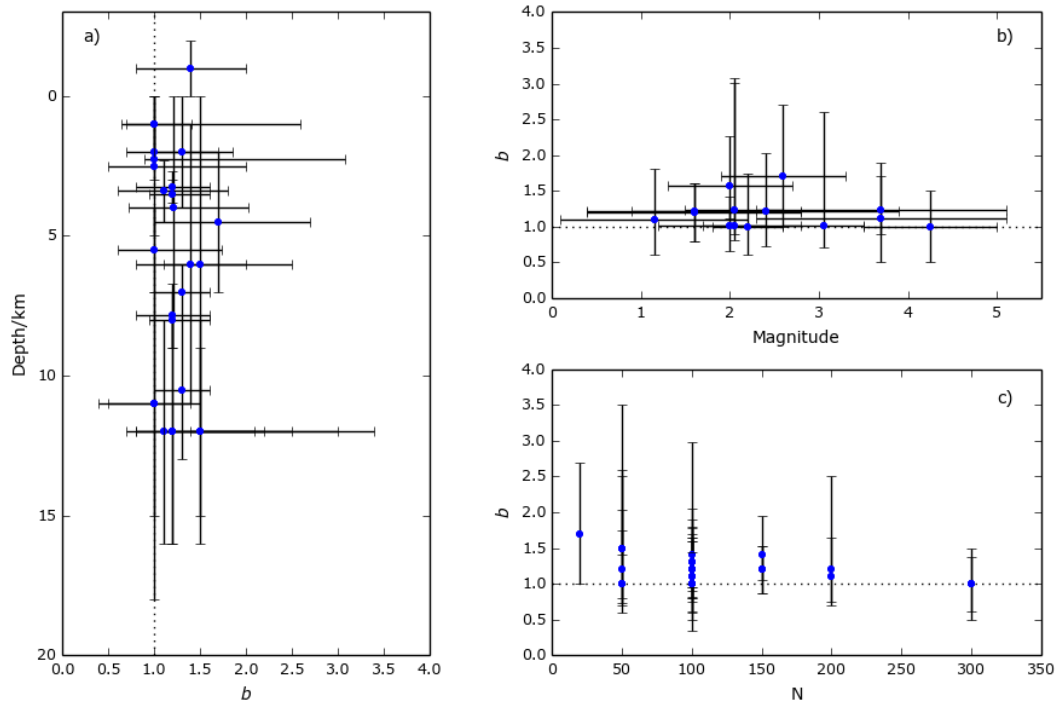

Figure 3.1 – Synthesis of *b*-value distributions compared to a) depth, b) magnitude, and c) the number of events in each catalogue, N_c. The errors bars show the minimum and maximum values of *b* from Table 1, and the range of depth/magnitude over which the catalogue was comprised. The blue dots show the typical *b*-values. The dotted line marks *b*=1.

In summary this review has highlighted a significant variability in the reported values of *b*, and a significant variability in the methods of analysis used in the

different studies. Typical *b*-values are usually in the range 1-1.2. They are never (for this list) less than one, and are occasionally very high (up to 3.5). The variability is much larger than any systematic trends, except that the *b*-value tends to decrease with increasing sample size. In this paper we use synthetically-generated data to address some of the most important origins of this variability, in particular the choice of threshold magnitude and the sample size.

3.5 Methods for analysis of Frequency-Magnitude Distributions

A variety of statistical methods have been used to model FMD's and to quantify whether those models are consistent with the observed data. Most methods involve modelling the proportion of the distribution above the completeness magnitude. Therefore there is a strong inter-dependence between estimates of the completeness magnitude and values of parameters of prospective FMD models. In this section we summarise the current methods used to address this problem.

3.5.1 Gutenberg-Richter parameters

There is well-established literature that describes the merits of different statistical methodologies for FMD analysis. Methods involving regression on cumulative frequencies, or using least-squares regression, are known to give biased estimates of the *b*-value (Naylor *et al.*, 2010) as they are known to give disproportionate weighting to higher magnitude events (Ghosh *et al.*, 2008). The maximum likelihood technique has become standard in seismic hazard analysis (Mignan and Woessner, 2012). The data are assumed to be exponentially distributed (as in Equation [3.1]) and the maximum possible magnitude is assumed to be at infinity (Aki, 1965). Physically, earthquakes must have a finite maximum size dependent on the size and strain limits within the Earth, but M_{max} is not well constrained by global data (Main *et al.*, 2008; Holschneider *et al.*, 2014). The maximum likelihood method weights each event equally and correctly allows for error structure of the data: in frequency data in the form of a Poisson distribution (Naylor *et al.*, 2010). Formally, the maximum likelihood estimate of the *b*-value is:

$$\tilde{b} = \frac{\log_{10} e}{\bar{M} - (Mc - \Delta M/2)} \qquad [\ 3.2\ ]$$

where $\tilde{b}$ is the estimate of the *b*-value, $\bar{M}$ is the mean magnitude, M_c is the completeness magnitude, and ΔM is the magnitude bin size of the histogram (Aki, 1965). Aki also showed the uncertainty on this estimate at one standard deviation (67% confidence) can be approximated to:

$$\sigma_{\tilde{b}} = \frac{\tilde{b}}{\sqrt{N_c}} \qquad [\ 3.3\ ]$$

Where N_c is the number of events in the complete part of the catalogue, or 1.96 times this value at 95% confidence.

A summary study by Marzocchi & Sandri, (2003), tested two further improvements on this estimation of *b* using binned magnitudes, Equation [3.4] (Bender, 1983), and an improved uncertainty estimate (Equation [3.5]) (Shi and Bolt, 1982; Marzocchi and Sandri, 2003):

$$\tilde{b} = \frac{1}{\ln 10[\hat{\mu} - (M_c - \Delta M)]} \qquad [\ 3.4\ ]$$

$$\sigma_{\tilde{b}} = 2.30\tilde{b}^2 \sqrt{\frac{\sum_{i=1}^{N}(M_i - \hat{\mu})^2}{N_c(N_c - 1)}} \qquad [\ 3.5\ ]$$

where $\hat{\mu}$ is the average magnitude of the sample, and ΔM is the binned magnitude width. The *b*-value is relatively insensitive to the upper magnitude cut-off, so assuming an infinite cut-off in deriving Equations [3.3] and [3.5] does not introduce a significant bias. However, in both cases the quoted error is formally conditional on the choice of *Mc*, which in practice must be estimated. This introduces an implicit source of bias that can be positive or negative. In this paper we will demonstrate that this additional source of uncertainty is comparable to or can greatly exceed the estimates from Equations [3.3] and [3.5].

3.5.2 Calculating the completeness magnitude

Most studies apply a lower threshold or cut-off magnitude, *Mc*, above which the catalogue can be regarded as completely recorded (Wiemer and Wyss, 2000). *Mc* is the lowest magnitude at which 100 per cent of earthquakes in a space-time volume are detected (Rydelek and Sacks, 1989; Woessner and Wiemer, 2005; Mignan and Woessner, 2012). Earthquakes with smaller magnitudes are less likely to be completely reported when their amplitude becomes smaller than that of the ambient noise. This introduces a high-pass filter to the FMD, which could in principle be modelled and fitted to the data. However, this is rarely (if ever) done explicitly. In practice most studies assume *Mc* is the magnitude at which the log(cumulative frequency)-magnitude curve departs from a linear trend of eq. 1. There are three main techniques commonly used to estimate this magnitude, namely the Maximum Curvature (MaxC) method, the Goodness-of-Fit test (GFT) (Wiemer and Wyss, 2000) and *b*-value stability (BVS) method (Cao and Gao, 2002).

The MaxC method calculates the highest value of the first derivative of the cumulative frequency-magnitude curve. In practice this matches the frequency-magnitude bin with the highest number of events (Figure 3.2a). The main limitation of this method is that it will systematically underestimate *Mc* unless there is a sharp transition between the incomplete and complete portion of the catalogue, as illustrated in Figure 3.2a.

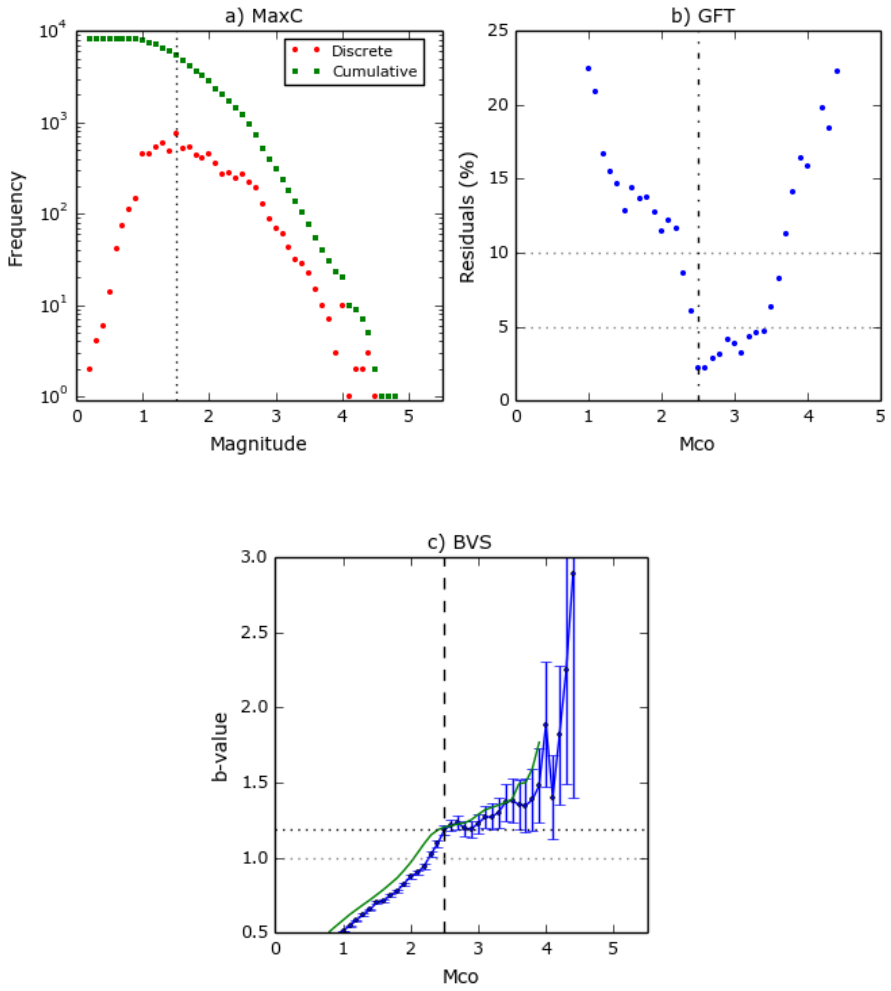

Figure 3.2 – a) Discrete and cumulative frequency-magnitude distributions, demonstrating the Maximum Curvature Method (MaxC). The vertical dotted line represents the estimate of *Mc* at the highest discrete magnitude bin at (*Mc*=1.5). b) Residuals of the Goodness-of-Fit method (GFT) as a function of trial cut-off. Once the residual falls beneath 5% the completeness magnitude is selected, in this case *Mc*=2.5. c) *b*-value stability curve showing the *b*-values for each cut-off magnitude. The vertical dashed line indicates when successive *b*-values (green line) fall within error of the *b*-value. Here *Mc*=2.5.

The GFT method calculates *Mc* by comparing the observed FMD with a synthetic one. The best-fit distribution is calculated for trial cut-off magnitudes using the maximum-likelihood estimates of *a*- and *b*-values of the observed dataset. The residuals between the data and the best fit distribution are then calculated as a function of cut-off magnitude (Figure 3.2b). The completeness threshold, *Mc*, is selected as being the first magnitude above which the residual between the synthetic straight line fit model and

observed data falls within a 95% confidence window. If 95% confidence cannot be obtained then a 90% confidence window can be used as a compromise. This method tends to give systematically low values for *Mc* although not as low as the MaxC method (Wiemer and Wyss, 2000).

The BVS method simply evaluates the estimated *b*-value as a function of the cut-off magnitude. The assumption here is that $\tilde{b}$ will initially increase as the cut-off magnitude increases, until the cut-off magnitude equals *Mc* after which $\tilde{b}$ will stabilise. The inferred *b*-value is deemed to have stabilised once the average $\tilde{b}$ for the five successive cut-off magnitudes falls within error of the selected cut-off magnitude (Figure 3.2c). The BVS method tends to have high *Mc* values relative to other methods (Woessner and Wiemer, 2005) and consequently higher $\tilde{b}$ values.

3.6 Results for synthetic catalogues

3.6.1 Generating synthetic catalogues

We now evaluate which of the three methods for calculating the *Mc* is the most accurate and reliable, by generating synthetic catalogues with known *Mc* and *b*-value, but different forms of the cut off below *Mc*. As a benchmark check we first generated synthetic data to determine $\tilde{b}$ and $\sigma_{\tilde{b}}$ for *b*=1 and *b*=2 as a function of the complete sample size N_c, conditioned on an exact value for *Mc*. This provided a good match to Fig. 1a,b of Marzocchi and Sandri (2003). However, in reality *Mc* is not known independently a priori. Ideally we would hope the incremental FMD would have a sharp and easily distinguishable peak at *Mc*, defining the lower limit of the complete catalogue (Figure 3.3a). In reality the peak of the distribution is often curved and much broader due to the complexity of the signal to noise ratio at the recording stations, and of locating and calculating magnitudes for small events, so defining *Mc* can be much more challenging (Figure 3.3b). This introduces an additional source of uncertainty that is the prime focus of the current paper.

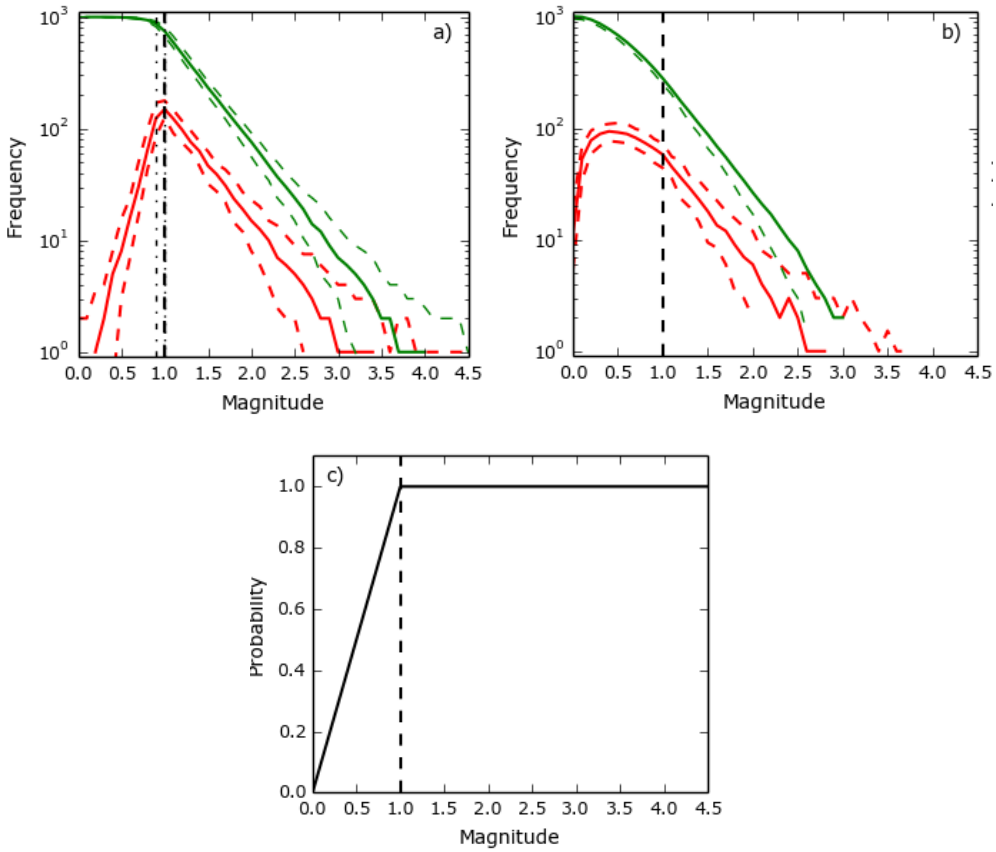

Figure 3.3 – a) Example of a sharp-peaked frequency-magnitude distribution. b) Example of a broad-peaked frequency-magnitude distribution. Both catalogues have an *Mc* of 1.0 and a *b*-value of 1.0. Discrete distributions are in reds, cumulative distributions are in green. The dashed lines show the 95% confidence intervals representing the scatter in the synthetic data c) The probability filter applied to b). Above *Mc*=1.0 all generated events are kept in the catalogue. Beneath *Mc*=1.0 there is a constantly decreasing probability that that will remain in the catalogue, creating the broad peak in the filtered discrete FMD.

To test each of the three methods, we use two end-member scenarios. The first has a sharp peak (Figure 3.3a) and the second a broader peak (Figure 3.3b). Both catalogues have *Mc* set to 1.0. The complete part of both catalogues was created by randomly generating individual events from an ideal parent Gutenberg-Richter law distribution with a *b*-value of 1.0. For the sharp-peaked distribution the incomplete part of the catalogue was generated using a filter with a linear slope of 3, for values below *Mc*=1.0 decaying to zero probability at M=0. For the broad-peaked distribution a GR distribution was used to generate events all the way down to M=0. The probability

function shown in Figure 3.3c was then applied as a filter to remove events below the known threshold *Mc*=1.0, until the required number of events were left in the complete catalogue.

To examine the role of catalogue size, catalogues were generated with a complete size of 50, 100, 200, 500, 1000 and 5000 events. Finally the *b*-value was varied from a typical tectonic value of 1.0 to a significantly high *b*-value of 2.0, to test whether each method can reliably calculate *Mc* and inferred *b*-values for the case that the underlying *b*-value is high.

For each catalogue size, *b*-value, and distribution shape; 100 catalogue were iteratively generated, and the estimated *Mc* and *b*-values determined using the different methods described in section 4. A bin size ΔM of 0.1 m is used throughout. Figure 3.3 shows both the average catalogue (solid line) and the spread of the outcomes associated with the finite sample size (dashed lines).

3.6.2 Synthetic results

3.6.2.1 Sharp-peaked distribution

In this case the simulations of Figure 3.4 demonstrate that the MaxC method performs the best in terms of calculating *Mc*, closely followed by the BVS method. The GFT performs adequately for N_c=5000 but fails when N_c=50 as for over 90% of the catalogues *b* is not even calculated correctly within ±1.0 of the known value. When *b*=1 and N_c=5000, MaxC and BVS both correctly lead to a correct calculation of *b* with <0.01 error.

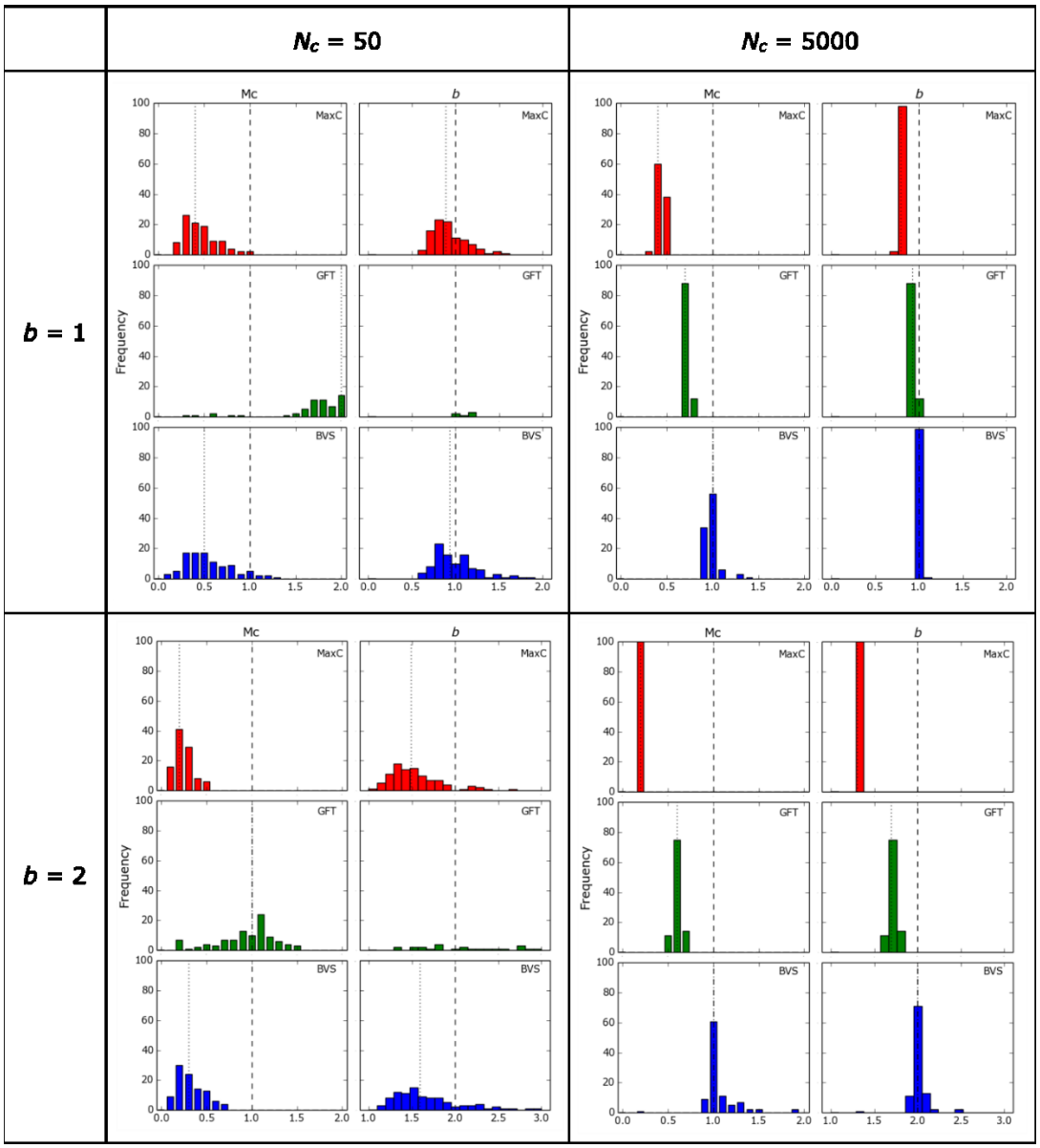

Figure 3.4 – Histograms for the estimated *Mc* and *b*-value for the MaxC (red), GFT (green), and BVS (blue) methods for different catalogue sizes (columns) and *b*-values (rows) for the sharp-peaked distribution. The known values of *Mc*=1.0 and *b*=1.0 are marked with vertical bold dashed lines. The median value calculated by each method is shown by the vertical dotted line.

3.6.2.2 Broad-peaked distribution

Figure 3.5 shows histograms of the best estimates of *Mc* for the three methods, for different catalogue sizes and *b*-values, for the case of the broad-peaked distribution. When N_c=50 for both *b*=1 and *b*=2, MaxC and BVS both systematically underestimate

Mc, because very few events have a greater magnitude than *Mc*=1.0 (Figure 3.6). Both MaxC and BVS methods give results with some scatter, centred on *b*=1, but several iterations had significantly higher *b*-values of 2 or above. Both methods perform poorly when *b*=2, as there too few events in the catalogue, with median values of $\tilde{b}$≈1.5. The GFT over-estimates *Mc* when *b*=1 but appears to give a reasonable estimate when *b*=2. However, the 95% confidence is only reached when *Mc* is very close to the maximum magnitude and thus the complete catalogue size is very small. This results in the inferred *b*-values being very high for both *b*=1 and *b*=2.

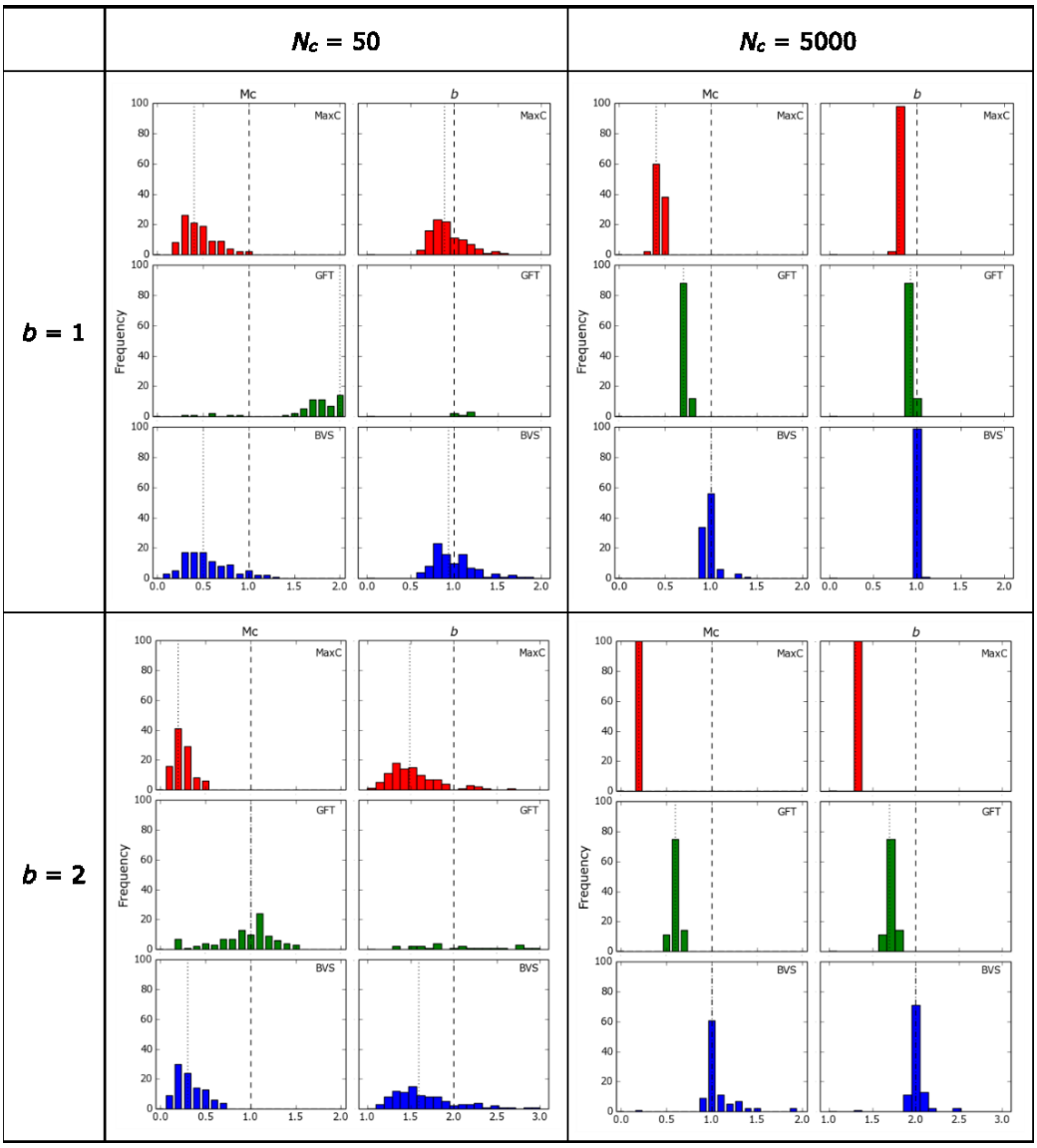

Figure 3.5 – Histograms as in Figure 3.4 except for a broad-peaked distribution.

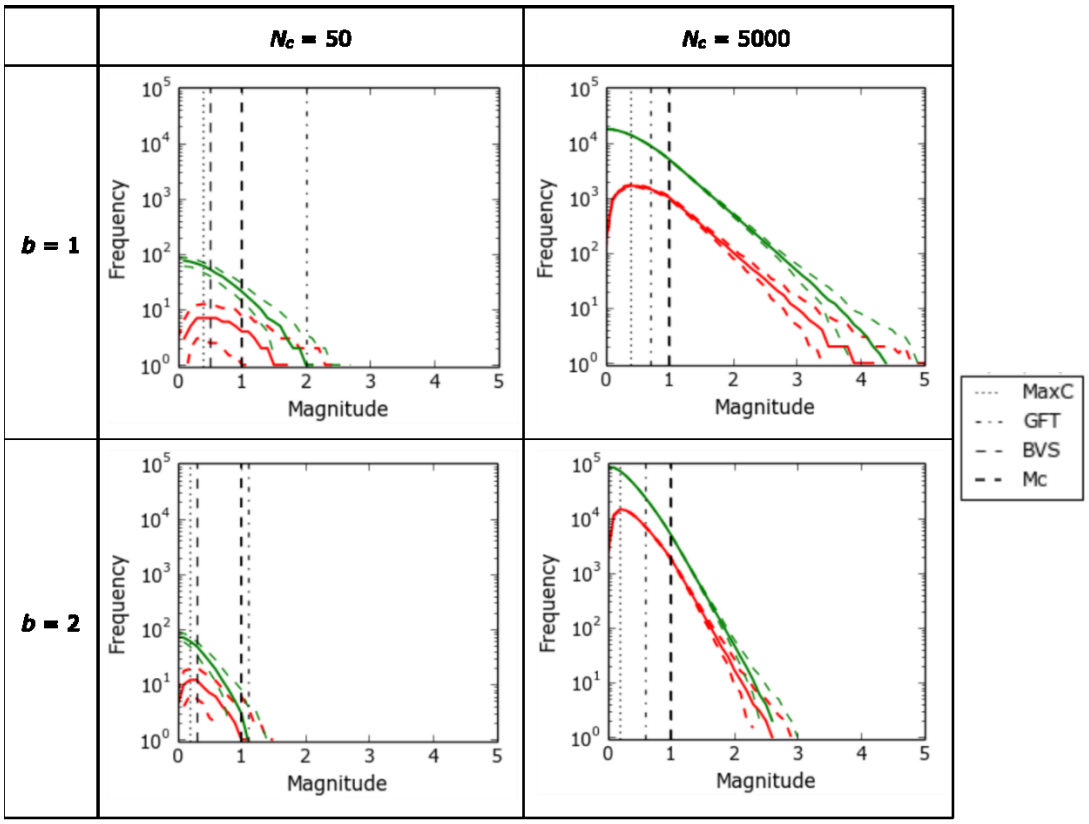

Figure 3.6 – Frequency-magnitude distributions for b=1 & 2, and N_c=50 & 5000 in the case of a broad-peaked distribution. Red shows discrete frequency and green the cumulative frequency. The solid red and green lines show the average values of the 100 catalogues. The dashed lines represent a 95% confidence window. The vertical dashed black lines show the known Mc of the catalogue, Mc=1.0, and the Mc's calculated by each method.

When N_c=5000 it becomes apparent that MaxC is not a good method for broad-peaked distributions. For b=1, Mc is heavily underestimated, with a median value of Mc=0.4, and resulting $\tilde{b}$-values all less than b=1. These underestimates are amplified when b=2 with median values of Mc=0.4 and $\tilde{b}$≈1.3. The GFT performs much better for both b=1 and b=2 however it gives a conservative estimate for both. The BVS method performs the best for a broad-peaked distribution, giving only a slightly conservative estimate of Mc with a median value of Mc=0.9 for b=1 and b=2. The BVS method returns the correct $\tilde{b}$=1.0 in over 80 iterations. The median value for b=2 is also approximately correct, however there is a very broad range of results with a slight skew towards values higher than b=2.0. This is a very large catalogue and the BVS method is clearly

the best when b=2. Our results show that it is intrinsically more difficult to calculate high b-values, however it is possible to find an estimate with a correct median value with the BVS method, albeit with a large spread in $\tilde{b}$.

3.6.2.3 Comparison of method performance

For a sharp-peaked distribution the MaxC method correctly calculates *Mc* the highest proportion of times for both high and low b-values. This outcome is not surprising as the MaxC method finds the magnitude bin with the highest number of events that, trivially, is the *Mc* set by the parent distribution. The BVS method performs almost as well as the MaxC method for low b-values, but with higher b-values the method returns too high estimates of *Mc*. However, as long as for larger catalogue sizes the BVS method continues to return good estimates of the b-value. The GFT method does not work with small catalogues as the 95% confidence threshold is only reached when the *Mc* is very close to the maximum magnitude event, therefore there are a minimal number of earthquakes left in the catalogue, and thus the uncertainty is very large. For larger catalogues GFT performs much better. However for both b=1 and b=2, using the GFT-calculated value of *Mc* results in fewer correct calculations of $\tilde{b}$ than the MaxC and BVS methods. Therefore we consider it to be the least-well performing method. For b=2 the steeper slope of the complete catalogue leads to a larger spread of calculated $\tilde{b}$-values for all three methods than for b=1. This is due to the random scattering of data due to sampling which has a greater influence on the FMD at high b compared to low b-values, and is not inherently linked to any of the methodologies.

Figure 3.7 and Figure 3.8 compare the performance of the different methods for the case of a broad-peaked distribution, using the mean and standard deviations of $\tilde{b}$ calculated from the data in Figure 3.6. For both b-values the GFT method does not reliably calculate *Mc,* resulting in a biased estimate of the b-value. For N_c≤500 the correct b-value is calculated within the statistical error, but the distribution is heavily skewed towards high b-values, meaning that this method performs sub-optimally for these small catalogue sizes. However for larger catalogues (N_c=1000 & 5000) the GFT

method does calculate accurate *b*-value estimates for both *b*=1 and *b*=2. The MaxC method returns a systematically-low estimate of *Mc* for all catalogue sizes, resulting in under-estimates of the *b*-value for both *b*=1 and *b*=2. We conclude that it is not an appropriate method for calculating *Mc* for a broad-peaked distribution.

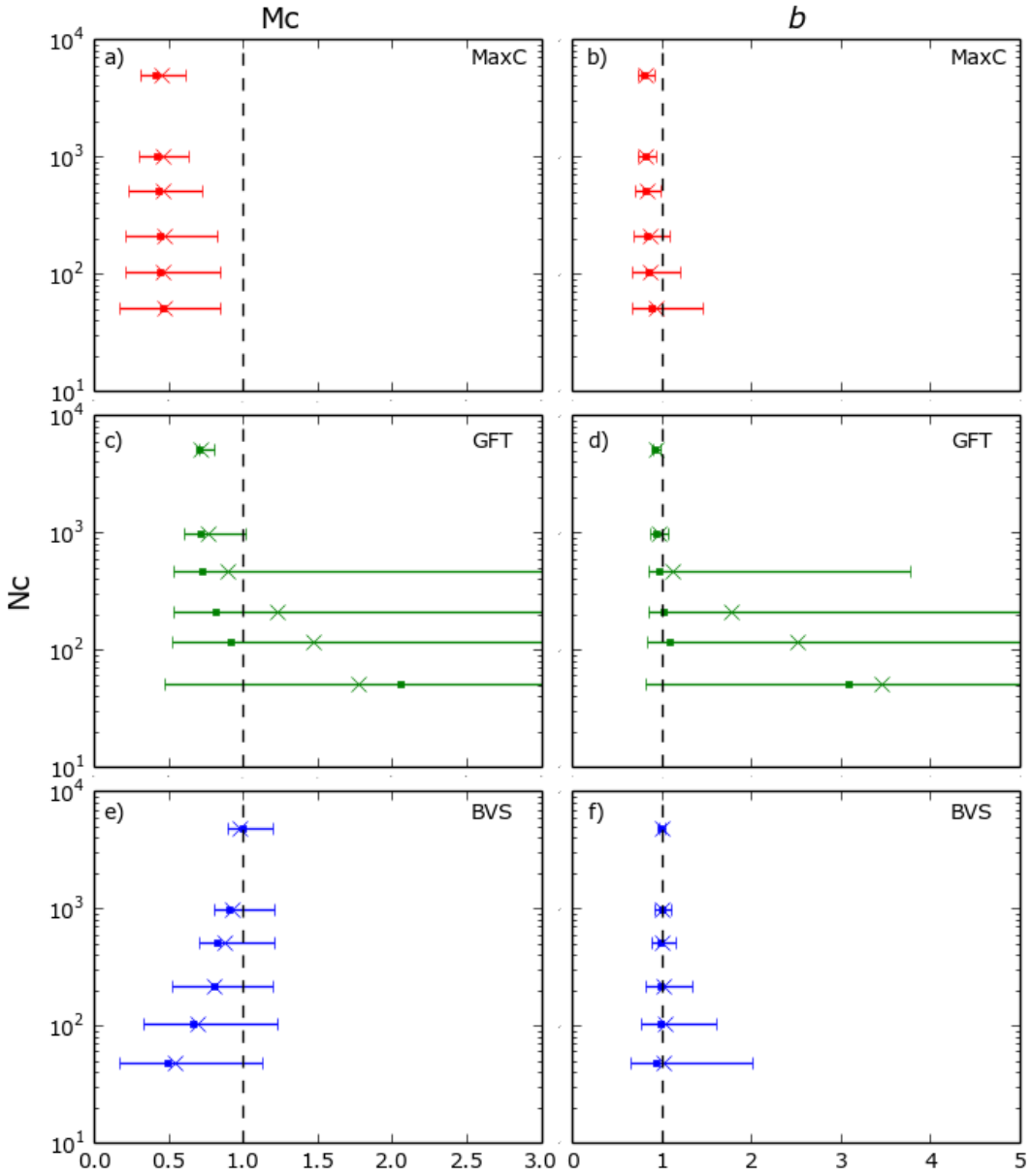

Figure 3.7 - Summary of histograms for broad-peaked distributions in Figure 3.5 for *b*=1. They show the spread of *Mc*'s and *b*-value's against catalogue size, *N*, for each of the three methods. Error bars represent a 95% spread of the data, with dots representing the median value and x's the average. The known *Mc*=1.0 and *b*=1.0 are marked with a vertical dashed line.

The estimates of *Mc* returned by the BVS method increase in accuracy with catalogue size. For N_c≥200 the BVS method correctly calculates *Mc* within the 95% confidence limits for both *b*=1 (Figure 3.7) and *b*=2 (Figure 3.8). When *b*=1 and the catalogue size is N_c≥200, the 95% confidence spread around the true *b*-value is very small, ±0.25. Using the BVS method with smaller catalogue sizes can result in *b*-value estimates as high as 2 even with *b*=1 (Figure 3.7). This observation suggests that care must be taken to not over-interpret high *b*-values calculated for small catalogues sizes. For *b*=2, the standard deviation of results is independent of catalogue size at about ±0.75. However, the median and mean of the $\tilde{b}$-value estimates tend towards the parent *b*=2 as catalogue size increases. Again for N_c≥200 for *b*=2 the BVS method estimates $\tilde{b}$ to within 95% confidence.

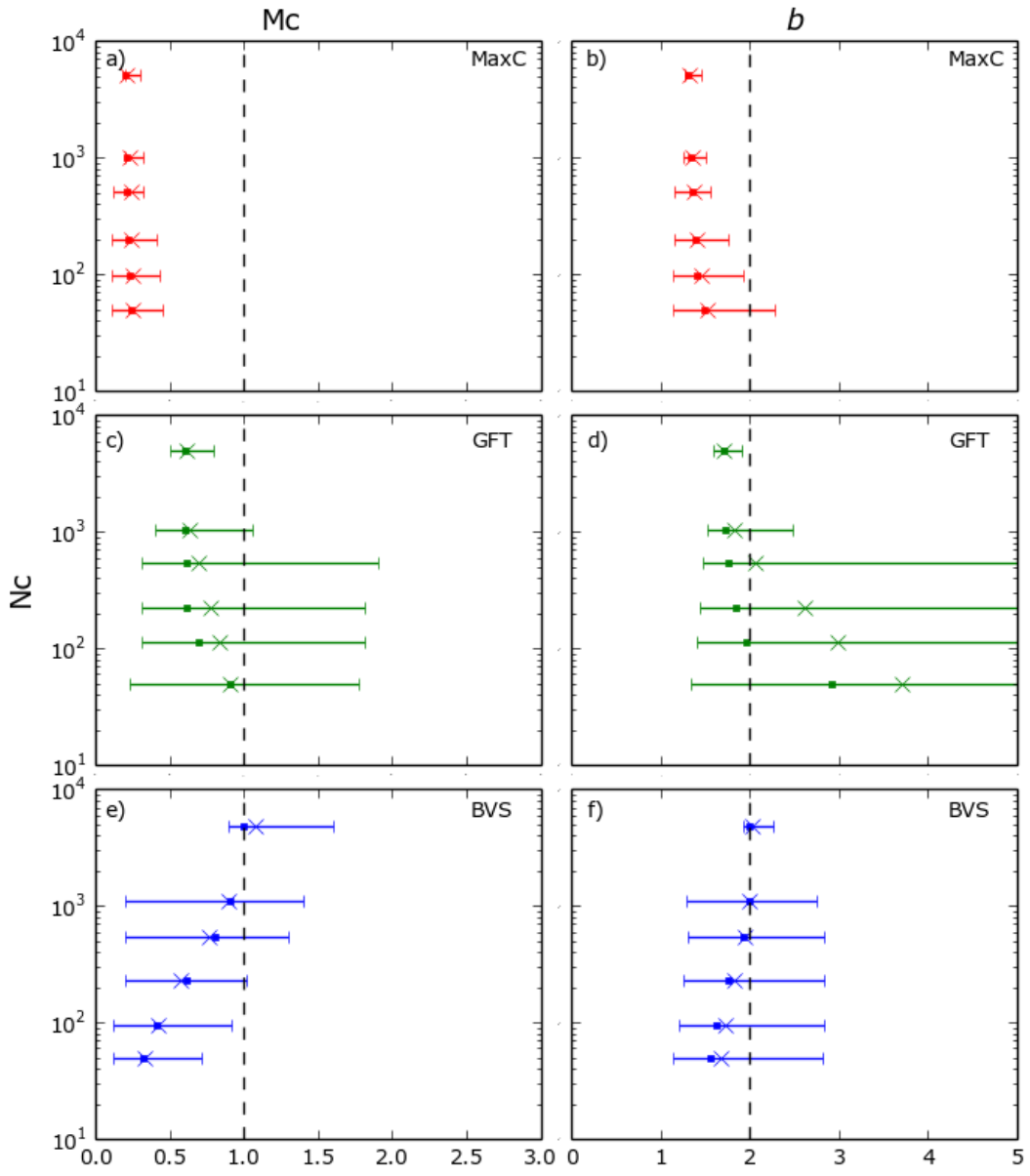

Figure 3.8 - Summary graphs as in Figure 3.7 but for b=2.

In terms of defining a threshold minimum complete catalogue size, when N_c≥500 our results show both b=1 and b=2 can be estimated accurately and precisely (Figure 3.7). For N_c=100 the statistical error in estimating b=1 is large, indicating a lack of precision, and for b=2 the average and median values are significantly below 2, indicating a residual bias. However, a threshold of 500 for completely-reported events is a relatively large number for many practical applications. From the results in Figure

3.7, a pragmatic choice of N_c=200 is an acceptable threshold for a trade–off between accuracy, precision, and realistic catalogue size.

3.6.3 A proposed workflow for the calculation of Mc

Informed by this analysis, we propose a workflow for analysing the FMD of volcanic earthquake catalogues (Figure 3.9). As discussed above, we considered that the minimum catalogue size for reliable estimation of the *b*-value is N_c=200.

First, *Mc* is estimated using each of the MaxC, GFT and BVS methods. If all three *Mc* estimates agree within ±0.1, the FMD can be modelled by a sharp-peaked distribution, and so the MaxC estimate of *Mc* should be used. If the *b*-value calculated using this *Mc* has an error of ≤±0.25 it should be considered to be reliable. An error of >±0.25 makes it difficult to interpret the *b*-value and may indicate an unreliable estimate of *Mc*.

If the three estimates of *Mc* vary by ≥0.1, or the *b*-value calculated from the MaxC estimate of Mc is ≥0.25, we recommend that the BVS method should be used. If the resulting *b*-value has an error of ≤0.25 it should be considered to be reliable. If this is not the case, the GFT analysis should be used. If a *b*-value with an error of ≤0.25 cannot be obtained using any of the 3 methods, we argue that the catalogue is too small for reliable FMD analysis. If the complete catalogue has over 5000 events and the *b*-value uncertainty is still too high, it is likely that the FMD is not consistent with an underlying Gutenberg-Richter distribution.

For the analysis of variations in FMDs, a large volcanic earthquake catalogue can be split on the basis of spatial or temporal windows, and this workflow applied to each sub-catalogue in turn. However, the same minimum complete catalogue size and reliability criteria rules apply to sub catalogues too.

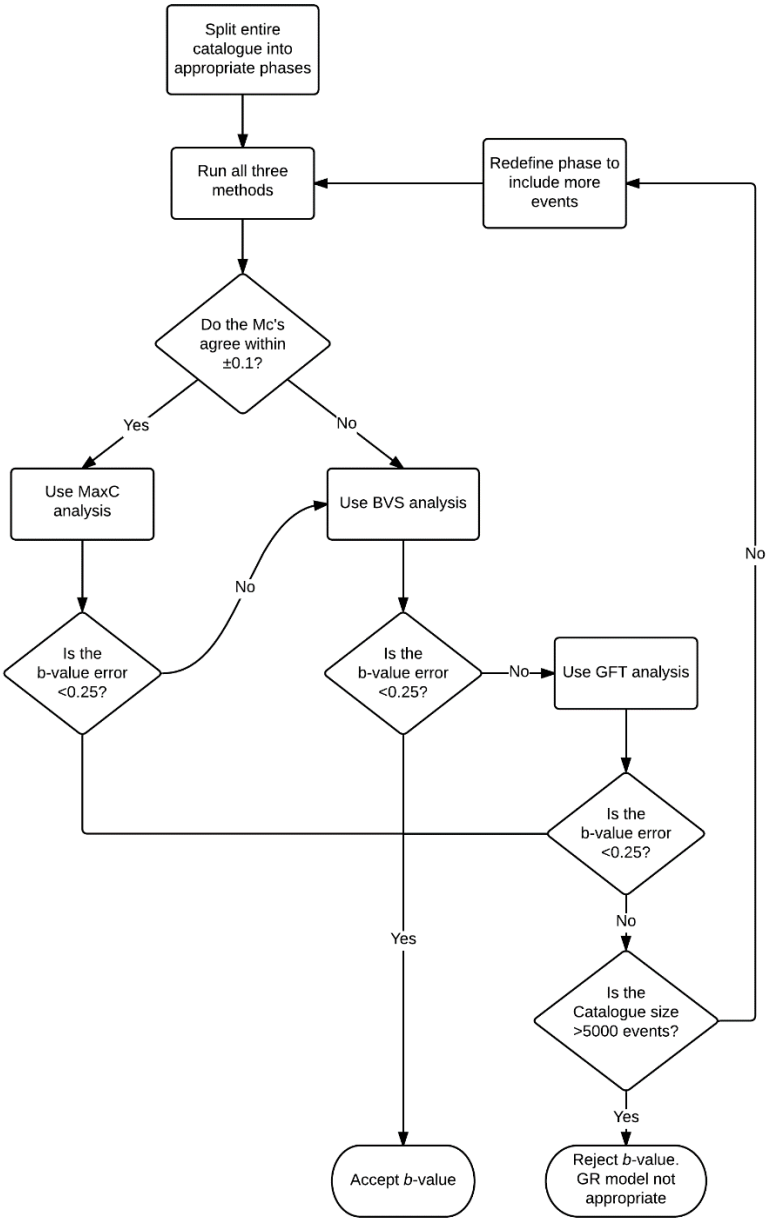

Figure 3.9 - Proposed workflow for best practice based on synthetic analysis.

3.6.4 Error introduced from the completeness magnitude

We now use the workflow of Figure 3.9 to consider the relative effect of *Mc* estimation for catalogues of different size on the accuracy and precision of the estimate of $\tilde{b}$ for the case of a broad-peaked distribution. Figure 3.10 shows a histogram of the $\tilde{b}$ for 100 catalogue realizations with b=2, along with examples of its standard deviation $\sigma_{\tilde{b}}$ estimated from equation 5. $\tilde{b}$ is beyond 1 standard deviation of b in more than 1/3 of

the cases, indicating a significant epistemic error in the estimation. We show in this section that this is due to the bias $\tilde{b} - b$ in the finite-sized sample. The error due to calculating *Mc* for individual realisations is illustrated as a blue bar at one standard deviation in Figure 9. The median $\tilde{b}$ is close to the true value (the central blue dot is near the vertical dashed line), so the residual bias due to estimating *Mc* is near zero for a large population of trials. However, the standard deviation in the error due to *Mc* is much larger than the average statistical error for similar *b*-values (the black error bars).

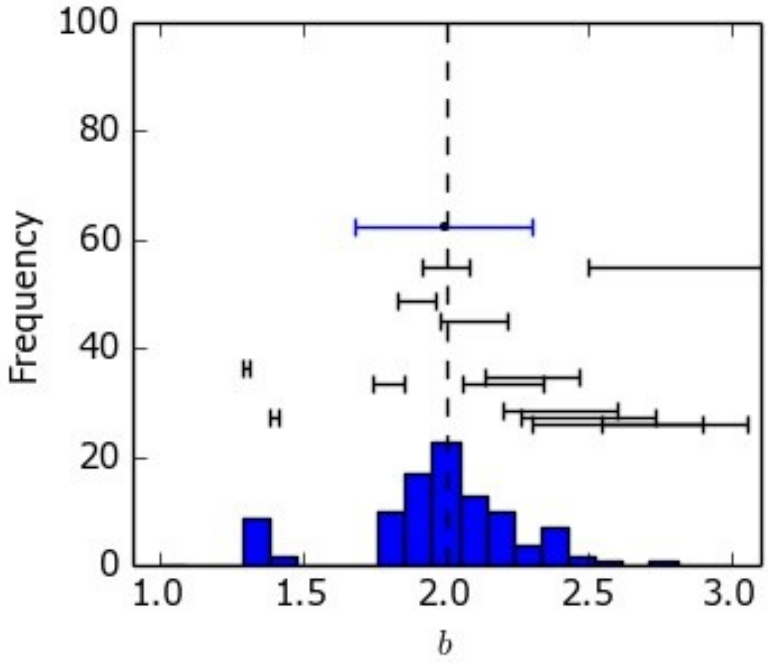

Figure 3.10 - *b*-value frequency plot for 100 synthetic catalogues when N_c=1000 and *b*=2. The blue (epistemic) error bar represents one standard deviation error in the data centred on the median *b*-value. The black error bars show the average aleatoric (Shi & Bolt *b*-value uncertainty) error for each bin.

To quantify this error in the general case, we ran many simulations for different values of b and N_c, with the results shown in Figure 3.11. Figure 3.11a shows the average statistical error from equation (5), Figure 3.11b the average error in $\tilde{b}$ due to propagating uncertainties in estimating *Mc* as illustrated by the blue horizontal error bar in Figure 3.10, and Figure 3.11c the ratio of the two. The ratio was calculated 5 times for each of 15 catalogue sizes between 50-5,000 events and *b*-values of 0.5, 1.0,

1.5, 2.0 & 3.0, with the average value indicated by the colour scheme in Figure 3.11. The ratio varies between 1.2 and a factor 14 or so for the range studied, implying that the sample bias error is always greater than, and often much greater than the estimated statistical uncertainty in $\tilde{b}$ from equation (5). This finding means that the statistical error commonly used on its own to quantify the $\tilde{b}$-value uncertainty is not an adequate description of the total error, though it approaches the total error for large numbers of events and low underlying b-values. In Figure 3.11c the ratio can reach an order of magnitude for b>2 and event numbers above 1000. This is because the statistical error $\sigma_{\tilde{b}}$ is very small when N_c is large. However the sample bias also increases with N_c for high b. This somewhat counter-intuitive result is because the magnitude range over which Mc can be calculated is much smaller at low N_c than at high N_c, so the uncertainty is bounded to a greater degree at low N_c, and hence reduces at low N_c. The template of Figure 3.11c can be used empirically to determine a more appropriate error for b-value estimation.

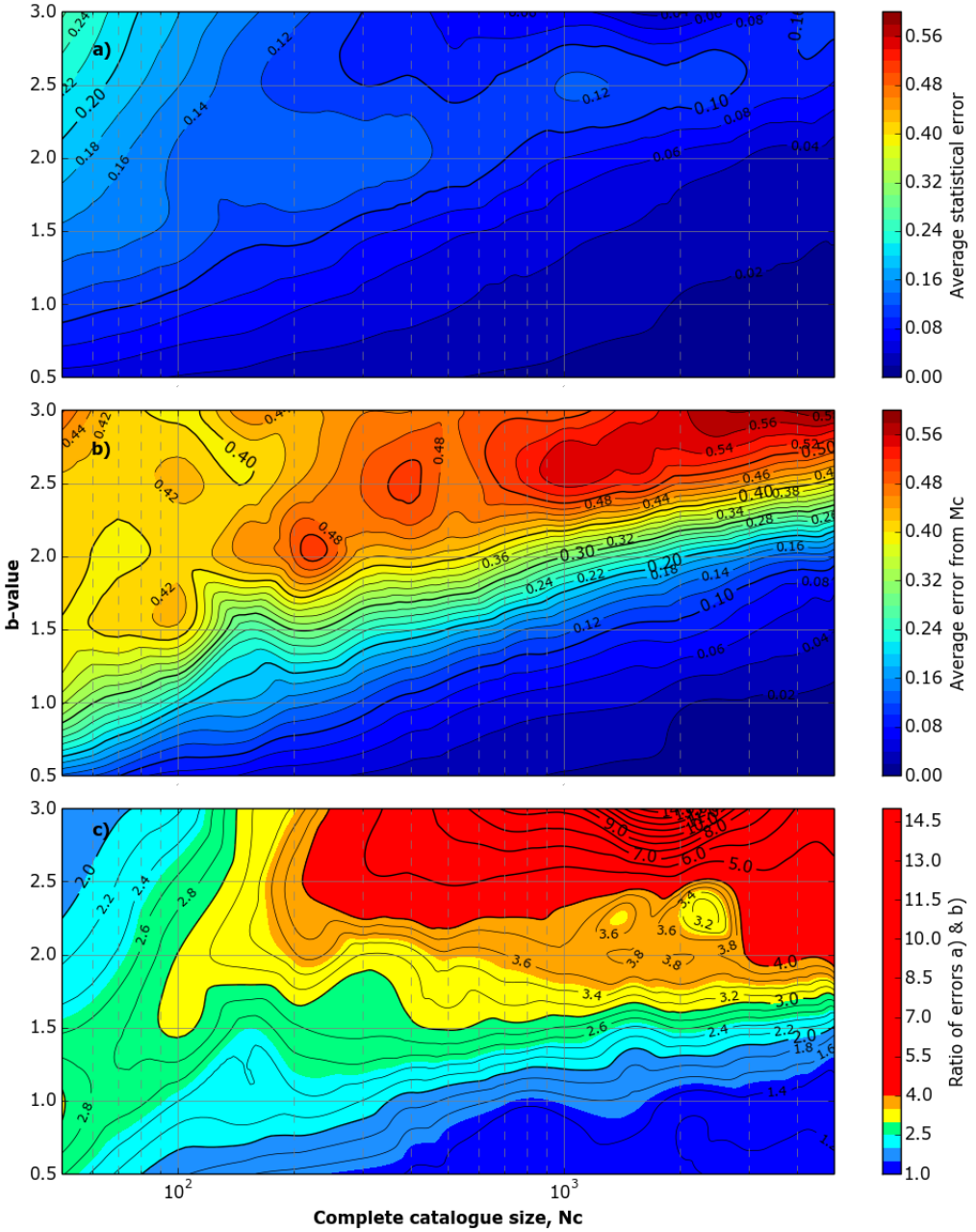

Figure 3.11 – Contour plots showing a) the statistical error in *b*-value estimated from eq. (5) as a function of varying complete catalogue size, N_c, and *b*-value. b) The error in *b*-value associated with the uncertainty in calculating *Mc*, estimated as in the example given in Figure 3.10 as a blue horizontal error bar. c) The ratio of the error in (b) to the statistical error in (a).

3.7 Application to volcanic catalogues

We apply our proposed workflow to earthquake catalogues for Mount Etna volcano, Sicily (Murru *et al.*, 1999; Murru *et al.*, 2005; Murru *et al.*, 2007) and El Hierro volcano, Canary Islands (Ibanez *et al.*, 2012; López *et al.*, 2012; Becerril *et al.*, 2013; Marti *et al.*, 2013b; García *et al.*, 2014) to test the reliability of any previously reported variations in *b*-values. This is simply to compare results from the proposed workflow to previous volcanic *b*-value's and not to make any interpretation about the behaviour of the volcanos.

We analyse the Instituto Geográfico Nacional (IGN) earthquake catalogue for El Hierro between July 2011 and December 2013, a period associated with significant seismic activity associated with magma emplacement, and including a submarine eruption that began on 10th October 2011 (Ibanez *et al.*, 2012; López *et al.*, 2012). The catalogue contains over 20,000 events, and so it is possible to subdivide it into several phases to analyse *b*-value variations. Figure 3.12 shows how each phase is defined by changes in event rate, with the first three phases following the scheme of Ibanez *et al.* (2012). The start of each phase is defined as midnight at the start of the selected day, however, if necessary the resolution of the boundaries can be increased as most catalogues give event time to the nearest second. All phases have over 200 events at or above *Mc*, thus the catalogues should be large enough to calculate reliable $\tilde{b}$-values following the synthetic analysis. At this stage the catalogue is simply divided temporally, so earthquakes may originate from different portions of the volcanic edifice. Should this occur, the *b* estimate may represent an average between sub-catalogues representative of different processes or stress conditions.

The results of applying our proposed workflow to the El Hierro catalogue are shown in Figure 3.12. These show a very high *b*-value of $\tilde{b}$=2.39±0.10 before the onset of the eruption, followed by a fluctuating $\tilde{b}$-value between 1-1.5 for the remainder of the catalogue. $\tilde{b}$-value uncertainties are determined using equation 5. The $\tilde{b}$-value is always above 1 within these statistical errors. These results are similar to those of

Ibanez *et al.* (2012), who reported a *b*-value before the eruption of 2.25±0.05 followed by values of *b*=1.34±0.04 and *b*=1.12±0.01 for the second and third phases respectively (Ibanez *et al.*, 2012). However, the Ibanez study used the 90% Goodness-of-fit method to estimate *Mc,* and least-squares regression to estimate *b*. The *Mc* values they report are significant under-estimates, and this means that the biased least-squares *b*-value estimates are, coincidently, close to the values reported here.

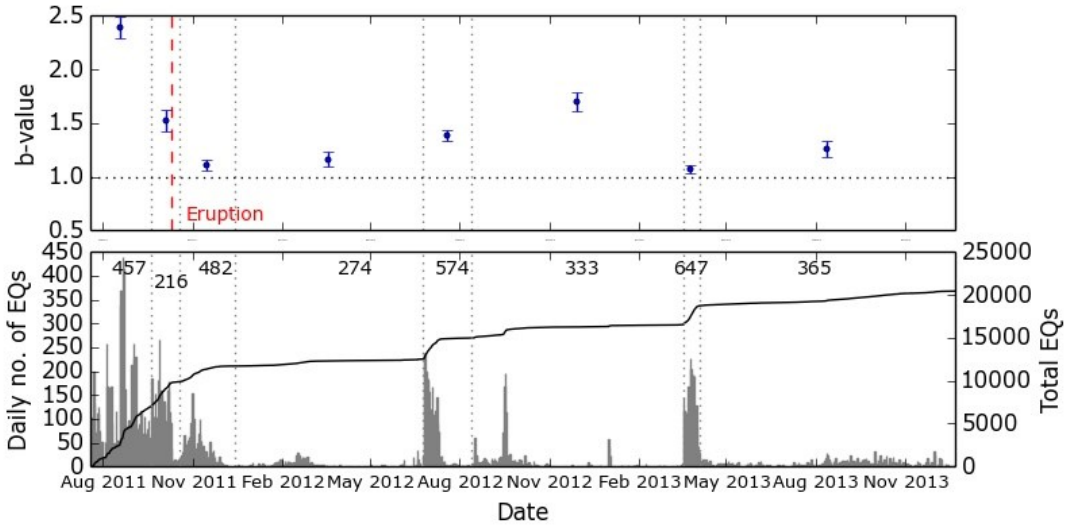

Figure 3.12 – Top: *b*-value variation through time for the July 2011 to December 2013 El Hierro seismic catalogue using the proposed workflow. The eruption date is marked by the red dashed line. Bottom: Daily number of events (grey bars) and cumulative number of events (black line). The phase divisions are marked by vertical grey dotted lines with the number of events in the complete catalogue of each phase noted at the top of the plot.

We also analyse the Istituto Nazionale di Geofisica e Volcanologia (INGV) earthquake catalogue for Mt Etna between January 1999 and December 2014. This catalogue spans several eruptive episodes, including the 2001 and 2002-03 flank eruptions and more recent paroxysmal activity at the new South East Crater. The catalogue contains 8000 events, with an event rate that is more stable through time than the El Hierro catalogue (Figure 3.12 and Figure 3.13). We divide the catalogue into 10 sub-phases on the basis of changes in earthquake rate, with each phase ideally containing between 200-5000 events.

Figure 3.13 shows the $\tilde{b}$-values calculated for Mt Etna using our proposed workflow. During the 2001 and 2002-03 flank eruptions the $\tilde{b}$-value is 1.5 or greater. However from the end of the 2002-03 flank eruption, the $\tilde{b}$-value appears to have stabilised at 1.0±0.2. Murru *et al.* (2007) analysed the spatial distribution of the b-value at Mt Etna between 1999 and 2005 and found an average of approximately 1.5, with an increase in average b-value with depth from b=1.2 to b=1.9.

Although the $\tilde{b}$-values for Mt Etna from 2004 onwards are close to 1.0 and there is no systematic trend in values, the $\tilde{b}$-values do not encompass b=1 within error for over half of the sub-phases in Figure 13. As the Shi & Bolt $\tilde{b}$-value uncertainty (eq. 5) defines one standard deviation error in the $\tilde{b}$-value we would expect 68% of the calculated b-values to capture b=1 within error if the underlying b-value is stationary. We might then conclude that the hypothesis that b=1 can be rejected at this confidence level. However, we have shown that the total error, including sample bias, can be significantly underestimated in Figure 3.11.

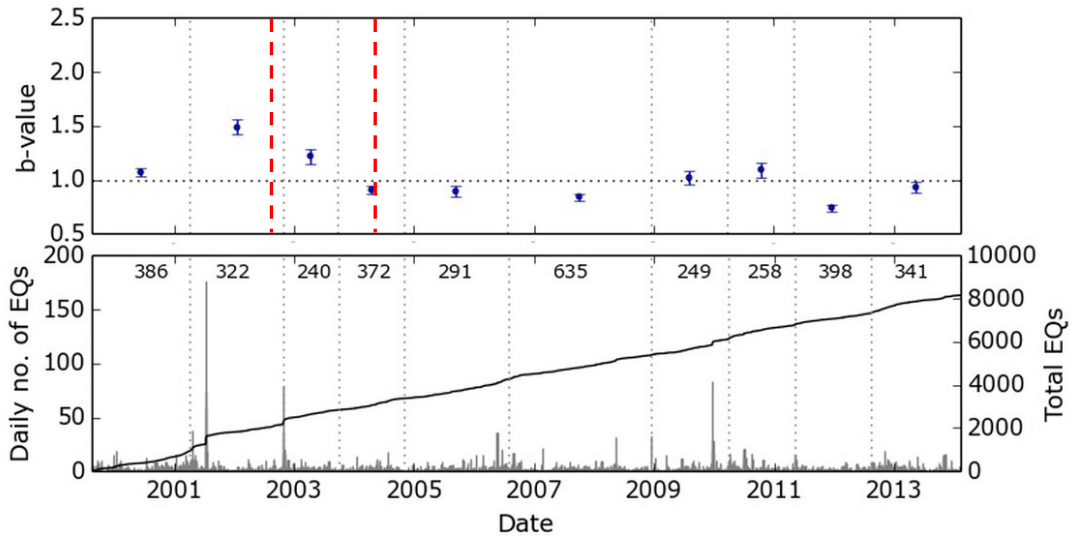

Figure 3.13 – Plots as in Figure 3.12 but for the 1999 - 2014 Mount Etna seismic catalogue. The initiation of the 2002 and 2004 flank eruptions are marked by the vertical dashed lines.

Accordingly we now apply the contour plot for the error multiplication values in Figure 3.11c to estimate a more realistic total error for our calculated *b*-value. For the 2011-13 El Hierro catalogue (Figure 3.14a) the high *b*-values at the start of the catalogue now have dramatically increased errors, and 3 of the 6 following *b*-values that sat between $1>\tilde{b}>1.5$ now lie within 1 standard deviation error around b=1.0. Using the Shi & Bolt uncertainty for the 2004-2014 Etna catalogue, the estimated $\tilde{b}$-values for only 2 of 10 phases (20%) lie within one standard deviation of b=1.0. However, once the modified error is applied to the catalogue (Figure 3.14b), the estimated $\tilde{b}$-value for 6 of the 10 phases (60%) lie within 1 standard deviation of b=1.0. The high *b*-values associated with the 2001 and 2002-03 flank eruptions also increase in error and could be consistent with *b*-value of no more than 1.5. The *b*-values for 3 of the 10 phases do not lie within 2 standard deviations of b=1 using the modified error. Therefore it would be hard to reject the hypothesis that *b* is a constant near unity for these phases, except at marginal significance.

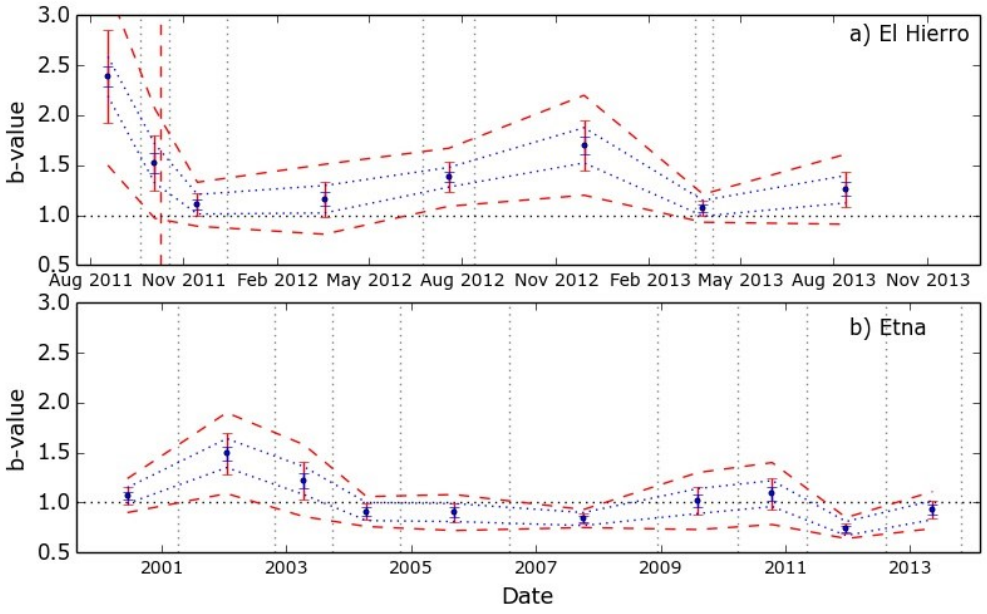

Figure 3.14 - *b*-value variation through time for a) the 2011-13 El Hierro catalogue, and b) the 1999 - 2014 Mount Etna seismic catalogue. Sample bias errors in are blue and estimated epistemic error are in grey. One standard deviation error is represented by the error bars and the grey dashed and blue dotted line respectively represent the 2 standard deviation error envelope.

3.8 Conclusions

The almost axiomatic inference that *b*-values are systematically higher for volcanic earthquakes is based on data and methodology that are often insufficient to address the question, notably the very small sizes of the samples used, the methods of parameter estimation and the different methods used to infer the completeness magnitude *Mc*. The Maximum Curvature method is simple, and can be used when a catalogue has a sharp peak in the discrete data. Otherwise the *b*-value stability method is the most favourable. If that does not generate a *b*-value with a standard error ≤0.25 the Goodness-of-Fit method can be used as a third option. If a stable value of *b* cannot be obtained then the sample size must be increased in space and/or time. Our results imply a pragmatic minimum of 200 events above *Mc* is generally needed. From further simulations, we also recommend a minimum of 500 events when dealing with raw incomplete catalogues before this workflow can be applied. This logic is captured in a new workflow for estimating *Mc*. Even when this best practice is followed, there can be a significant residual error from calculating *Mc* in a single sample. This is comparable to or much greater than the statistical error, particularly for higher values of *b*. Nevertheless, when this is accounted for we confirm *b*-values for the El Hierro catalogue are generally higher than 1 at a confidence level of 95%, and may be significantly higher during eruptive phases. For Mount Etna the hypothesis *b*=1 can be rejected for only two time intervals, one associated with a flank eruption. We conclude seismic *b*-values can be high for volcanic earthquake populations, especially when associated with eruptive phases. Otherwise they appear to be very close to those obtained for tectonic earthquakes at the 95% confidence level.

3.9 Acknowledgements

Nick Roberts is a NERC funded PhD student at the University of Edinburgh. We thank the Instituto Geográfico Nacional and INGV Sezione di Catania for making the seismic catalogues for El Hierro and Mount Etna respectively available, Mark Naylor for providing feedback on earlier drafts of the paper, and three anonymous reviewers, and Jackie Caplan-Auerbach for improving the paper with their critical feedback.

Chapter 4 – Mode-Switching in Volcanic Seismicity: El Hierro 2011-13

This paper takes the form of a published paper, re-formatted for the thesis style, without further edits. It addresses research questions 1), 2), 3), 4) and 7) from Section 2.5.1. The current methods used to sample frequency-magnitude distributions were discussed in Section 2.2.2. In this paper I propose a novel solution to minimising bias in the selection of sub-catalogues and consequent analysis of the El Hierro catalogue, as in Chapter 3. This solution presents a higher resolution in *b*-value variations through time, as well as calculating a non-linear error structure. This is opposed to calculating discrete *b*-values with a Gaussian error distribution, as is the general approach in the current literature.

Paper

Nick. S. Roberts[1], Andrew F. Bell[1], Ian G. Main[1]

[1]School of Geosciences, University of Edinburgh, James Hutton Road, Edinburgh, UK. EH9 3FE

Submitted to Geophysical Research Letters, 27 January 2015

Accepted 14 April 2016

Accepted article published online 28 April 2016 2016

4.1 Abstract

The Gutenberg-Richter *b*-value (Gutenberg and Richter, 1954) is commonly used in volcanic eruption forecasting to infer material (Jordan *et al.*, 2011) or mechanical properties (Scholz, 1968; Sammonds *et al.*, 1992; Schorlemmer *et al.*, 2005) from earthquake distributions. Such studies typically analyse discrete time windows or phases (Wyss *et al.*, 2001; Murru *et al.*, 2007; Ibanez *et al.*, 2012), but the choice of such windows is subjective, and can introduce significant bias. Here we minimise this sample bias by iteratively sampling catalogues (Kamer and Hiemer, 2015) with randomly-chosen windows and then stacking the resulting probability density functions for the estimated $\tilde{b}$-value to determine a net probability density function, taking the global maximum as the most probable $\tilde{b}$-value. We examine data from the El Hierro seismic catalogue during a period of unrest in 2011-2013 (Ibanez *et al.*, 2012; López *et al.*, 2012; Marti *et al.*, 2013a; Marti *et al.*, 2013b; López *et al.*, 2014), and

demonstrate clear multi-modal behaviour. Individual modes are relatively stable in time, but the most probable $\tilde{b}$-value intermittently switches between modes, one of which is similar to that of tectonic seismicity. Multi-modality is primarily associated with intermittent activation and cessation of activity in different parts of the volcanic system rather than with respect to any systematic inferred underlying process. These results add a new dimension to the interpretation of seismic $\tilde{b}$-value changes associated with volcanic seismicity in terms of underlying mechanisms, and pose questions to be addressed in developing predictive models that account for mode-switching.

4.2 Introduction

The b-value of the Gutenberg-Richter relation (Equation [2.1]), describes the relative proportions of large and small magnitude earthquakes in a catalogue. Theoretical and experimental studies suggest that b-values are influenced by a variety of factors, including stress (Scholz, 1968), mechanical properties (Schorlemmer *et al.*, 2005), and material damage. At volcanoes, the temporal evolution of the b-value has been used to infer changes in the physical processes controlling the approach to eruption, including material failure, and have been proposed as a potential forecasting tool. However, existing methods typically calculate b within either a series of independent finite-time windows or overlapping fixed-width moving windows. In order to achieve the necessary fine-scale resolution of b-value changes, these studies often use small sub-catalogue sizes, and assume a single value of the completeness magnitude. Consequently the errors in the b-values are likely to be large, correlated, and under-estimated, and potentially give rise to anomalous results.

Here, for the first time, we show the full probability distribution of the b-value for a volcanic earthquake catalogue as it evolves with time. This result is achieved by combining two new methods. Firstly, a stochastic windowing technique is used to recover fine-scale resolution of b-value changes, whilst avoiding arbitrary choices of window edges and small sub-catalogue sizes. Secondly, a more realistic uncertainty

estimate for the b-value is determined for each sub-catalogue by joint estimation with the completeness magnitude. This process is iterated, typically 100 times, and the resulting b-value samples and their errors combined to construct the full b-value probability distribution. A key benefit of this approach is that it is able to resolve different b-values associated with contemporaneous processes in the case where some generate high rates of events for short durations and others low rates for longer durations, characteristics that are typical for many volcanic processes.

After testing and benchmarking on synthetic catalogues (Figure 4.2), we applied the new method to seismicity data from El Hierro volcano, Canary Islands (Ibanez *et al.*, 2012; López *et al.*, 2012; Becerril *et al.*, 2013; Marti *et al.*, 2013b; García *et al.*, 2014) to generate a temporally-evolving $\tilde{b}$-value probability density function (PDF), denoted $P'(\tilde{b})$. We analyse the Instituto Geográfico Nacional (IGN) earthquake catalogue for El Hierro between July 2011 and December 2013 - a period containing over 20,000 earthquakes associated with magma emplacement and a submarine eruption that began on 10th October 2011 (Ibanez *et al.*, 2012; López *et al.*, 2012). Some 4100 individual $\tilde{b}$-values were generated over 100 iterations, these were then converted first to Gaussian PDF's for individual windows, and stacked to determine the net $P'(\tilde{b})$ using a 50-point moving window.

4.2.1 Mode-switching definition

Here 'mode-switching' behaviour in the b-value is defined as an immediate change for one stable value to another. As the methodology proposed in this chapter does not use discrete errors, the amount of change between values is not quantified. Instead it is a visual interpretation that the b-value increases/decreases instantaneously (not gradually), after which the new b-value stabilises for a period of time.

4.3 Methods

4.3.1 *b*-value calculation

Where the catalogue is completely reported, the frequency-magnitude distribution commonly takes the form of a Gutenberg-Richter relation (Gutenberg and Richter, 1954):

$$\log(N_c) = a - bM, \qquad [\ 4.1\ ]$$

where N_c is the total number of earthquakes of magnitude equal to or greater than M, and a and b are real, positive constants. The b-value is best calculated using the maximum likelihood method (Mignan and Woessner, 2012):

$$\tilde{b} = \frac{1}{\ln 10[\hat{\mu} - (M_c - \Delta M/2)]} \qquad [\ 4.2\ ]$$

Here $\hat{\mu}$ is the average magnitude of the sample, M_c is the completeness magnitude, and ΔM is the binned magnitude width, usually 0.1 units. The uncertainty at one standard deviation confidence (Marzocchi and Sandri, 2003) is commonly estimated as:

$$\sigma_{\tilde{b}} = 2.30\tilde{b}^2 \sqrt{\frac{\sum_{i=1}^{N}(M_i - \hat{\mu})^2}{N_c(N_c - 1)}} \qquad [\ 4.3\ ]$$

where N_c is the number of events in the complete catalogue. Here we modify this error using the calibration in Figure 3.11c to account for calculating the completeness magnitude.

4.3.2 Iterative sampling methodology

First, the catalogue is divided into sub-catalogues of random size between a predefined minimum and maximum number of events. Three iterations are illustrated in Figure 4.1a. For each sub-catalogue *Mc* is selected using the workflow in Figure 3.9. The $\tilde{b}$-value with associated error $\sigma_{\tilde{b}}$ is calculated for the complete part of the sub-catalogue using Equations [4.2] and [4.3]. The error multiplication factor

$R(\tilde{b}, N)$ from Figure 3.11c is then used to determine the total error $R\sigma_{\tilde{b}}$, i.e. including the uncertainty introduced in estimating *Mc*. The average time and event number for the sub-catalogue is then calculated, allowing the $\tilde{b}$-value to be plotted as a function of either. Figure 4.1b shows the cloud of data points produced by 100 iterations. The advantage of plotting by event number is it normalises the event rate making it easier to see variations when the event rate is high. This process is then iterated a desired number of times, each time using different random sub-catalogue sizes. Following enough iterations a cloud of data points spanning the whole catalogue is created.

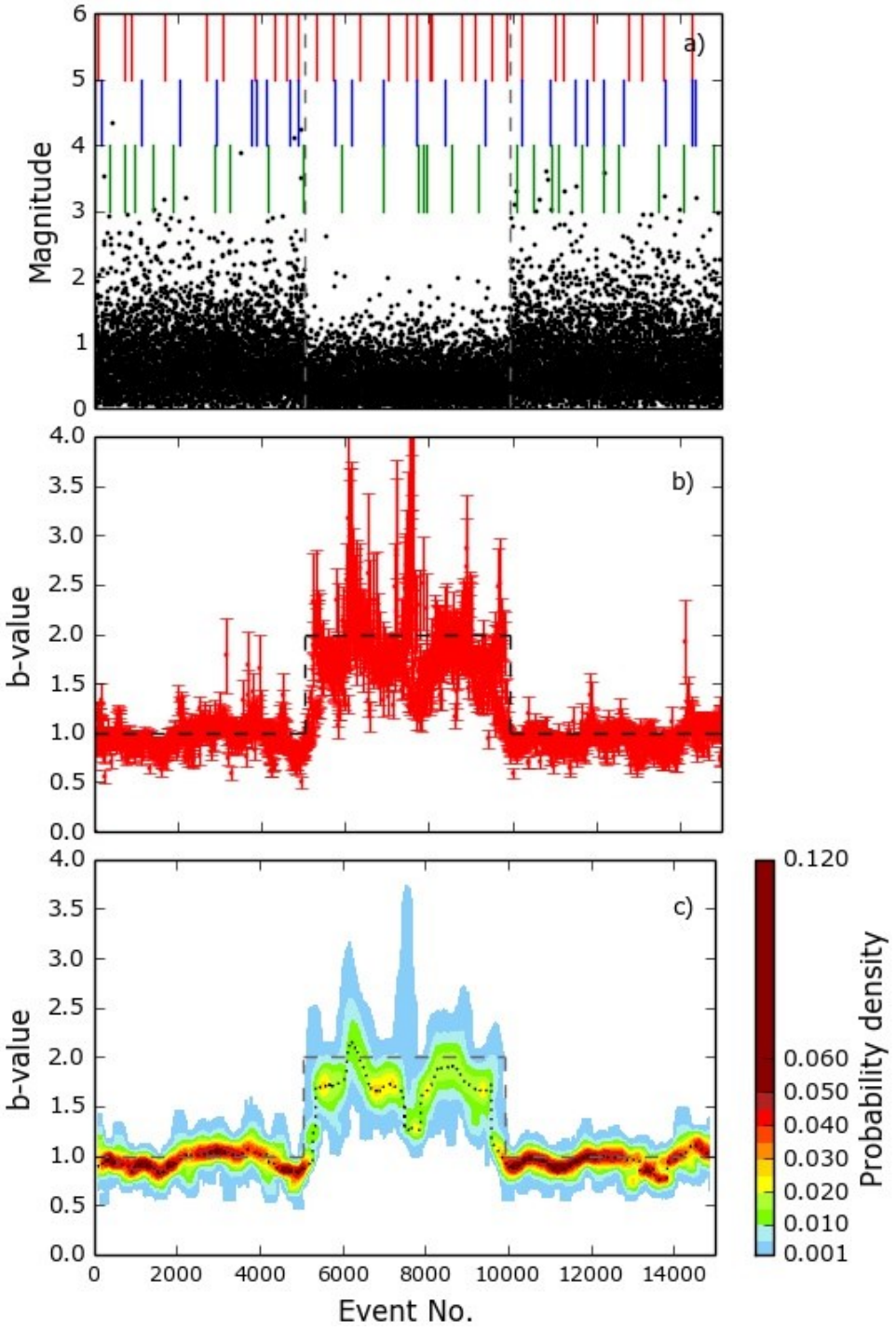

Figure 4.1 - The synthetic catalogue has a parent Gutenberg-Richter distribution above *Mc*=1.0, with *b*=1 for the first and last 5000 events, and *b*=2 for the middle 5000. a) Each event is shown as a black dot. The red, blue and green lines show the boundaires of each catalogue in three succesive iterations. b) Cloud of data points produced by 100 iterations. c) The $\tilde{b}$-value probability density by event number. The dashed grey line shows the underlying known *b*-value. The dotted black line marks $\tilde{b}_P$.

For this method to be used as a real-time analysis tool, it is important we are able to identify $\tilde{b}$-value variations in the most recent events. To make sure the most recent events are always sampled, the catalogue is divided into sub-catalogues by starting with the youngest event then working back in time. This means the oldest events may be under-sampled if the number of remaining events if less than the minimum sample size.

4.3.3 Converting to a probability density function

Each data point for a given randomly-generated window has a $\tilde{b}$–value, an error, $\sigma_{\tilde{b}}$, and a multiplication factor R. For consistency with Equation [4.3], we use the parametrised version of the normal distribution to calculate the relative probability for any given b-value, b_i.

$$P\left(b_i; \tilde{b}, \sigma_{\tilde{b}}, R\right) = \frac{1}{R\sigma_{\tilde{b}}\sqrt{2\pi}} e^{-\frac{1}{2}\left(\frac{b_i-\tilde{b}}{R\sigma_{\tilde{b}}}\right)^2} \qquad [\ 4.4\ ]$$

$P(b_i)$ is calculated over a b-value range from 0-4, at a resolution of 0.01 units.

4.3.4 Monte-Carlo simulation of error structure using moving windows

Stacking data improves signal-to-noise ratios therefore, stacking enough individual PDF's at the randomly-sampled times should reveal the true structure of the overall PDF. However, from Equation [4.4] $\tilde{b}$-values with smaller error contribute more to a stacked curve. As the size of the error is proportional to the $\tilde{b}$-value (Equation [4.3]), higher $\tilde{b}$-values will also have higher errors (Figure 4.1). Therefore care must be taken not to stack too may data points so that brief periods of high $\tilde{b}$ will not be hidden due to over smoothing.

To stack the PDF's we take a fixed number of data points and sum the individual PDF's for all b_i and then normalise the summed curve so that $\sum_{i=0}^{i=4} P(b_i) = 1$. This allows us to compare the peak probability for all the stacked PDF's. We take the time stamp for a given window to be respectively the average event number and average time, and do this for all times and event numbers. The results are visualised as a

contour plot in probability-time space rather than as error bars at discrete points. Figure 4.2 shows sensitivity testing for 10, 20, 50, 100, and 200 events in each window. We chose 50 events as the ideal trade-off for resolution and smoothness.

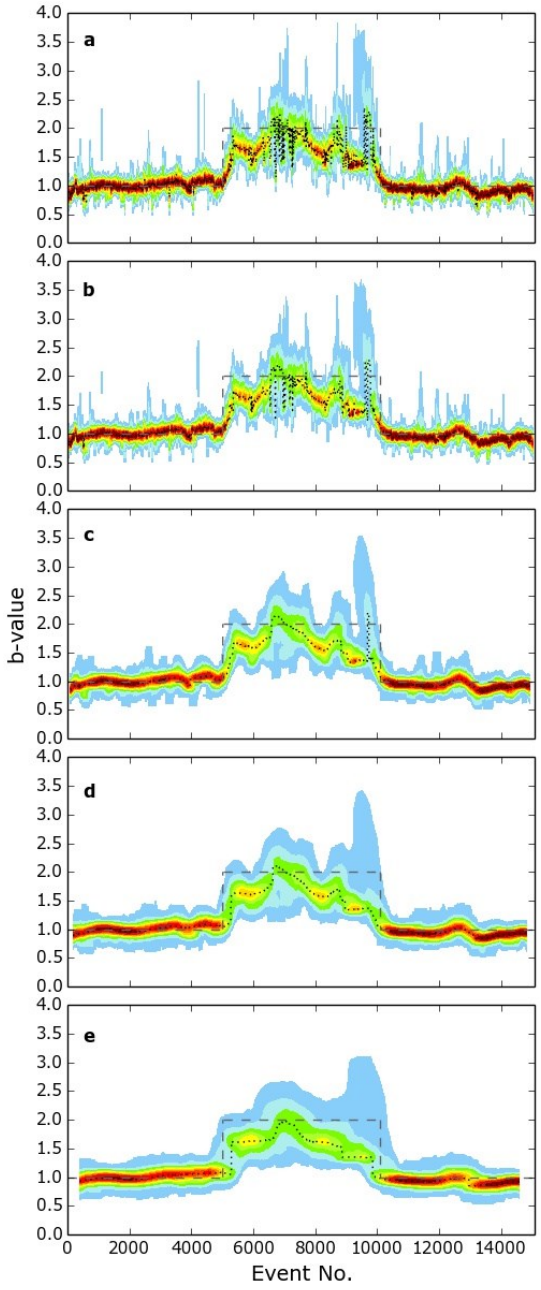

Figure 4.2 - Sensitivity testing of the size of the window used to create the $\tilde{b}$-value probability density function. a) Uses 10 data points, b) 20, c) 50, d) 100 and e) 200. 50 data points were chosen as a compromise between eliminating noise and over-smoothing the data. However, every window size shows the major steps in the modal $\tilde{b}$-value.

4.3.5 Choice of parameters

The key choice of parameters is choosing the minimum/maximum catalogue size. In Chapter 3 I propose a minimum complete catalogue size of N_c=200 for a complete catalogue (or N=500 for an incomplete catalogue with a gradual roll-off at low magnitude). As the catalogue is randomly divided into sub-catalogues before any frequency-magnitude analysis is performed, N=500 for incomplete catalogues should be used. The ideal compromise in resolution and reliability of calculated $\tilde{b}$-values was found to be a minimum catalogue size of 50 events and maximum of 1000. This gives an average catalogue size of 525 events.

The number of iterations required depends of on how dense you wish the data points to be. Equation [4.5] approximates this:

$$it \approx \frac{(S_{min} + S_{max})/2}{E_p} \qquad [\ 4.5\ ]$$

Where it is the number of iterations, S_{min} and S_{max} are respectively the minimum and maximum sample size, and E_p is the number of events you wish be represented per data point. Therefore with $S_{min}, S_{min} = 50, 1000$; 100 iterations will produce approximately one data points per five events.

4.4 Results

The results are shown as a function of both event number (Figure 4.3a) and time (Figure 4.3b). We use both plots because it is possible to see the fine structure clearer on the event number plot during times of high event rate. The periods with red colours in Figure 4.3 have the highest probability density $P'(\tilde{b})$. The $\tilde{b}$-value with peak probability $\tilde{b}_P$, is marked with a black dotted line to show how the maximum likelihood $\tilde{b}$-value varies through time.

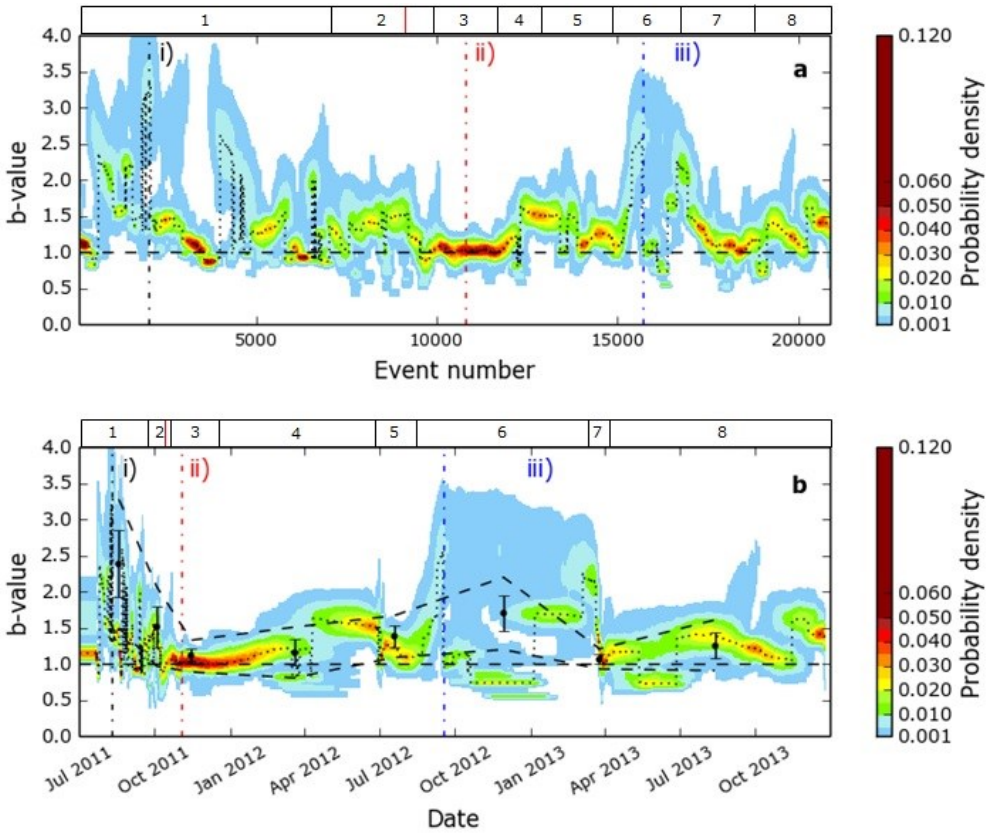

Figure 4.3 - The $\tilde{b}$-value probability density plotted by a) event number, and b) time, using the iterative sampling method described in the methods section. The dotted black line traces $\tilde{b}_P$. The vertical dot-dashed black, red and blue lines mark the times of the events: i) Event 2020 on 9/8/2010, ii) Event 10800 on 2/11/2010, and iii) Event 15720 on 18/12/2011. Overlain is a comparison of results in Figure 3.14a using fixed, subjectively chosen windows. The error bars show the total $\tilde{b}$-value at one standard deviation, accounting for the error in *Mc*. The dashed lines show two standard deviations error (approximately 95% confidence limits). The bars with numbers 1-8 shows the phases in Table 4.1. The red line in phase 2 indicates the time of the eruption on 10/10/11.

The results show $\tilde{b}_P$ typically being between 1.0-1.5, and that it is best constrained when $\tilde{b}_P \approx 1$. Prior to the eruption $\tilde{b}_P$ can be as high as 3.25 with several periods of $\tilde{b}_P > 2.0$. However, the most striking aspect of Figure 4.3 is the rapid switching between alternately higher and lower $\tilde{b}_P$. The $\tilde{b}_P$ value does not increase or decrease smoothly through the catalogue; it jumps between values then remains relatively constant until it changes again. This behaviour is contrary to experimental observations, where $\tilde{b}$-values evolve more gradually with time (Henderson *et al.*, 1994; Main, 1996) and is reminiscent of a 'mode-switching' process (Ben-Zion *et al.*, 1999) observed in some models for tectonic earthquakes. Post-eruption, the $\tilde{b}$-values stabilises at $\tilde{b}$=1 for several months until a period from July 2012 – April 2013 where the $\tilde{b}$-value is very poorly constrained, with $P'(\tilde{b}) < 0.020$. The net $P'(\tilde{b})$ is clearly multi-modal, e.g. with persistent local peaks in the range 0.6-2.5, in the time period October 2012 - December 2012.

Figure 4.3b also compares $\tilde{b}_P$ with inferred $\tilde{b}$-values obtained by conventional finite-time windows, using phase boundaries based on previously reported changes in hypocentre location (Roberts *et al.*, 2015). The uncertainty structure is much richer and more informative for the new method. While the previously inferred $\tilde{b}$-values and uncertainties are not unreasonable using the conventional windowing method, they do not capture the multi-modal behaviour and mode-switching in $\tilde{b}_P$. There are also significant periods when $\tilde{b}_P$ does not agree with $\tilde{b}$ within its uncertainty, shown as two standard deviations, or approximately 95% confidence. In September 2012 and March 2013 $\tilde{b}_P$ is systematically above this two standard deviation window, and through October-December 2012 and in May 2013 it is systematically below it.

Our method allows for the analysis of the full PDF, rather than assuming a Gaussian distribution (Aki, 1965), giving a much greater insight into the error structure and its potential multi-modal character. The time or event number associated with each stacked window is taken to be the average event number or time, so it is possible to examine snapshots of the net PDF for any given event or time. Figure 4.4 shows three

examples at different times corresponding to three significant events: i) where $\tilde{b}_P$ is very high (>3), ii) where $\tilde{b}_P \approx 1$, and iii) where $\tilde{b}_P$ is multi-modal. These examples are indicated in Figure 4.3 and Figure 4.5. Event (i) has the highest $\tilde{b}_P$ in the whole catalogue where $\tilde{b}_P$ = 3.25, with a broad, low-amplitude peak value $P(\tilde{b}_P)$ of only ~0.006. There is a subsidiary peak at $\tilde{b}$=1.3 corresponding to the baseline b-value both before and after the period of very high $\tilde{b}_P$. The window when $\tilde{b}_P$=3.25 is only a few hundred events wide. This would be very hard to identify by eye in a time series since it occurs during a period with very high event rates.

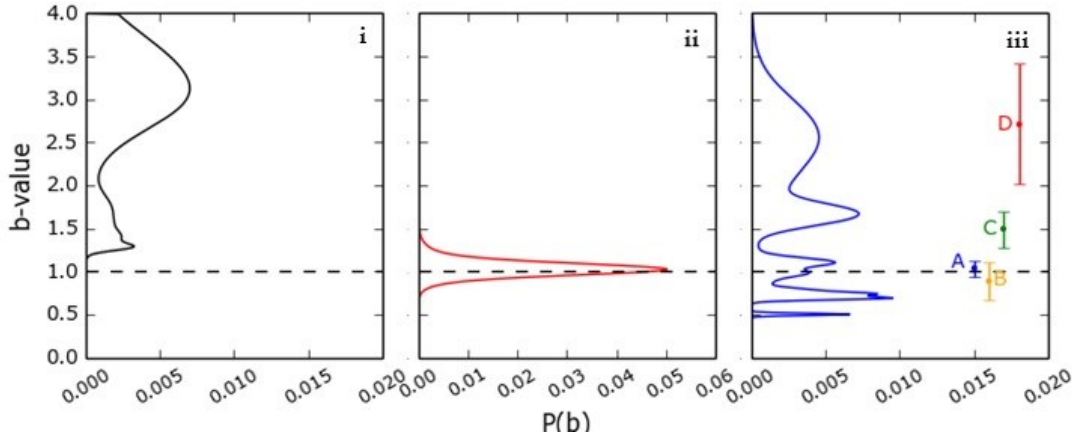

Figure 4.4 – Cross-sections of the $\tilde{b}$-value probability density function marked in Figure 4.3, using a 50 data point window. Coloured error bars in iii) represent the $\tilde{b}$-values calculated for the clusters in Figure 4.5.

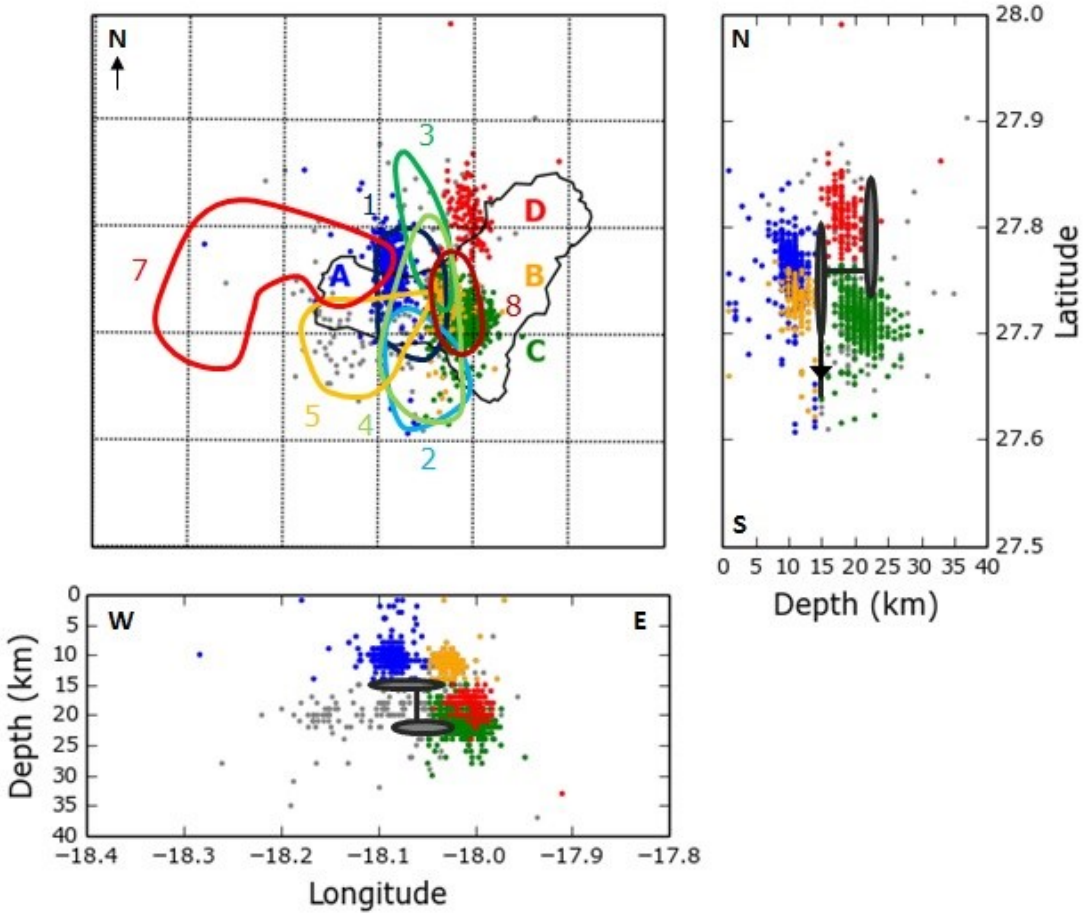

Figure 4.5 – Epicentral and hypocentral locations of earthquakes above magnitude 0.0 in phase 6 (Table 4.1). Each colour marks a separate cluster of events, A-D. All clusters ceased activity by 18/3/13. Cluster A started on 13/8/12. Clusters B and C started on 14/9/12. Cluster D began on 31/12/12. Events coloured grey were judged not to be part of any of the clusters of events. The coloured polylines show where the majority of events in phases 1-5, 7 and 8 are clustered. The black and grey ovals and lines in the cross section indicate the relative position of the magma chamber described in Marti *et al.* (2013a, 2013b). The direction of migration in phase 2 is marked with an arrow.

In the post eruption phase (Figure 4.4ii) $\tilde{b}$ is very well constrained to $\tilde{b}_P$=1.0, similar to that of tectonic seismicity There is a single peak with a narrow symmetric base, indicating simple uni-modal behaviour. Figure 4.4iii shows the net PDF associated with event (iii) in December 2012. The PDF is clearly multi-modal, with five notable peaks at $\tilde{b}$ = 0.5, 0.7, 1.1, 1.7 and 2.6, although the peak at 0.5 has a very small cumulative probability (<1%) associated with it, and hence may not be significant.

The question arises – what might be the underlying cause of the four peaks that do make a significant contribution to the cumulative probability?

Closer inspection of the seismic catalogue reveals there are four clusters (A-D) of events that can be separated spatially (Figure 4.5) as well as temporally, with A starting first, B and C second at the same time but at different depths, then finally D. All clusters then ended at approximately the same time. Accordingly we determined $\tilde{b}$ and its error bar for the four clusters. Clusters A-C contain >500 events in the incomplete catalogue, therefore with an average sampled catalogue size of 525 the calculated $\tilde{b}$-values should be discernible from one another. Cluster D contains 113 events, so although it will be much harder to sample, the minimum catalogue size of 50 events should allow for it to be suitably represented in the PDF with given enough sampling iterations.

Clusters B and D both have complete catalogue sizes significantly below the advised threshold (Roberts *et al.*, 2015) of $N \geq 200$ (89 and 38 respectively), and so the results should be treated with caution. However, the calculated $\tilde{b}$-values for all four clusters fit well within error to the four most significant peaks in the PDF (Figure 4.5). The mode-switching behaviour can then be attributed to different parts of the volcanic system being activated at different times, each with an otherwise relatively stationary or slowly-evolving $\tilde{b}$-value and location. Tis is instead of a systematic change in say the global stress state for the whole area of unrest that may have been the preferred interpretation using the current standard practice.

Comparison of the hypocentres and characteristics of the clusters with previously published volcanological models of the activity preceding and during the eruption (Ibanez *et al.*, 2012; López *et al.*, 2012; Marti *et al.*, 2013a; Marti *et al.*, 2013b; López *et al.*, 2014) shows Clusters C and D are likely to be associated with eastwards lateral magma emplacement, originating from a magma chamber in the upper mantle at ~20 km depth. Clusters A and B at ~12km depth occur just above the inferred location of the upper magma chamber at the Moho discontinuity, ~14km depth. Table 4.1 shows

the modal $\tilde{b}_P$-values for all eight phases between July 2011 and December 2013. The two most common modes are $\tilde{b}_P = 1.0$ and 1.5. Spatio-temporal clustering is associated with inferred changes in the magma volume inducing events above the upper and lower chambers and lateral magma emplacement (laterally propagating clusters). There is no apparent systematic correlation between these inferred processes and $\tilde{b}_P$. Instead $\tilde{b}_P$ changes systematically as different parts of the volcano system are activated or de-activated, each having its own characteristic $\tilde{b}$-value.

This ability to resolve multiple clusters of varying $\tilde{b}$-values occurring at overlapping time-windows is the most important advance compared to current methodology. Conventional windowing effectively masks any multi-modality and mode-switching behaviour, in cases where the full net uncertainty structure is not actually Gaussian, for example due to different parts of the volcanic system being activated at different times.

Table 4.1 – Phases of seismic activity at El Hierro from July 2011 to Dec 2013 (Figure 4.5). A description of the inferred process of the events are given, the time and event ranges are stated. Phases 1-3 have been previously defined by (Ibanez *et al.*, 2012). Modal $\tilde{b}_P$ and appriximate 95% $\tilde{b}$ range are all identifed using Figure 4.3. The $\tilde{b}$-values given in the final column are from Figure 3.12 and shown in Figure 4.3b for comparison. *95% range estimated from PDF producing multi-modal errors in Figure 4.4iii.

Phase no.	Observation	Inferred process	Time range
1	Spatially stationary events at 8-16 km depth.	Magma intrusion and accumulation in upper chamber(Marti *et al.*, 2013b)	19/7/11 to 20/9/11 (Ibanez *et al.*, 2012)
2	Southward laterally migrating events at 10-18 km depth.	Sill migration along Moho discontinuity (Marti *et al.*, 2013b; López *et al.*, 2014)	20/9/11 (Ibanez *et al.*, 2012) to 18/10/11 (Ibanez *et al.*, 2012)
3	Spatially stationary events at 15-25 km depth	Deflation above lower chamber (Marti *et al.*, 2013b)	18/10/11 (Ibanez *et al.*, 2012) to 14/12/11
4	Spatially stationary events at 9-18 km depth.	Expansion above recharging upper chamber (Marti *et al.*, 2013b)	14/12/11 to 24/6/12
5	South-westward laterally migrating events at 17-24 km depth.	A magma intrusion (Marti *et al.*, 2013b)	24/6/12 to 13/8/12
6	Four clusters of spatially stationary events (Figure 4.5) at varying depths	Deflation above both chambers	13/8/12 to 18/3/13
A	*Spatially stationary events at 9-13 km depth.*	*Deflation above upper chamber*	*13/8/12 to 18/3/13*
B	*Spatially stationary events at 11-14 km depth.*	*Deflation above the upper chamber*	*14/9/12 to 18/3/13*
C	*Spatially stationary events at 17-24 km depth*	*Deflation above and to the south of the lower chamber*	*14/9/12 to 18/3/13*
D	*Spatially stationary events at 16-20 km depth*	*Deflation above and to the east of the lower chamber*	*31/12/12 to 18/3/13*
7	Westward laterally migrating events at 12-20 km depth	A magma intrusion	18/3/13 to 4/4/13
8	Spatially stationary events at 9-14 km depth	Deflation above upper chamber	4/4/13 to 22/12/13

Further columns of Table 4.1.

Phase no.	Event no. range	modal $\tilde{b}_P$	95% $\tilde{b}$ range	$\tilde{b} \pm 2\sigma$ from Figure 3.12
1	0-7033	1.0, 2.3, 3.2	0.8 – 3.6	2.39 ± 0.39
2	7034-9883	1.5	0.7 – 1.9	1.52 ± 0.27
3	9884-11706	1.0	0.8 – 1.4	1.11 ± 0.10
4	11707-12503	1.0, 1.5	0.6 – 1.8	1.16 ± 0.16
5	12504-14956	1.2,1.5	0.8 – 2.5	1.38 ± 0.13
6	14957-16492	0.6, 0.7, 1.1, 1.7, 2.6	0.6 – 2.8	1.70 ± 0.27
A	*501 events*	*1.1*	*0.94-1.26**	*1.03 ± 0.10*
B	*645 events*	*0.7*	*0.69-0.94**	*0.89 ± 0.22*
C	*772 events*	*1.7*	*1.38-1.96**	*1.49 ± 0.21*
D	*113 events*	*2.6*	*1.963.12**	*2.71 ± 0.70*
7	16493-18720	1.1, 2.0	0.8 – 2.5	1.07 ± 0.06
8	18721-20385	0.8, 1.2, 1.5	0.6 – 1.9	1.26 ± 0.16

4.5 Conclusions

In summary, we have developed and applied a new iterative sampling method to the 2011-13 El Hierro catalogue. The method minimises bias associated with finite sampling of time windows and reveals a complex net probability density function in the real volcanic data. We report high $\tilde{b}$-values of up to 3.25 before the main submarine eruption on 10th October 2011, followed by a relatively stable period when $\tilde{b}$=1, i.e. similar to that of natural tectonic seismicity. From August 2012 to March 2013 we observe strongly multi-modal behaviour with four significant local peaks. Through further investigation into the catalogue we discover these can be associated with spatially separate concurrent clusters of seismic activity (Figure 4.5) and that high $\tilde{b}$-values are not necessarily inherently linked with a specific volcanic process. Our results confirm that conventional windowing with a linear (Gaussian) error structure often provides a good first order estimate of the $\tilde{b}$-value at a given time, but lacks resolution and detail of our iterative sampling method, and misses key intervals where the $\tilde{b}_P$-value is outside the estimated error. Critically we observe mode-switching of $\tilde{b}_P$ as it jumps between otherwise stationary values. In one time period multi-modality is associated with different component parts of the plumbing system being active at different times. This introduces a new possibility in interpreting b-values, and may motivate an effort in physical modelling of volcanic processes to explain the mechanical bases for mode-switching behaviour, as well as a re-appraisal of the how b-values and their full uncertainty structure may be used in eruption forecasting.

4.6 Acknowledgements

Ian Main and Andrew Bell both provided extensive feedback on this manuscript before submission.

Chapter 5 - A Systematic Study of Earthquake Scaling in a Range of Volcanic and Tectonic Settings

5.1 Introduction

In the two previous chapters I have developed, tested and validated three new ways of improving the current standard practice for calculating the Gutenberg-Richter *b*-value and its uncertainty. These are: (a) standardising the workflow used to calculate completeness magnitude of a catalogue (b) quantifying the resulting total error in the estimate of *b* (both summarised in Chapter 3), and (c) eliminating sources of bias in the selection of temporal catalogue divisions by iteratively randomly-sampling the entire catalogue (Chapter 4). In these chapters the methods were applied to El Hierro and Mount Etna as initial test cases. This begs the question of how general the conclusions are, given the complexity and variability of volcanoes.

In this chapter I address research questions 1), 3), 4) and 7) from Section 2.5.1. This new methodology is applied in a consistent way to nine volcanic seismic catalogues (including additional analysis for Mont Etna and El Hierro). In order to test whether volcanic seismicity differs from tectonic seismicity in a consistent manner (i.e. using the novel methodology in Chapter 4), I also analyse two tectonic seismic catalogues as a control. The aim of this chapter is to address the following research questions:

1) Can we reject the conventional hypothesis that b=1?
2) Do these catalogues have phases with robustly high b-values (b≥1.5)?
3) If so, what is the underlying cause of the high b-value?

The results show that at tectonic settings b does equal 1 and at volcanoes b is often greater than 1 and can be as high as 3.3. However, b is also often equal to 1 at volcanoes. Each volcano has different characteristics and multi-modal b-values are often reported. On occasions high event rates appear to be associated with high b-values (McNutt, 2005; Roberts *et al.*, 2015), but so do cyclical variations in completeness magnitude (Jónsdóttir *et al.*, 2009), and some distributions do not conform to the Gutenberg-Richter law at all. The major result is that there is no common inferred underlying cause of high b-values. Each volcano must be analysed individually to infer the cause of any change in b-value, and the inference will depend very much on the unique character of the volcano of interest.

5.2 Methodology

For each study the total incomplete catalogue was processed using the methodology outlined in Figure 3.9. For the first pass the parameters listed in Table 5.1 were used. These were adjusted accordingly if necessary; for example if the original catalogue is small, N<1000, the maximum sample size will need to be reduced. From Equation [4.5] the criteria in Table 5.1 produce approximately one data point for every five earthquakes in the catalogue.

Table 5.1 – Original parameters used for the random sampling method.

Parameter	
Minimum sample size, S_{min}	50
Maximum sample size, S_{max}	1000
No. of iterations, it	100
No. of events in smoothing window	50

The resulting PDF contour plot (for example as shown in Figure 5.1) illustrates the evolution of the most likely inferred b-value and its confidence limits. Figures such as these were also used to record the 'typical' b-value, i.e. the baseline value of $\tilde{b}_P$ throughout the catalogue, selected by eye. The maximum value of $\tilde{b}_P$ is also recorded.

Wherever $\tilde{b}_P > 1.5$ the approximate range of events (i.e. event numbers 2000 to 3000) containing the high b-value were examined in closer detail to try and determine other aspects of the seismicity that may be associated with the high b-value. For example it may be associated with to a period with a relatively high event rate, a cluster of concurrent events, or a swarm of relatively low magnitude earthquakes with no obvious 'mainshock'. This is achieved using plots of the frequency-magnitude distribution, the distributions of epicentre and/or hypocentre, and the daily-cumulative event rate. Key examples are plotted in this chapter, and a full list of plots can be found in Appendix B for reference and easy comparison. In some cases these plots are used to define separate phases using similar criteria as those described in Section 3.7 for El Hierro and Mount Etna. These diagrams, and the characteristics of the phases used to define them (for example a period of high event rate), were then used in an attempt to infer the underlying physical cause for the magnitude and variability in b-value.

5.3 Data sets

The catalogues used in this Chapter cover a broad range of type of volcanoes summarised in Table 5.4. They are as follows:

1) El Hierro, Canary Islands (IGN, 2016)
2) Mount Etna, Sicily (INGV, 2016)
3) Kilauea, Hawaii (Klein *et al.*, 1987; Nakata and Okubo, 2009)
4) Tungurahua, Ecuador (IGEPN, 2016)
5) Bárðarbunga, Iceland (IMO, 2016)
6) Eyjafallajökull, Iceland (IMO, 2016)

7) Grímsvötn, Iceland (IMO, 2016)
8) Katla, Iceland (IMO, 2016)
9) Tjörnes Fracture Zone, Iceland (IMO, 2016)
10) South Iceland Seismic Zone (tectonic) (IMO, 2016)
11) South California (tectonic) (Hauksson *et al.*, 2012)

The catalogues are not filtered in terms of earthquakes types, however they mainly consist of Volcano-Tectonic events, except for Tungurahua where the catalogue is composed of long-period events.

5.4 Results

In this section the probability density distributions for each catalogue are presented as figures in terms of event number, to easily identify b-value variations regardless of event rate. Further figures are presented in Appendix B showing the distributions by date; the magnitude of events; the daily event rate and cumulative number of events; and a map of the epicentres and hypocentres of the earthquakes. Any observed 'mode-switching' behaviour is defined previously in Section 4.2.1.

5.4.1 El Hierro

El Hierro is an active shield volcano in the Canary Islands. The submarine eruption on 10th October 2011 is the only recorded eruption since the 18th century (GVP, 2015). The 2011-13 El Hierro seismic catalogue and its analysis has previously been discussed in Chapter 4, but some of the main conclusions are repeated here for reference with the other volcanoes analysed in this chapter, as well as some new analysis for phases identified but not investigated in detail in Chapter 3. The modal $\tilde{b}_P$-values for each of the eight phases are recorded in Table 4.1. The two most common modes are $\tilde{b}_P = 1.0$ and 1.5 with a maximum of 3.3 (Figure 5.1). This figure is presented as part of Figure 4.3, but reproduced here for completeness and comparison with similar figures for the other test cases analysed in this Chapter. A key observation is that $\tilde{b}_P$ does not vary steadily through time (Figure 5.1), instead it jumps between modal values.

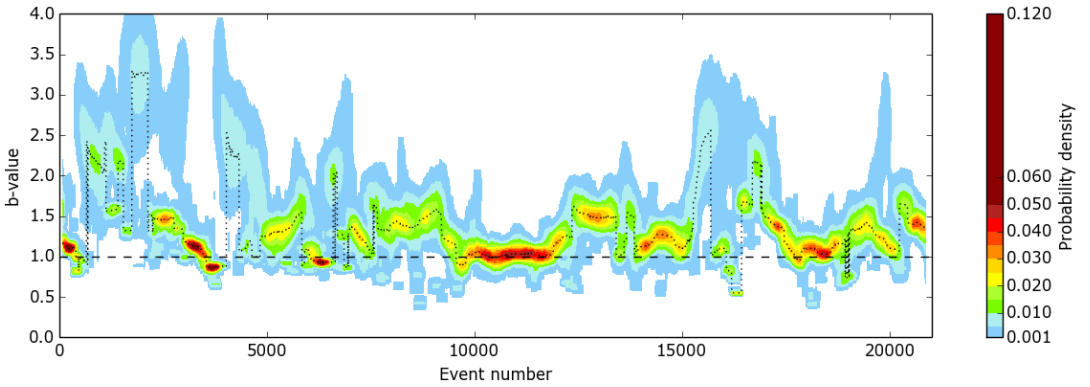

Figure 5.1 – The $\tilde{b}$-value probability density function at El Hierro from July 2011 to December 2013 containing ~21000 events. The dashed line shows the null hypothesis b=1 for reference, and the maximum likelihood value is indicated by the dotted line.

5.4.1.1 Phase 1

This phase has the highest values of $\tilde{b}_P$ at 3.4 (Figure 5.2), and also has the highest event rates averaging ~100 events per day with a maximum of 440 (Figure 5.3). Four sub-phases with high b-values are noted in Table 5.2.

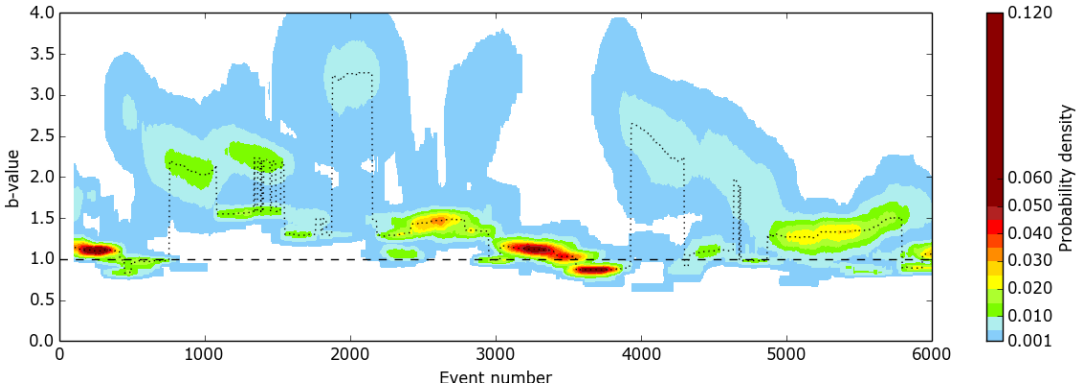

Figure 5.2 - The $\tilde{b}$-value probability density function at El Hierro for the first 6000 events of phase 1 containing multiple periods with high b-values. Plotted as in Figure 5.1.

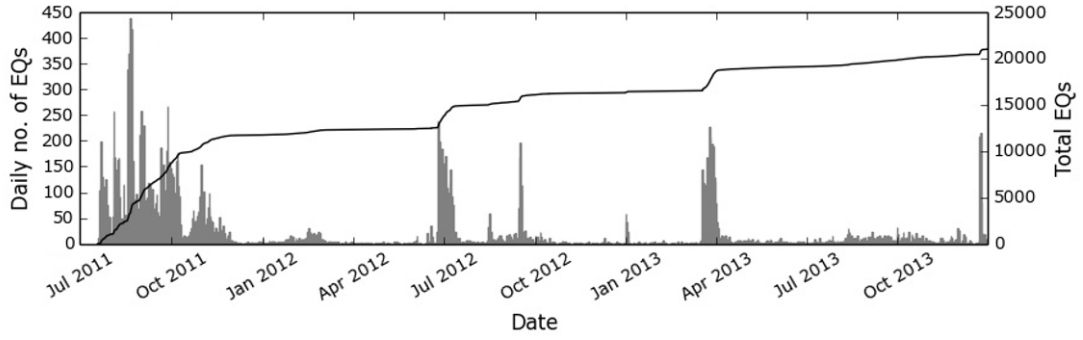

Figure 5.3 – Daily event rate (grey bars) and cumulative number of events (black line) for El Hierro.

All four of my estimates of $\tilde{b}_P$ concur with the $\tilde{b}$ calculations using the standard methodology. For second sub-phases $\tilde{b}_P$ jumps between 2.2 and 1.5 as the peak probability is essentially equal for each mode. The third sub-phase is well defined as $\tilde{b}_P = 3.2$. The fourth sub-phase is the only example where $\tilde{b}_P$ decreases steadily through time from 2.5 to 2.1 rather than switching to the next mode.

Table 5.2 – Sub-phases of El Hierro. Phase 1 containing high *b*-values identified in Figure 5.2. $\tilde{b}$ is the discrete value calculated using the workflow in Figure 3.9. $\tilde{b}_P$ is an estimate of the modal *b*-value during the sub-phase from Figure 5.2.

Events no.	$\tilde{b}$	$\tilde{b}_P$
720-1060	2.05 ± 0.76	2.2
1066-1771	2.23 ± 0.48	1.5 and 2.2
1780-2100	3.19 ± 1.17	3.2
3915-4460	2.76 ± 0.85	2.5 down to 2.1

Here *b*>2.0 for the first three contiguous sub-phases. These sub-phases also contain an underlying second mode of *b*=1.0 or 1.5. This is due to the phases of high *b* being relatively short-lived, typically containing 500 or fewer events. The iterative sampling method uses catalogue samples of up to 1000 events. This may contain multiple internal periods of high *b*-value, but when combined *b* is calculated to be lower for the larger sample. The random temporal sampling removes bias associated with the

operator defining phases. This is essentially due to lack of resolution, and is one of the disadvantages of the method in cases like these, balanced against the shorter random samples correctly identifying short periods of elevated b-value. Overall, in all four cases presented here $\tilde{b}_P$ successfully selects the higher b-value when averaged over all of the samples of different duration.

5.4.2 Mt. Etna

Mount Etna is an active Stratovolcano in Sicily, Italy. It has been regularly active for the past century with the most recent period beginning on 3rd September 2013 and continuing through until May 2015 (GVP, 2015).

The 1999-2014 Mount Etna, Sicily, seismic catalogue has previously been discussed in Section 3.7 with discrete $\tilde{b}$-values calculated for each of the 10 identified phases shown in Table 5.3. The catalogue spans several eruptive episodes, including the 2001 and 2002-03 flank eruptions and more recent paroxysmal activity at the new South East Crater. The two most common modes are $\tilde{b}_P = 0.9$ with a maximum of 3.7 (Figure 5.4). The modal $\tilde{b}_P$ agrees with the discrete $\tilde{b}$-values for all 10 phases.

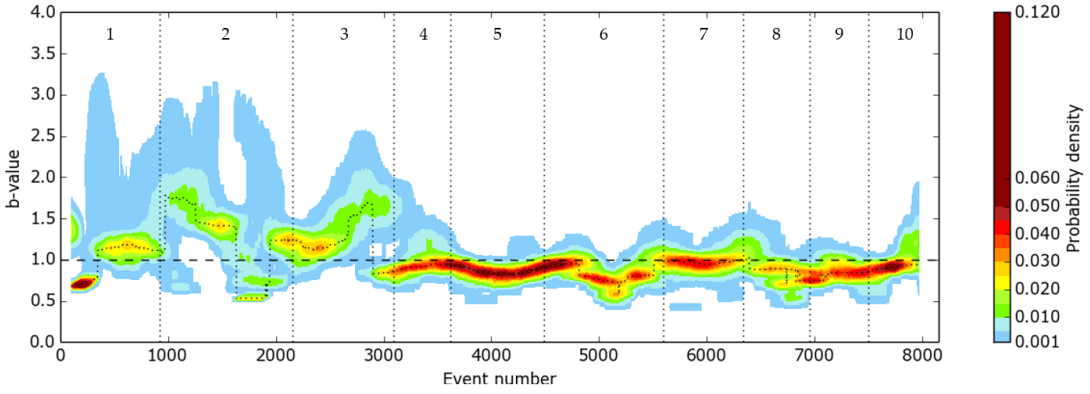

Figure 5.4 - The $\tilde{b}$-value probability density function at Mount Etna from August 1999 to February 2014 containing ~8000 events. Vertical dotted lines highlight the phase boundaries listed in Table 5.3. Plotted as in Figure 5.1.

From Figure 5.4 two clear periods with differing characteristics are identified. From 1999 to late 2003 (Phases 1-3 of Table 5.3) the $\tilde{b}$-value has several modalities and $M_c \geq 2.5$ (Figure 5.5). From 2004 (Phases 4-10), $\tilde{b}$ is more confidently constrained, $\tilde{b}_P$ varies smoothly at approximately 0.8-0.9, with only minor mode-switching events; and M_c decreases to ≥ 2.5. This change correlates to the change in style of volcanism from flank eruptions to crater activity (Section 3.7).

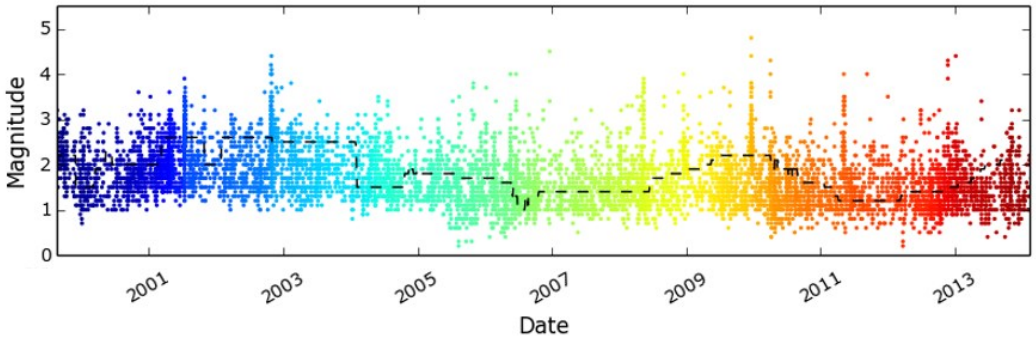

Figure 5.5 – Event magnitude through time at Mount Etna, coloured by event number. Dashed line shows the completeness magnitude obtained through the iterative sampling method.

Table 5.3 – 10 phases for the Mount Etna 1999-2014 seismic catalogue as defined in Section 3.7 and depicted in Figure 5.4. $\tilde{b}$ is the discrete value calculated using the workflow in Figure 3.9. $\tilde{b}_P$ is an estimate of the modal b-value during the sub-phase from Figure 5.4.

Phase	Date	Events	$\tilde{b}$	$\tilde{b}_P$
1	19/8/99 to 8/4/01	0-918	1.07 ± 0.17	0.7, 1.1
2	8/4/01 to 26/10/02	919-2150	1.49 ± 0.41	0.5, 1.4,1.7
3	26/10/02 to 27/9/03	2151-3097	1.22 ± 0.36	1.2,1.5
4	27/9/03 to 29/10/04	3098-3617	0.91 ± 0.15	0.9
5	29/10/04 to 26/7/06	3618-4489	0.90 ± 0.18	0.9
6	26/7/06 to 15/12/08	4490-5594	0.84 ± 0.09	0.9
7	15/12/08 to 27/3/10	5595-6341	1.02 ± 0.28	1.0
8	27/3/10 to 5/5/11	6342-6954	1.09 ± 0.31	0.9
9	5/5/11 to 9/8/12	6955-7500	0.74 ± 0.11	0.8
10	9/8/12 to 13/2/14	7501-8153	0.93 ± 0.18	0.9

Taking the discrete $\tilde{b}$-values from Table 5.3 $\tilde{b} = 1.0$ within one standard deviation error for 7 of 10 phases, therefore the null hypothesis of b=1 cannot be rejected at this level of confidence. However, $\tilde{b}_P$ is outside of one standard deviation of error of b=1 for phases 1-3; then for phases 4-10 $\tilde{b}_P$ is always less than or equal to one, although

the hypothesis b=1 cannot be rejected within this error. Unlike El Hierro no $\tilde{b}_P$-values of over 2.0 are reported.

5.4.3 Kilauea

Kilauea is an active shield volcano in Hawaii. It is the most active volcano of the Hawaiian volcanic chain, being almost constantly active for the past 200 years since records began. The Halemaumau crater and SE rift zone have been active since 1893 (GVP, 2015). This catalogue focuses on the previous active period of the Kilauea caldera.

The 1959-1984 Kilauea seismic catalogue is focussed solely on the caldera and contains ~11000 events. It has different characteristics to the El Hierro and Mount Etna catalogues as the $\tilde{b}_P$ -value changes smoothly through time; there are no large mode-switching events. $\tilde{b}_P$ is typically between 1.0-1.4 with a minimum of 0.9 and a maximum (excluding the initial high at the start of the catalogue occurring as an artefact of the sampling method) of just 1.6 (Figure 5.6). Typically the modal value is $\tilde{b}_P = 1.2$.

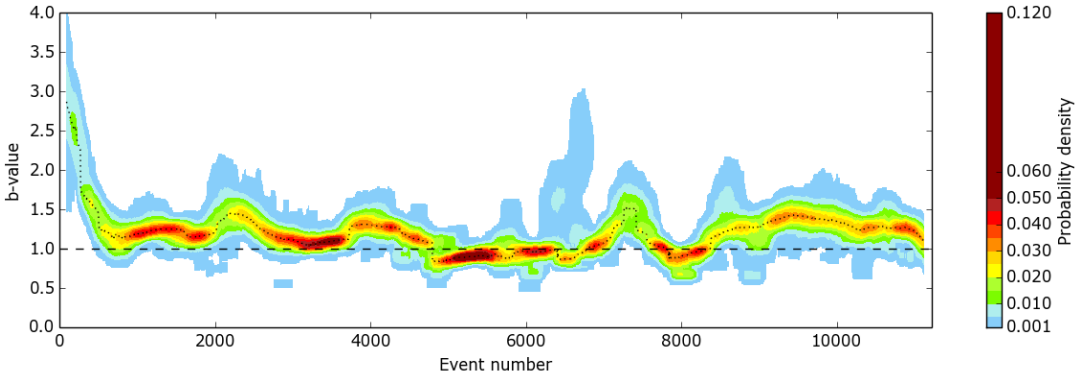

Figure 5.6 - The $\tilde{b}$-value probability density function at Kilauea from January 1959 to December 1984 containing ~11000 events. Plotted as in Figure 5.1.

5.4.4 Tungurahua

Tungurahua is an active Stratovolcano in Ecuador. Volcanic activity recommenced on August 19, 1999 and is ongoing as of 2013, with several major eruptions since that period, the last starting on 6 August 2015 (GVP, 2015). The 1999-2015 Tungurahua seismic catalogue differs from all the others as it contains long-period events rather volcano-tectonic events. The catalogue only contains times and magnitudes of events, therefore it is not possible to spatially constrain or interpret and b-value variations.

As the catalogue contains over 165,000 events the sampling window size was increased from 50 data points to 200 in order to reduce the noise in $\widetilde{b}_P$. Figure 5.7 shows the two most common modes are $\tilde{b}_P = 1.5$ and 2.0 with a potential third mode at 1.1 in the first half of the catalogue, and a maximum of 2.6. Figure 5.8 shows that Mc remains very constant throughout only varying between 2.1-2.4M. The catalogue shows mode-switching behaviour throughout with the two main modes being frequently used. $\tilde{b}_P$ drops beneath 1.0 once after ~82000 events, and it is rare for P($\tilde{b} \leq 1.0$) ≥ 0.001. Although the catalogue does not appear to have the extreme high b-values of greater than two, the null hypothesis of b=1.0 is incorrect for Tungurahua, it is typically between 1.5 and 2.0.

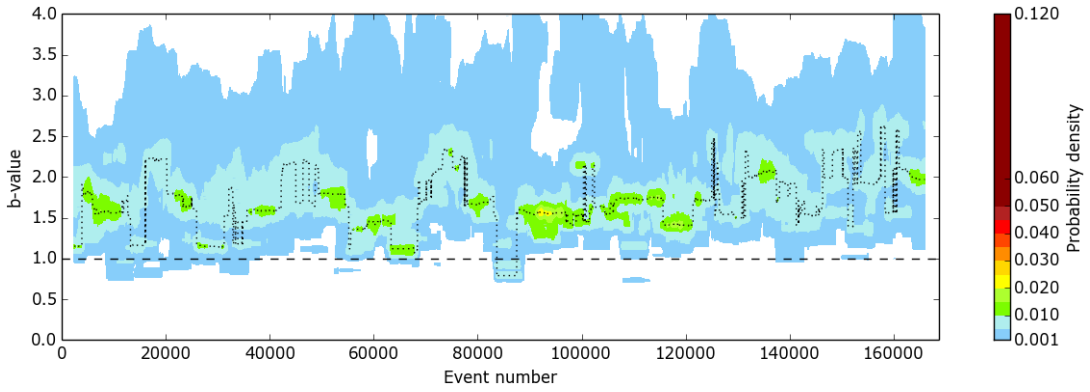

Figure 5.7 - The $\tilde{b}$-value probability density function at Tungurahua from January 1999 to August 2015 containing ~165000 events. Plotted as in Figure 5.1.

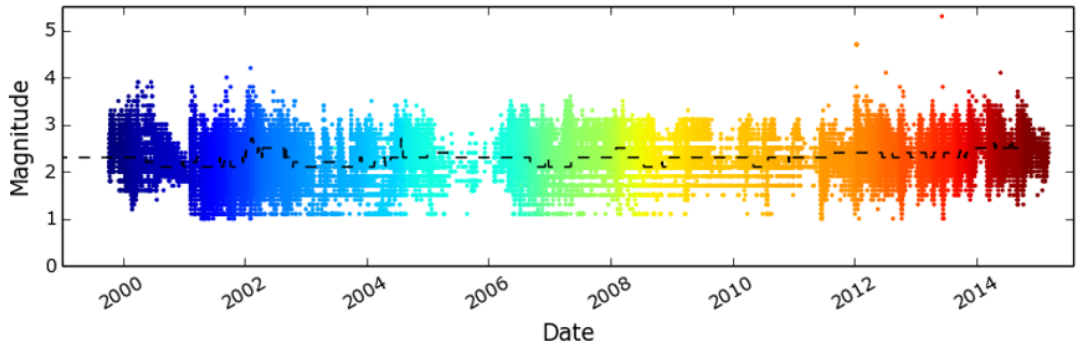

Figure 5.8 - Event magnitude through time at Tungurahua. Coloured by event number. Dashed line shows the completeness magnitude obtained through the iterative sampling method.

5.4.5 Bárðarbunga

Bárðarbunga is an active stratovolcano located underneath the Vatnajökull icecap in Iceland. It has been sporadically active during the last century. The most recent fissure eruption occurred in the Holuhraun lava field starting on the 29th August 2014 and ending on the 27th February 2015 (GVP, 2015).

Figure 5.9 shows the locations of earthquakes associated with the eruption from June 2014 to January 2015. On 16th August 2014 a swarm of earthquakes initiated under the caldera (Figure 5.10) signalling the onset of subsurface magma movement (Gudmundsson *et al.*, 2014; Green *et al.*, 2015; Riel *et al.*, 2015; Sigmundsson *et al.*, 2015). The earthquakes propagated north-eastward with eight segments of migration; lengthening of the dyke ceased on 27th August. A minor fissure eruption occurred in Holuhraun for four hours on the 29th August; then a new eruption began on the 4th September and ceased on the 28th February 2015.

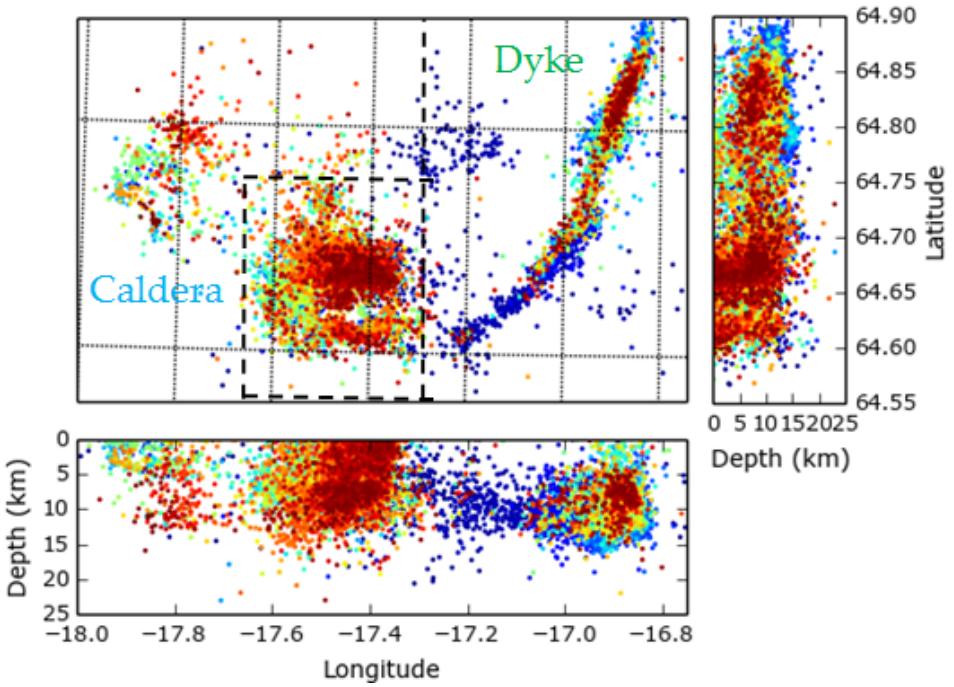

Figure 5.9 – Hypocentres and epicentres of earthquakes surrounding the Bárðarbunga caldera, dyke emplacenment and fissure site between June 2014 and July 2015. Events are coloured blue to red, from oldest to most recent. The two dashed boxes incidate the two sub-catalouges used in Figure 5.10 to Figure 5.13.

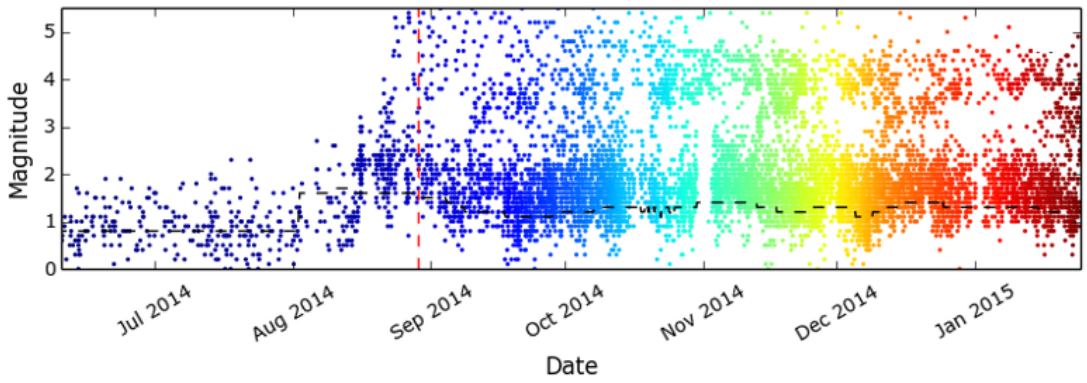

Figure 5.10 - Event magnitude through time at Bárðarbunga caldera, coloured by event number. Dashed line shows the completeness magnitude obtained through the iterative sampling method. Vertical dashed red line shows the onset of the eruption.

Preliminary *b*-value analysis using the work flow from Figure 3.9 is shown in Figure 5.11. The catalogue is divided into two sub-catalogues: the caldera and the dyke (Figure 5.9). The whole catalogue is divided into 10 phases based on the start of the earthquake swarm, the eruption, and changes in event rate post-eruption (Figure 5.11b). Pre-swarm the background seismicity near the caldera and what will become the dyke zone has a $\tilde{b}$-value of approximately 1. At the eruption site it is approximately 0.8, however there are very few events there. Once the swarm begins and while the dyke is being emplaced $\tilde{b}$~1.2 over the region of the dyke, and the $\tilde{b}$-value at the caldera dramatically drops to ~0.5. After the onset of the eruption, $\tilde{b}$ climbs at the dyke to a peak of 2.0 then slowly falls to 1.5. At the caldera $\tilde{b}$ remains between 0.4-0.5 throughout.

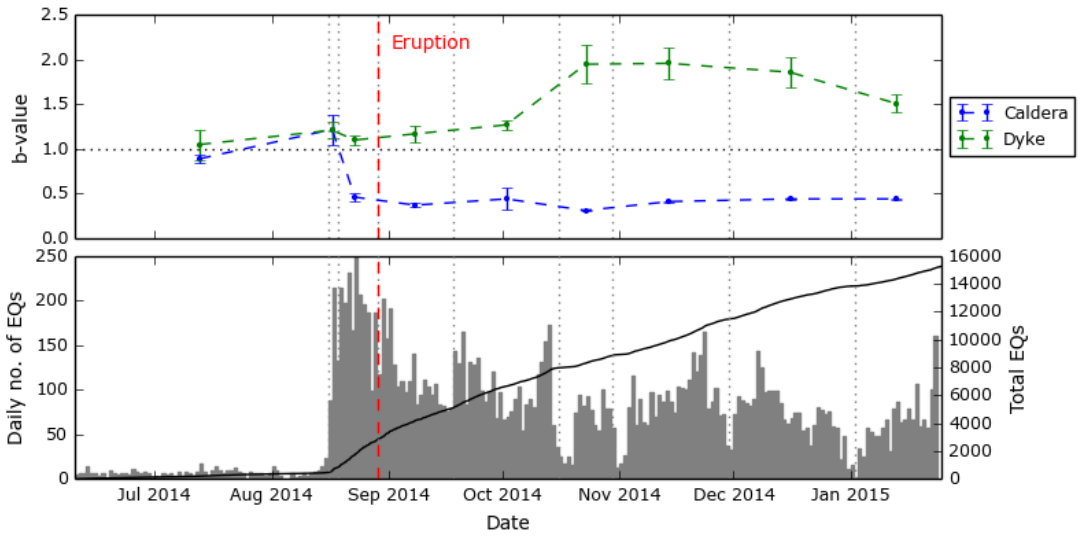

Figure 5.11 – Top: discrete b-values calculated using the workflow in Figure 3.9 for each of the caldera, dyke and eruption sites at Bárðarbunga between June 2014 and July 2015. Bottom: daily event rate (grey bars) and cumulative number of events (solid black line) with the phase boundaries (dotted vertical grey lines) and eruption date (dashed vertical red line).

Figure 5.12 shows the PDF for the entire catalogue. Although for the first ~2000 events $\tilde{b}_P$ ranges between 1.0-1.5, once the dyke swarm starts $\tilde{b}_P$ is well defined between 0.3-0.8 for the duration of the catalogue. From the results in Figure 5.11 this is not representative of the results as a whole, the iterative sampling cannot pick out the multimodality on the data as it is too heavily biased by the events occurring at the crater. On this occasion the entire catalogue needs to be split into the three sub-catalogue in order for the iterative sampling method to be successful.

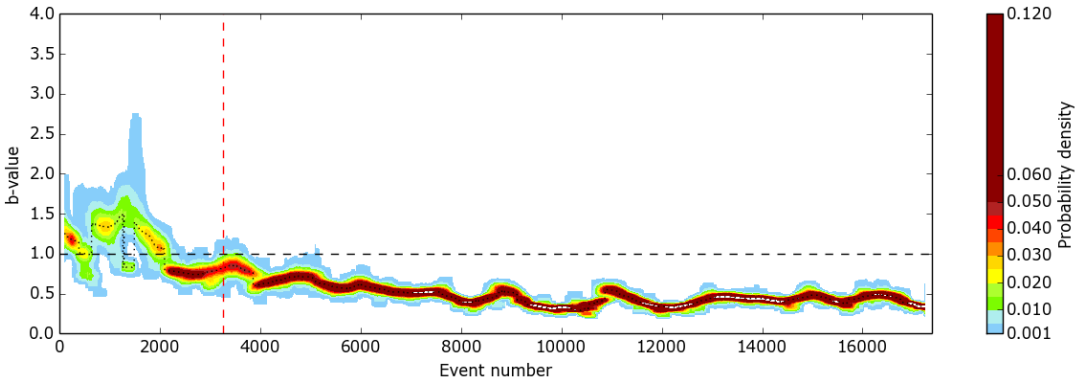

Figure 5.12 - The $\tilde{b}$-value probability density function at Bárðarbunga from June 2014 to Janurary 2015 containing ~16000 events. Plotted as in Figure 5.1.

5.4.5.1 Caldera

Figure 5.13 shows the PDF for the crater catalogue. It has a very similar $\tilde{b}_P$ to the PDF for the entire catalogue, except it stabilises at 0.3-0.5 after 200 events and remains consistent throughout. This $\tilde{b}_P$-value is far lower than would be expected in any seismic regime following a Gutenberg-Richter distribution as it requires a high proportion of relatively large magnitude earthquakes.

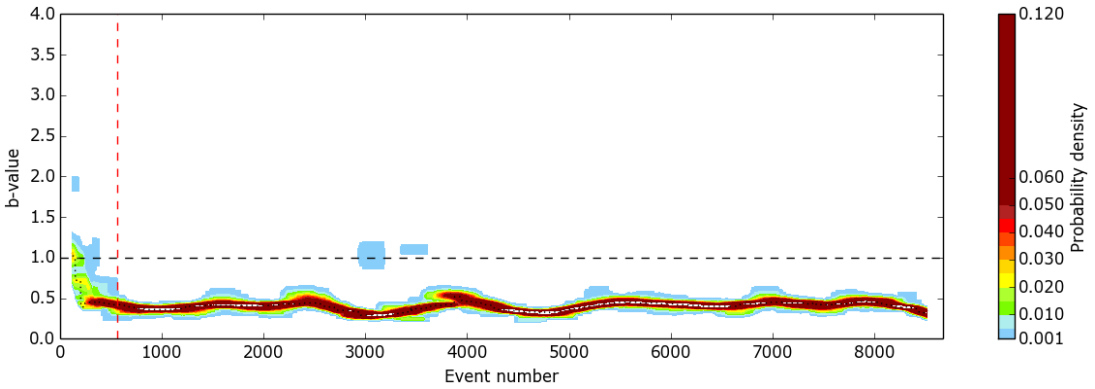

Figure 5.13 - The $\tilde{b}$-value probability density function at Bárðarbunga caldera from June 2014 to Janurary 2015 containing ~8500 events. Plotted as in Figure 5.1.

Further analysis of the frequency-magnitude distribution reveals the distribution is not Gutenberg-Richter. Figure 5.14a shows the FMD is bimodal with peaks in the discrete distribution at 1.6M and 3.9M, and a dip in the number of recorded events

between 2.5M to 3.5M. This distribution can be observed in the magnitude-time plot in Figure 5.10. Using the workflow from Figure 3.9; the MaxC method picks the first peak giving M_c=1.6; the GFT method does not reach the required confidence interval until after the second peak at M_c=3.8; and the BVS method selects an M_c on the downward slope of the first peak, at M_c=2.2, allowing for the best approximate fit of the entire second peak in the distribution. This provides a $\tilde{b}$-value of 0.35±0.01, much lower than either of the individual slopes in either part of the distribution and shows why the $\tilde{b}_P$-values are so low in Figure 5.13.

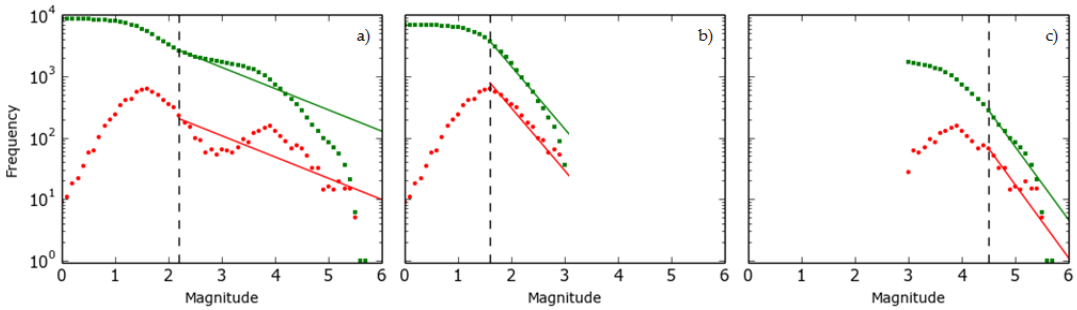

Figure 5.14 – Frequency-magnitude distribution of the Bárðarbunga caldera between 10th June 2014 and 25th January 2015. a) The entire magnitude range with bi-modality in the discrete distribution (red); $\tilde{b} = 0.35 \pm 0.01$. b) The FMD for the first mode of magnitudes up to and including 2.9M; $\tilde{b} = 1.02 \pm 0.02$. c) The FMD for the second mode of magnitude from 3.0M upwards; $\tilde{b} = 1.19 \pm 0.15$.

By splitting the catalogue in two then applying the same workflow; the first peak, including magnitudes up to 2.9M, has M_c=1.6 and $\tilde{b} = 1.02 \pm 0.02$; the second peak, magnitudes 3.0M upwards, has M_c=4.5 and $\tilde{b} = 1.19 \pm 0.15$. These are both more in line with expected $\tilde{b}$-values.

A similar characteristic distribution has previously been identified in the Mount St. Helens seismic catalogue prior to the 1980 eruption (Main, 1987). The interpretation being that there were two modes of seismic energy release; the superposition of 'tectonic' earthquakes and 'volcanic' tremor. Also from discussion with Dr. Kristin S. Vogfjörð, (Director of Research Veðurstofu Íslands, Icelandic Meteorological Office), we believe the catalogue to be incomplete as only high quality events had been

reviewed when the catalogue was obtained, and for events where M≥3.0 the magnitude is increasingly underestimated. That said, the events at the caldera do have extremely low frequencies and a fully complete catalogue is unlikely to significantly change the characteristic nature of the catalogue.

Riel *et al.* (2015) have proposed a conceptual model for the mechanics causing the events at the caldera (Figure 5.15). The initial seismic activity around the southern edge of the caldera and subsequent propagation of the dyke led to depressurisation of the magma chamber. This resulted in subsidence of the caldera surface and overlying ice. Deflation of the magma chamber led to the initiation of M≥3.0 events located along the caldera rim. The large compensated linear vector dipole components in the focal mechanisms are characteristic of both downward vertical motion and horizontal expansions, or rupture on a curved fault.

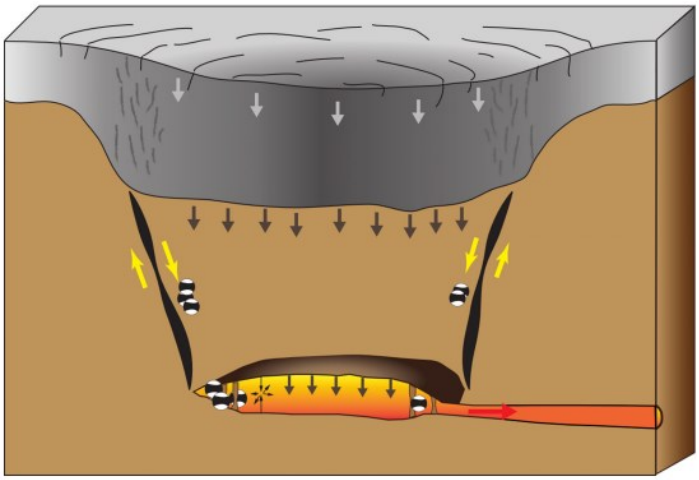

Figure 5.15 – Conceptual model for the mechanics of the collapsing caldera (Riel *et al.*, 2015).

5.4.5.2 Dyke

Figure 5.16 shows the PDF for the dyke catalogue. $\tilde{b}$ is relatively poorly defined for the first ~1500 events with $\tilde{b}_P$ varying between 0.5 and 1.9. It then stabilises at $\tilde{b}_P \approx$ 1.0 before slowly rising to 1.8 by the end of the catalogue. This is different to the behaviour shown by the discrete sampling in Figure 5.11 where $\tilde{b}_P$ rose to 2.0 post-

eruption then slowly deceased to 1.5. Mode-switching is only apparent in the first 1500 events where $\tilde{b}$ is poorly defined, after this any changes in $\tilde{b}_P$ are gradual.

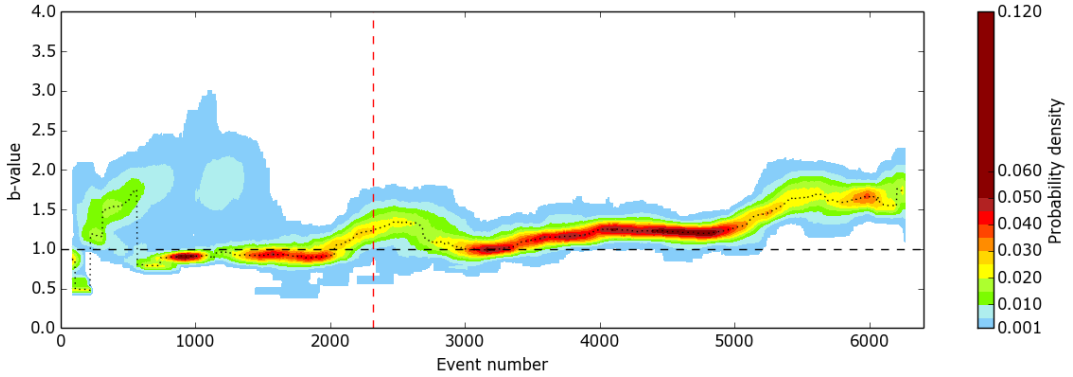

Figure 5.16 - The $\tilde{b}$-value probability density function at Bárðarbunga dyke intrusion from June 2014 to Janurary 2015 containing ~6000 events. Plotted as in Figure 5.1.

The dyke is believed to have grown over a period of two weeks from 16th to 29th August (Sigmundsson *et al.*, 2015). It first propagated in a SE direction, then with seven further segments of growth in an approximately NE direction towards what would become the fissure eruption site. Event numbers 188 to 2315 in Figure 5.16 occur between these dates. We see that this is the period where $\tilde{b}_P$ is relatively poorly defined with two potential modes at b=0.9 and 1.5≥b≤2.0. Once the fissure eruption starts and the stress on the dyke is relived, $\tilde{b}_P$ stabilises then gradually increases through time as fewer large events are occurring (Figure 5.17).

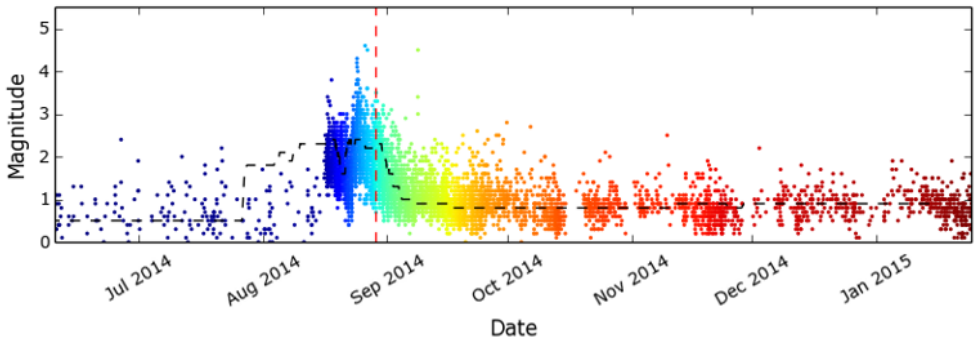

Figure 5.17 - Event magnitude through time at Bárðarbunga dyke, coloured by event number. The dashed line shows the completeness magnitude obtained through the iterative sampling method. Vertical dashed red line shows the onset of the eruption.

5.4.6 Grímsvötn

Grímsvötn is a caldera volcano under the Vatnajökull icecap in Iceland. It is the most frequently active volcano in Iceland. The most recent eruption was just seven days long starting on the 21st May 2001 in the south-west part of the caldera. There was very little recorded seismicity associated with the eruption. Figure 5.18 shows a background daily event rate of 0-5 events with a peak of 45 events on the day of the eruption. Following the eruption there was almost no activity for three years, then in 2014 seismicity returned to background levels.

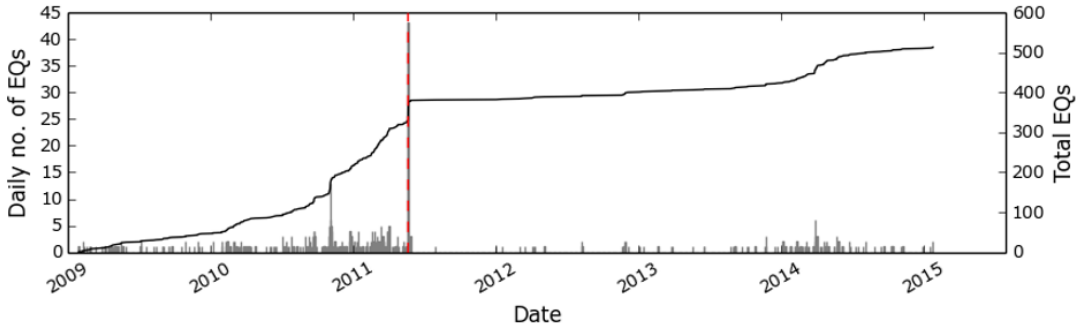

Figure 5.18 - Daily event rate (grey bars) and cumulative number of events (black line) for Grímsvötn.

The main problem with performing analysis on this catalogue is that there are only 513 events. In 3.6.3 it was recommend that at least 500 events are included in an incomplete catalogue, so in order to divide this catalogue into multiple sub-catalogues to perform iterative sampling analysis, it simply is not possible to adhere to this recommendation. Here the maximum sample size was reduced from 1000 to 200 events so as to allow for several sub-catalogues to be created; therefore the reliability of these results is questionable at best, but at least provides potentially greater insight than a single discrete $\tilde{b}$-value calculation.

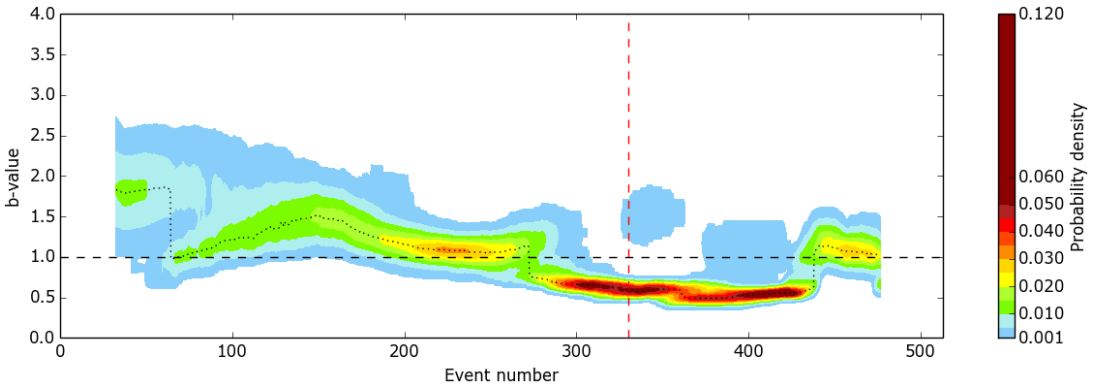

Figure 5.19 - The $\tilde{b}$-value probability density function at Grímsvötn from January 2009 to August 2015 containing ~500 events. Plotted as in Figure 5.1.

Figure 5.19 shows pre-eruption $\tilde{b}_P$ varies between 1.0 and 1.5, there is then a mode-switching event as it drops to ~0.6 between event numbers 270-420. After which it jumps back up to just above 1.0. These events with the low $\tilde{b}_P$-value occur between March 2011 and September 2013. This encompasses the eruption period. Figure 5.20 shows the FMD for this period; although poorly defined due to there only being 135 events the discrete distribution appears to have a bi-modal characteristic distribution, as at the Bárðarbunga caldera. This FMD appears to be controlled solely by the events above 2.0M on the day of the eruption (Figure 5.21). This cluster of high magnitude events lowers the $\tilde{b}_P$-value to beneath 1.0, and although the sample size has already been reduced to between 50-200 events, it cannot be resolved temporally by this method.

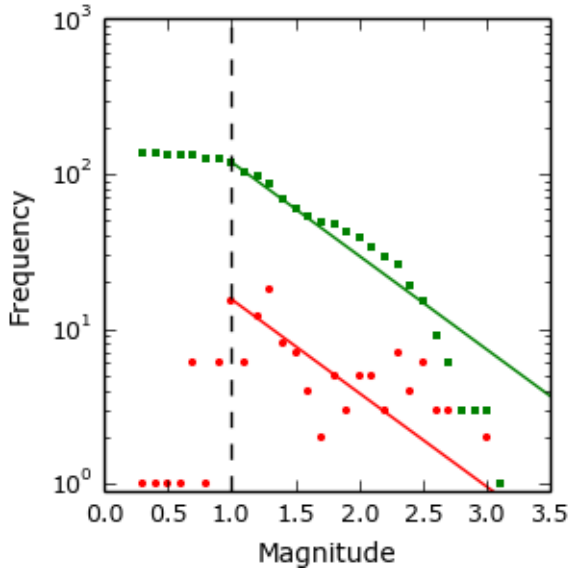

Figure 5.20 – Frequency-magnitude distribution for Grímsvötn between 10th March 2011 and 1st September 2013 (event numbers 275 – 410). $\tilde{b} = 0.61 \pm 0.14$, however the discrete distribution (red circles) has a potentially bi-modal characteristic distribution rather than following the Gutenberg-Richter relationship.

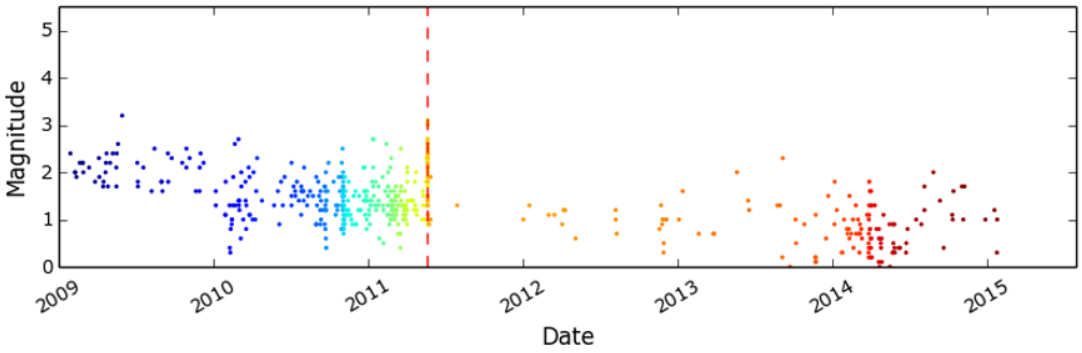

Figure 5.21 - Event magnitude through time at Grímsvötn, coloured by event number. Vertical dashed red line shows the onset of the eruption.

5.4.7 Eyjafallajökull

Eyjafallajökull is an ice-covered stratovolcano in Iceland southern Iceland. Although active during historical time it has been less active than other volcanoes in recorded history (GVP, 2015). However the most recent eruption from 14th April to 23rd June 2010 caused major global disruption to air travel due to the ash cloud produced during the eruption. The catalogue covers the first six months in 2010 with the seismicity mainly preceding the eruption.

Figure 5.22 shows $\tilde{b}_P$ is always greater than or 1.0 other than within the first 500 events. There are several mode-switching events with the most common modes at 1.1 and 1.5, with $\tilde{b}_P$ more generally fluctuating between 1.1 and 2.0. The period between events 2500 and 3000 is the only occasion where there may be evidence of multi-modality, shown by the jump up to $\tilde{b}_P$=2.1 and the much broader spread of the probability density function before that.

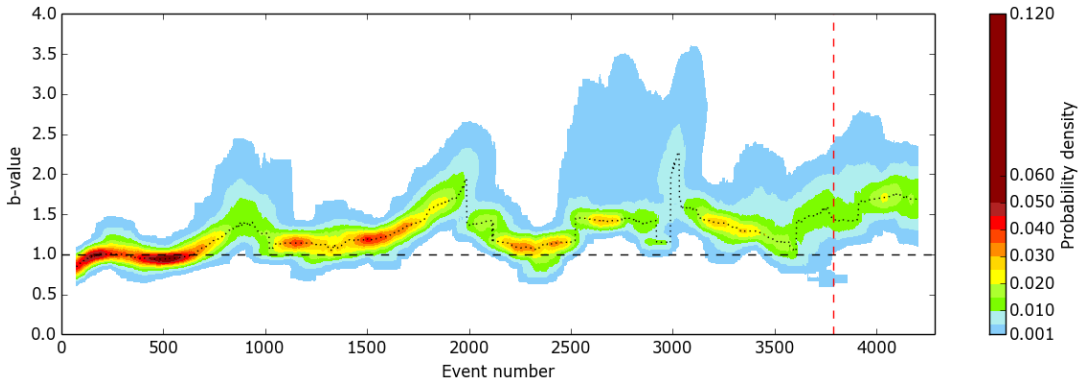

Figure 5.22 - The $\tilde{b}$-value probability density function at Eyjafallajökull from January to May 2010 containing ~4000 events. Plotted as in Figure 5.1.

Figure 5.23 shows the FMD for the three day period in March containing the ~660 events with the increased spread in the PDF as well as the peak of $\tilde{b}_P$=2.1. It shows a discrete $\tilde{b}$-value of 2.46 ± 0.58. For such a high $\tilde{b}_P$-value it is reasonably well-defined with a complete bandwidth of 0.8M and ~100 complete events; this is less than the advised minimum of 200, however there is no clear roll-off at higher magnitudes so the high value does appear to be real.

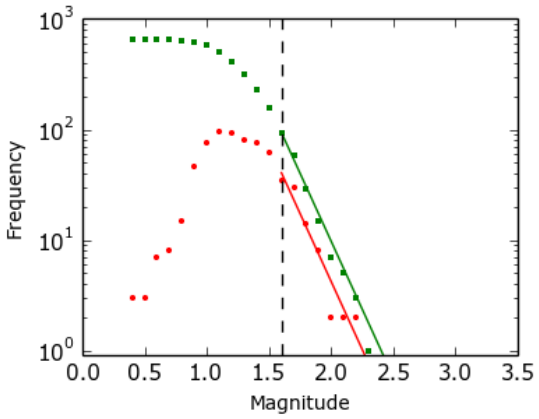

Figure 5.23 – Frequency-magnitude distribution for Eyjafallajökull from 15th – 18th March 2010 (event numbers 2459 - 3279). $\tilde{b} = 2.46 \pm 0.58$.

From Figure 5.24 this high $\tilde{b}_P$-value appears to correlate strongly to the second peak in daily event rate prior to the eruption. The previous two peaks in $\tilde{b}_P$ of 1.4 and 1.7 both occur around the same time as the first spike in daily event rate, however they do not match as well. Nonetheless, here there appears to be evidence to at least suggest $\tilde{b}_P$ is stable when the daily event rate is low, then when the event rate increases this may cause spikes in the $\tilde{b}_P$-value.

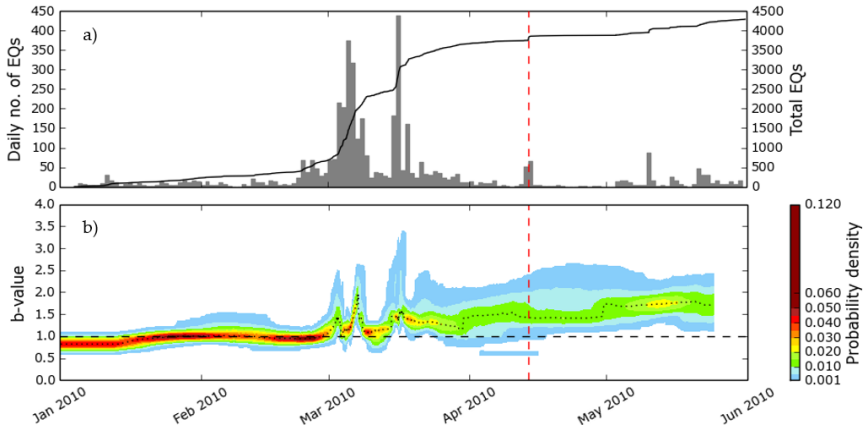

Figure 5.24 – a) Daily event rate (grey bars) and cumulative number of events (black line) for Eyjafallajökull. b) The $\tilde{b}$-value probability density function through time at Eyjafallajökull as plotted as in Figure 5.1. The red dashed line shows the start of the eruption.

5.4.8 Katla

Katla is a subglacial volcano in southern Iceland. There has not been a major eruption since 1918 (GVP, 2015). There has been more recent minor eruptions that have not breached the ice cover in 1995, 1999 and 2011. From 1995 to 2001 only ~1000 event were recorded with a poorly defined $\tilde{b}_P$-value varying between 0.6 and 1.4 (Figure 5.25). From Figure 5.26 we also see that events are predominantly only being recorded in the second half of the year for this period. From 2001 a much greater number of events are recorded; the $\tilde{b}_P$-value then becomes well defined at 0.6 slowly rising to 1.1 over three years and a 9000 event period.

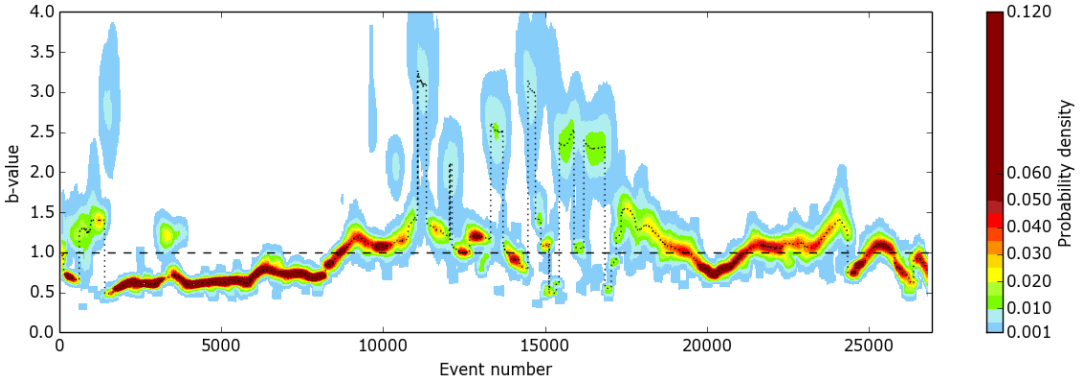

Figure 5.25 - The $\tilde{b}$-value probability density function at Katla from January 1995 to August 2015 containing ~27000 events. Plotted as in Figure 5.1.

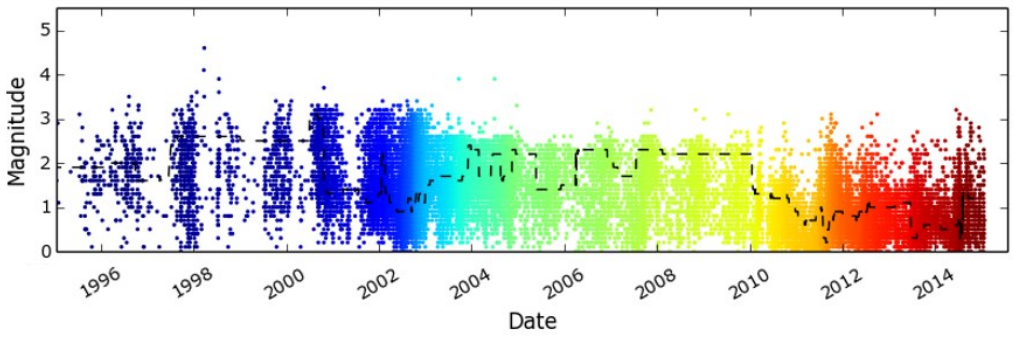

Figure 5.26 - Event magnitude through time at Katla, coloured by event number. Dashed line shows the completeness magnitude obtained through the iterative sampling method.

Over a six year period from 2004 to the end of 2009 (event numbers 11000 to19000 (Figure 5.25)), the characteristics of the $\tilde{b}_P$-value PDF change showing dramatic mode-switching behaviour. The baseline $\tilde{b}_P$-value remains between 0.6-1.4, however there are six periods where $\tilde{b}_P$ is greater than 2.0 and as high as 3.2. During this period the *Mc* is very high relative to the maximum magnitude; 2.0M compared to 2.5M respectively (Figure 5.26). From 2005 onwards the *Mc* falls to ~1.0M and the $\tilde{b}_P$-value stabilises again between 0.6-1.4.

Figure 5.27 shows the FMD's of two of the periods with high $\tilde{b}_P$. Figure 5.27a is between events 14570 to 14720 (20th September to 12th November 2006). Here $\tilde{b}_P$=2.7. The FMD is not Gutenberg-Richter with an almost flat top in the discrete data between 0.0-2.0M earthquakes, with a sharp drop of in higher magnitude events and a *Mc* of 2.2. In this case the presence of a high $\tilde{b}_P$ indicates a non-GR distribution rather than a truly high $\tilde{b}_P$-value. Figure 5.27b is the high $\tilde{b}_P$ the following year between events 15480-15870 (17th September 2007 to 8th January 2008). It has a very similar shape distribution except with more events. The number of events between 0.0-2.0M is still fairly consistent with a steep drop off above *Mc*=2.3M causing the high $\tilde{b}_P$-value of 2.2. Although the bandwidth of complete events is 1.0M, and the fit is good for the sharp roll-off in the discrete data, it is still not a typical Gutenberg-Richter distribution

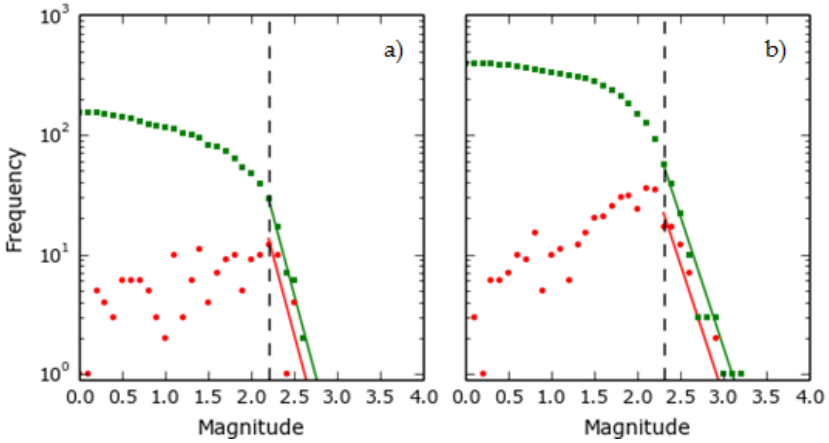

Figure 5.27 – Frequency-magnitude distributions at Katla show high $\tilde{b}_P$-values for a) events 14570 to 14720 (20th September to 12th November 2006) where $\tilde{b} = 2.71 \pm 0.99$, and b) events 15480-15870 (17th September 2007 to 8th January 2008) where $\tilde{b} = 2.19 \pm 0.72$.

5.4.8.1 Annual cyclicity

Katla is known to have seasonal seismicity with higher event rates in the later part of the year (Jónsdóttir *et al.*, 2007; Jónsdóttir *et al.*, 2009). The seismicity is interpreted to be related to the deloading of the thin crust above the magma chamber due to the summer melting of the ice cap, and to high groundwater pressure in the caldera roof at the same time (Soosalu, 2002). To test the annual cyclicity of the $\tilde{b}_P$-value I have taken the data from the iterative sampling technique and stacked the results from the six years from 2004 to 2009.

Figure 5.28 shows the raw data and the contoured PDF function. There are two clear modes at $\tilde{b}_P$=0.6 and 1.1 and a third that is less well defined due to it being so high, at 2.5. The peak $\tilde{b}_P$-value will nearly always pick out $\tilde{b}_P$≈0.6 due to the minimal size of the errors relative to the high b-values. However from Figure 5.28 we can see that $\tilde{b}_P$≈0.6 is much more strongly defined in the second half of the year, and conversely $\tilde{b}_P$≈2.5 is better represented in the first half of the year.

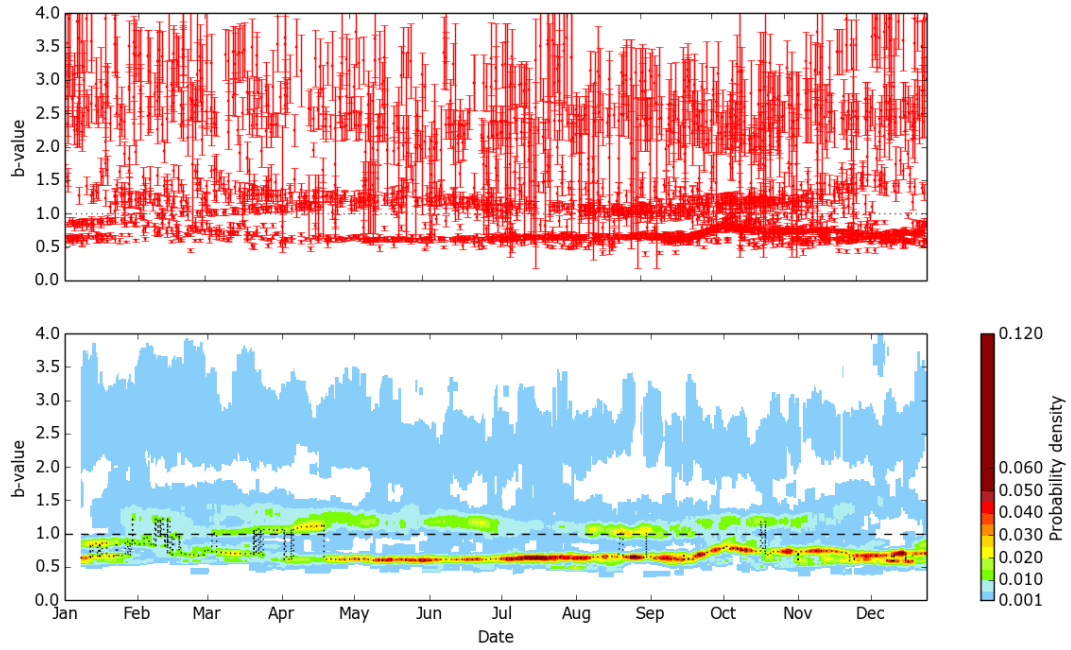

Figure 5.28 – Annual stacking of the Katla 2004 to 2009 catalogue. Top: raw data from iterative sampling technique. Bottom: contoured PDF with peak $\tilde{b}_P$-value marked with the dotted line. Plotted as in Figure 5.1.

Figure 5.29 plots the monthly average $\tilde{b}_P$-value with one standard deviation error and the monthly event rate. Although on average the b-value decreases, the resolution of the results does not show a true representation of the $\tilde{b}_P$-value as we know there are three modal values. However, it does give a clearer indication that there is a greater proportion of high $\tilde{b}_P$-value earlier in the year and lower $\tilde{b}_P$-values later. The maximum average $\tilde{b}_P$-value occurring in February and minimum in September. Figure 5.29 shows high b-values and low-event rates, and vice versa, do not correlate exactly, however the relationship is clear to be seen.

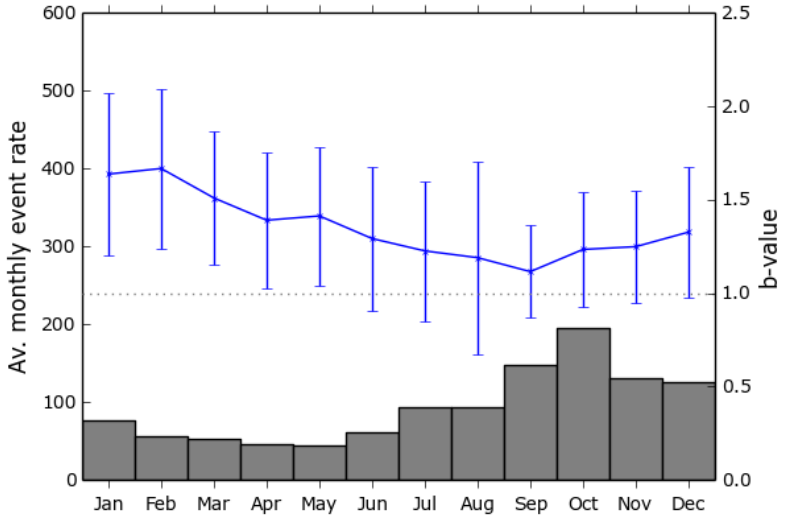

Figure 5.29 – Average number of event per month (grey bars) and average $\tilde{b}_P$-value with one standard deviation error (blue error bars) for the Katla 2004 to 2009 catalgoue.

In the second half of the year the lower on average $\tilde{b}_P$-values observed in Figure 5.29 and well-defined $\tilde{b}_P \approx 0.6$ in Figure 5.28 contradict the high discrete $\tilde{b}$-values calculated from the FMD's in late 2006 and 2007 in Figure 5.27. This is due to the sampling method and unfortunate bias towards low $\tilde{b}_P$-values when stacking the data.

Jónsdóttir *et al.* (2009) concluded that the shallow long-period events occurring in the Goðabunga region in the second half of the year are due to glacial movements not magmatic activity or other direct volcanic effect, thus the non-Gutenberg-Richter distribution and consequent very high and low $\tilde{b}_P$-values can be attributed to this.

5.4.9 Tjörnes Fracture Zone

The offshore Tjörnes Fracture Zone is an oblique transform zone that separates the northern volcanic zone of Iceland from the Kolbeinsey Ridge, part of the Mid-Atlantic Ridge north of Iceland. A submarine eruption was reported during 1867-1868 at the SE part of the fissure system off the northern coast of Iceland along the Manareyjar Ridge immediately north of Manareyjar Island. This catalogue is from 1995 to 2015 and contains ~70000 events. Figure 5.30 shows a map of the seismicity. There are two main stands of activity here separated by the dashed line. These then form two separate catalogues, one to the north-east, and one to the south-west. The NE catalogue is focused on the Grimsey lineament, and the SW on the Husavik-Flatley Fault, and includes the Dalvik lineament (Gudmundsson, 2007).

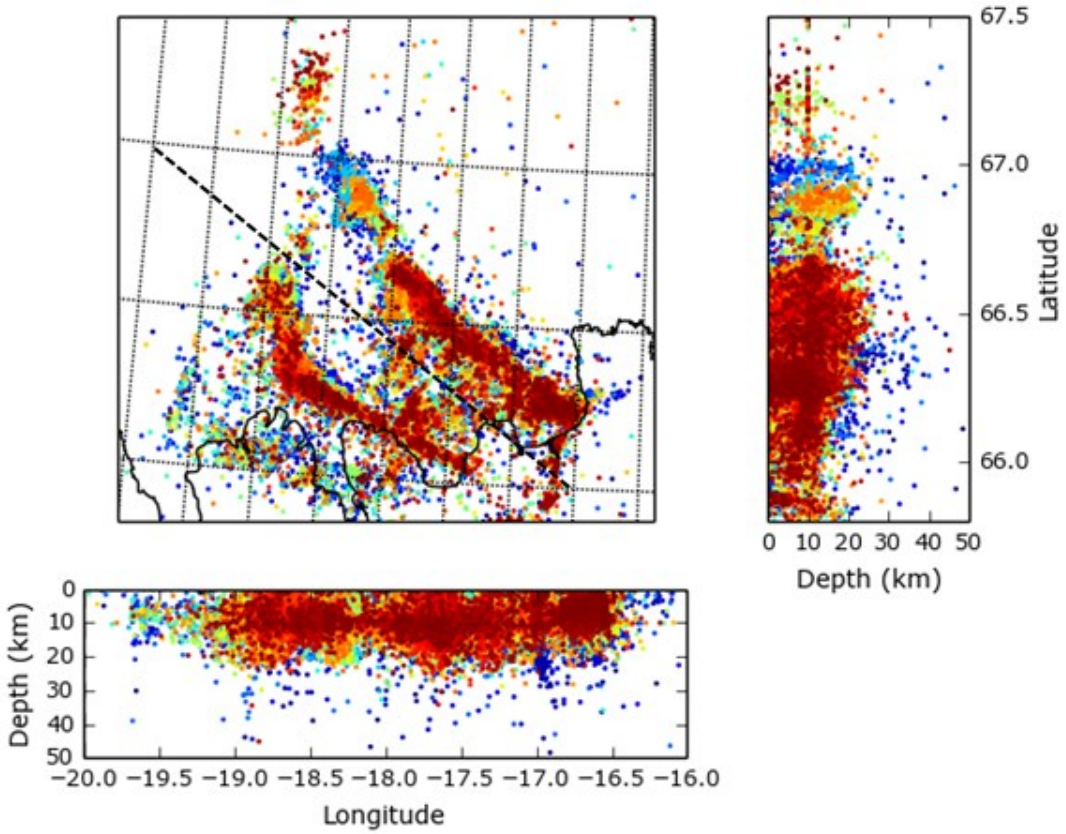

Figure 5.30 - Hypocentres and epicentres of earthquakes in the Tjörnes fracture zone from 1995 to 2015. Events are coloured blue to red from oldest to most recent. The dashed line indicates the split between the north-east and south-east sub-catalogues.

Figure 5.31 shows the NE catalogue typically has $\tilde{b}_P$-values fluctuating between 0.7 and 1.4 with a maximum of 1.9 for a brief period after ~4000 events. There are a few mode-switching events but typically the $\tilde{b}_P$-value varies smoothly, almost sinusoidal is character. In general $\tilde{b}_P$ appears to varying around 1.0 even if it is rarely stable.

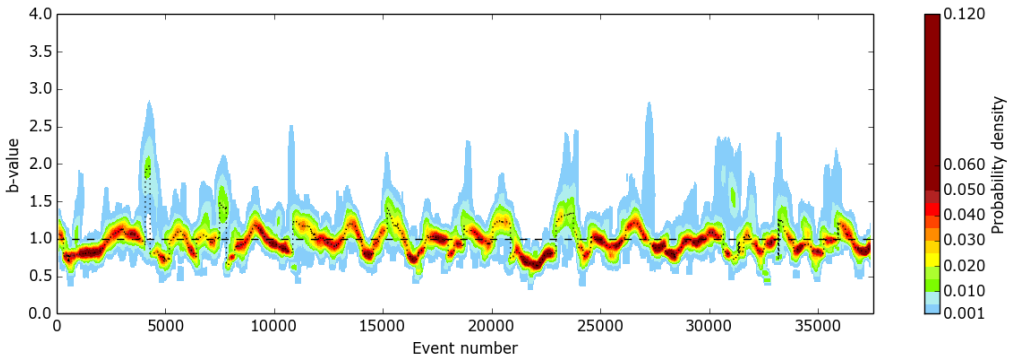

Figure 5.31 - The $\tilde{b}$-value probability density function for the NE cluster of the Tjörnes fracture zone from January 1995 to August 2015 containing ~37000 events. Plotted as in Figure 5.1.

Figure 5.32 shows the $\tilde{b}_P$ for the SW catalogue. It shows very similar behaviour to the NW in that $\tilde{b}_P$ fluctuates about 1.0 between 0.7 and 1.4. However, it has no mode-switching events, $\tilde{b}_P$ just varies smoothly through time. Unlike the NE it has a period between 18000 and 22000 events where $\tilde{b}_P$ is consistently above 1.0 with a maximum of 1.7. There are two cycles of the $\tilde{b}_P$-value and when compared to the plot by time Figure 5.33), it spans two years in 2008 and 2009.

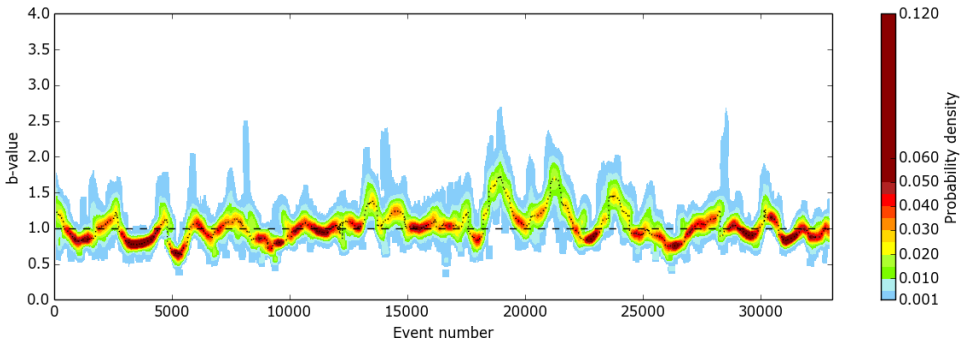

Figure 5.32 - The $\tilde{b}$-value probability density function plotted by event number for the SW cluster of the Tjörnes fracture zone from January 1995 to August 2015 containing ~33000 events. Plotted as in Figure 5.1.

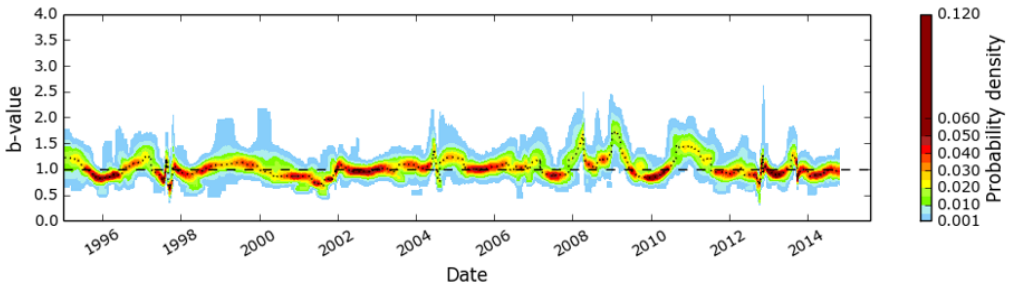

Figure 5.33 - The $\tilde{b}$-value probability density function plotted by timefor the SW cluster of the Tjörnes fracture zone from January 1995 to August 2015. Plotted as in Figure 5.1.

5.4.9.1 Annual cyclicity

As at Katla, the $\tilde{b}_P$-value at the Tjörnes Fracture Zone appears to vary annually. The same methodology is applied to two sub-catalogues that appear to exhibit this behaviour: four years from 2003 to 2007 for the NE catalogue (Figure 5.34a) and three years from 2007 to 2010 (Figure 5.34b). Both catalogues seem to vary around 1.0, with a minimum of ~0.7 and a maximum of ~1.5. The $\tilde{b}_P$ in the NE catalogue appears to vary more smoothly than the SW because the event rate is more constant.

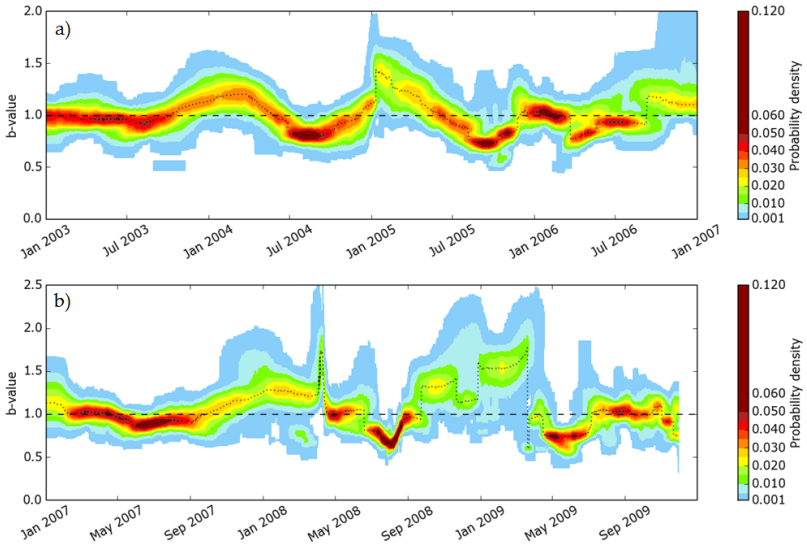

Figure 5.34 - The $\tilde{b}$-value probability density function showing the cyclical nature of the b-value, for a) the NE cluster of the Tjörnes fracture zone from January 2003 to January 2007, and b) the SW cluster of the Tjörnes fracture zone from January 2007 to January 2010. Plotted as in Figure 5.1.

Figure 5.35 shows the average monthly number of events, $\tilde{b}_P$-values, and minimum, maximum and completeness magnitudes for both the NW and SE catalogues. Unlike at Katla there is no clear trend in the monthly number of events. Both catalogues have a peak in August then again in December/January, however the SW catalogue is distorted by a period of seismic activity in April 2009 where over 200 events were recorded in one day (Figure 5.36). In general the baseline event rate is constant throughout the year for both catalogue, with the average being biased by these intense periods of events.

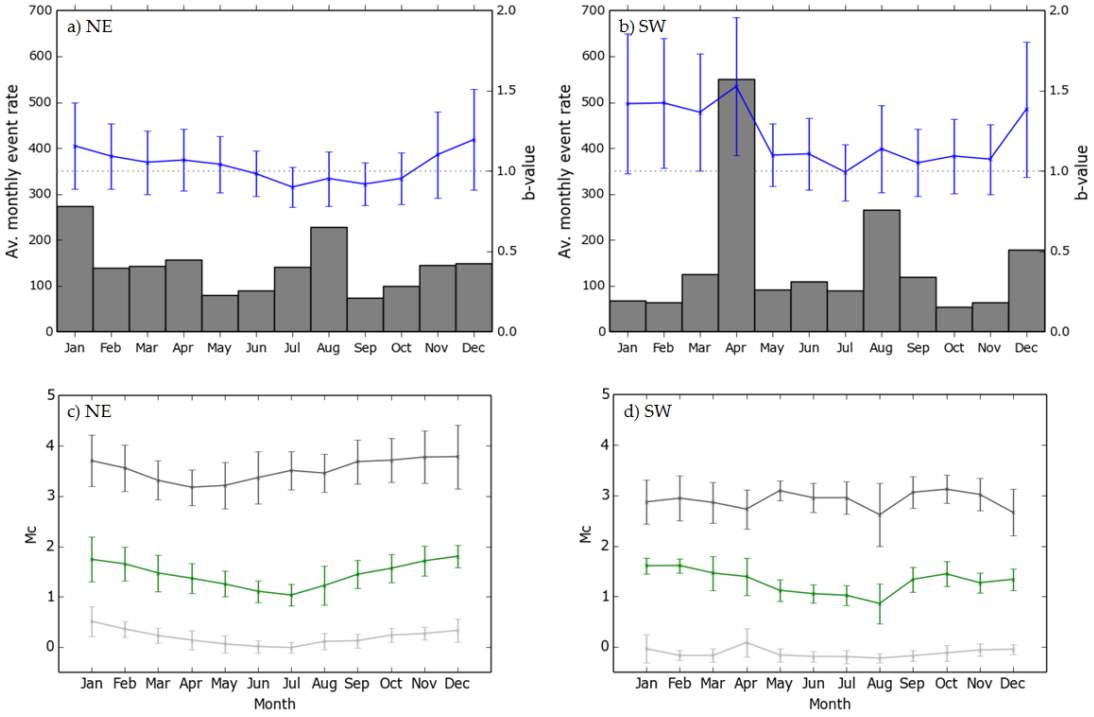

Figure 5.35 - Average number of event per month (grey bars) and average $\tilde{b}_P$-value with one standard deviation error (blue error bars) for a) the NE Tjörnes catalogue from 2003-2007, and b) the SW Tjörnes catalogue from 2007 to 20010. Average monthly minimum magnitude (light grey), completeness magnitude (green) and maximum magnitude (dark grey) for c) the NE Tjörnes catalogue from 2003-2007, and d) the SW Tjörnes catalogue from 2007 to 2010.

When comparing the average monthly maximum magnitude of recorded events in Figure 5.35c and d, again there is no clear correlation. However, the minimum and *Mc* for the NE, and the *Mc* for the SW, all show a similar trend with a minimum value

in July/August and a maximum in January. The average minimum magnitude in the SW remains approximately constant. The variation in *Mc* is very important as it is raised by ~0.5M from summer to winter, and as the maximum magnitude does not increase significantly this means the bandwidth of the complete catalogue is reduced through winter.

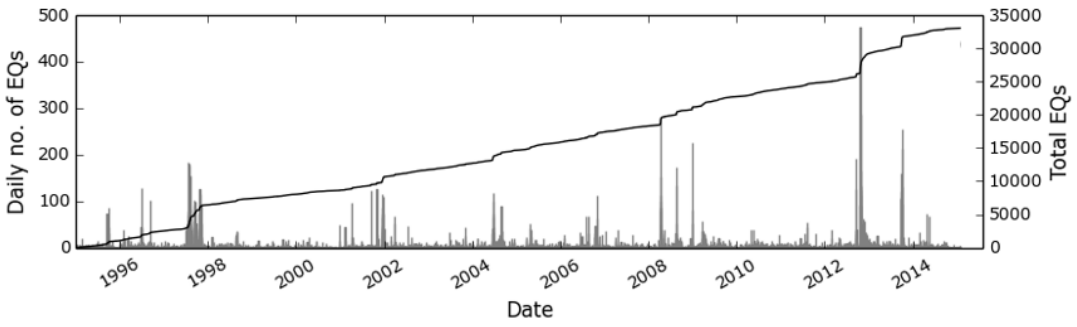

Figure 5.36 - Daily event rate (grey bars) and cumulative number of events (black line) for the SW Tjörnes catalogue.

For both catalogues this appears to translate to the average $\tilde{b}_P$-value (Figure 5.35a,b). The contoured PDF's are shown in Figure 5.37. In both catalogues the minimum occurs in July with a maximum early in the year. In The NW catalogue this is January, in the SW the peak is in April but the $\tilde{b}_P$-value is elevated from between January and April. In the NE the average varies between 0.9 and 1.2 with *b*=1 being captured every month within 65% confidence. In the SW the average is always greater or equal to 1.0 with a maximum of 1.5. *b*=1 is not captured within 65% confidence from February to April.

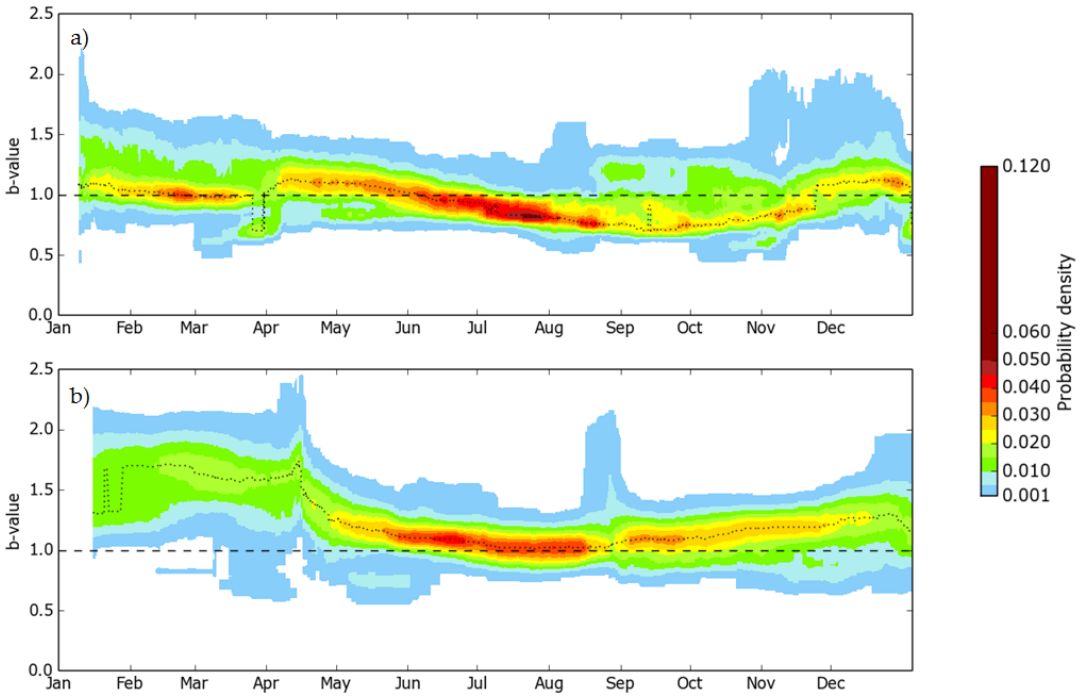

Figure 5.37 - Annual stacking of for a) the NE cluster of the Tjörnes fracture zone from January 2003 to January 2007, and b) the SW cluster of the Tjörnes fracture zone from January 2007 to January 2010. It is a countoured contoured PDF with peak $\tilde{b}_P$-value marked with the dotted line. As plotted in Figure 5.1.

In summary, the event rate at both Tjörnes catalogues does not vary cyclically, however the *Mc* is lower in the summer and higher in the winter. This may be due to increased noise due to winter storms offshore Northern Iceland. Consequently the bandwidth decreases in the winter raising the b-value in both catalogues. For the time periods selected the $\tilde{b}_P$ varies between 0.9 and 1.2 in the NE and 1.0 and 1.5 in the SW, however, Figure 5.38 demonstrates nicely that is the data from the entire 20 year catalogue is stacked then in both cases $\tilde{b}_P$=1. In both catalogues there is a decrease to $\tilde{b}_P$~0.8 at the start of August, and in the SW catalogue there is a bi-modality between $\tilde{b}_P$~1.0 and ~1.5 through April.

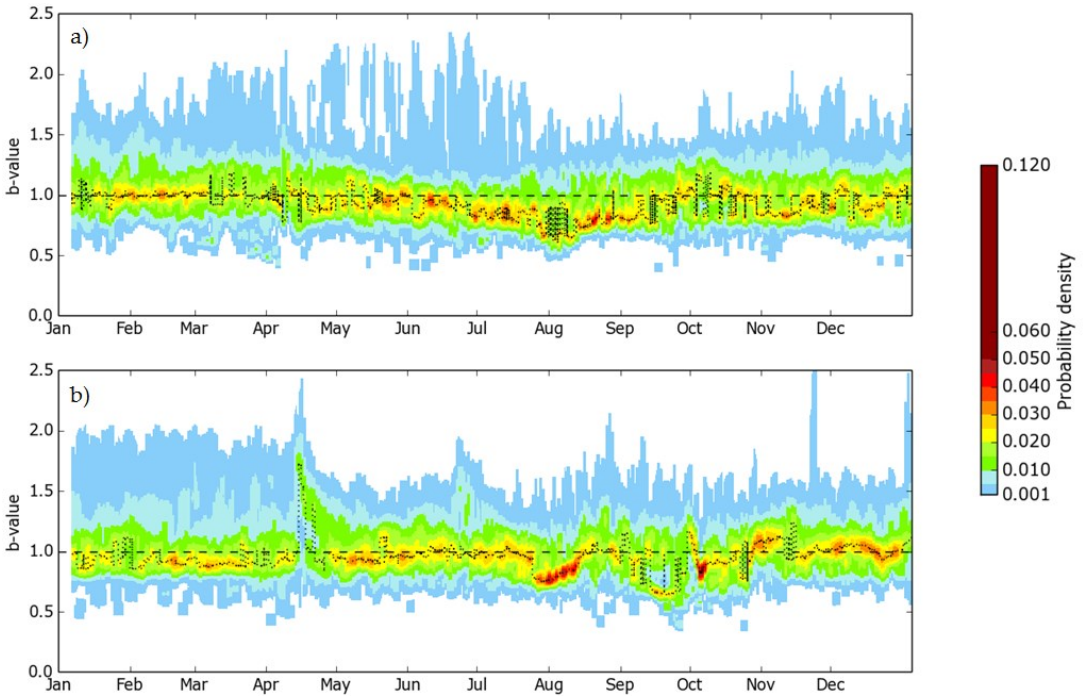

Figure 5.38 - Annual stacking of the Tjörnes 1995 to 2015 catalogue for a) the NW catalogue and b) the SE catlouge. It is a countoured contoured PDF with peak $\tilde{b}_P$-value marked with the dotted line. Plotted as in Figure 5.1.

The two following catalogues from the South Iceland seismic zone (SISZ) and Southern California are both tectonic seismic catalogues, not volcanic. The premise being to test the null hypothesis of b=1 at tectonic settings.

5.4.10 South Iceland Seismic Zone

The SISZ is a transform zone connecting the eastern and western rift zones of south Iceland. The zone trends E-W and has a left-lateral sense of shear however earthquakes occur along a N-S striking right-lateral slip faults (Clifton and Einarsson, 2005). The catalogue has ~60000 events from 2000 to 2015. Figure 5.39 shows $\tilde{b}_P$ typically varies around 1.0 with a maximum of 1.5 and minimum of 0.6. The catalogue does have a few mode-switching events between 20000 and 30000 events, and has a bi-modality between $\tilde{b}_P$=0.8 and 1.4.

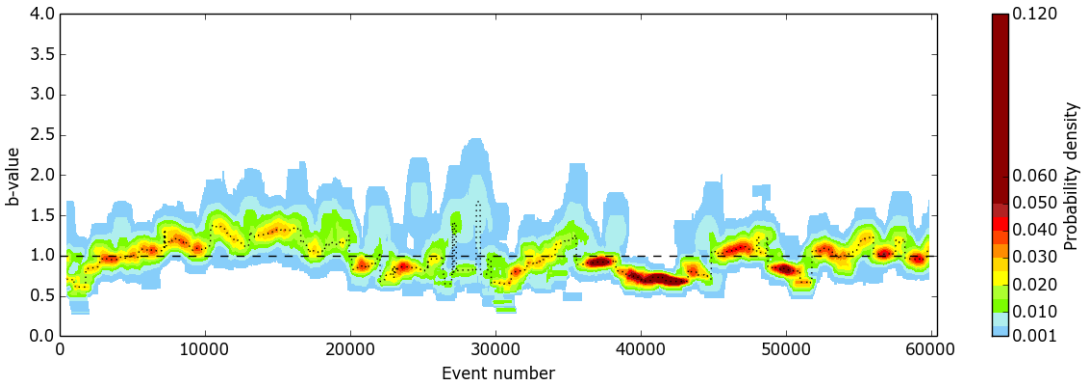

Figure 5.39 - The $\tilde{b}$-value probability density function for the South Iceland seismic zone from January 2000 to August 2015 containing ~60000 events. Plotted as in Figure 5.1.

$\tilde{b}_P$ is not often stable at 1.0, however there are no periods of sustained high $\tilde{b}_P$-values ($\tilde{b}_P$>1.5). Interestingly stacking the PDF annually (Figure 5.40) reveals a general bi-modality in the catalogue as the $\tilde{b}_P$ is constantly mode-switching between $\tilde{b}_P$~0.75 and ~1.0. Although $\tilde{b}_P$ is not constantly equal to 1.0 both general observations and stacking of the PDF suggest that through time the underlying $\tilde{b}_P$-value can be taken to be 1.0. There is no evidence for high $\tilde{b}_P$ values.

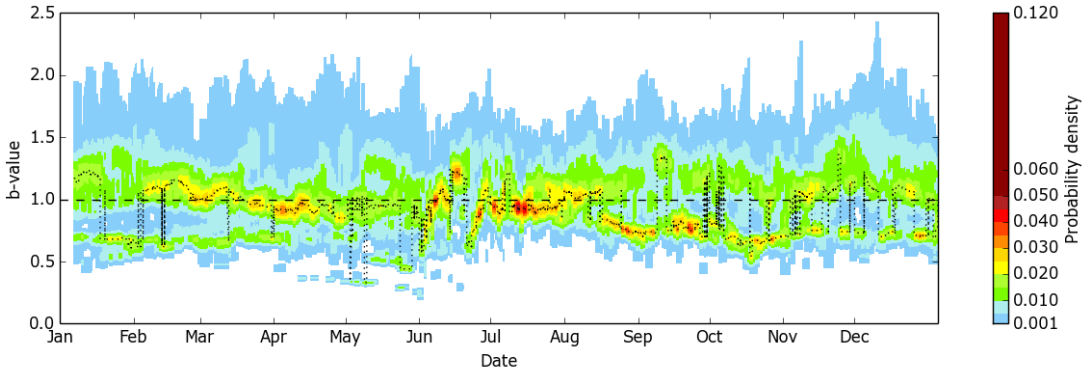

Figure 5.40 - The Annual stacking of the Southern Iceland seismic zone catalogue from 2000 to 2015. It is a countoured contoured PDF with peak $\tilde{b}_P$-value marked with the dotted line. Plotted as in Figure 5.1.

5.4.11 Southern California

The Southern California seismic network surrounds the San Andreas Fault. It is a right-lateral strike-slip fault. Again it is a tectonic regime, not volcanic, therefore b is expected to be 1.0. The catalogue has ~72000 events from 1984 to 2002. Figure 5.41 shows $\tilde{b}_P$ typically varies around 1.0 with a maximum of 1.4 and minimum of 0.5. Throughout the catalogue $\tilde{b}_P$ is very well defined compared to all of the previously analysed catalogues. There are almost no recognisable mode-switching events or high $\tilde{b}_P$-values; however $\tilde{b}_P$ does jump down to 0.5 on three occasions. Stacking the PDF in Figure 5.42 shows the $\tilde{b}_P$-value is actually just above 1.0 throughout the year rather than being equal to 1.0 as the null hypothesis suggests, however $\tilde{b}_P$ can be taken as constant and not atypically high for a tectonic setting.

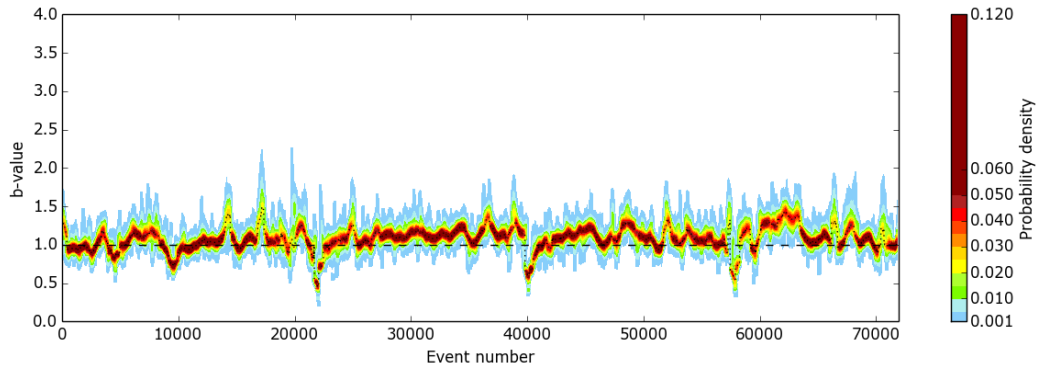

Figure 5.41 - The $\tilde{b}$-value probability density function South California from January 1984 to December 2002 containing ~72000 events. Plotted as in Figure 5.1.

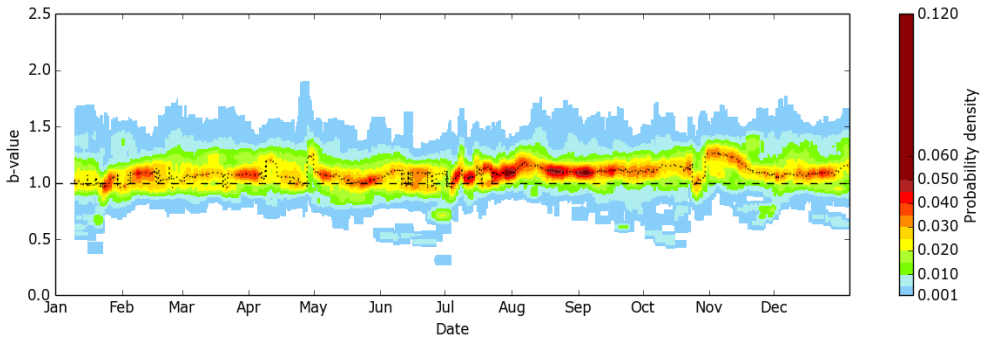

Figure 5.42 - Annual stacking of the Southern California catalogue from 1984 to 2002. It is a countoured PDF with peak $\tilde{b}_P$-value marked with the dotted line. Plotted as in Figure 5.1.

5.4.12 Summary

- Table 5.4 summarises the results from the 11 seismic catalogues presented in this chapter, noting both the typical modal and maximum reported $\tilde{b}_P$-values.
- First observed at El Hierro mode-switching of $\tilde{b}_P$-values is relatively common throughout the analysed catalogues. $\tilde{b}_P$ does not steadily progress through time, it jumps instantaneously from one constant value to another. The proposed reasoning for this phenomena at El Hierro, that is possibly more generally applicable, is that a spatial cluster of events will have a b-value controlled by the local stress and volcanic process causing the earthquakes. As a separate process initiates a new cluster of events will have their own discrete b-value. If these values are different the b-value will not gradually equilibrate between the two, the iterative sampling method will record the PDF with multiple $\tilde{b}_P$ modes where $\tilde{b}_P$ will switch to the most well defined mode.
- At Bárðarbunga this is not the case, the $\tilde{b}_P$ for the dyke and eruption catalogues increases smoothly through time showing a gradual equilibration of stress as fewer large earthquakes are recorded increasing the $\tilde{b}_P$-value.
- The Bárðarbunga caldera and potentially also the Grímsvötn caldera, have a characteristic frequency-magnitude distribution with two peaks in the discrete distribution. This means when calculating the maximum likelihood estimation of b, firstly the Gutenberg-Richter distribution is not an appropriate fit, and secondly very low $\tilde{b}_P$-values of 0.4 and 0.6 respectively are calculated.
- At Eyjafallajökull, three high $\tilde{b}_P$ appear to be correlated to an increase in event rates, however generally throughout the study there is no correlation between high event rates and elevated $\tilde{b}_P$-values.
- There is seasonal cyclicity in $\tilde{b}_P$-values and events rates observed at Katla; an increase in event rate leads to a decrease in the $\tilde{b}_P$-value in winter. Long period events in second half of the year are attributed to glacial movements not

volcanic activity (Jónsdóttir *et al.*, 2009) so the resultant very high (2.7) and very low (0.6) $\tilde{b}_P$-values observed in the catalogue are not of consequence for this study into volcanic $\tilde{b}_P$-values.

- There is a seasonal cyclicity in $\tilde{b}_P$-values and the completeness magnitude observed at the Tjörnes Fracture Zone. In winter there is more noise, possibly due to offshore weather, raising *Mc*, decreasing the bandwidth of the complete catalogue and consequently raising the observed $\tilde{b}_P$-values.
- The baseline $\tilde{b}_P$-value of the two tectonic catalogues analysed, Southern Iceland Seismic Zone and Southern California, is 1.0 and 1.1 respectively. This agrees with the null hypothesis that $\tilde{b}_P$=1.0. $\tilde{b}_P$-values as high as 1.5 and as low as 0.5 are reported however no atypically high $\tilde{b}_P$-values are found in either catalogue.

5.4.12.1 Comments on the methodology

- Mode-switching behaviour is the result of the iterative sampling method being able to successfully distinguish two concurrent discrete $\tilde{b}_P$-values.
- In Phase 1 of the El Hierro catalogue the iterative sampling method means catalogues containing up to 1000 events are sampled. If this happens to combine two sub-phases with discretely high *b*-values, the resulting $\tilde{b}_P$-value for the combined catalogue can be much lower producing a lower modal $\tilde{b}_P$-value in the PDF plot.
- Calculating stacked monthly averages can reveal annual trends however it does not account for bi-modality in the $\tilde{b}_P$-value.

Table 5.4 – Summary of results from the application of the random sampling methodology to the eight volcanic seismic and two tectonic seismic catalogues.

Volcano	Notes	N	Dates	$\tilde{b}_P\ max$	$\tilde{b}_P\ typ$	Primary type
El Hierro		21000	Jul 11 – Oct 13	3.3	1.0, 1.5	Shield
Etna		8100	1999-2013	1.7	0.9	Complex Strato
Kilauea		11000	1959-1983	1.6	1.2	Shield
Tungurahua	LP events	165000	1999 - 2015	2.6	1.5, 2.0	Strato
Bárðarbunga	Caldera	8500	Jun 14 – Jan 15	1.0	0.4	Strato
	Dyke	6000	Jun 14 – Jan 15	1.7	1.0	
Eyjafjallajökull		4000	Jan 10 – July 10	2.0	1.1, 1.5	Strato
Grímsvötn		500	2009-2015	1.8	1.0	Caldera
Katla		27000	1995-2015	3.0	0.6, 1.0, 2.2	Subglacial
Tjörnes Fracture Zone		70600	1995-2015	1.9	1.0	Submarine
South Iceland Seismic Zone		60000	2000-2015	1.3	1.0	Tectonic
South California		72000	1984-2002	1.4	1.1	Tectonic

5.5 Conclusions

The iterative sampling method shows that in tectonic settings b does equal 1. For volcanic catalogues although b-values as high as 3.3 are reported the modal $\tilde{b}_P$-value is often still 1.0. 'High' b-values (>1.5) are regularly reported in volcanic catalogues however each volcano has its own unique character. Although in some examples high event rates appear to cause high $\tilde{b}_P$-values this is certainly not the case for every period of intense seismicity. At Bárðarbunga, Grímsvötn and Katla, high $\tilde{b}_P$-values are also linked with non-Gutenberg-Richter frequency-magnitude distributions.

The iterative sampling method provides much greater insight into $\tilde{b}_P$-value evolution however results for each catalogue must be scrutinised individually in order to identify and validate and high $\tilde{b}_P$-values.

Chapter 6 – Fractures in a Magma Chamber: Isle of Rum

6.1 Introduction

6.1.1 Rationale

In this chapter I address research question 1), 5) and 6) from Section 2.5.1. The successful modelling of model seismic frequency-magnitude distributions is a key tool in eruption forecasting, but it is also important we attempt to study and quantify the processes that may be causing these volcanic earthquakes. Earthquakes recorded in an active seismic catalogue may occur many kilometres below the Earth's surface and so cannot be directly observed. The Isle of Rum in the Northwest Scottish Highlands is an exhumed ancient volcanic magma system. Studying the outcrops here allows for the opportunity to study the fossilised remains of a magma chamber and associated deformation features wthin the chamber. The results can then be compared with and used to interpret modern earthquake data from currently-active volcanoes.

There is an undoubtedly complex history and evolution of deformation features at Rum. However, by focusing on the youngest, and last major unit of volcanic rocks to be emplaced, it is possible to unravel the geological history of the magma chamber, identifying the key processes forming the fracture zones that may have produced seismic events. There is excellent exposure in the Central Intrusion, allowing for very detailed studies to be undertaken and robust data to be collected. In particular there

is extensive exposure of the fracture zones associated with magma emplacement. This chapter describes the results of a field campaign to map these fracture systems and their relationships to magma emplacement processes. Later in the thesis the results will be used to perform a fractal dimension analysis that can be compared with a similar analysis of data from the seismic catalogue of an active volcano, El Hierro, in Chapter 7. I am not aware of such a direct quantitative comparison of scaling exponents from an exhumed volcano with a modern one in the current literature.

6.1.2 Structure of this chapter

In Section 6.3 field observations from three years of study are presented and analysed to develop the understanding of the Rum Central Intrusion. The main units are defined and a newly identified intra-magma chamber breccia flow is mapped and described in context with a large collapse event within the base of the magma chamber. Fundamentally, the timing of the faults in terms of pre- syn- or post-volcanism needs to be determined. Typically at active volcanos earthquakes are not associated with syn-magmatic intra-magma chamber process, more with processes surrounding the chamber. However, at Rum there is strong field evidence to confine the timing of the observed fractures to being syn-magmatic in the solid, recently solidified, base/ walls of the magma chamber.

In Section 6.4.1 the results of quadrant-sampling of fracture densities and orientations across the study area are presented, followed by six local transects surrounding a gulley thought to be a major fault in the area in order to try and understand the local sense of deformation. In Section 6.5 the lineaments observed on satellite imagery are similarly analysed to understand how they have formed in relation to the magma chamber collapse and movement of the strike-slip fault cutting through the region.

It is important to collect and interpret data across a multitude of scales where possible, (from millimetre to hundreds of metre scale), as the consistency of results across several orders of magnitude is a far more scientifically robust procedure than simply relying on the results of one of the three methods. Also, it also means in

Chapter 7 when estimating magnitudes of earthquakes from these observations there is much greater confidence that the scale-invariant Gutenberg-Richter law is appropriate.

6.2 Methodology

The field study on Rum had two main components: lithological and structural mapping, and collecting structural data of the fracture zones. In order to be able to use and quantify fracture and fault data it was imperative to determine which features are associated with tectonic movement along the Long Loch strike-slip fault and which were formed by volcanic processes. The processes are inherently linked as the Long Loch Fault (LLF) is thought to be a feeder system for the (Central Intrusion) CI, however the null hypothesis is that the major deformation seen in the local units are in some way related to movement on the fault. Through ground-truthing with field mapping it is demonstrated here that the observed structures are in fact due to volcano-tectonic activity.

6.2.1 Study Area

The focus of the study was on an area of approximately 4 km^2 focused on the Central Intrusion (CI) around the Long Loch Fault (LLF), marked by the red box in Figure 2.8. This area stretched from the main Harris track to the north of Long Loch down through the contact with the WLI and CI to the low-lying area near the LLF with minimal exposure. To the south-east of LLF the exposure of the CI was very good, however the key localities were to the west of the fault.

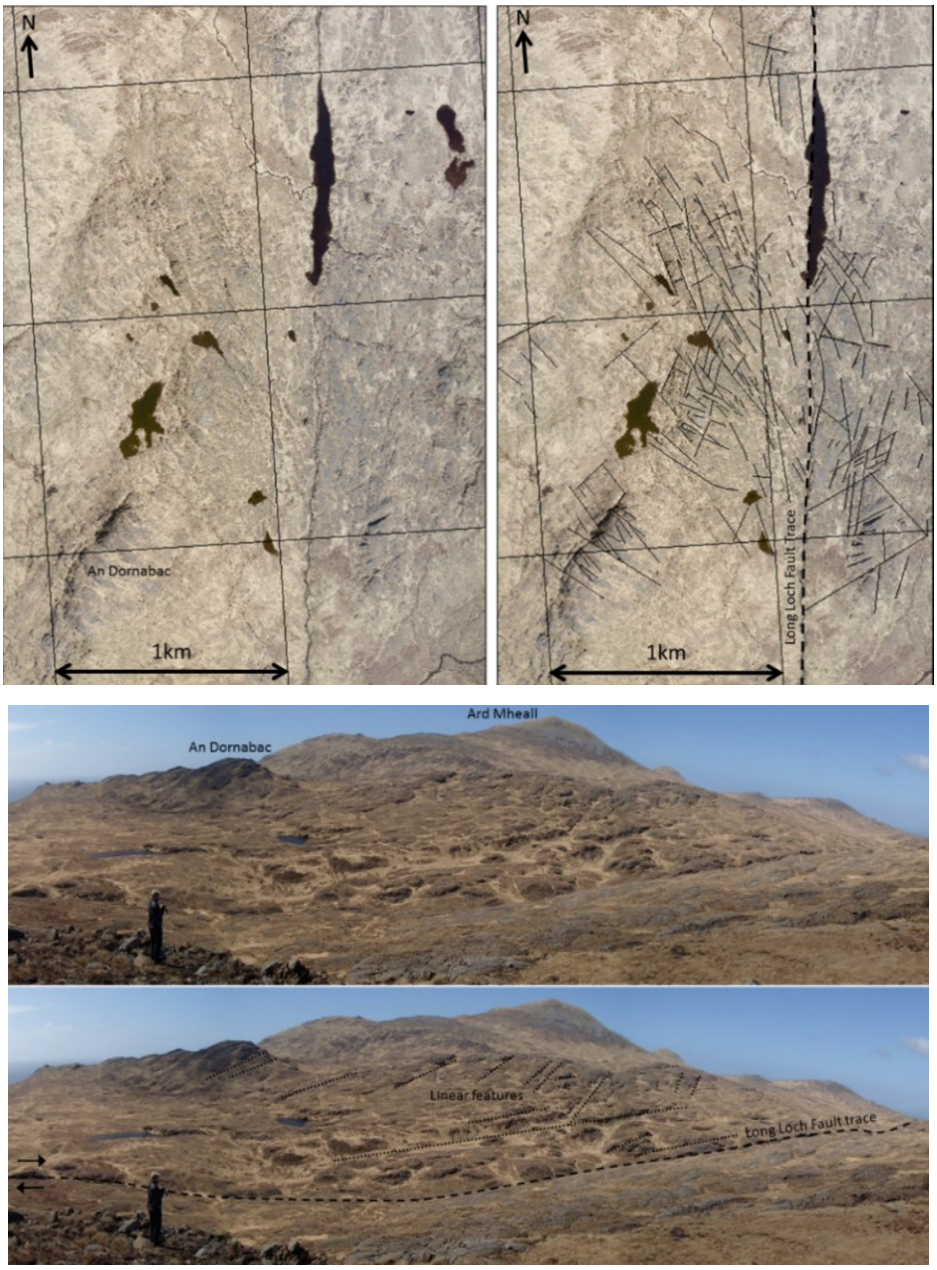

Figure.6.1 - a) Satellite image (Bing, 2015) of the Long Loch area identifying linear features on a 5-200 m scale in the Central Intrusion. b) Photo from the slopes of Barkeval, looking west at the Central Intrusion. The linear features can be seen cutting the outcrop.

6.2.2 Field mapping

Nine key units and major faults were mapped on the western side of the LLF, focusing on the intrusive breccia's forming the boundary between the WLI and the CI. To the east a smaller area was mapped, focusing on one faulting sequence.

6.2.3 Data collection

Linear features, of length 10-200 m, were identified using satellite images on either side of the LLF. By mapping the local units we gain insight into how these lithological boundaries correlate to these linear features. As discovered in the field, most of these major features were grass-filled gullies so, once the mapping was complete, 37 localities were sampled using a $1m^2$ quadrant across the study area in order to quantify the following:

- Number of fractures/ fracture density
- Fracture orientation
- Fracture length
- Fracture aperture
- Fracture offset/offset direction
- Fracture lithology

This allowed us to identify an area of key interest with the highest density of fractures within the WLI. Here six transects of length 10-50 m were used to measure the same characteristics of the fractures, from which we could interpret the underlying structure forming the fractures as well as using the data to perform density analysis of the fracture spacing.

Along each transect the following measurements were made:

- Strike of every fracture
- Distance between each fracture
- Lithology of the fracture

- Offset and offset direction if quantifiable
- Major fault zones were recorded as a summation of individual fractures.
- Distance of outcrop covered by grass.

6.3 Results of field mapping

6.3.1 Units

There are essentially three rock types in the mapped area; peridotite, troctolite and breccia, subdivided into the following nine units. They are listed and described below:

Unit symbol	Unit name
U_W	WLI peridotite
U_C	CI peridotite
U_f	Feldspathic peridotite
E_T	Troctolite
E_A	Allivalite
E_B	Sliding basal facies
ΔU	Intrusive breccia
ΔU_D	CI peridotite with diffuse clasts
ΔU_P	Pebble breccia

- WLI peridotite – Generally an ultrabasic cumulate sequence (Figure 6.2a), however there are areas containing a more plagioclase-rich Harrisitic texture (Figure 6.2b), typically occurring at the top of ultramafic layers (O'Driscoll *et al.*, 2007).

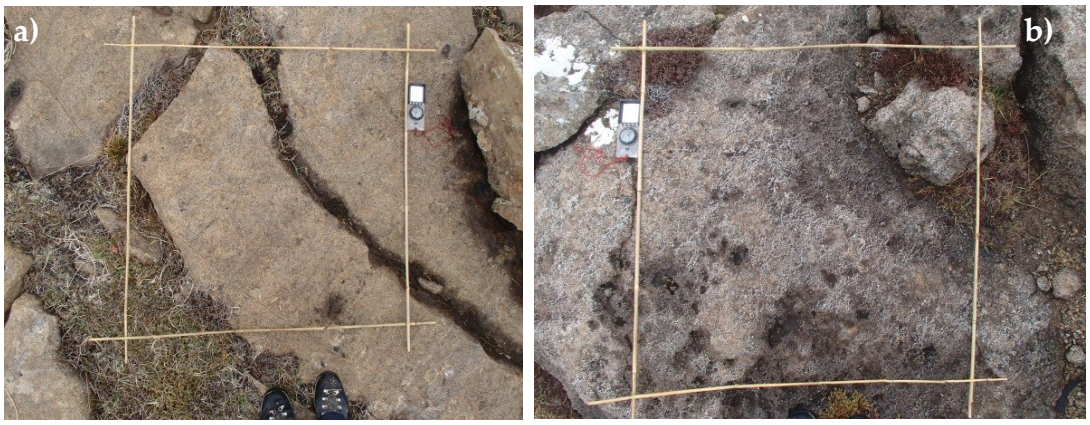

Figure 6.2 - a) Ultrabasic peridotite of the WLI. b) Harrisitic peridotite of the WLI. 1 m^2 quadrant for scale.

- CI peridotite – Typically ultrabasic, containing a higher percentage of olivine than the WLI, thus it weathers to a very vivid orange colour (Figure 6.3). It is an olivine cumulate rock with up to 30% plagioclase (Mattsson *et al.*, 2014).

Figure 6.3 – Ultrabasic peridotite of the CI containing feldspathic intrusive material. Compass for scale.

- Troctolite – Forms very distinctive grey-layers. Bytowinite-troctolite, henceforth called 'troctolite, is a plagioclase-olivine cumulate with between 50-90% plagioclase (Wadsworth, 1961; Emeleus *et al.*, 1996). West of Long Loch the troctolite is massive and homogeneous (Figure 6.4a), in places having a high clinopyroxene content to appear like a more gabbro.

Figure 6.4 – Troctolite found on the west side of the Long Loch Fault.

- Allivalite – Technically the same composition as the troctolite, but here we make the distinction when there is clear cumulate layering as seen in Figure 6.5. Rarely seen on west of Long Loch but there is a prominent bed east of LLF very close to the fault zone.

Figure 6.5 – Allivalite block displaying clear dipping cumulate layers.

- Sliding basal facies – A combination of CI peridotite and troctolite. Found at the base of a mega-block, several layers of troctolite have acted as a lubricated basal plane over which the block has moved (Figure 6.6).

Figure 6.6 – The visible grey layers are the troctolite that have acted as a low friction layers over which the orange peridotite megablock has moved. The basal facies is simialr in process to breccia type 5 shown below in Figure 2.11. Boulder in forground is 1 m across.

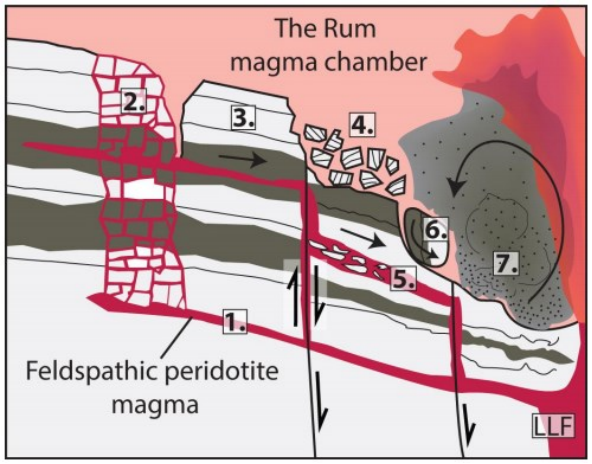

Figure 2.11 – Repeated figure from Section 2.3.4 showing a conceptual model of the breccia formation.

- Intrusive Breccia – Forming on the margins of the CI as feldspathic peridotite intrudes the cumulate layers. As shown above in Figure 2.11 there are many different observed mechanisms for producing the breccias. Figure 6.7 shows some examples of differing outcrops within the study area. The intrustive breccia is mapped as a singular unit however many different processes are associated with it depending on the locality and the dynamic nature of the breccia.

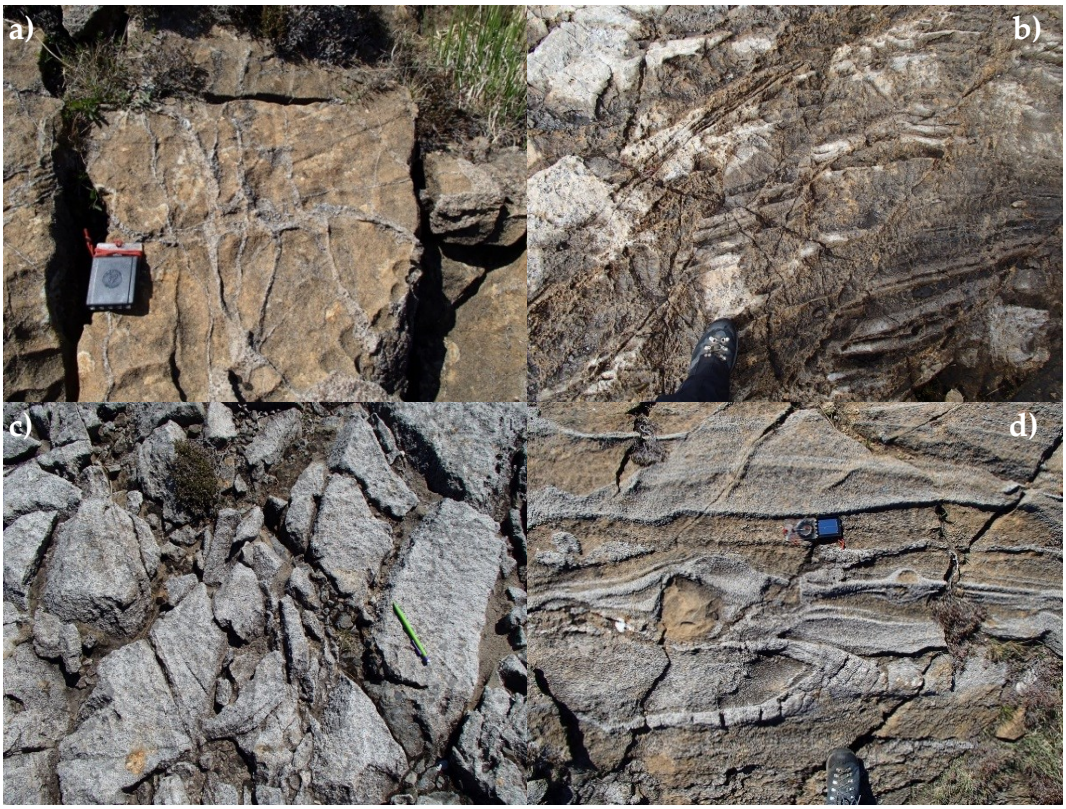

Figure 6.7 – Various examples of intrusive breccia: a) Pervasive intruding veins of feldspatchic peridotite at the CI-WLI boundary as in Figure 2.11.2. The clasts are not yet mobilised. b) A large heavily fractured allivalite clast with the mobilised intrusive breccia. c) Angular troctolite clasts that have been mobilised but over a short distance. Not talus deposits but similar to those shown in Figure 2.11.4. d) Very mobile breccia, the clasts appear to have rotataed and partially melted, as in Figure 2.11.5.

- Pebble breccia – Stratigraphically the youngest unit in the central intrusion. It is an upwards coarsening breccia containing varying clast sizes from mm to cm scale. The clasts are ultrabasic peridotite. The matrix is a feldspathic material.

Figure 6.8 – Pebble breccia of the CI. Rounded peridotite clasts between 1 mm to 3 cm in size, within a feldspathic matrix. Pencil for scale.

6.3.2 History of the Central Intrusion

6.3.2.1 Stratigraphy

Figure 6.9 is my geological map of the studied area within the northern CI. Figure 6.10 is a sketched stratigraphic column showing how the various units relate to each other. Figure 6.11 is a schematic cross-section of the stratigraphy described below. The oldest rocks in the sequence are the peridotites of the WLI. The exposure is moderate to poor, however it can be observed that the easterly dipping beds steepen from ~20° to nearer 40° as they approach the intrusive breccia. There are outcrops with weakly developed harrisitc texture proximal to the western granite near the track at the western edge of the study area. There is no evidence of any clasts within the WLI peridotite other than one 20 m x 1.5 m allivalite block (Figure 6.5). There is no evidence for any turbulent movement of the block, or any other clasts in the vicinity.

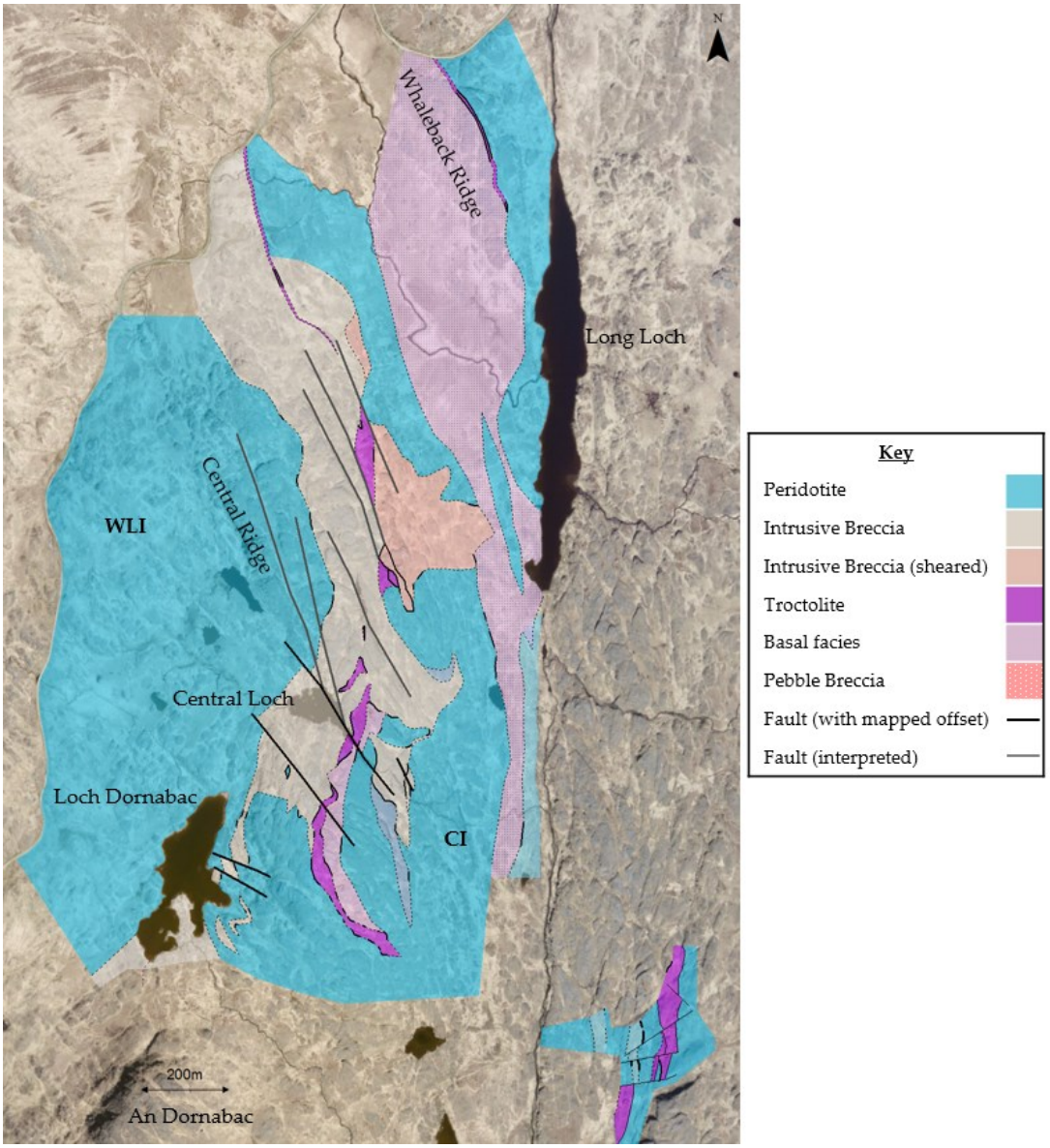

Figure 6.9 - Map of the field study area. The Western Layered Intrusion and Central Intrusion are seperated by intrusive breccais and a layer of troctolite, with debris flows cascading down into the still active Central Intrusion within the magma chamber. Key localities are marked for orientation. Colour scheme based on the solid geology map compiled by Emeleus, 1994.

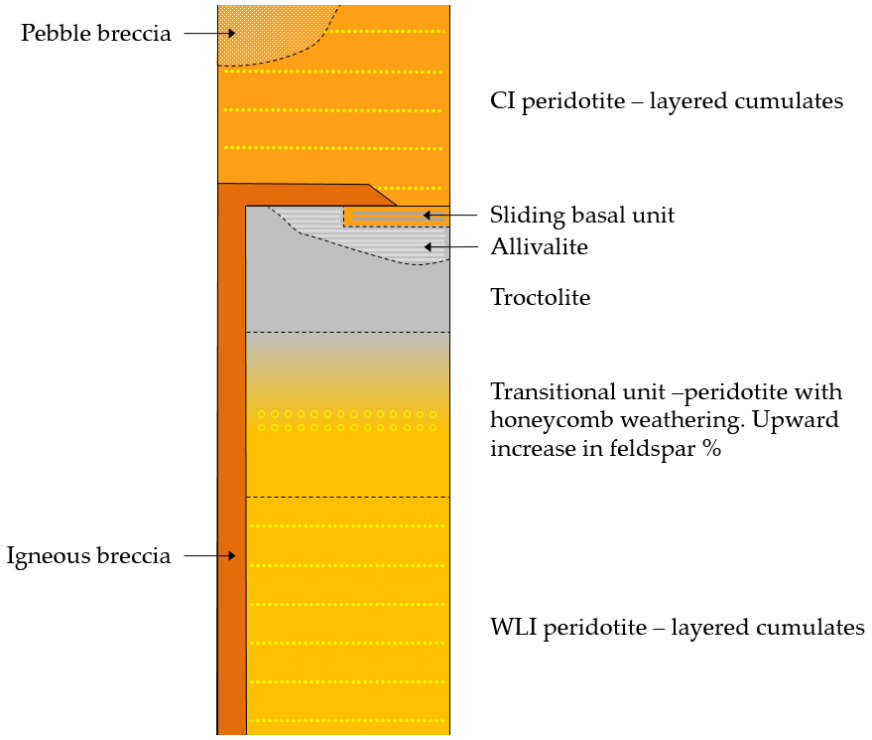

Figure 6.10 - Stratigraphic sequence of the igneous rocks in the study area. Thickness of the transitional peridotite unit, troctolite, allivalite and sliding basal unit all vary through the area. Combined thickness of those units may be ~20-50 m.

The sequence at the cliff face, and ridge-top to the east of Loch Dornabac, gradates up into peridotite with 'honeycomb' weathering (Figure 6.10), conceivably the poikilomacro-spherulitic texture identified by Donaldson (1973). There is then a ~10 m thick transitional unit as the peridotite becomes more felsic, leading into the base of the troctolite unit (Figure 6.6). This gradational unit is not visible further north due to the intrusive breccia. The troctolite unit is up to 20 m thick near the Central Loch, but typically 5-10 m thick, thinning to just a few metres further north, but it is still traceable through the diminishing outcrop. The top of this layer becomes the sliding basal facies, where the top of the troctolite has melted and acted as a lubricant for a large peridotite sliding block. The transitional unit, troctolite and allivalite are all lithologically and rheologically heterogeneous throughout the study area varying significantly is thickness and appearance often on the outcrop scale.

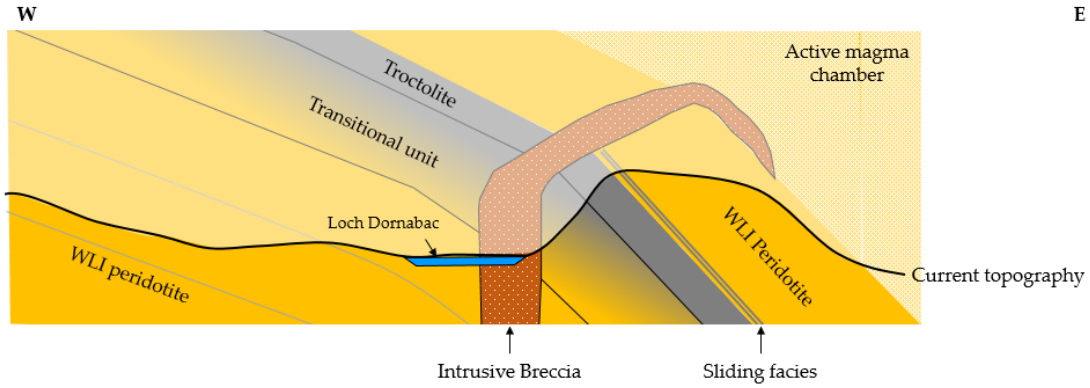

Figure 6.11 - West-east schematic (not to scale) cross-section through Loch Dornabac showing the stratigrahpy of the peridotite units and the relationship with the intrusive breccia.

Excluding the intrusive breccia, the next unit in the sequence are the CI peridotites. These peridotite, including the sliding block, are the youngest in the sequence of cumulate stratigraphy. The bright orange colour typifies the olivine-rich peridotites of the CI.

Although these are historically mapped as two separate units, there are no field observations to support that the CI peridotite is anything but a continuation of the cumulate sequence forming the WLI within the study area. To the west of Loch Dornabac is the easterly dipping WLI, and to the west easterly-dipping CI peridotite, with intrusive breccia inferred within the loch.

The Intrusive breccia, sliding block and pebble breccia will all be described in this section, however it is important to note that they are intra-magma chamber processes – they are occurring within, or at the base of, the active magma chamber.

6.3.2.2 Intrusive breccia and collapse event

The intrusive breccia striking approximately north-south, can be traced through the entire study area, but has varying thicknesses and characteristics. The western margin is exposed in almost its entirety. It is a vertical contact with feldspathic (grey) material intruding into the layered peridotite (orange) at the margin the contact is gradational

across ~5 m with, starting with heavy veining at locality A (Figure 6.12) in Figure 6.13a. The percentage of the feldspathic matrix increases until the host rock is completely broken apart forming a matrix-supported breccia (Figure 6.13b). This is the same mechanism as previously described in Figure 2.11.2 (Mattsson *et al.*, 2014).

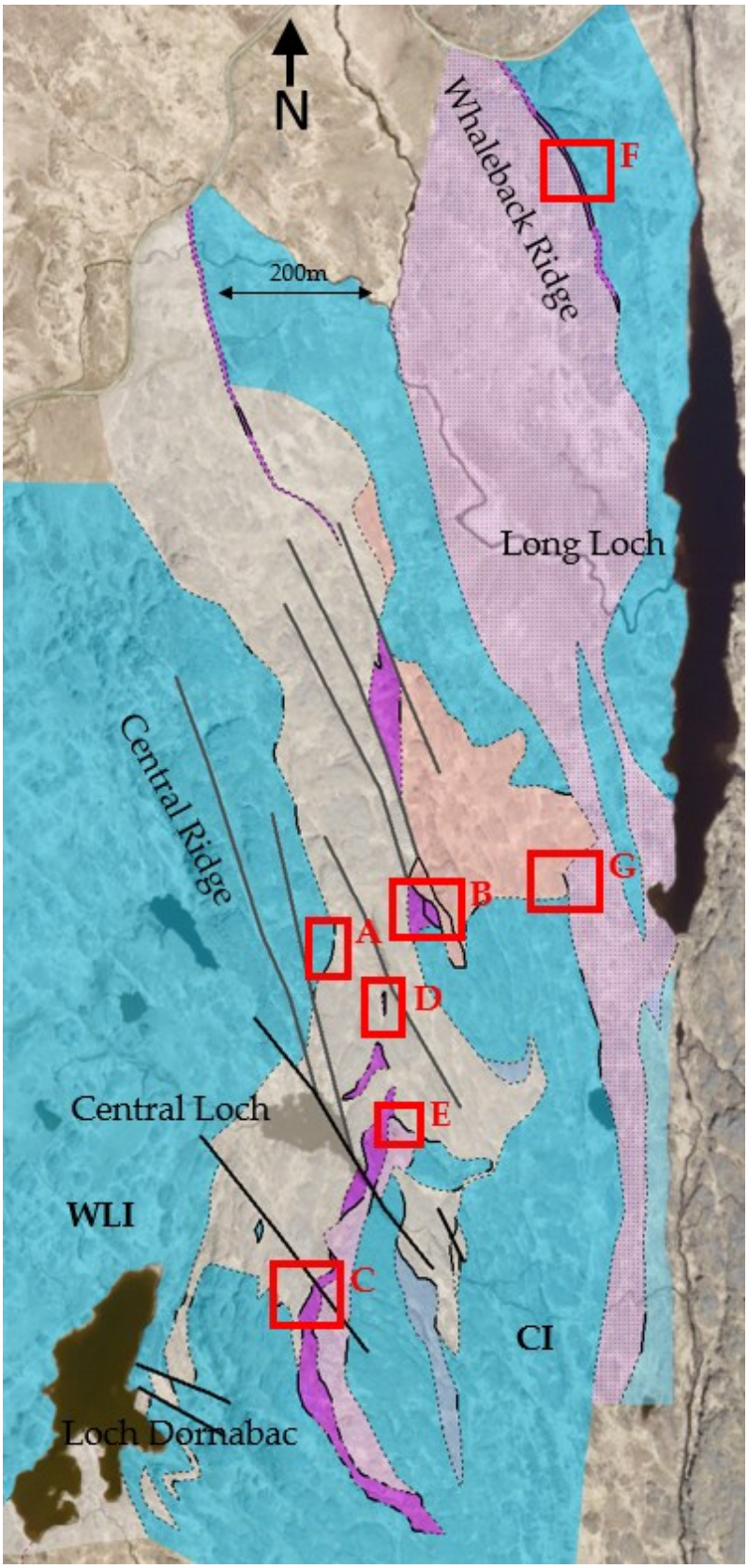

Figure 6.12 – Localities A-G

Figure 6.13 - Locality A. a) Heavy feldspathic veining within the WLI peridotite at the margin with the intrusive breccia. b) Intrusive matrix-supported breccia. Peridotite host rock is completely broken into clasts that have been disaggregated.

The eastern margin of the intrusive breccia is more complex than the west, however again we observe examples of a vertical contact. At locality B the intrusive breccia intrudes past the troctolite (Figure 6.14). At the margin partially melted layers of troctolite can be seen to be 'peeled' off and incorporated into the breccia matrix (Figure 6.15).

Figure 6.14 - View north at locality B. a) Breccia intruding vertically past the troctolite. b) Sketched boundaires shown in black and interpreted fault scarps in grey, mapped in Figure 6.9.

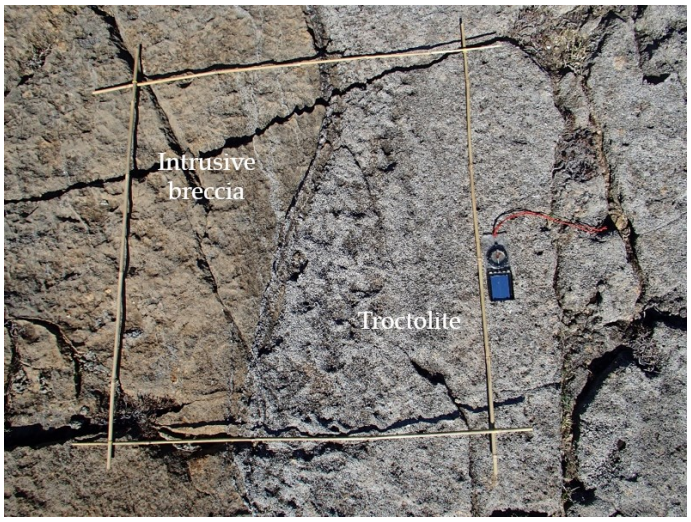

Figure 6.15 - Contact between the intrustive breccia and troctolite at locality B in Figure 6.13 At the margin the troctolite is partially melted and starting to be incorporated into the breccia matrix. Compass for scale.

South-East of Central loch the contact with the underlying peridotite becomes sub-horizontal as the breccia appears to flow over the peridotite. This is why the breccia appears to be much thicker here compared to the north and south of the study area. The breccia intrudes to the west of the flows to the east. Figure 6.16 at locality C shows the eastern exposure of the breccia as it comes into contact with the troctolite. Again there is evidence for melting and incorporation of the troctolite at the margin.

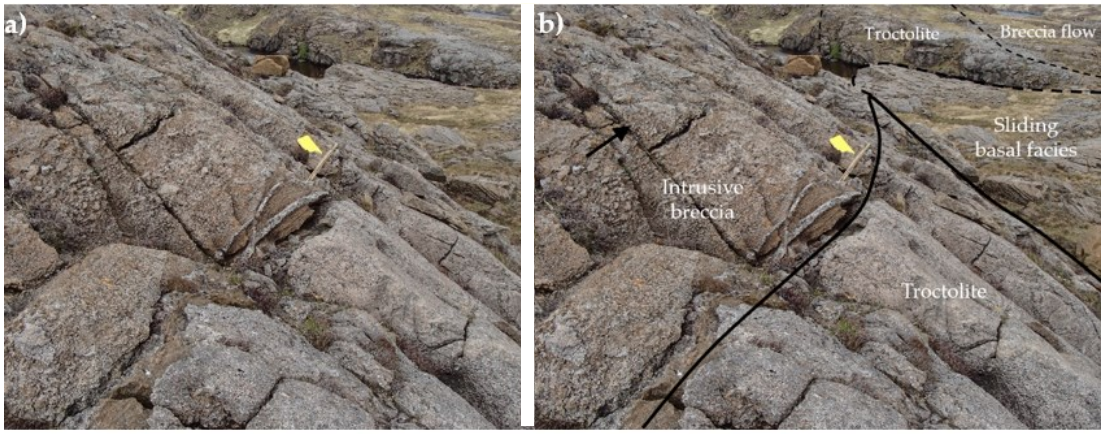

Figure 6.16 - View to north at Locality C. Intrusive breccia flowing up and over underlying troctolite. The arrow shows the direction of flow. Note also the ~5 m right-lateral offset of the troctolite across the loch. Notebook for scale.

At locality D, to the north of Central Loch, there is further evidence for the breccia overlaying the troctolite. In Figure 6.17 the breccia is now flowing down to the east towards the Long Loch fault.

Figure 6.17 - View to north at Locality D. Intrusive breccia flowing over the top of the troctolite. The arrow shows the direction of flow. Notebook for scale.

The breccia appears to flow down slope within the magma chamber so it is more apt to describe it as a breccia flow rather than an intrusive breccia. Outcrops at locality E show the turbulent nature of the debris flow: rounded clasts are suspended within a peridotitic matrix have varing orientations; partially melted layers of feldspathic material also show ductile deformation around the clasts as they have been mobilised.

Figure 6.19 shows a heavily melted lobe of troctolite that is being rotated clockwise as the flow moves east down the hill. Figure 6.18 shows a near spherical peridotite clast. The clast is no longer angular in shape suggesting that it may have been transported a long distance within the flow like the clasts seen near the margin in Figure 6.13.

Figure 6.18 - View to north at Locality E. Near sperical peridoite clast within the breccia flow. Troctolite bands flowing around the clast. The arrow shows the direction of flow. Compass for scale.

Figure 6.19 - View to north at Locality E. Heavily melted troctolite lobe rotating within the breccia flow. Melted troctolite is being incorporated into the matrix. The arrow shows the direction of flow. Compass for scale.

The breccia flow can be traced down slope for several hundred metres until the clasts become smaller and more diffuse. South of locality E and east of locality C a thin layer of the breccia outcrops on top of the orange CI peridotite. This is believed to be part of the same flow but due to erosion the outcrop is not clearly joined to exposures at

C and E. The breccia flow is an alternative interpretation of the locality to Mattsson *et al.* (Figure 12a, 2014), who state that between two breccia units are several peridotite and troctolite layers dipping towards Long Loch Fault. We see no evidence for these layers in this outcrop, just the breccia flow, which is similar to our interpretation further south.

6.3.2.3 Sheared intrusive breccia

Locality B is a very prominent knoll that has several different facies of troctolite. Figure 6.14 shows homogeneous un-deformed troctolite 20 m north of the knoll. On the knoll itself, at the western margin is the heavily fractured troctolite shown in Figure 6.20a. Here the troctolite has clearly been stressed and fractured, but has no form of intrusive material, nor have the clasts been mobilised. The face of the scarp in shown 50 m east at the edge of the knoll (Figure 6.20b). Here the clasts have been partially melted and clasts have been smeared. This unit has not flowed like the breccia flow just to the south but appears to have been sheared. The orientation of shearing is approximately north-south parallel to the interpreted fault scarps mapped in Figure 6.9. To the north and east of the knoll, the unit marked as sheared intrusive breccia, contains troctolite clasts likely to be from the same troctolite unit, but with a higher percentage of matrix material. This will form part of the same body as the intrusive breccia but the driving force in the movement of the clasts is shearing rather than upward intrusion, or a gravitational flow.

Figure 6.20 - Locality B. a) Heavily fractured troctolite. Looking east, bag for scale. b) Sheared troctolite breccia. looking NW, person for scale.

6.3.2.4 Sliding block and basal facies

South of Central Loch along the eastern margin of the troctolite. Several thin layers of troctolite have been smeared along the base of the peridotite block as it slid down towards the Long Loch Fault, as seen in Figure 6.6. The eastern extent of the block is not well constrained due to poor exposure, but it is approximately 500 m long north-south, 200 m wide and 10 m thick. This basal sliding unit is not homogeneous troctolite, nor is it a cumulate layered sequence of the CI, therefore I have mapped it as a distinct basal sliding unit. The breccia flow sits on top of the block constraining the thickness.

6.3.2.5 Pebble breccia

The pebble breccia onlaps all other units, with no evidence for any younger deposition, making it the final magmatic event in the central intrusion. Previously only mapped on the whaleback ridge (Mattsson *et al.*, 2014), we found further outcrops south of Long Loch within 50 m of the LLF. The contact with the underlying units is erosive. At locality F, in Figure 6.22, the pebble breccia has melted and partially incorporated the westerly dipping troctolite. At locality G, in Figure 6.21 the pebble breccia is onlapping and partially melting a distal outcrop of the sheared intrusive breccia. Here all structures are easterly dipping. The opposite dip directions

of localities F and G suggest a syncline structure striking NNW through the current topographic low. There is no further field evidence supporting this due to lack of outcrop between either limbs of the syncline. The pebble breccia is thought to be the deposit from a convection cloud within the magma chamber (Figure 2.11 - breccia type 7.). A syncline, or graben, structure, at the base of the magma chamber would allow for the deposition of such a unit.

Figure 6.21 - View to north at Locality G. Pebble breccia onlapping onto a distal outcrop of the intrusive breccia.

Figure 6.22 - View to north at Locality F. Pebble breccia eroding into layered allivlite. A strip of allivalite can be seen being incorporated into the breccia. The clipboard provides a scale.

6.3.2.6 Faulting in the East

The structure of the CI east of the LLF was not the main focus of this study. However an approximately 400 m by 400 m area was mapped (Figure 6.23), focusing on an allivalite bed as it is a clear marker of offset along any potential faults. Four east-west striking faults were identified, as well as two north-south striking faults.

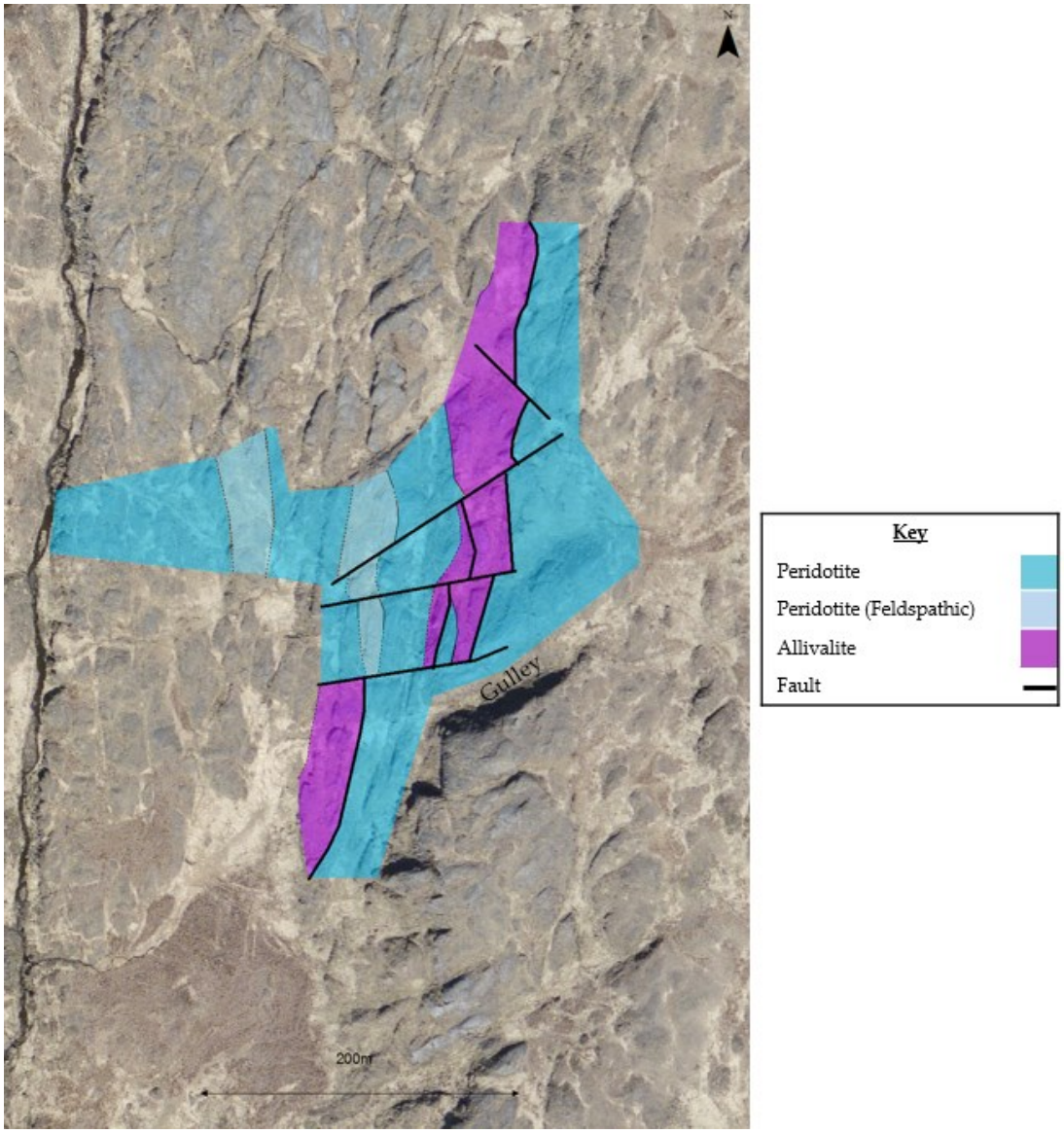

Figure 6.23 – Map of the faults allivalite in the SE of the field area.

The north-south faults are older, being contemporaneous to the active magma chamber. One of these faults bounds the eastern edge of the allivalite. It is a 70° westward dipping normal fault. Figure 6.24 shows the allivalite in the hanging wall being ripped apart as it subsides. The allivalite had clearly solidified at the time as angular clasts have been broken off. However, some clasts are frozen in suspension meaning a fluid matrix must have been intruded as the allivalite collapsed. This fault can be traced for ~400 m before the outcrop disappears. The second fault is ~20 m west of the first cutting straight through the allivalite bed. Offset must be on a metre scale or less. It can be traced through several outcrops but only for ~50 m in length.

Figure 6.24 – Hanging wall of a westerly dipping fault. Allivalite is being torn apart as it subsides, with a newly intruded matrix holding clasts in suspension. View to north, notebook for scale.

The east-west striking faults are younger than the latest volcanic units. They create several metres of offset between outcrops but much like the interpreted faults on the west side of LLF, they form gulleys covered in grass. The top three mapped faults all

follow the path of linear features that can be observed on the satellite images. However, surprisingly the southernmost fault, with the greatest offset (~40 m), is 20 m north of the large gulley marked in Figure 6.23. There is no observable offset within this gulley; the eastern margin of the allivalite is not offset across it.

The allivalite bed can be traced further north, swinging westward to meet the LLF just south of Long Loch. There is believed to be ~800 km of left-lateral offset on the LLF so it is probable that this is the same allivalite unit found on the whaleback ridge.

6.4 Fracture sampling

The fractures mapped in the field exercise were observed within the WLI and CI layered cumulates, but do not cut the intrusive breccia. Therefore their deformation must have occurred after the main cumulate sequence had been deposited but before/during the collapse event associated with the intrusive breccia. This is conclusive evidence that the fractures were contemporaneous with the magmatism. This inference was quantified further using the quadrant sampling described below.

6.4.1 Quadrant sampling

Some 37 localities were sampled across the field study area using a 1 m^2 quadrant. Figure 6.25 shows an example of several fractures with several centimetres of displacement. Within the quadrant, whether offset was observable or not, the orientation of the fractures was recorded. After the first fieldwork season, these results were plotted as rose diagrams and are shown plotted on the geological map in Figure 6.26. The size of each diagram is proportional to the number of observed fractures.

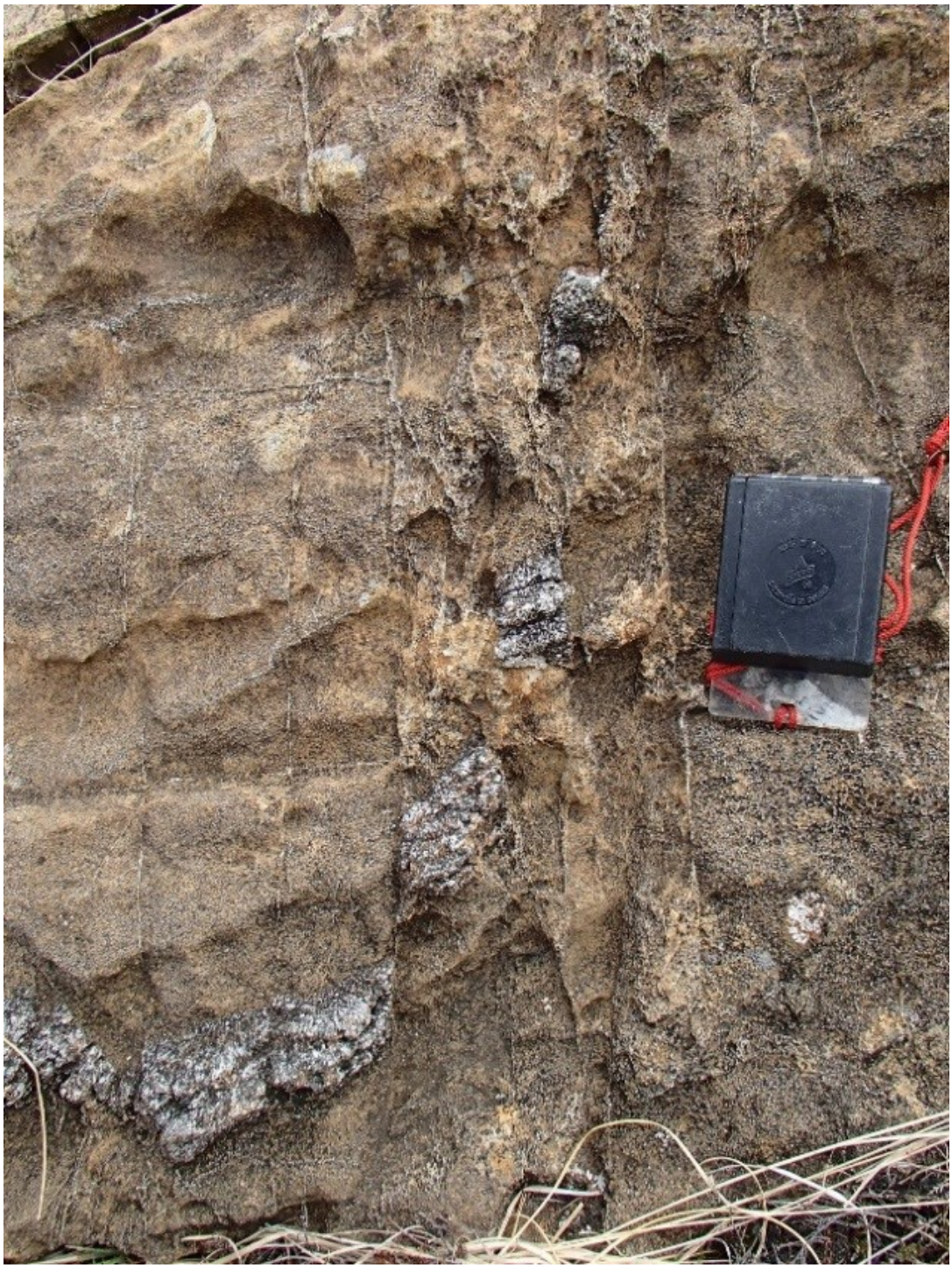

Figure 6.25 – Example of offset along fractures at transect 5. Individual fracture may have several centimetres of offset, but summed over the whole fracture zone this can add up to metres of offset.

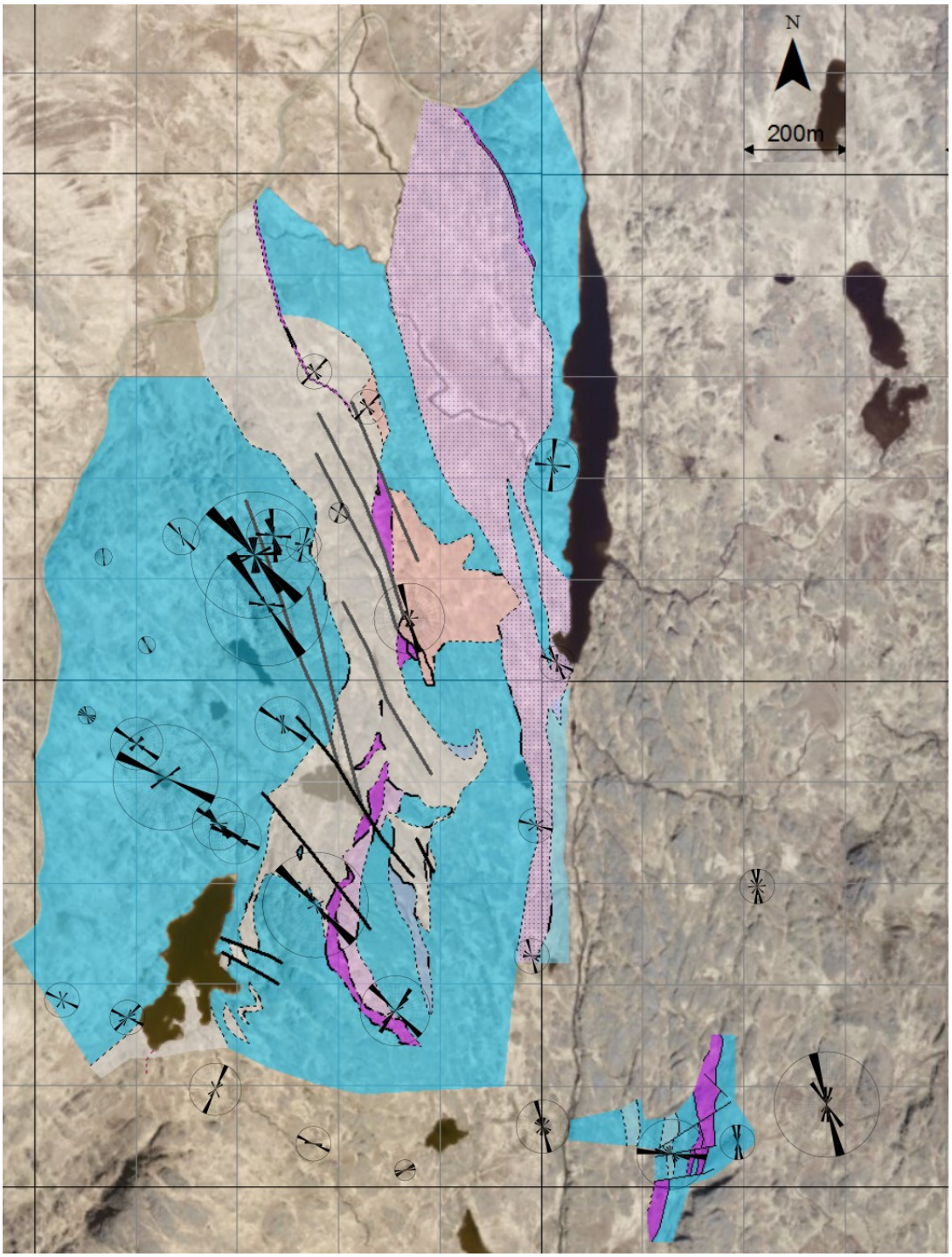

Figure 6.26 – Rose diagrams for each of the sampled quadrants overlain on the map in Figure 6.9. They show fracture orientation and density for 37 quadrant sites. The size of the rose diagram is proportional to the peak number of fractures in one 10° bin. One grey square is 200 m.

The highest concentration of fracturing was along the Central Ridge (Figure 6.9) with a maximum of 25 fractures observed in one quadrant. There is relatively little deformation proximal to the LLF with >10 fractures being observed in all five quadrants on the west bank of the LLF. Most importantly for constraining the timing of the fractures, none were observed cutting the matrix of the intrusive breccia, however fractures were observed within the clasts. This means the fractures formed whilst the magma chamber was still active.

6.4.2 Transects

As the Central Ridge had the highest fracture density and is bounded by two large gulleys, this locality was chosen to perform 6 transects, ranging in length from 13-27 m (The raw data is in Appendix C). Figure 6.27 shows transects 1, 3 & 5 on the west side of the gulley on the eastern side of the ridge. Transects 2, 4 & 6 are on the east side. As the transects are a one-dimensional (1D) sampling method they are orientated with a ENE strike so they are perpendicular to the NNW striking gulley. This may create a bias in the sampling as fractures with a similar strike to the transects may not be recorded, however every effort was made in the field to reliably sample the transects.

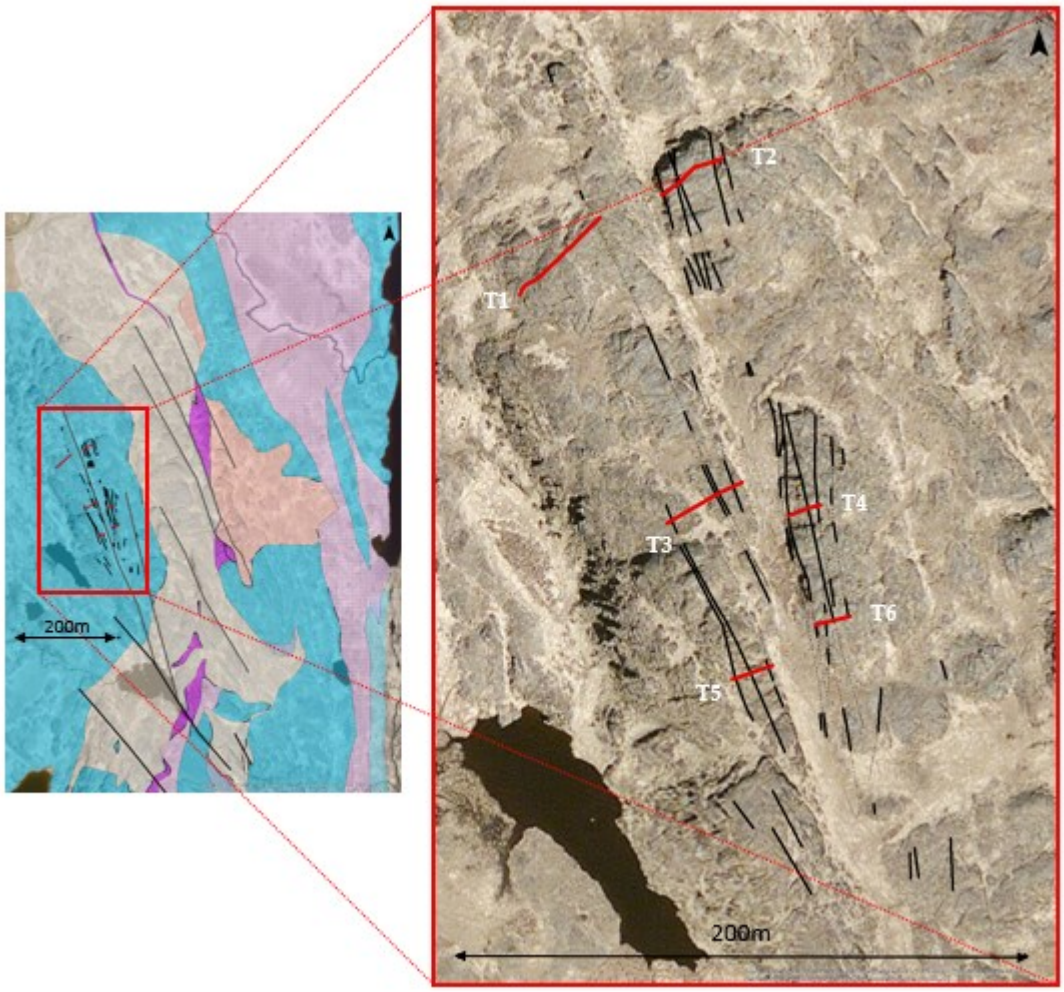

Figure 6.27 – Location of the 6 transects within the WLI along the Central Ridge. Red lines show the transects, black lines are mapped fault zones.

Major fault zones with clear offset were also mapped in Figure 6.27, an example of which is shown in Figure 6.25. These zones tended to be 10-100 cm in width and contain multiple fractures measured in the transects. In general a large proportion of observed offset was accounted for across these fault zones. The idea being the strikes of the fracture, mapped fault zones, and lineaments of the satellite images will provide a comparison on three different scales.

6.4.3 Transect data

The transect data is visualised in Figure 6.28. The x- and y- axes show the orientation of the transects relative to due north and east. The distances are only relevant for the spacing of the fractures and areas of no outcrop; the lines representing the fractures are plotted to a metre in length to help visualise the strike. In reality the fractures may be much longer or shorter. The precision of the field measurements for fracture spacing was up to a few mm.

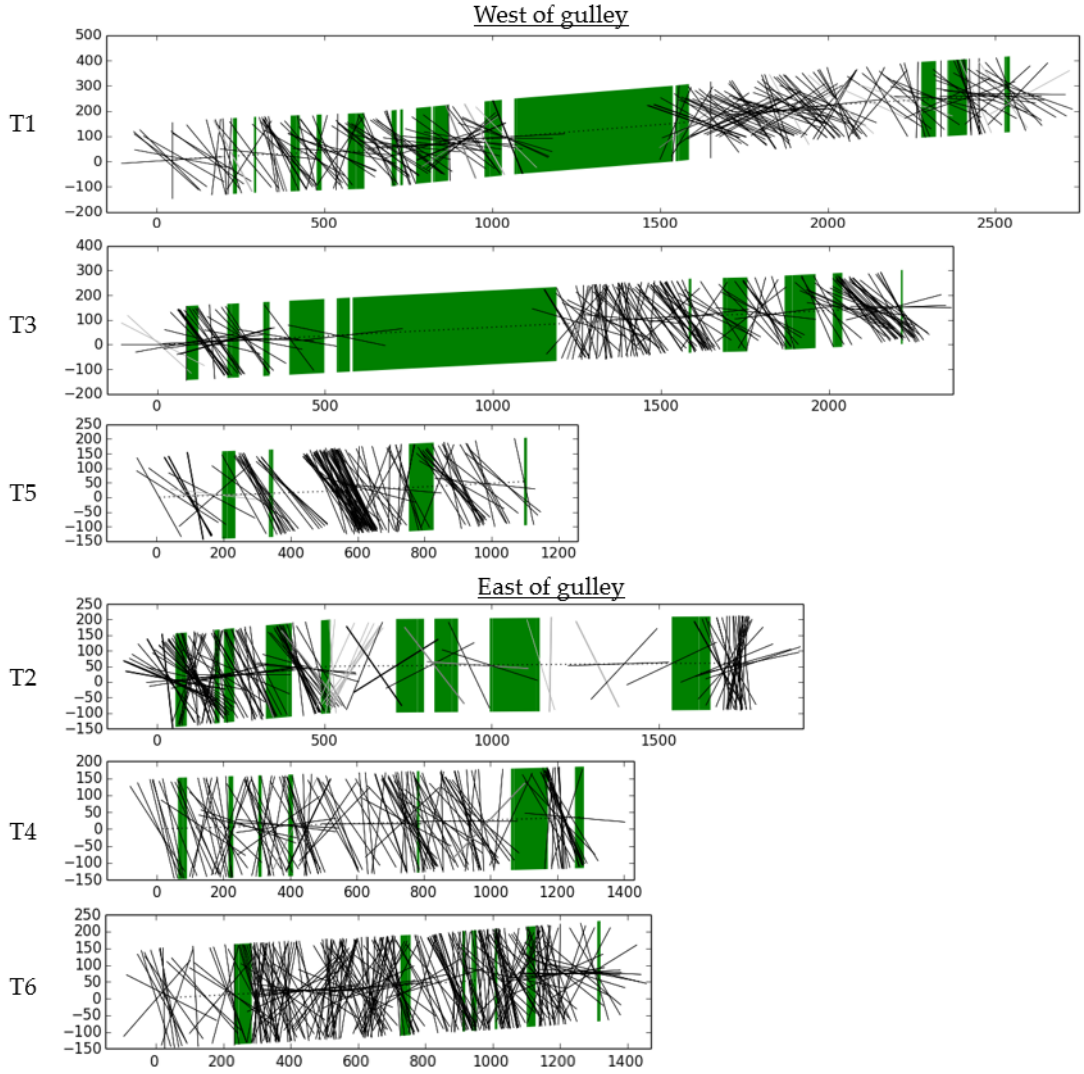

Figure 6.28 – Visulisation of the data for the six transects. The dotted line shows the orientation of the transect. Solid black lines show the orientation of the fractures. Solid grey lines show the orientation of gabbro veins. Green polygons indicate there was no outcrop for this section. Scale in centimetres.

The fractures densities for each transect are plotted in Figure 6.29. The data is binned in 1 m intervals. If one bin had 100% outcrop exposure the number of fractures within that metre could simply be counted. If there was less than 100% exposure, the number of fractures is divided by the ratio of outcrop:no-exposure to give a fracture density, per metre, for the outcrop. Bins containing a mapped fault zone are highlighted to provide an easier interpretation.

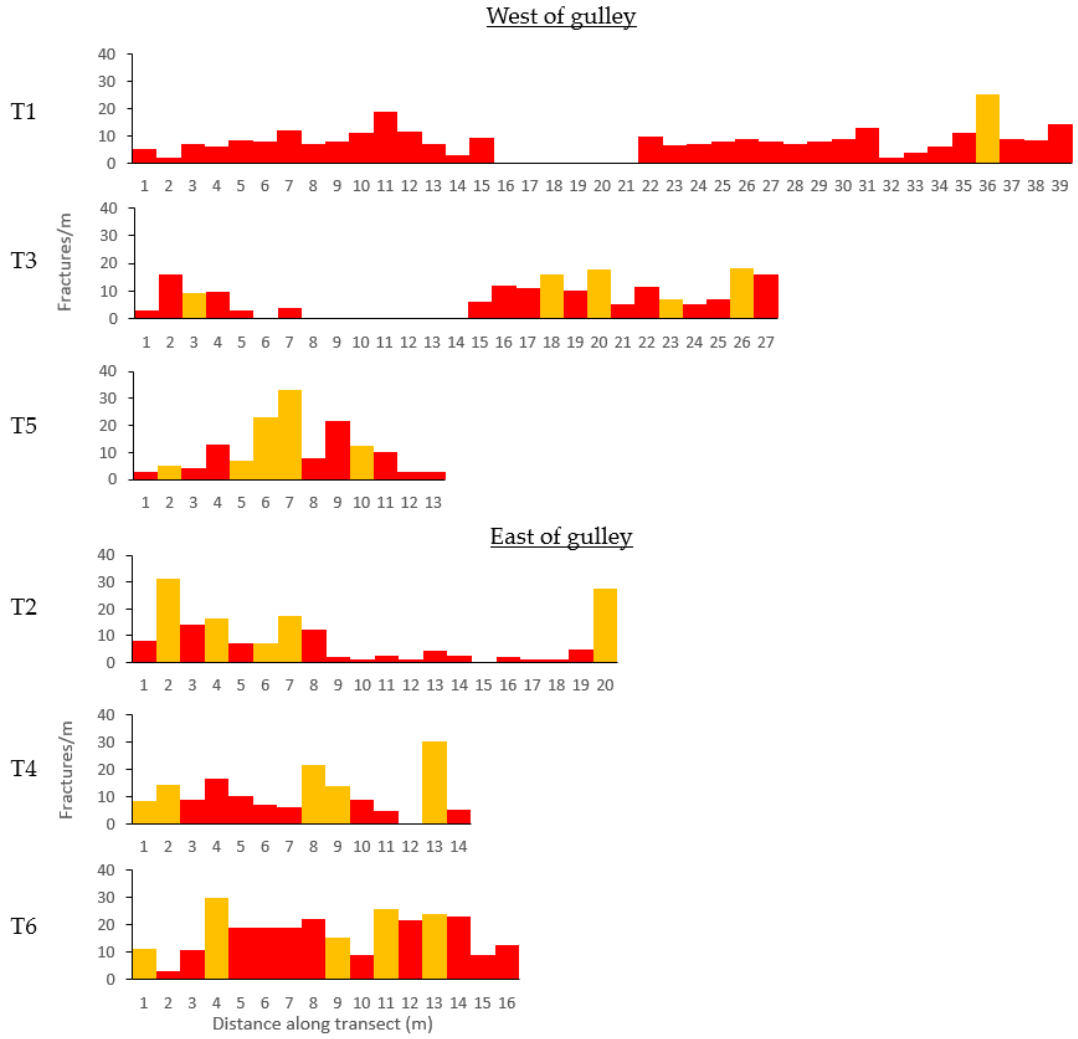

Figure 6.29 – Fracture density (fractures per metre) for each transect. Yellow coloured bins contain a mapped fault, red bins do not.

Figure 6.30 shows bi-directional rose diagram plots for: all the transect data, combined transect data for the three transects east and west of the gulley, and each

individual transect. The mean strike has been calculated with one standard deviation either side of the mean. This shows the range and skew of the data, i.e. are all the fractures going in the same direction or is there likely to be more than one predominant direction of strike? Figure 6.31 is a bi-directional rose diagram showing only the fractures with observed offset on them.

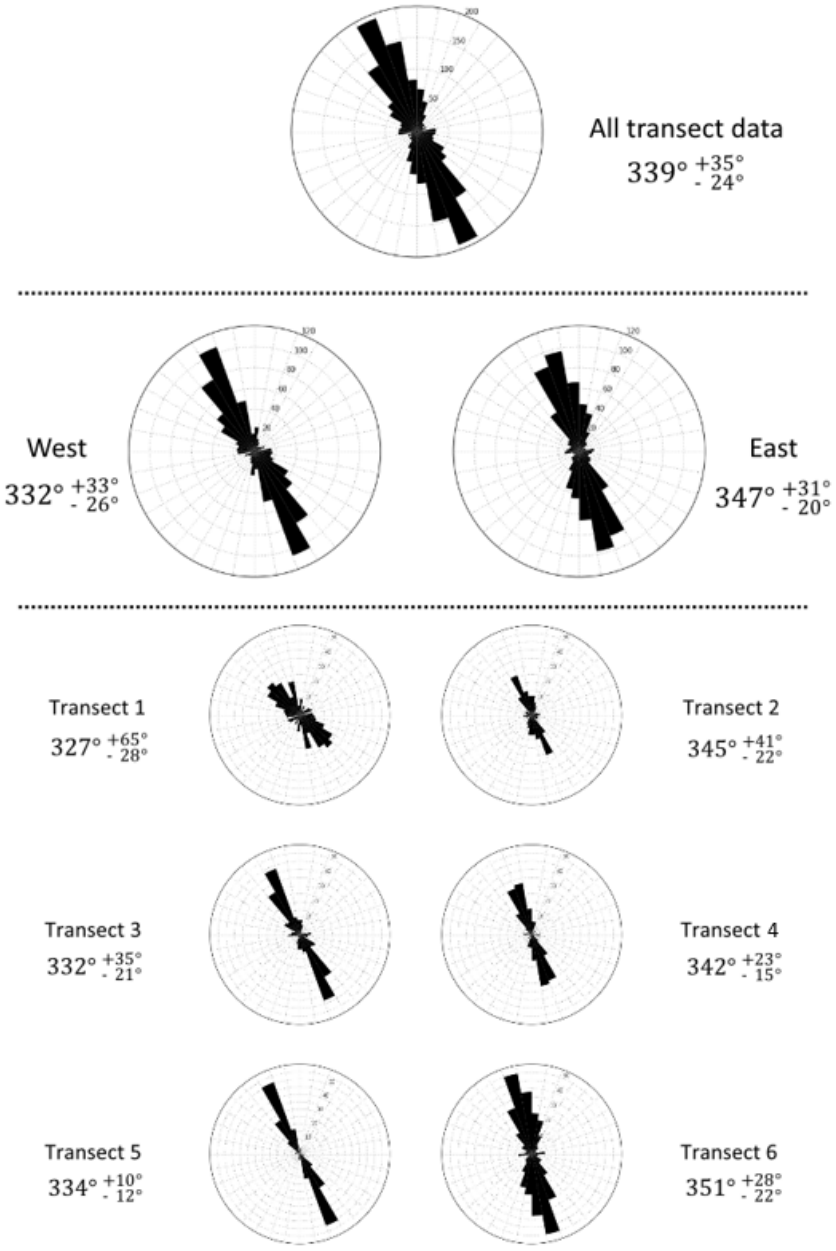

Figure 6.30 – Bi-directional rose diagram plots for all the transect data; three transects east and west of the gulley; and each of the individual 6 transects. For reference, the main gulley has a strike of 340°.

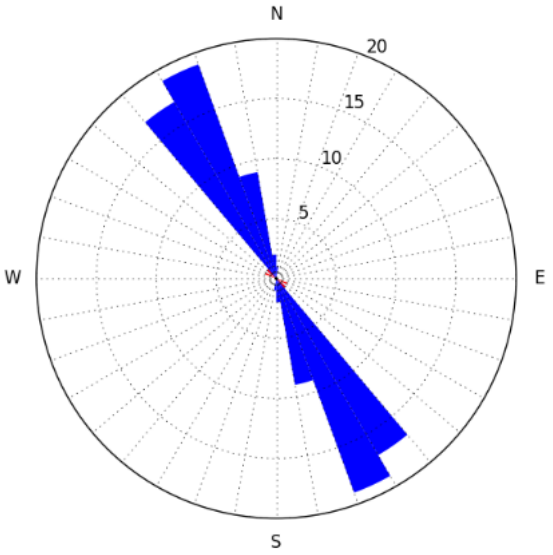

Figure 6.31 – Bi-directional rose diagram showing the strike of 49 fractures with observed left-lateral offset (blue), and 2 fractures with right lateral offset (red).

6.4.4 Observations from transect data

Table 6.1 summarises the data from Figure 6.29 to Figure 6.31. The following observations are made from the data:

- Fracture density is generally slightly higher on the eastern side of the gulley – specifically when comparing T5 to T6, but from general observations more fractures and more mapped faults are present to the east of the main gulley.
- The fracture density increases southward – south of the transects the main gulley appears to join the other major gulley bounding the west side of the central ridge.
- On the west side of the gulley fracturing is localised, concentrated around fault zones with areas of relatively little fracturing in between – visual observations of T5 in Figure 6.28 show several regions of heavy fracturing with few fractures in between. It is also apparent from Figure 6.29 that the peaks in the fracture density histograms correlate with the mapped faults highlighted in yellow.

- Fracture on the east side are more evenly distributed – T4 and T6 have a more even distribution of fractures, however the peaks in fracture density still correlate well with mapped faults. T2 has two zones: from 0-8 m there is dense fracturing throughout the outcrop; from 9 m onwards there are very few fractures until the next mapped fault where the fracture density increases again.
- Modal strike bin is 330-340° on the west side and 340-350° on the east - Figure 6.30 shows there is a 15° difference in the average strike of fractures on either side.
- The modal strikes for both T1 and T2 are less than those typically seen in the southern transects – the strike of the main gulley also swings west further north so the fractures relation to the gulley remains the same.
- Nearly all observed slip has a left-lateral displacement component – although two faults were observed with right-lateral slip they were on the order of centimetre scale. Generally the direction of slip is quite subjective as observations can only be made on a 1D surface. However a scarp just north of T2, provided excellent outcrop showing a major mapped fault with apparent left-lateral slip on the horizontal surface and apparent vertical eastward extension on the vertical surface. Figure 6.32a is a photo of the vertical exposure of this outcrop, with Figure 6.32b highlighting the faults and gabbro vein being downthrown to the west.

Figure 6.32 – a) Southward facing photo of exposure just to the north of transect 2. b) Faults are drawn in black, with a westward downthrown gabbro vein highlighted in grey.

- Some faults bound lithological units – all the faults are clear brittle boundaries, not intrusive, therefore the observed changes in lithology either side of the faults is likely to be due to fluid flow with the fault acting as an impermeable barrier. In most outcrops observed offset is no more than a metre or two, however in Figure 6.33, an outcrop approximately 100 m north of Transect 2, a metre-wide unit of troctolite material has been downthrown between two peridotite units. It is not possible to calculate any offset as the troctolite is not present on either side of the bounding faults. Figure 6.34 summaries the left-lateral and vertical-faulting seen at Transect 2, as well as demonstrating how the various faults control the changes in lithology.

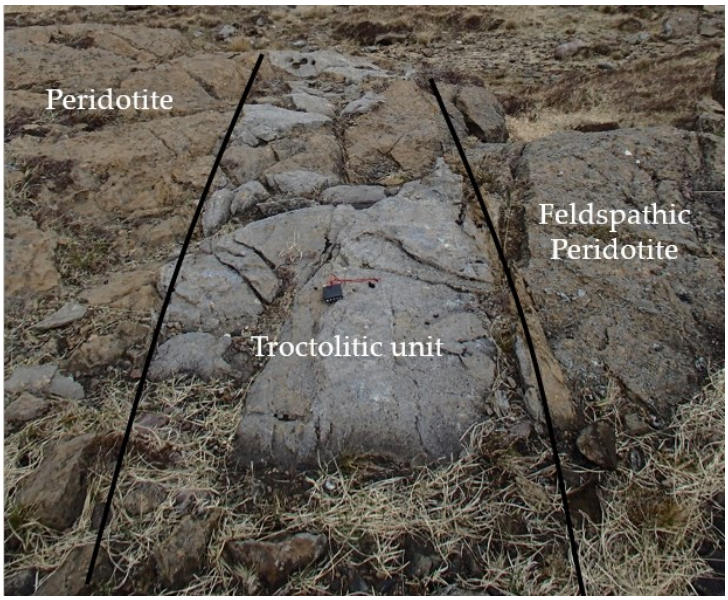

Figure 6.33 - Troctolitic unit bounded by two faults.

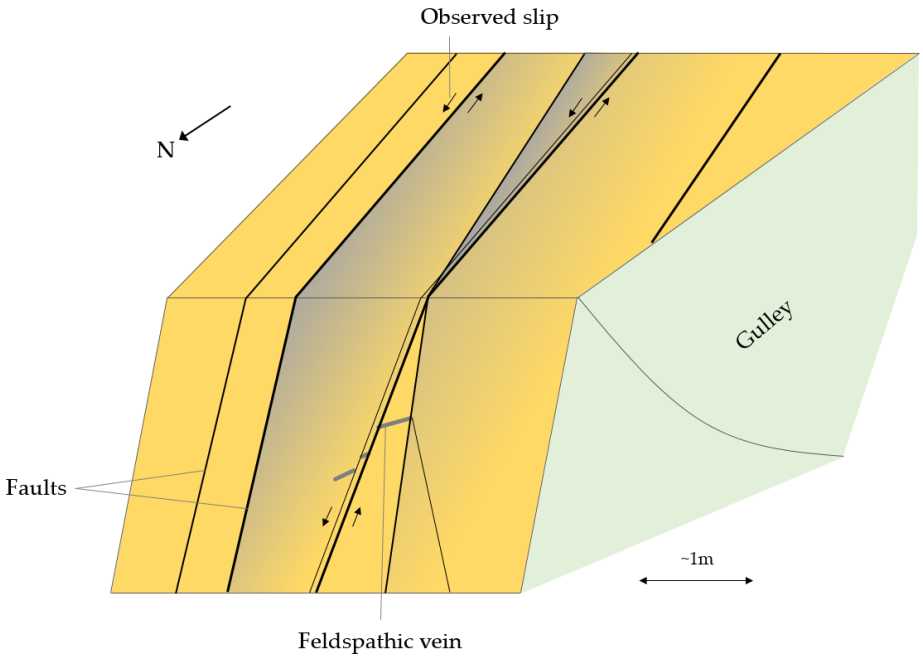

Figure 6.34 – Sketch of mapped faults intersecting transect 2. Apparent left-lateral slip is visible on the top horizontal surface. Apparent vertical-slip is visible on the north-facing vertical exposure (Figure 6.32). Orange colour indicates peridotite, however, more feldspathic units (grey) are bounded by some of the faults.

- Faulting is most intense nearest the gulley – west of the gulley there are several mapped faults, however all can be traced back into the gulley. Further

west next to the gulley bounding the western side of the central ridge there were no mappable faults. Likewise, on the eastern side of the gulley after 20-30 m there are very few mappable faults. All the outcrops of WLI peridotite, west of the intrusive breccia, were observed and fracture density was observed to decreases away from the gulley.

- Faults up to and greater than 100 m in length - all mappable faults could be traced the entire length of the outcrop with one fault of the west side of the gulley traceable for ~200 m. Fault of this length could have offset of several metres. The gulley itself is ~500 m long so it is not unreasonable to suggest there may be 10's of metres of offset on it.

Table 6.1 – Summary of the modal bin of the strikes, and mean fracture density for each transect and fractures with offset, in comparison to the strike of the main gulley.

	Modal strike bin (°)	Mean strike (°) ± σ	Mean fracture density (Fractures/m)	n
Main gulley	-	340	-	1
Transect 1	310-320	$327 \pm {}^{65}_{28}$	7.9	234
Transect 3	330-340	$332 \pm {}^{35}_{21}$	10.2	181
Transect 5	330-340	$334 \pm {}^{10}_{21}$	11.2	131
Transect 2	330-340	$345 \pm {}^{41}_{22}$	7.5	154
Transect 4	340-350	$342 \pm {}^{23}_{15}$	10.7	148
Transect 6	340-350	$341 \pm {}^{28}_{22}$	16.8	256
Left-lateral offset	330-340	$334 \pm {}^{9}_{9}$	-	49
Right-lateral offset	-	295 & 313	-	2

6.5 Lineaments on satellite imagery

A lineament is a linear feature in a landscape, which is an expression of an underlying geological structure, such as a fault. From satellite images 405 linear traces were identified within the field area (Figure 6.35), ranging in length from 10-200 m. The ultimate aim of the fieldwork was to identify if these features have any identifiable offset on them and if so how do they fit into the overall volcano-tectonic regime? It is shown from the field mapping in Figure 6.9 that very few units have mappable offset; some are just interpreted as faults from field inferences, therefore it is important to collect field data in proximity to these traces to attempt to unravel their structure.

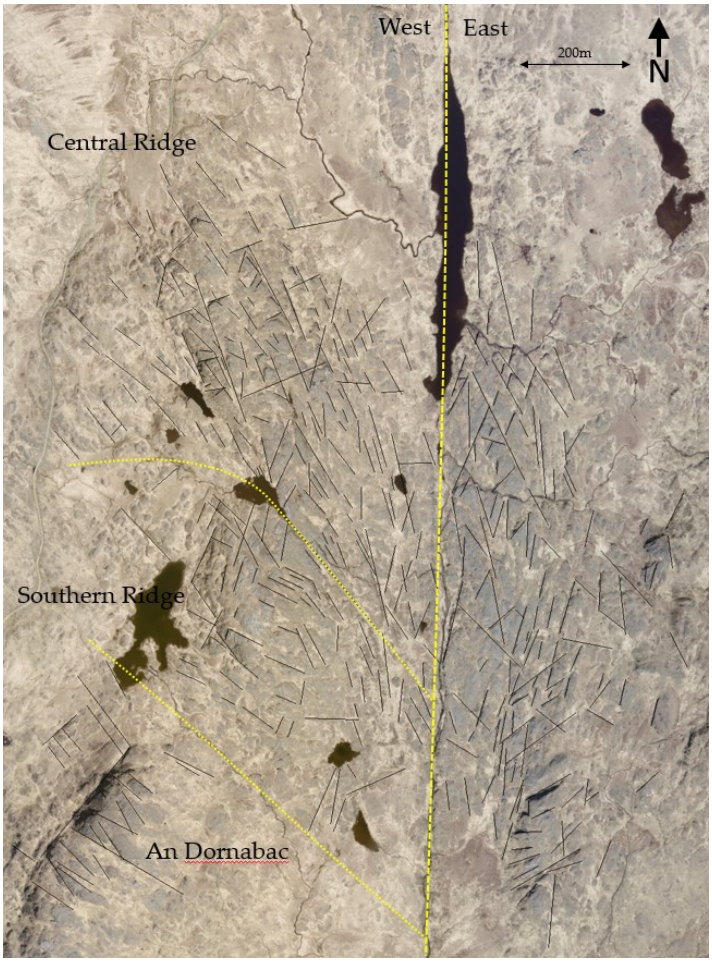

Figure 6.35 - Sattelite imagery (Bing, 2015) with 405 highlighted lineaments. The study area has been divided east and west, then the west side has been divided in 3 sub-areas; Central, Ridge, Southern Ridge and An Dornabac. Rose diagrams for these areas are shown in Figure 6.37.

6.5.1 Mattsson *et al.* 2014 study

Mattsson *et al.* (2014) produced a similar study by identifying 447 on satellite images (Figure 6.36a) and a further 71 faults/lineaments in the field and extrapolated field data (Figure 6.36b). Three main striking groups were identified from the satellite image analysis: i) NW-SE, ii) NNE-SSW, and iii) NE-SW. In the field the fault splays were seen to be dipping steeply towards the LLF, giving the eastern CI the appearance of a half graben. In the western CI the splays are mainly NW-striking.

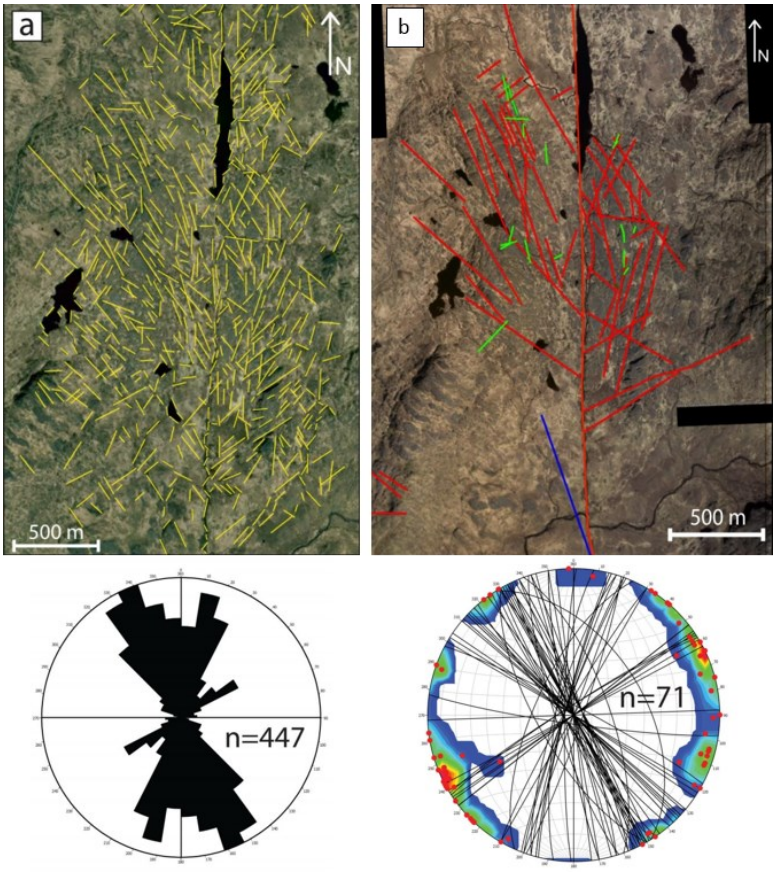

Figure 6.36 – Results from Mattsson et. al. (2014) of satellite image analysis. a) Satellite image analysis of lineaments assumed to represent fractures and faults with Rose diagram showing the strikes of the lineaments. b) Fault traces identified in the field projected onto a stereoplot.

The satellite image analysis is of the same resolution as Figure 6.35, however this study is furthered by splitting the field area into 4 zones to better understand the local structure. The interpretation of the fault lineaments in Figure 6.36b will also be

improved upon. As noted above most gulleys in the field do not offset any units so without evidence on a smaller scale to justify these interpretations, this analysis may be flawed.

6.5.2 Lineaments data

Figure 6.37 shows bi-directional rose diagram plots for: all the lineament data, east-west divisions either side of the LLF, and three divisions in the west: Central ridge, Southern ridge, and An Dornabac (Figure 6.35). The mean strike has been calculated with one standard deviation either side of the mean.

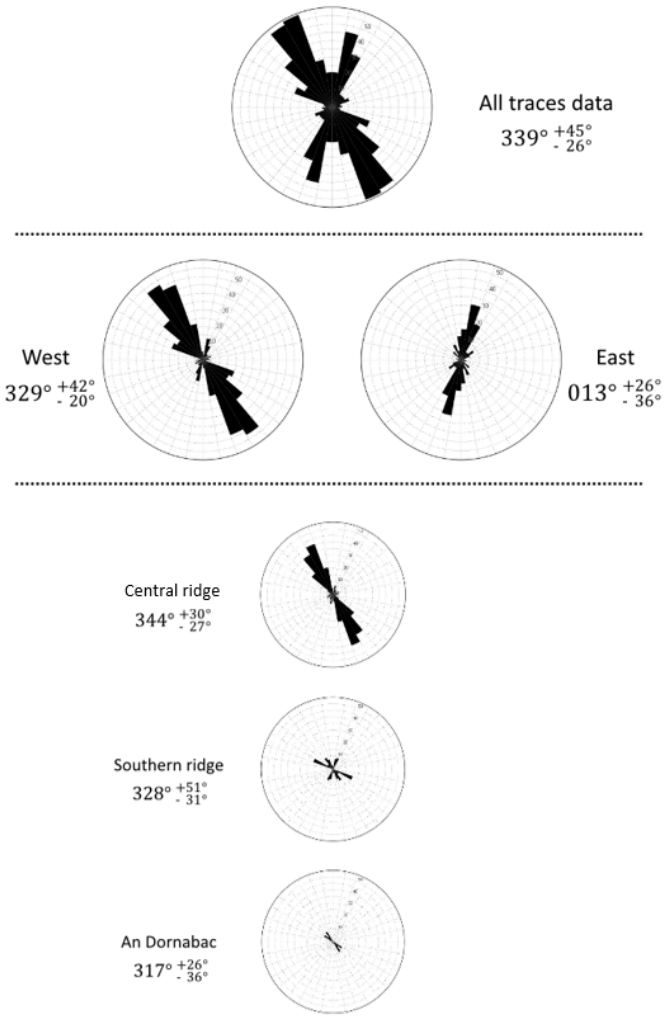

Figure 6.37 - Bi-directional rose diagram plots for all the lineament traces data, east and west divisions either side of the Long Loch Fault, three divisions in the west: Central ridge, Southern ridge and An Dornabac.

Figure 6.38 is a comparison of the data sets from the three different sampled scales: Fracture data (metres), mapped faults (10s of metres), and lineaments on satellite images in the Central Ridge zone (100s of metres).

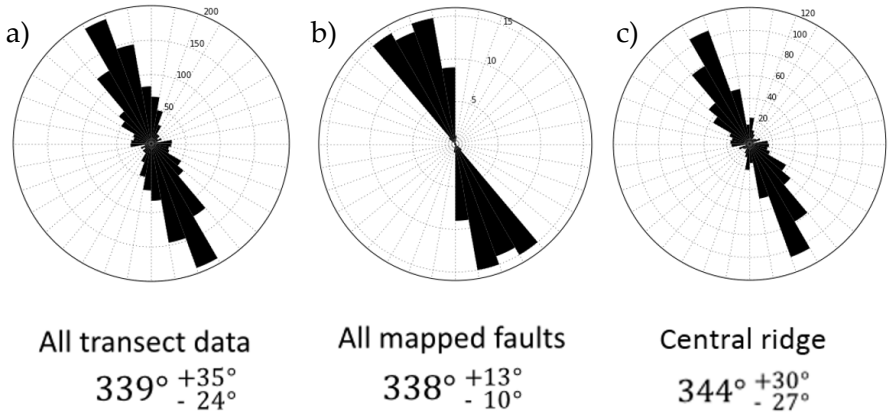

Figure 6.38 – Bi-directions rose diagrams for a) all of the fractures data from the six transects, b) all the mapped faults in Figure 6.27, and c) the Central ridge zone lineaments.

Table 6.2 summaries the scales of which the measurements in Figure 6.38 were taken as well as general comments on the observed offset.

Table 6.2 – Summary of observations for each of the three scales of measurement.

	Fractures	Mapped faults	Lineaments
Method of observation	Transects	Field mapping	Satellite imagery
Scale/ aperture width	0.5-2 mm	10-100 cm	1-10 m
Length of individual feature	observed up to 10 m	observed up to 200 m	observed up to 500 m
Observed offset	Offset observed on 51 of ~1000 fractures - 49 with left-lateral offset. Offset from mm to m scale	Offset accumulated across multiple fractures within a fault zone - typically on a metre scale	Offset not directly observed but estimated to be up to 10's of metres
Mean strike (°)	339	338	334

6.5.3 Observations from lineaments data

- For all of the trace data we find similar modal striking groups to Mattsson *et al.* (2014) bearing: NNW-SSE and NW-SE. Our data does not highlight the NE-SW groups on the same scale, however a small peak in the data is visible. When separated into East and West of Long loch these two main groups also separate.
- West of the LLF the average strike is 329° (NW-SE). There is a small group of NNE-SSW trending lineaments.
- East of Long Loch the average strike is 013° (NNE-SSW). This is similar to the faults mapped in Figure 6.23.
- Splitting the west into three zones: The Central Ridge zone has an average strike of 344°. When compared to both the mapped faults and all the transect data in Figure 6.38 all three have a very similar average strike and range of results. There are no E-W trending mapped faults decreasing the standard deviations. The southern ridge has an average strike of 328° and An Dornabac, 317°. The orientation of the lineaments becomes more westerly further south in the field area.
- Figure 6.38 shows the mean strike of the faults in the focused study area is consistent from 1 m to 100 m scale, thus it is possible to suggest that observations made in the field from the transect data can be upscaled to the lineaments. Therefore even though no discernible offset can be mapped on these lineaments we suggest that the predominant stress regime consists of a combination of left-lateral and extensional movement.

6.5.4 Strike-slip faulting

The structure formed by the satellite images captures the final active tectonic processes in the region. There is no evidence in the field for any deformation post-dating the structures in the gulley observed in the images. By reconstructing movement on the LLF, Mattsson *et al.* argue the northern central intrusion has a negative flower structure or transtensional graben that converges to the same strike-

slip fault at depth. The fractures observed in the satellite images are proposed as Riedel shears for right-lateral strike slip faulting.

Here we provide evidence showing that the observed faulting patterns cannot be explained by right-lateral trans-extension on the Long Loch Fault. I explore the alternate hypothesis that they have been formed due to subsidence within the magma chambers and reactivated by later movement on the Long Loch Fault.

6.5.4.1 Does strike-slip faulting fit?

Riedel structures consist of conjugate shear bands arranged in en-echelon arrays forming R and R'-bands that form at an angle of $\phi/2$ and $90-\phi/2$ to the general shear zone (Riedel, 1929). Figure 6.39a shows a comparison of the expected geometry of Riedel shears for a right-lateral strike-slip fault, (i.e. the Long Loch Fault) compared to the observed geometry of the lineaments and fractures proximal to the Central ridge (Figure 6.39d). In either scenario where the lineaments are Riedel shears to the LLF, or the fractures are Riedel shear to the lineaments; the strike of the observed shears is reflected to those required in the models, and the direction of slip is opposite to the expected geometry. Thus, Riedel shears are not a solution. The same is true for horse-tail splays (Figure 6.39b) and extensional grabens/negative flower structures (Figure 6.39c) associated with right-lateral strike-slip faults; the observed geometry and offsets are opposite.

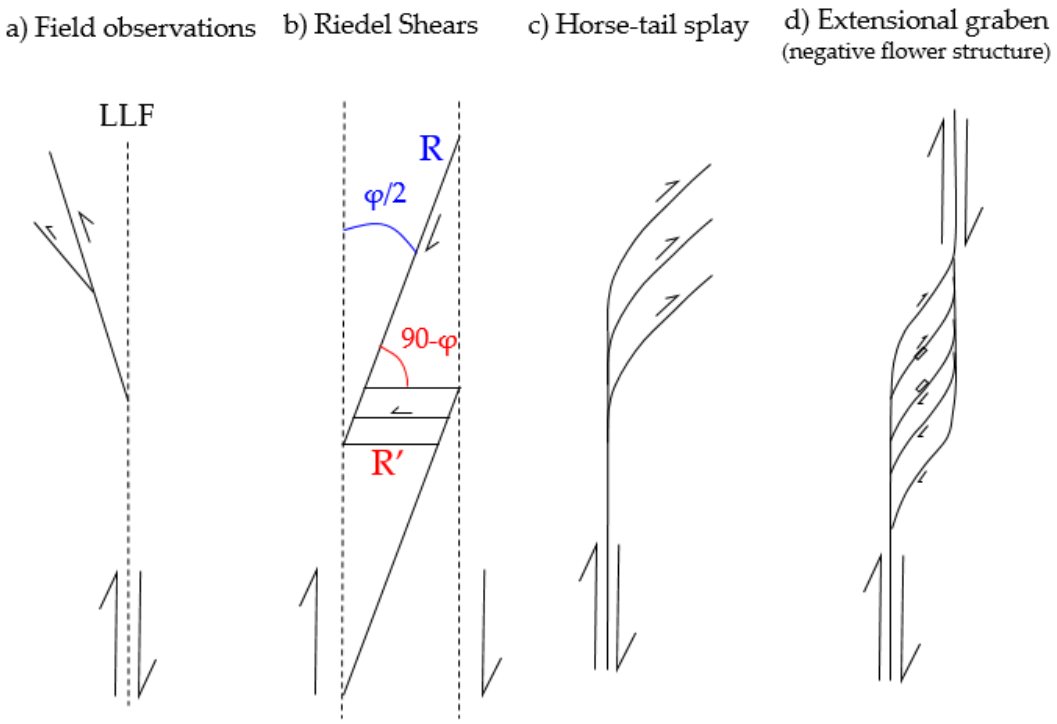

Figure 6.39 - a) Sketch of the orientation and diretion of offset of the lineaments and fractures in Figure 6.27 relative to the Long Loch Fault. The observations do not correspond to Riedel Shears of a right-lateral strike-slip fault.b) Basic Riedel shear strutcutres forming right-lateral conjugate shear zones. R and R′ and synthetic and antithetic shear bands. Φ is the angle of internal friction (Katz *et al.*, 2004). b) Horse-tail splay termination at the end of a right-lateral strike-slip fault. d) Extensional duplex or negative flower-structure form where there is an offset in the plane of the main strike-slip fault.

There are two possible alternative explanations for the observed geometry and offsets:

1) There was a period of inversion along the LLF allowing for a period of left-lateral strike-slip movement which would have allowed for the formation of the structures in Figure 6.39d – This is unlikely as there is no other field evidence for left-lateral movement of the LLF. The final offset is 800 m right-lateral. Also, if left-lateral structures have formed for a short period of inversion, why is there no evidence of a much more prolonged period of right-lateral slip?

2) The fractures and gulleys were originally formed contemporaneously during the shearing and collapse event associated with the intrusive breccia. Once the magma chamber had frozen there was then a period of right-lateral slip on the LLF, where displacement caused the reactivation of some of the major lineaments – new structures did not form typically, as in Figure 6.39a-c, as there were already planes of underlying weakness.

Scenario 2 is the preferred option. There is no evidence for left-lateral slip on the Long Loch fault itself, therefore we assume the simplest solution where there has only been right-lateral slip and no inversion. We see a lots of left-lateral slip at outcrop scale and can constrain the timings of these events to be syn-magmatic and pre- or syn-chamber collapse. By upscaling the observations made on an outcrop scale to those made with the use of the satellite images, is it probable the larger faults, hidden by the gulleys, were also formed at this time.

6.6 Summary and discussion of field data

Figure 6.40 is a simplified solid geology map showing the key units and structures of the western side of Long Loch. It clarifies the boundary between the intrusive breccia and where it flows to the east. It also highlights the major gullies that have been interpreted as faults and the direction of slip on them. A syncline has been inferred as the topographic feature into which the pebble breccia was deposited.

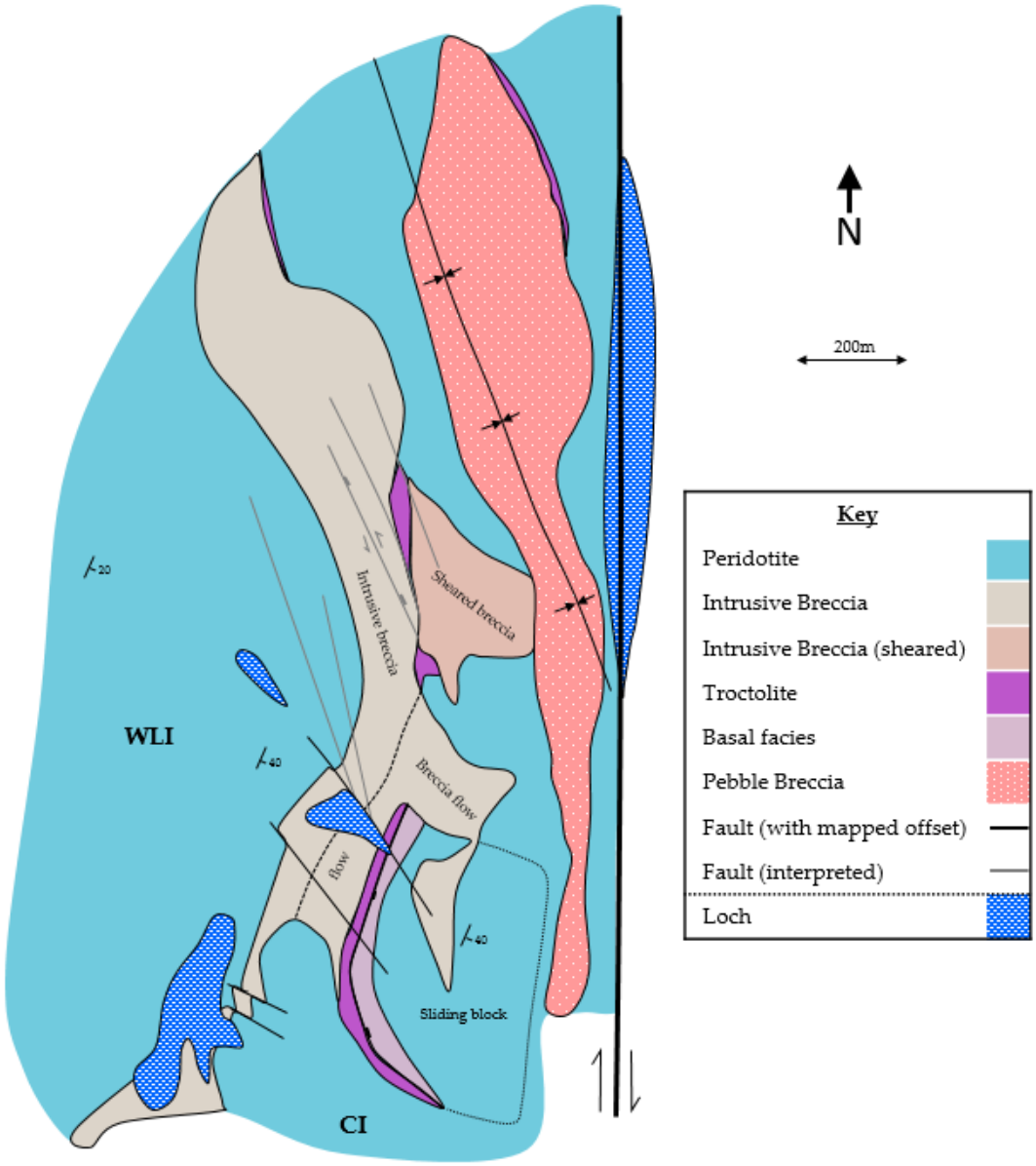

Figure 6.40 – Simplified solid geology map of west of Long Loch with key structural features.

6.6.1 West of Long Loch

The sequence of events forming units and structures observed in the field are summarised below:

1) The Western Layered Intrusion and Central Intrusion are one continuous sequence of easterly-dipping layered cumulates. Peridotite grades upwards in feldspathic content until a ~5-10 m thick layer of troctolite is deposited. On top of this is an olivine-rich peridotite.
2) Focused on the Central Ridge are faults with both left-lateral and extensional displacement being downthrown to the east pre-dating the intrusion breccia.
3) A collapse event occurs due to upward magma movement from a depth greater than the visible outcrops.
    - An intrusive breccia intrudes near-vertically into the layered cumulates. East of Central Loch the breccia flows eastward down the underlying topography.
    - Further south, a ~500 m wide block of peridotite slides eastwards along a low-angle normal fault using the troctolite as lubricated plane. These two events are visually expressed in a simplified 2D sketch in Figure 6.41.
    - Subsidence due to magma evacuation caused both extensional faulting and shearing of the troctolite to the north.
    - No fractures are present in the matrix but they can be found in the clasts, thus placing the first period of fracturing before the intrusion.

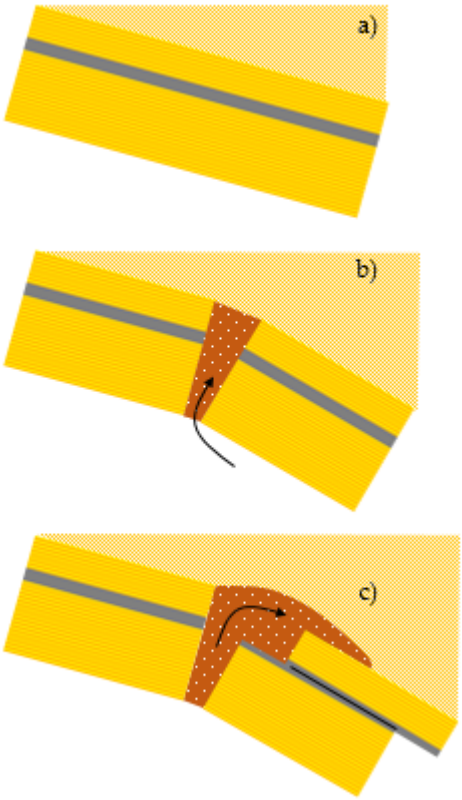

Figure 6.41 – Schematic 2D diagrams of the formation fo the intrusive breccia and peridotite siding block at the base of the active magma chamber. a) eastward dipping layered peridotite (orange) with troctolite layer (grey). b) Subsidence in the east due to magma evacuation. Intrusive breccia intrudes vertically. c) Peridotite block slides along lubricated troctolite layer. Breccia flows down over the top of the peridotite to the north.

4) Pebble breccia, formed by the settling of intra-magma chamber convection clouds, is the final magmatic deposition, within the syncline structure formed by the collapse event.
5) Magmatism ceases, all the observed units solidify.
6) Later right-lateral movement on the Long Loch Fault causes some of the large faults to reactivate. These are used preferentially as planes of existing weakness rather than forming new structures.

The unresolved question surrounding the breccia flow is whether it was a flow at the base of a crystalline magma chamber or a large lubricating layer between two

solid units? The breccia is topographically the highest unit in the area so there is no exposure of the units directly overlying the breccia. To the south, the sliding basal facies on which the sliding block is moving contains smeared layers of troctolite but not large clasts, suggesting it is not an inter-block unit. The pebble breccia at locality G is a large cumulate convection cloud deposit, onlapping the tail of the breccia, which would suggest the breccia was the uppermost solid unit when the pebble breccia was deposited.

6.6.2 East of Long Loch

- Steep westward-dipping normal faults offset the allivalite unit in many places.
- A second generation of faulting cuts these faults. Some, but not all, of these faults correspond to linear features observed on the satellite images. This generation is probably contemporaneous with the late right-lateral movement on the Long Loch Fault.

6.7 Conclusions

- Field observations on the Isle of Rum have allowed new insight into the formation of the Central Intrusion peridotites and intrusive breccias. A single collapse event occurred due to the movement of magma at a depth below current topography. The intrusive breccia forced its way up through the layered cumulate sequence then flowed eastward into a topographical low within the magma chamber. Subsidence due to magma evacuation caused both extensional and left-lateral faulting. This event also caused a large (100 m's scale) block of peridotite to slide eastward on lubricate layers of troctolite. A pebble breccia deposit, thought to be the settling of an intra-magma chamber convection cloud formed as a result of the collapse event, is found close to the Long Loch Fault at the top of the stratigraphic sequence. There is no evidence for any further magmatic activity within the magma chamber.

- Measuring fractures along six transects, three on either side of a gulley suspected to be a several hundred metres long fault, revealed offset was predominantly left-lateral and extensional, with near-vertical faults dipping eastward towards the Long Loch fault. Fracture density was most intense nearest the gulleys, diminishing in either direction away from the main gulley, showing it to be a major structure in the area. There were two families of faults identified; those parallel to the gulley striking at 347°, and to the west of the gulley a set of possible Riedel shears at 332°. On most outcrops it was not possible to quantify offset, but where offset-markers were present an offset of more than 1 m was never recorded.
- Orientations of lineaments on satellite images were measured. In the Central Ridge area containing the transects the average strike was 344°, consistent with the fracture data. Therefore it was possible to assume the structures observed in the transects could be up-scaled, and that these lineaments, present in the field as grassy gulleys, were formed under the same stress regime as the fractures. These structures are interpreted as originally being formed during the early stages of the collapse of the magma chamber. Post-volcanism these structures are reactivated during movement of the Long Loch Fault. They are used preferentially as planes of existing weakness rather than forming new structures. They are not the correct orientation of typical structures formed due to right-lateral strike slip faulting.

6.8 Acknowledgements

Andrew Bell has spent countless hours in the field with me on Rum as part of this project and his own broader study of the Central Intrusion on Rum. His help and knowledge was invaluable in piecing the puzzle together. Many thanks also go to Mark Naylor for his input in the field early on in the project.

Tobias Mattson of the Uppsala University, Sweden, produced a very useful unpublished Masters Thesis that complied much of the literature on the geological history of Rum.

Chapter 7 – Analysis of Fault Population Data in Comparison with Modern Volcanic Seismicity

7.1 Introduction

7.1.1 Rationale

In this chapter I address research question 1) and 6) from Section 2.5.1. The main aim of this chapter is to compare seismic data from an active volcano with field measurements of fault and fracture data from an extinct exhumed volcano. One way of doing this is to compare the frequency-magnitude distributions inferred for the exhumed volcano with that of a modern seismic catalogue. The inferred *b*-value can then be compared with the estimates of *b*-value already presented in Chapters 3-5. In order to do this it is necessary to estimate the magnitude of an earthquake for the faults mapped in Chapter 6. In principle this can done by using the following relationship between the subsurface rupture length R and the magnitude M (Wells and Coppersmith, 1994):

$$M = 4.38 + 1.49 \log(R) \qquad [\ 7.1\ ]$$

This relationship holds for strike-slip, normal and reverse faults. From Equation [7.1] a 1.0M earthquake would yield a subsurface rupture 5 m in length; a 2.0M would be 25m; 3.0M would be 120 m; and a 4.0M, 560 m.

From the 405 lineaments observed on the satellite imagery in Figure 6.35, the majority of the observed traces would be range from 2.0-4.0M if they were assumed to be

seismic. Indeed fractures observed in the transects described in Section 6.4.2 were often traceable for 10's of metres, making them potential sources of earthquakes of over 1.0M.

Another way of comparing the data for faults and fractures with earthquake catalogue data is to examine the spatial distribution of the fractures from the transect data, and earthquake locations from the seismic catalogue. This is done using several independent techniques, which characterises the pattern by a range of scaling exponents known as 'fractal dimensions' (Section 2.4). Spatial fractal dimensions are most sensitive to the degree of clustering in the spatial pattern. This is important because the localisation of deformation of the population of faults, fracture and the clustering of earthquake hypocentres is a key control on the potential to generate larger events, and to develop pathways for subsurface fluid flow, including magma. Here the most important fractal dimensions are the capacity dimension D_0 and the two-point correlation dimension D_2 introduced in Section 2.4.

The satellite lineaments observed on Rum are the cumulative expression of all of the deformation that has occurred within the rocks, not just events associated with active volcanism. However, the study area (the Central Intrusion) was chosen because a) it is the youngest volcanic suite (Section 2.3.3), and b) the observed outcrops are associated with one single intra-magma chamber collapse event (Section 1.1.1). There may have been post-volcanic re-activation of the large gulleys but there is no direct evidence to support this. The El Hierro the catalogue is sampled over just two years in which eight separate phases of seismicity have been identified. This is just a 'snapshot' of the deformation occurring over geological time, but it does provide an active analogue for a relatively short period of deformation as seen on Rum.

Both catalogues are limited by a finite size effect. Rum's upper limit is restricted by the finite size of the study area, and the lower limit is controlled by the sampling resolution (measuring errors). At El Hierro the minimum magnitude cut-off is controlling the lower limit. This requires the definition of power-law scaling regime

(Section 2.4.3) between a minimum and maximum length. This bandwidth is important, so this is made explicit by vertical dashed lines in all of the relevant figures in this chapter.

7.1.2 Structure of this chapter

Firstly in Section 7.2 the estimated magnitudes for the Rum lineaments data are calculated. A *b*-value is then calculated for the frequency-magnitude distribution using the techniques described in Chapter 2 and Chapter 3. In Section 7.3 1D fractal dimension analysis is performed in the Rum fracture data set discussed in Section 6.4, using the box-counting, pair-correlation and nearest neighbour techniques described in Section 2.4.4.1. In Section 1.1 the same methods are applied to the El Hierro seismic catalogue in 1D, 2D and 3D. Then in Section 7.5 the results from both data sets are compared and the intensity of clustering observed in both catalogues at all scales is interpreted.

7.2 Rum frequency-magnitude distribution

Using the lineaments from satellite data in Figure 6.35 it is possible to first show the frequency-length distribution (Figure 7.1). Then, with some assumptions listed explicitly below, and by applying Equation [7.1] it is possible to estimate a frequency-magnitude distribution (Figure 7.2) and calculate the resulting *b*-value. The small-scale data from the transect observations in Section 6.4.2 could not be used to increase the size of the catalogue as lengths of the fractures were not measured, only the spacing.

Figure 7.1a shows the frequency-length distribution for the lineaments identified by satellite observation in 25 m bins. The minimum length measured is 9 m and the maximum is 418 m. The modal bin is between 50-75 m containing 92 lineaments. Figure 7.1 shows the frequency-$\log_{10}$(length) distribution with bins of width 0.1. This is more directly related to seismic frequency-magnitude distributions, as the

magnitudes depend logarithmically on source scale. Some 95% of the data spans from 26 m to 236 m - nearly one order of magnitude.

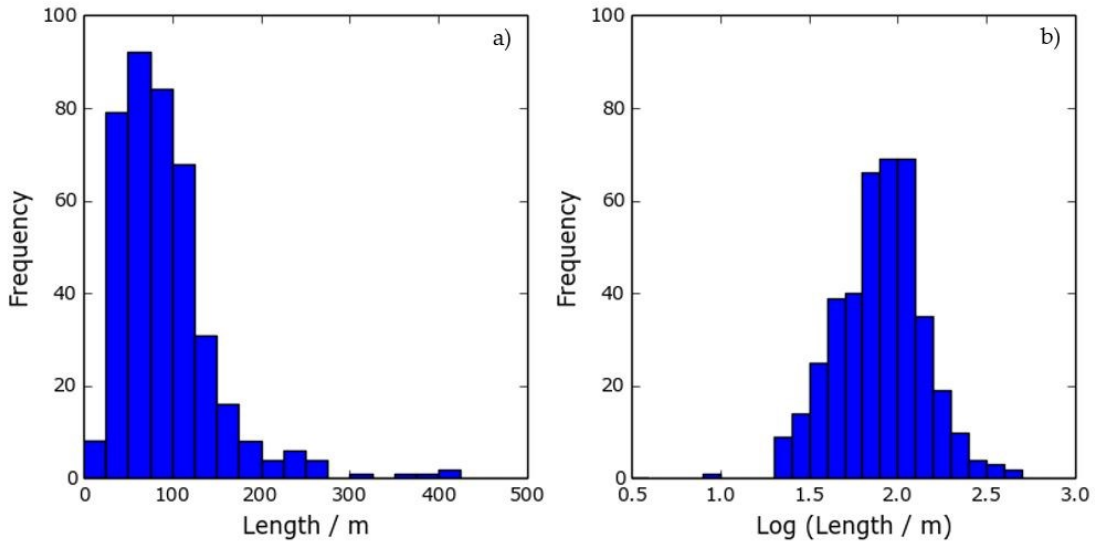

Figure 7.1 – Frequency-length distributions of the Rum lineament data. Containg 405 measurements from Figure 6.35. a) Frequency-length distribution with 25 m bin size. b) Frequency-$\log_{10}$(length) distribution with 0.1 bin size.

In order to calculate the equivalent frequency-magnitude distributions of these lineaments several assumptions need to be made:

- Each lineament is associated with a fault and is not just a topographical feature.
- The observed length of the each lineament is the total rupture length, therefore allowing Equation [7.1] to be used to calculate a magnitude for each lineament.
- The predominant fault mechanism is lateral-slip for Equation [7.1] to be applied.
- The fault ruptured along the entire observed length and any observed offset occurred in one single event.
- The underlying frequency-magnitude distribution above the completeness threshold is a Gutenberg-Richter distribution.

The first assumption is consistent with the observations detailed in Section 6.5.3. The second is the least likely to hold in general, and more complex modelling would be needed in future to examine the likely effect of any associated bias. It is possible to have a high confidence in the third assumption from the field observations, which confirm that horizontal slip (both left-lateral and extensional) is observed the transect data (Section 6.4.3). The fourth assumption implies all calculated magnitudes are maximum estimates. This assumption is not unreasonable, given the observed deformation was most likely associated with a single intra-magma chamber collapse event (Section 6.6.1). Finally, with less than one order of magnitude, it is not possible to reject the hypothesis that the underling distribution may not be a power law. This assumption is made so that it is possible to compare the frequency-magnitude distributions directly with modern seismic data, which are almost always consistent with this assumption where the data have sufficient bandwidth to make the model selection clearly (Mignan and Woessner, 2012).

Given these assumptions, the FMD for the lineaments can be created (Figure 7.2). The minimum reported magnitude is 1.32 and maximum is 3.82, giving a total bandwidth of 2.5M and a total of 405 events. From Section 3.6.3 the recommended minimum number of events in an incomplete catalogue in order to complete successful FMD analysis is 500. Although this catalogue has fewer than the recommended minimum number of events in Section 3.6.3, this is a sufficient data set to test the hypothesis that the lineaments could have produced earthquake populations similar to those observed in a modern active data, based on data from one source of field observations.

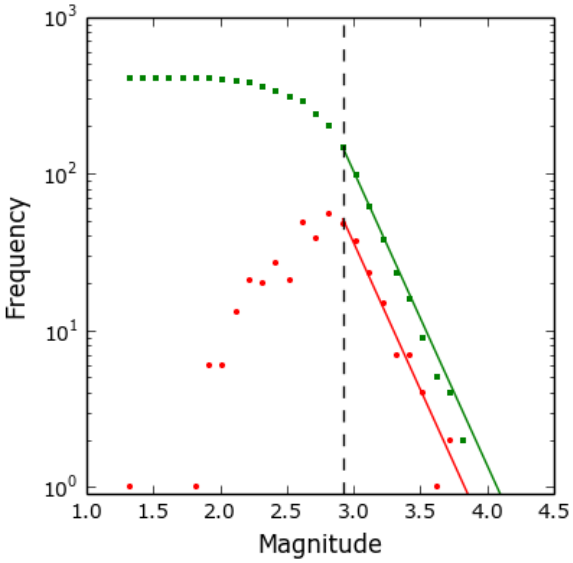

Figure 7.2 – Frequency-magnitude distribution of the estimated magnitudes of the Rum lineaments dataset in Figure 6.35. Discrete frequency is plotted in red, and cumulaltive frequency in green. The workflow in Figure 3.9 is used to calculate the completenss magnitude (vertical dashed line). The maximum likelihood estimation of b (red and green lines) is $\tilde{b} = 1.87 \pm 0.40$. Nc = 146.

From the workflow in Figure 3.9 a completeness magnitude of 2.9 is calculated. The error modification from Figure 3.11c is applied giving a resulting $\tilde{b}$-value of:

$$\tilde{b} = 1.87 \pm 0.40$$

There are 146 events in the complete catalogue, again less than the recommended 200 (Section 3.6.3), however the complete events span nearly one order of magnitude and for a high b-value, the FMD in Figure 7.2 appears to be reasonably well-defined. This $\tilde{b}$-value is higher than 1.0 within the stated uncertainty, consistent with observed results from real seismic catalogues in Table 5.4. As far as I am aware this is the first time a b-value has been successfully inferred from satellite imagery data assumed to define a fault population.

7.3 Rum fractal dimensions

7.3.1 1D fractal dimension analysis

For each of the six transects the spacing between fractures was recorded, so it is possible to apply the 1D box-counting method (the ruler method, Section 2.4.2.1) to calculate the capacity dimension D_0 (Figure 7.3 and Figure 7.4); and to apply both the 1D pair-correlation function (Figure 7.5) and the 1D nearest neighbour distribution (Figure 7.6) to calculate the correlation dimension, D_2.

7.3.1.1 Capacity dimension

As with the lineament data in the Section 7.2, there are several assumptions that need to be made in order to use the transect fracture data:

- Each transect is associated with a fault and not just a fracture or veining.
- The precision of the field measurements for fracture spacing was up to a few mm (Section 6.4.3). Accordingly an initial estimate of the minimum sample length was taken to be $10^{-2.5}$m.
- The upper limit is determined by the finite size effect, i.e. when the largest fractures exceed the size of the largest box. The initial estimate for this was taken to be the box length for a probability of occupancy of 1. The actual lower and upper limits used in calculating the correlation dimensions were set in practice using the assumption of power-law scaling in source size as defined in Section 2.4.
- At the given sampling resolution of a millimetre scale all of the fractures along the transect were measured – the spacing between each fracture is not being underestimated due to under-smapling.

Figure 7.3 shows the results of the 1D box-counting technique for all 6 transects. The number of fractures in each transect are listed in Table 7.1. There is no strong evidence for deviation from a straight line on Figure 7.3 at the smallest length scales, so no adjustment to the minimum threshold was needed.

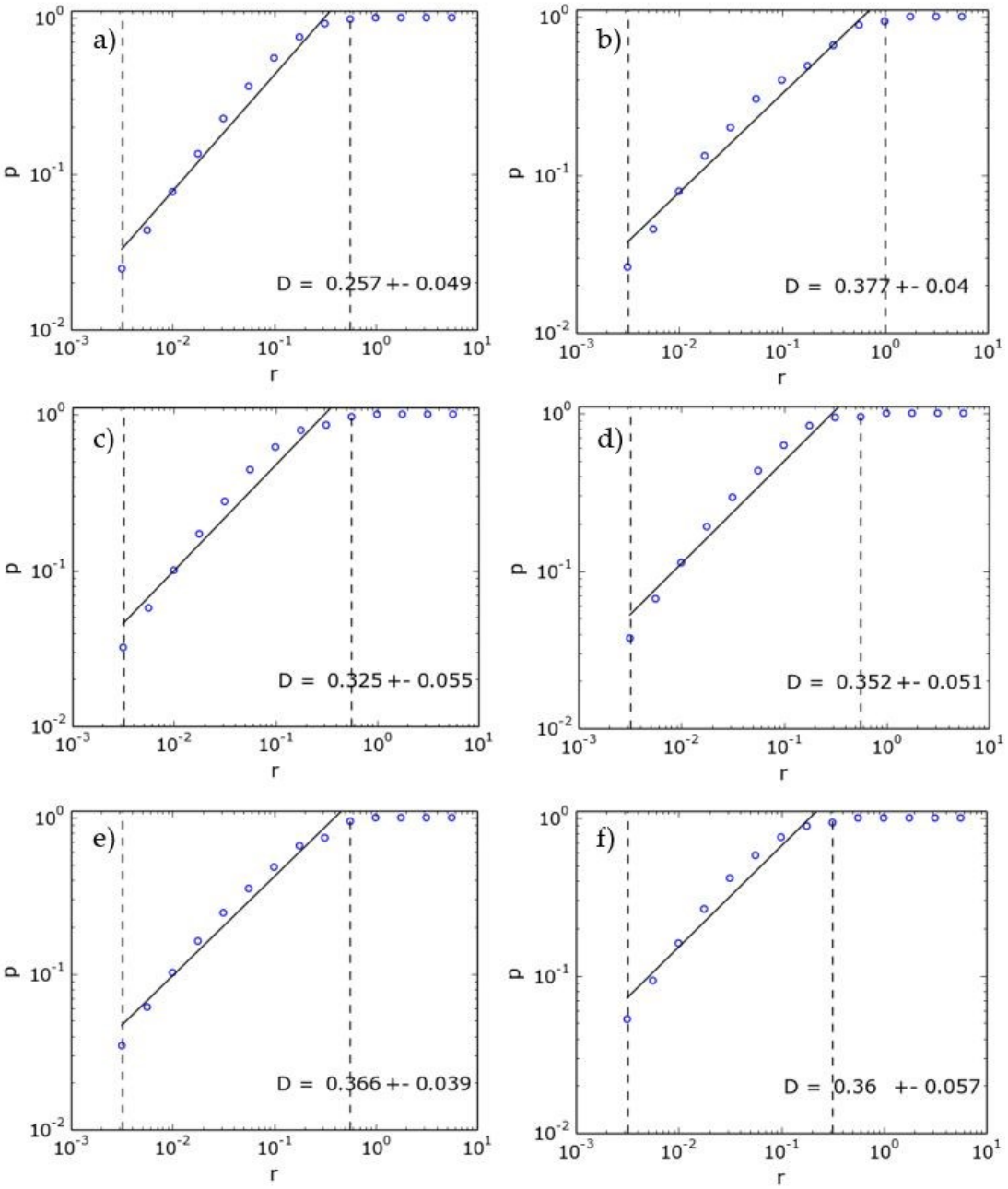

Figure 7.3 – 1D box-counting analysis of the 6 Rum transects (Section 6.4.2). The circles plot the fraction of intervals, *p*, of length *r*, that include at least one fracture. The solid line is the best-fit to a power-law distribution Equation [2.9]. In this case the fractal dimension *D* is the capacity dimension D_0.

All six transects produce similar capacity dimensions with an average of $D_0 = 0.340 \pm 0.120$. For a 1D sample the Euclidean dimension for a line is *D*=1, and for a

point D=0. For a Cantor Set D=0.6039 (Figure 2.12a), thus the fractures observed on Rum are more heavily clustered than a Cantor Set.

The data do appear to be heavily curved on Figure 7.3, especially at the larger lengths of r. There is not a clean transition from power-law distribution at p=1. This is almost certainly due to the finite size effects of sampling for large r. Accordingly, Figure 7.4 shows the distributions when a lower maximum threshold of $p \leq 0.8$ is used. The results give a systematically lower capacity dimensions with an average of $D_0 = 0.191 \pm 0.080$. This estimate of the capacity dimension may be more reliable despite the narrower bandwidth, since it avoids the finite size effect.

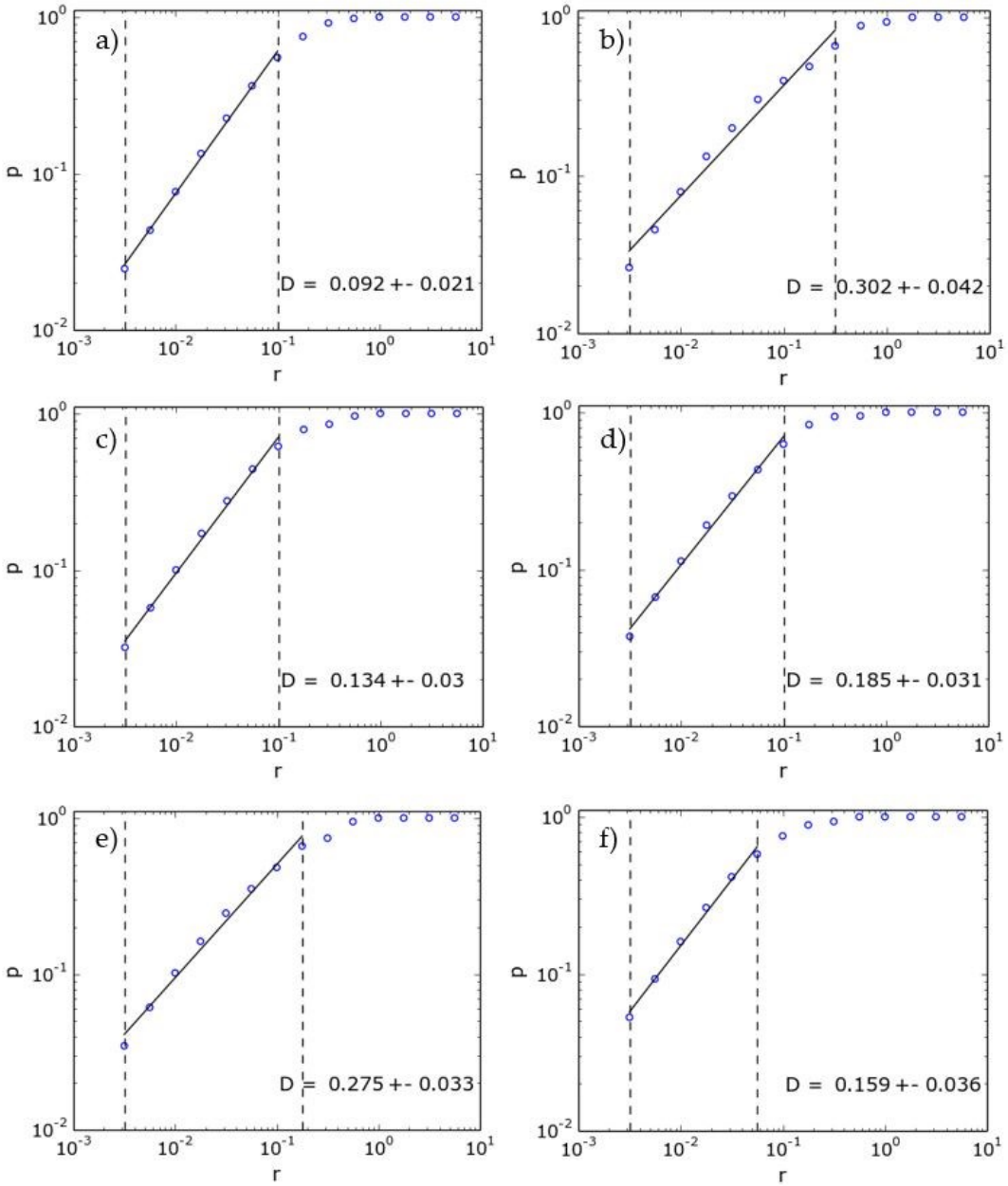

Figure 7.4 – Plots as in Figure 7.3 but with a maximum cut-off in r defined by $p \leq 0.8$ instead of $p < 1.0$.

7.3.1.2 Correlation dimension

Figure 7.5 shows the results of the pair-correlation for the six transects.

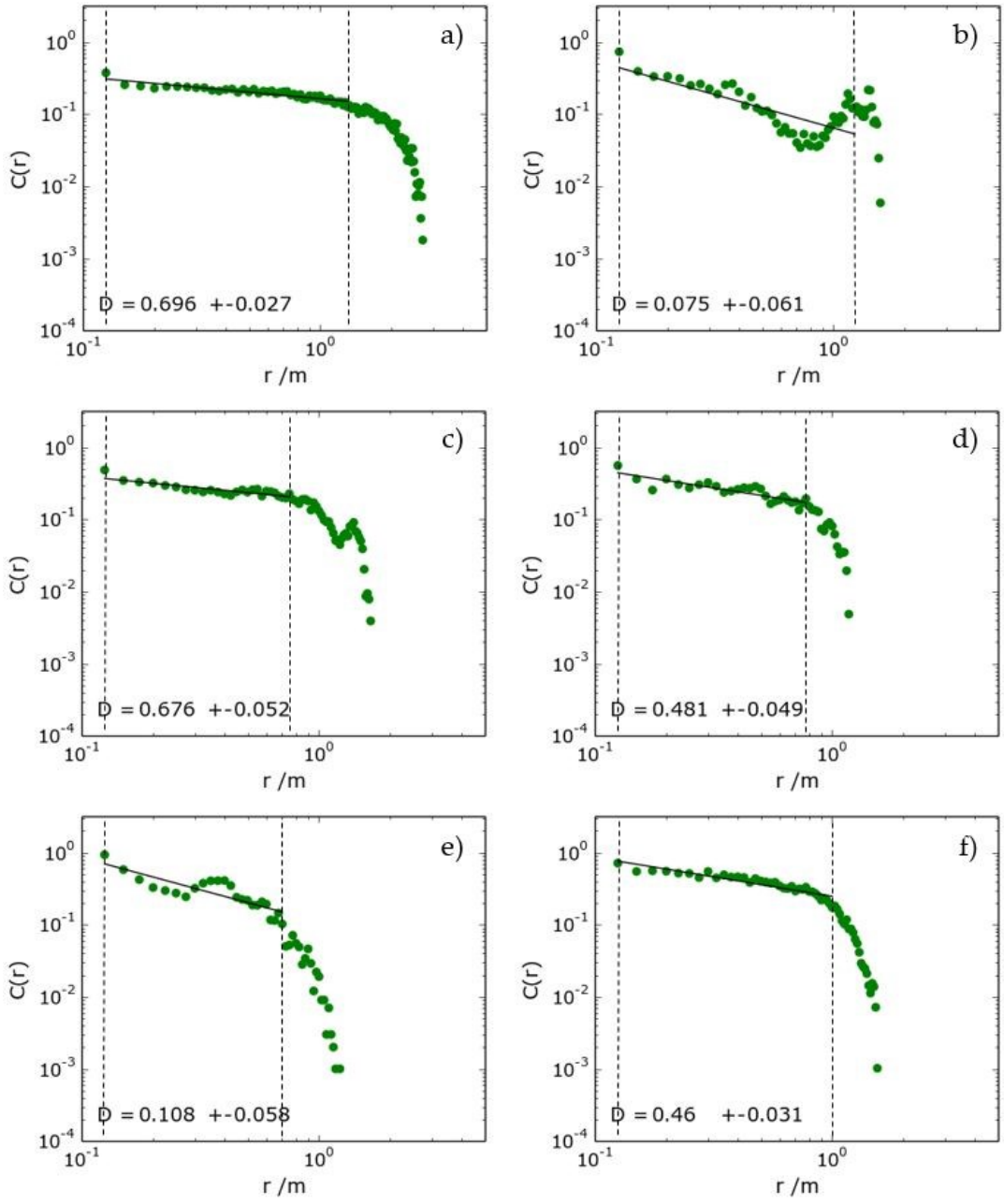

Figure 7.5 – The pair-correlation distribution, *C(r)*, as a function of spacing, *r*, for the 6 Rum transects. The solid line is the best fit correlation, described in Equation [2.14] for *r* up to half the total transect length. (vertical dashed line to the right on both diagrams).

The pair-correlation function uses the distance from every fracture to every other fracture, and does not always follow a strict power law. For transect 2 (Figure 7.5b) we observe a dip in the distribution where r=0.5-2 m. From the visual inspection in Figure 6.28b, it is clear that this is due to an absence of fractures in the middle of the transect due to lack of exposure. The roll-over at high r is again an artefact of the finite size of the sample, due to r approaching the length of the transect. For this reason the best-fit line was only used for r up to half the length of the transect, as from visual inspection this is approximately when a linear fit is still applicable.

There is a greater variation in the correlation dimensions calculated for each transect compared to the capacity dimensions inferred from Figure 7.4. Nevertheless the average value of $D_2 = 0.416 \pm 0.118$ is higher than the best estimate of the capacity dimension $D_0 = 0.191 \pm 0.080$, even allowing for the stated uncertainties. Transects 2 and 5 (Figure 7.5b and Figure 7.5e) lower this average as they both have very small values of D, indicating even more extreme clustering. This is consistent with the observation in Figure 6.28 that these two transects have visually the highest degree of clustering.

Figure 7.6 shows the nearest neighbour correlation for the six transects. These plots are based on a subset of the observations used to plot Figure 7.5.

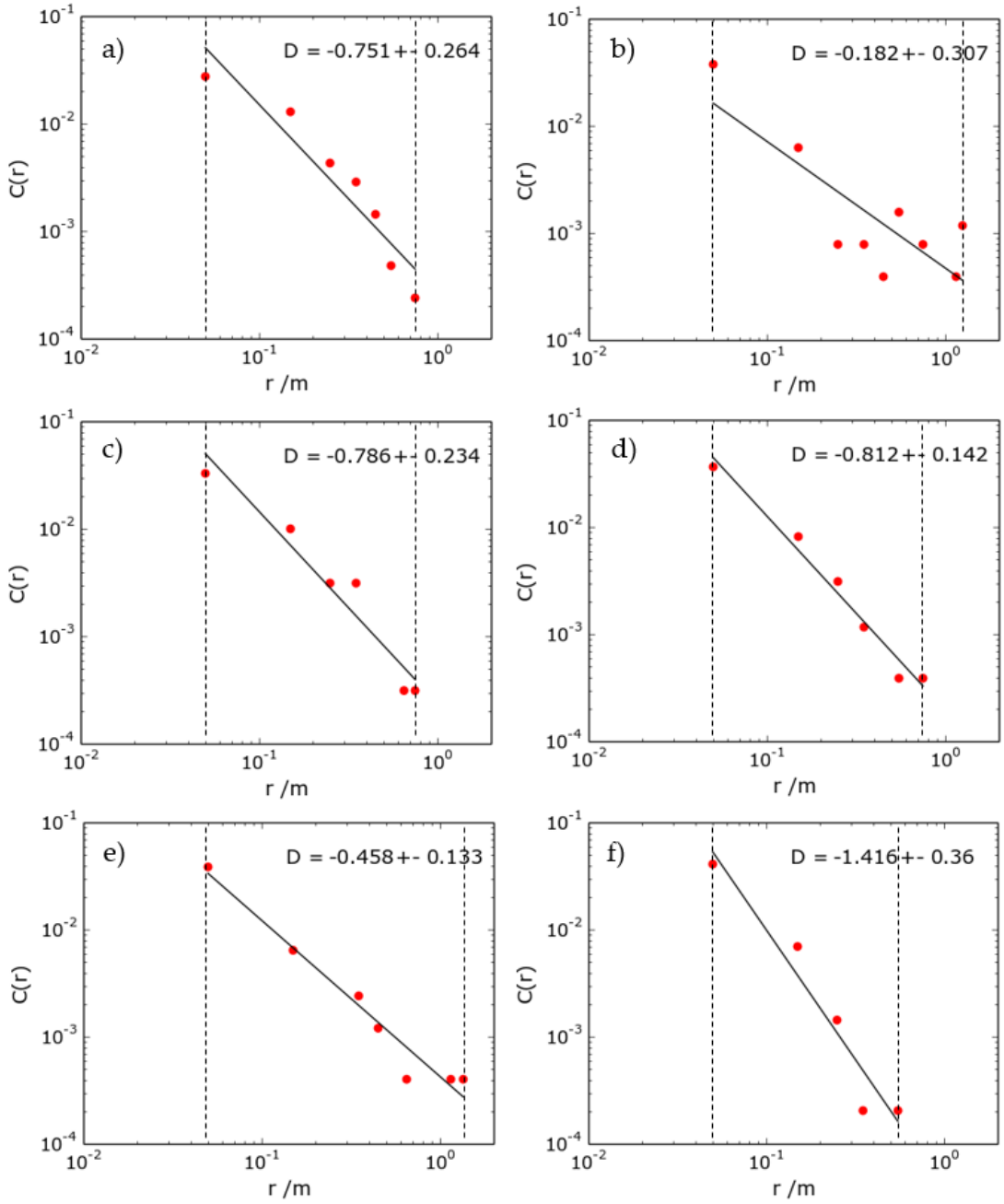

Figure 7.6 - The near neaighbour distribution, *C(r)*, as a function of spacing, *r*, for the six Rum transects. The solid line is the best fit correlation.

The analysis here is similar to that of the pair correlation function, except that only nearest-neighbour pairs are considered, i.e. the minimum distance to another fracture

on the transect. A trade-off had to be found between the size of the bins and the number of data points for all but transect 2 (Figure 7.6b) there appears to be a good fit.

Using Equation [2.18], $D = d - |gradient|$, all calculated dimensions are less than zero with an average of $D = -0.734 \pm 0.621$. As the transects are sampled in one dimension, for Equation [2.18] d=1. However as all the gradients (negative slope on Figure 7.6) are greater than one this leads to negative dimension values using the formula Equation [2.18]. This is impossible because as the Euclidean dimension of a point (the lowest possible dimension) is zero. The most likely reason for this discrepancy is that the fit is done to a reduced data set that may be heavily contaminated by the finite size effect, resulting in too steep a slope on Fig 1.3. Accordingly this dimension is not considered further.

7.3.1.3 Summary of fractal dimension analysis

The calculated fractal dimensions from Figure 7.3 to Figure 7.5 are summarised in Table 7.1. The average values for box-counting using an upper bound defined by (p<1.0) and the pair correlation both overlap within error. However, the more reliable box-counting method (p≤0.8) average is less than these two values due to the lower maximum threshold in r, that is $D_o \neq D_2$. Thus we can reject the hypothesis that the lineaments form a *mono-fractal* set, where $D_i = D_0$ for all orders i. Instead a continuous spectrum of exponents D_i, is needed, forming a *multifractal* set (Section 2.4.6).

Table 7.1 - Summary of the fractal dimensions calculated for each of the six Rum transects, using the 1D box-counting method to calculate D_0; the 1D pair collection and 1D nearest neighbour methods to calculate D_2.

	1D box-counting (p≤0.8)		1D box-counting (p<1.0)		1D pair-correlation	
	D_0	Error ±	D_0	Error ±	D_2	Error ±
Transect 1	0.092	0.021	0.257	0.049	0.696	0.027
Transect 2	0.302	0.042	0.377	0.040	0.075	0.061
Transect 3	0.134	0.030	0.325	0.055	0.108	0.058
Transect 4	0.185	0.031	0.352	0.051	0.460	0.031
Transect 5	0.275	0.033	0.366	0.039	0.676	0.052
Transect 6	0.159	0.036	0.360	0.057	0.481	0.049
Average	**0.191**	**0.080**	**0.340**	**0.120**	**0.416**	**0.118**

7.4 El Hierro fractal dimensions

Each event in the El Hierro seismic catalogue is attributed a time, magnitude, longitude, latitude and depth. In 2D and 3D space it is simple to treat each event as a point in space and apply the box-counting and pair-correlation methods to epicentre and hypocentre data respectively. However, to make direct comparisons to the Rum transect data we need to sample these in 1D transects. This is not straightforward because focal mechanisms are not available for this data set at the time of writing, so it is not possible simply to repeat the analysis of Section 7.3.1. Instead I introduce a new method of randomly-sampling all possible orientations for potential fault planes with length set by the magnitude via Equation [7.1].

7.4.1 2D ruler method sampling

In order to sample the seismic data each data point needs to be converted into a line (2D) or plane (3D). Unfortunately there are no focal mechanisms associated with this dataset so no orientations are known, therefore each event can only be approximates as a circle (2D) or sphere (3D), through which the rupture would have occurred in an unknown orientation.

Using Wells & Coppersmith's (1994) approximation for subsurface rupture length (Equation [7.1]) to be twice the radius of the circle, and the centre of the circle to be the epicentral coordinates. Figure 7.7 shows a schematic diagram of a) how a circle representing an event with no known orientation can be intersected by a transect line intersect, and b) how if the focal mechanism was known the orientation of the same fault could be modelled as a line rather than a circle. In this case the transect would not intersect the fault plane. Figure 7.8 shows how all events can be plotted as circles in 2D space.

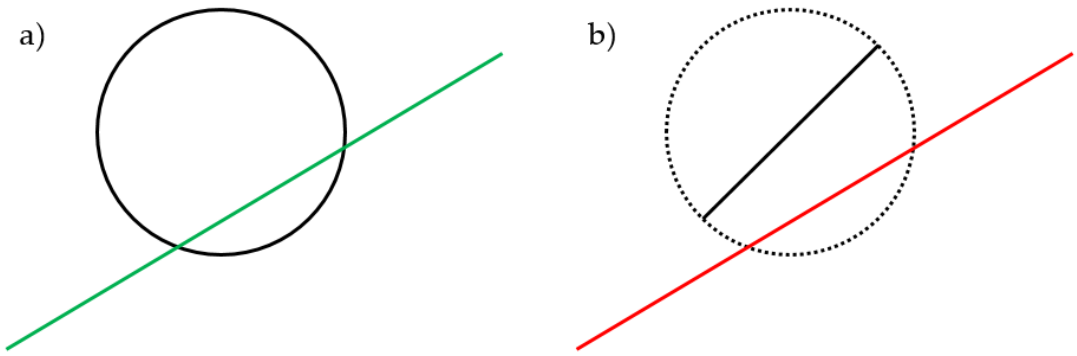

Figure 7.7 – Schematic diagrams demonstrating how the 2D ruler method is used. a) an event with a known magntude but unknown focal mechanism is represented in 2D space as a circle. The randomly orientated transect (green line) cuts the circle. b) for the same event, if the focal mechansm was known the event could be represented as a line/fault plane (red line) rather than a circle; in this example the transect would not interset the line.

Although the Rum box-counting method is considered to be one-dimensional and the data was collected along a line, the transects themselves are still a 1D sampling method in 2D space. Therefore, sampling a 2D dataset with randomly orientated 1D transect lines at El Hierro is still an equivalent comparison

One approach might be to have transects sampling evenly along lines of latitude and longitude, however this is then effectively sampling on a fixed 2D grid, which would preferentially sample faults oriented in N-S and E-W directions. Instead the transects were randomly positioned and randomly orientated, using repetitive sampling to sample their entire area equally, as illustrated in Figure 7.8. In this case each rupture length, *r*, was only sampled 50 times, and it is clear the 2D space has not been exhaustively sampled. This diagram however, allows a direct comparison with the epicentre locations for illustrative purposes. Figure 7.9 shows the coverage of the chosen values of 1000 samples for each rupture length. This confirms a more 'blanket' sampling of the possibilities, covering (and obscuring) the epicentre data almost completely.

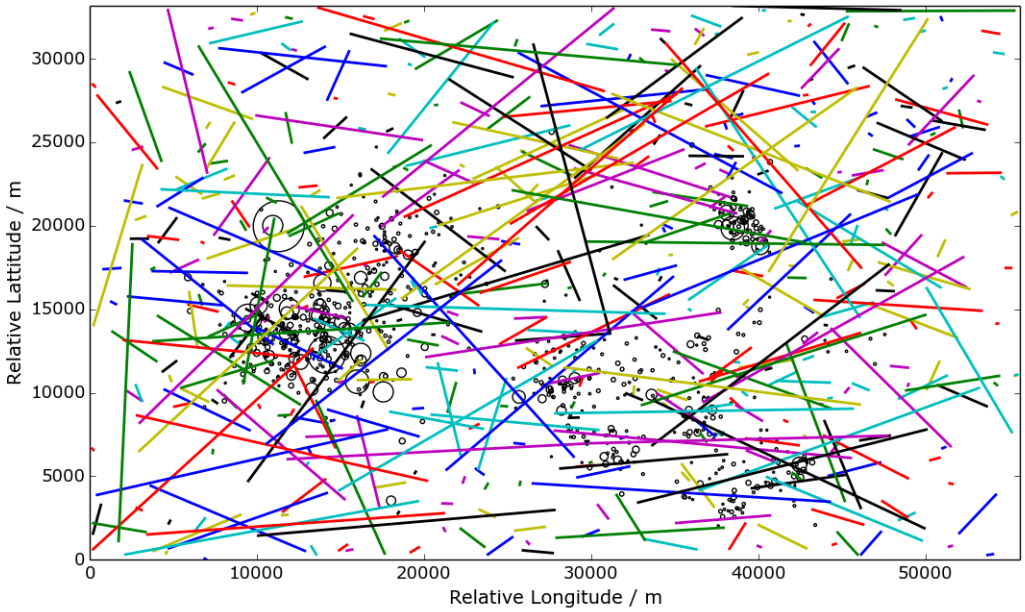

Figure 7.8 - 2D ruler method sampling of the 2011-2015 El Hierro data set. Circles represent one event with the diameter being equal to the rupture length calculated using Equation [7.1]. The minimum magnitude here is 3.0M. The lines are the randomly orientated transect lines, *r*, varying in length from 100-17783 m. There are 50 samples of each length.

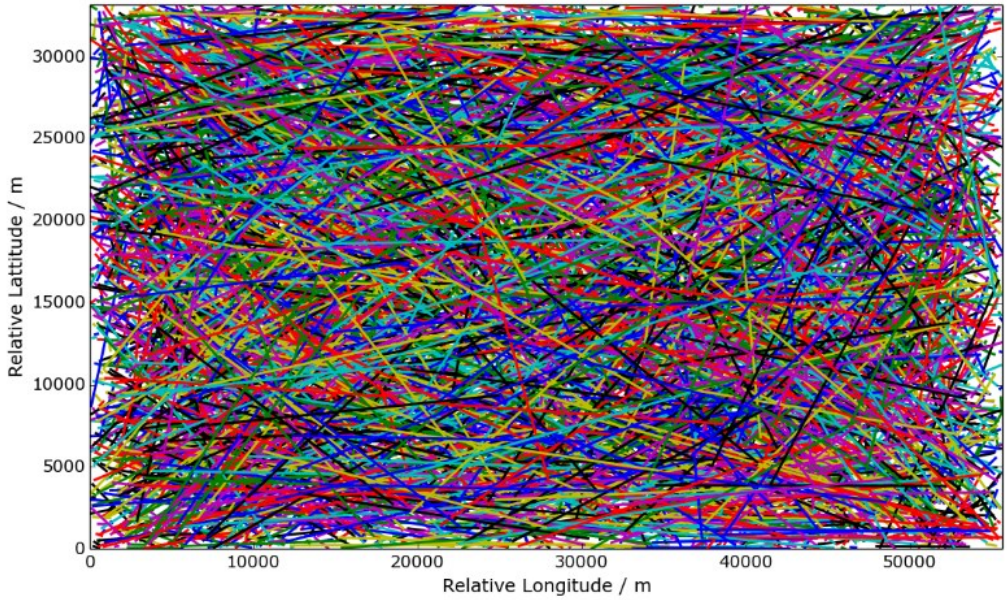

Figure 7.9 - 2D ruler method sampling of the 2011-2015 El Hierro data set. The lines are the randomly orientated transect lines, r, varying in length from 100-17783 m. There are 1000 samples of each length. This shows complete sampling of the possible fault planes.

For a transect to intersect an event it must either touch or cross a circle. When sampling the Rum data each transect was split in N segments of length r; whereas here the El Hierro data is sampled by 1000 transects each of length r. Therefore the final probability for a length of transect, r, is simply the percentage of transects intersected by at least one circle.

The minimum sampled value of r is approximately equal to the minimum rupture length: sampling beneath the lowest resolution of the data introduces bias into the data, as a transect could be contained entirely within a circle but not actually touch or cross it.

7.4.2 1D analysis results

The El Hierro catalogue is sampled from 1st July 2011 to 31st January 2015. This is a year's extension on the catalogue used in Sections 3.7, 4.4 and 5.4.1, as the analysis was performed more recently so the maximum available catalogue size was used. The catalogue is analysed using trial minimum magnitude thresholds of 2.0, 3.0 and 4.0M0 m to assess the effect of magnitude threshold in determining the fractal dimension. For the Rum transect data the 1D box-counting, pair-correlation and near neighbour correlation methods were assessed. Table 7.2 summarises the equivalent analysis for the El Hierro seismic catalogue from Figure 7.10, Figure 7.11 , and Figure 7.12. The results for M_{min}=2.0 could not be completed due to the time taken to run the code for such a large number of events.

Figure 7.10 shows the results of the 2D ruler method for the 3 different minimum magnitude thresholds. The number of fractures in each transect are shown in Table 7.2.

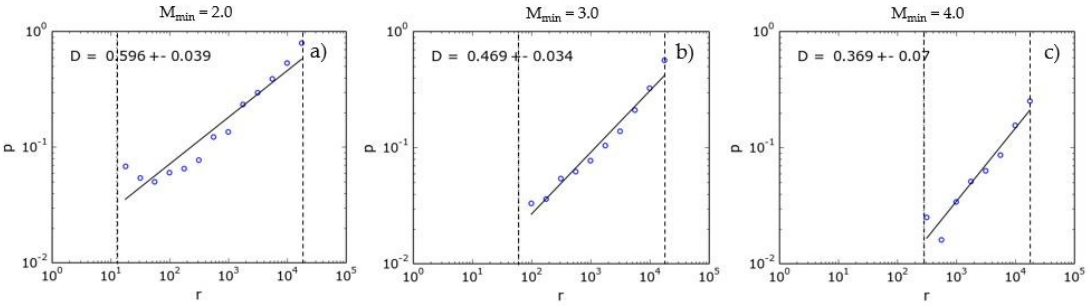

Figure 7.10 – Fraction of transects, *p*, of length *r*, that intersect an event for the 2011-15 El Hierro seismic catalogue. The circles represent the data and the solid line is the best-fit power law function described in the 'box-counting' method in Section 2.4.3. a) A mimimum magnitude of 2.0M with a minimum sampling length of *r*=18 m b) A mimimum magnitude of 3.0M with a minimum sampling length of *r*=100 m. c) A mimimum magnitude of 4.0M with a minimum sampling length of *r*=316 m. In all cases the maximum box length is 18000 m. The fractal dimensions *D* here are the capacity dimension D_0.

The results show very clear power-law trends (the straight lines fitted to the data in Figure 7.10) over up to three orders of magnitude. The average capacity dimension is $D_0 = 0.478 \pm 0.087$. The uncertainty is much less than for the field data in Table 7.1, because the number of data points is much higher and bandwidth of inferred fault length is greater. The best estimate of D_0 is somewhat higher than the values reported from Figure 7.1 but it decreases as the minimum magnitude threshold increases. This systematic error is due to the decreasing number of events and the associated reduction in bandwidth of observations in each catalogue. Even though the minimum sampling length is adjusted to some extent to allow for this, there is still an order of magnitude fewer events with each step up in minimum magnitude. The method uses 2D sampling in 1D space, so the shorter transects are just less likely to intersect an event's circle.

The lack of focal mechanisms and the resulting need for the construct in Figure 7.8 introduces another source of potential bias. In reality each event would rupture along a line not across the whole area of the circle, as shown in Figure 7.7. Accordingly there is an increase probability of a transect intersecting an event. This effect is amplified

as r deceases, as $Area \propto r^2$, therefore the gradient would increase, and from Equation [2.18] D_0 would decrease, so D_0 can be considered an upper bound.

Figure 7.11 shows the 1D pair-correlation plots. For M_{min}=3.0 the pair-correlation distribution not a power law; there are too many clusters of events through time to be able to fit one exponent, thus this value is discarded in terms of the average in Table 7.2. For M_{min}=4.0 there are two clusters in the distribution with a void of data between 50-200 days. A steeper fit could be applied to t<50, producing a lower value for D_2, however as N=44 it is decided that all the data points used. Here $D_2 = 0.764 \pm 0.045$, this is the highest value of D_2 calculated for any 1D distribution, implying relatively low levels of clustering.

Figure 7.12 shows the 1D near-neighbour distributions. The variations seen in the pair-correlation are removed by only using the nearest data point, leaving a power-law distribution for both M_{min}=3.0 & 4.0. Unfortunately for M_{min}=3.0 the gradient is greater than 1.0 meaning D_2 is negative; the data shows greater clustering than a single point. This confirms that this method can eliminate too many data points producing results that are not physically possible, as found earlier for the Rum lineament data. Again it is not considered further. For M_{min}=4.0, $D = 0.380 \pm 0.148$; this is more in line with a heavily clustered fractal set.

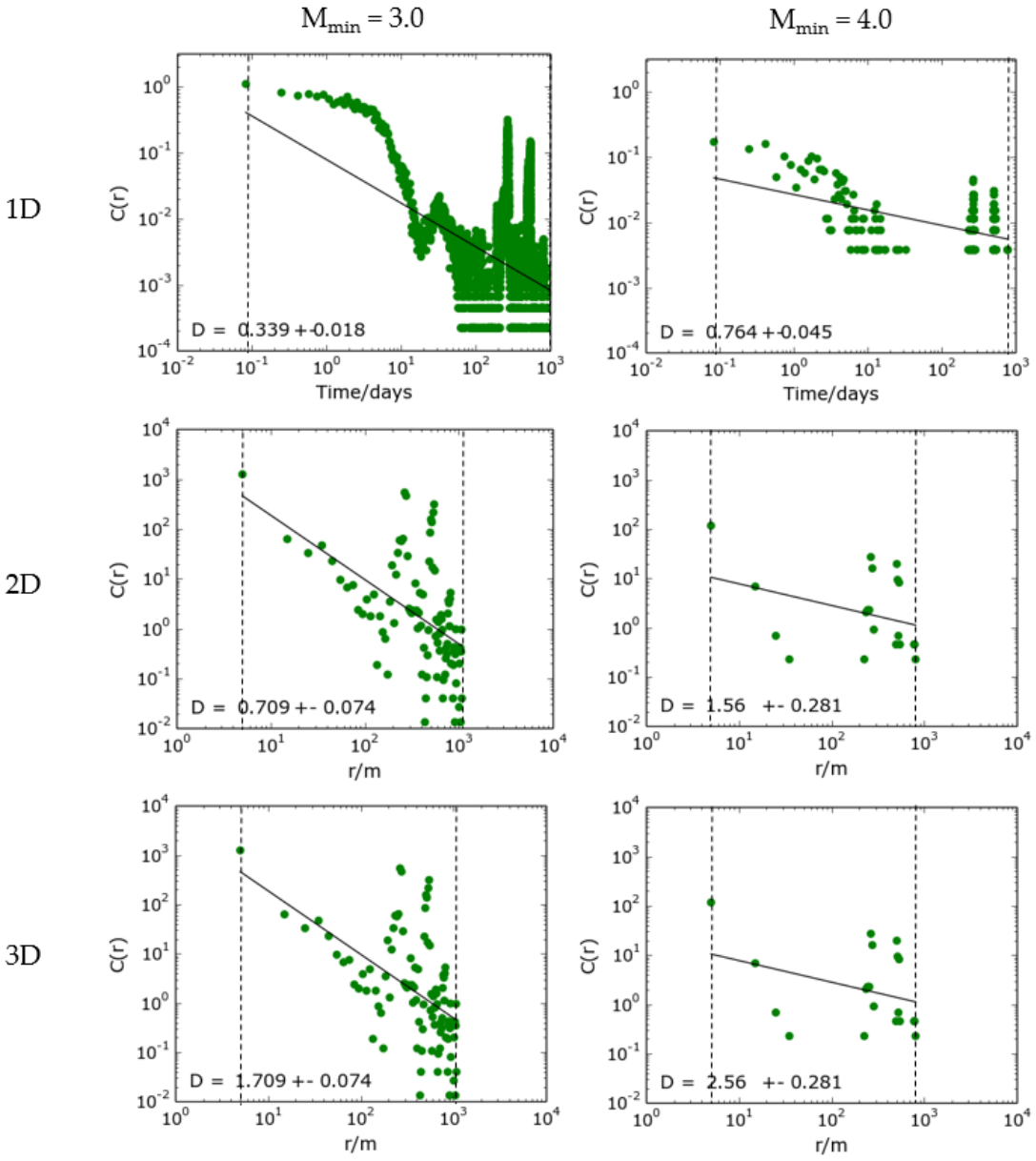

Figure 7.11 - The pair-correlation distribution, *C(r)*, as a function of spacing, *r*, for the 2011-15 El Hierro seismic catalgoue. 1D,2D and 3D distributions for M_{min}=3.0 and 4.0. The solid line is the best fit correlation function, described in Equation [2.14].

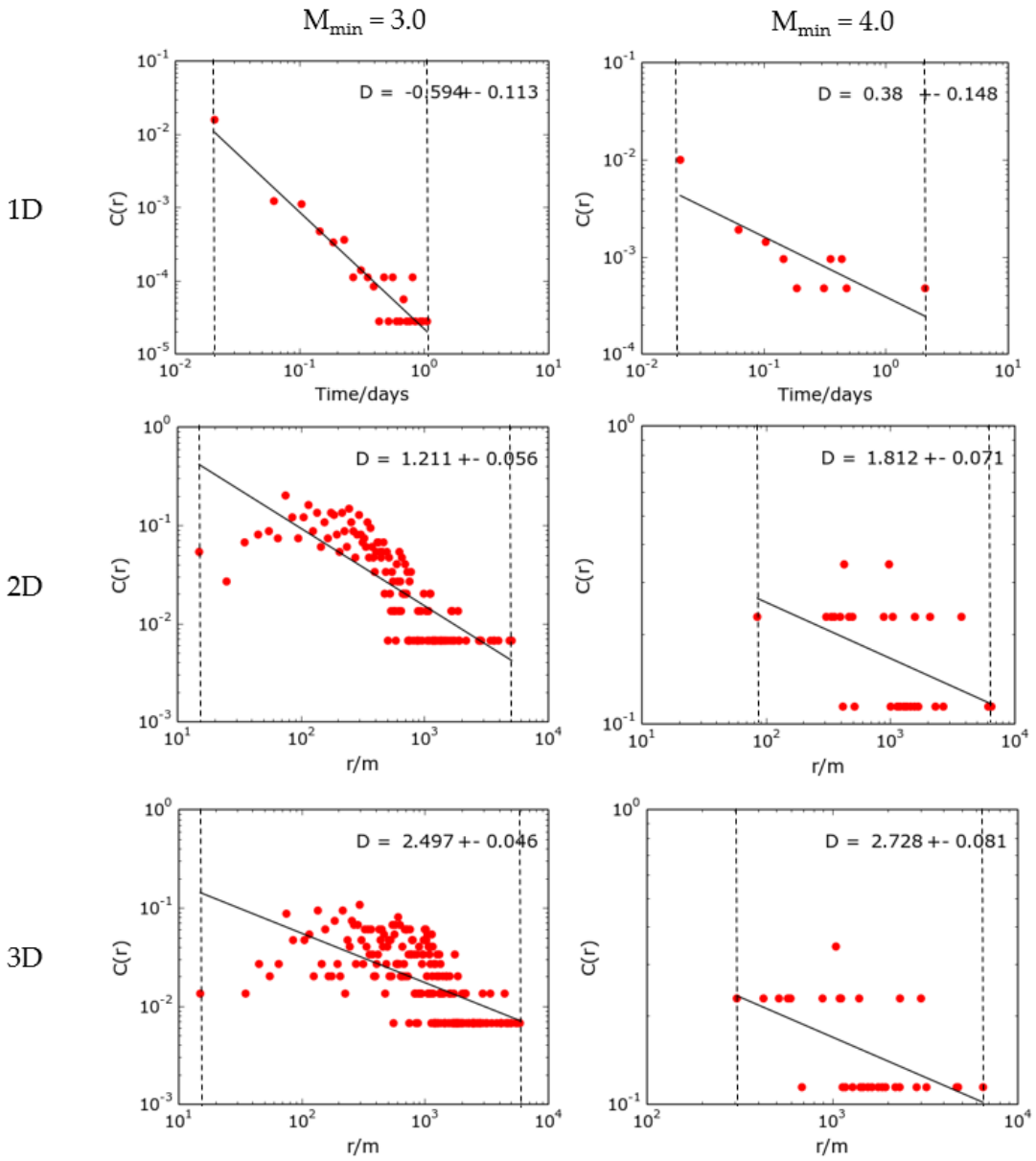

Figure 7.12 - The near neaighbour distribution, *C(r)*, as a function of spacing, *r*, for the 2011-15 El Hierro seismic catalogue. 1D, 2D and 3D distributions for M_{min}=3.0 and 4.0 The solid line is the best fit correlation.

Table 7.2 - Summary of the fractal dimensions calculated the El Hierro seismic catalogue for minimum magnitude thresholds of 2.0, 3.0 and 4.0M. The 1D box-counting method was used to calculate D_0; the 1D pair collection and 1D nearest neighbour methods to calculate D_2. Italicised values are not used in the average.

M_{min}	1D box-counting (2D ruler method)		1D pair-correlation		1D nearest neighbour		N
	D_0	Error ±	D_2	Error ±	D_2	Error ±	
2.0	0.596	0.039	-	-	-	-	6819
3.0	0.469	0.034	**0.339**	**0.018**	*-0.594*	*0.113*	752
4.0	0.369	0.070	*0.764*	*0.045*	*0.380*	*0.148*	44
Average	**0.478**	**0.087**	-	-	-	-	

For data with a similar magnitude threshold, this table confirms $D_o \neq D_2$. Again it is possible to reject the hypothesis that the population of rupture sources form a mono-fractal set.

7.4.3 2D and 3D analysis results

For completeness the location and magnitude data was also analysed in 2D & 3D. In 2D the event are still modelled as circles, in 3D they are modelled as spheres. This is not directly comparable to the 1D Rum transect data, but the results are still of interest because they might help relate the 1D results to the more general case. The results are summarised in Table 7.4.

Figure 7.13 shows the results of the 2D box-counting. As with the 1D ruler method in Figure 7.10 there is a clear power-law trend for all three minimum magnitudes. The average capacity dimension is $D_0 = 1.264 \pm 0.087$, however once again for similar reasons the capacity dimension decreases as the minimum magnitude increases. Again the low exponent indicates spatial clustering. For M_{min}=2.0, it was not possible to reduce r to equal the minimum rupture size due to the time it would have taken to run the code.

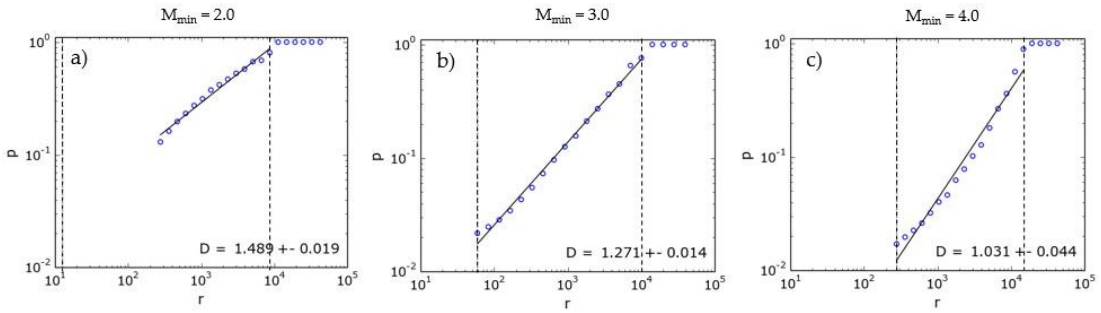

Figure 7.13 – 2D box-counting plots for the 2011-15 El Hierro seismic catlogue. The circles given the fraction of transects, *p*, of length *r*, that intersect an event. The solid line is the best-fit correlation function described in Equation [2.9]. A, b and c) with sampling thresholds as in Figure 7.10.

Figure 7.11 shows the 2D and 3D pair-correlation plots. The first thing to notice is that including the depths to use hypocentres in 3D instead of epicentres in 2D, makes negligible difference to the distributions, with D_2 simply being exactly 1 greater in 3D (Table 7.3) due to the extra dimension of sampling, as expected for a self-similar geometry of objects (Turcotte, 1997). Consequently, 3D pair-correlation results are not analysed further. For M_{min}=3.0, the 2D distribution is not as erratic as in 1D, however for r>200 m, there is next to little or no correlation between events. For *r*<200 m, the inferred value of D_2 appears to be slightly less than the best-fit of $D_2 = 0.709 \pm 0.074$. A value of D_2<1 for this 2D distribution suggests a high degree of clustered events in both dimensions, to the point where D_2 is less than the Euclidean dimension of a line (D=1). For M_{min}=4.0 there are too few events to replicate this distribution, however a value of $D_2 = 1.560 \pm 0.281$ is consistent with an intermediate degree of clustering.

Table 7.3 – Summary or 2D and 3D pair correlation results from Figure 7.11 showing with D_2 being exactly 1 greater in 3D due to the extra dimension of sampling.

	2D pair-correlation		3D pair-correlation	
	D_2	Error ±	D_2	Error ±
M_{min} = 3.0	0.709	0.074	1.709	0.074
M_{min} = 4.0	1.560	0.281	2.560	0.281

Figure 7.12 shows the 2D and 3D near neighbour plots. Here the introduction of depth does produce physically plausible values for D_2, and a degree of additional insight. For M_{min}=3.0 in 3D there is a wider scatter of data and a marginally increase percentage of low r (r<200 m) values, meaning the gradient decreases and D_2 relatively increases for the smaller events. For M_{min}=3.0 the gradient is marginally increased from 2D to 3D, however due to the lack of data points this is still likely to be within error.

Table 7.4 - Summary of the fractal dimensions calculated the El Hierro seismic catalogue for minimum magnitude thresholds of 2.0, 3.0 and 4.0M. The 2D box-counting method was used to calculate D_0; the 2D pair collection and 2D & 3D nearest neighbour methods calculated D_2. Italicised values are not used in the average.

	2D box-counting		2D pair-correlation (distance)		2D nearest neighbour (distance)		3D nearest neighbour (distance)	
	D_0	Error ±	D_2	Error ±	D_2	Error ±	D_2	Error ±
M_{min} = 2.0	1.489	0.019	-	-	-	-	-	-
M_{min} = 3.0	1.271	0.019	*0.709*	*0.074*	1.211	0.056	2.497	0.046
M_{min} = 4.0	1.031	0.044	**1.560**	**0.281**	1.812	0.071	2.728	0.081
Average	**1.264**	**0.052**	-	-	**1.512**	**0.090**	**2.613**	**0.093**

For the box-counting method increasing M_{min} decreases D_0 (Table 7.4). The opposite is the case for the pair-correlation and near neighbour methods. This appears to be due to the shape of the distribution for M_{min}=3.0. For r>200 m the scatter of the data is greater and the trends are different to r<200 m. For M_{min}=4.0 the reduction in data points means this threshold in the data is not visible and so the best-fit line has a shallower gradient and therefore higher D_0.

In summary, given the broader bandwidth of the data, we can be more confident the underlying distributions are power-law, and hence form a fractal set. The data from Table 7.4 confirm that the difference between the Euclidean sampling dimension d and the correlation dimension D_2 is a constant within error. This implies that the

fractal set is isotropic or self-similar, rather than self-affine. They also show that the capacity and correlation dimensions are not equal within the stated error for similar magnitude thresholds. Thus again we can reject the hypothesis that the source ruptures form a mono-fractal set, and that the underlying spectrum of dimensions forms a multifractal set.

7.5 Comparison of Rum and El Hierro fractal dimensions

Figure 7.14 shows graphically all the data points from the Rum transects and the El Hierro seismic catalogue for each of the three methods: box-counting (blue) and pair-correlation (green) analysis. The Rum fracture set was only analysed in 1D, whereas it was possible to look at 2D and 3D analysis for the El Hierro data.

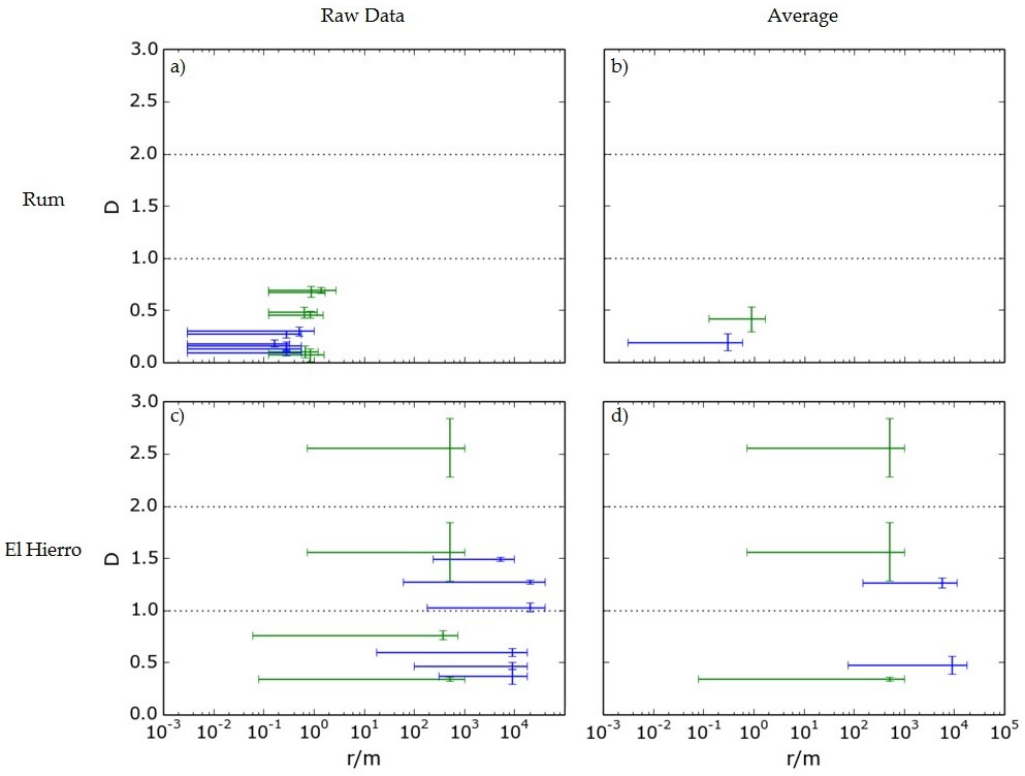

Figure 7.14 – a & c) Graphic representation of the Raw data from Table 7.1, Table 7.2 & Table 7.4 for the Rum transect data and El Hierro seismic catalogues. b & d) Average or selected values from these tables, previosuly highlighted in bold. Vertical error bars are the error calculated with the best-fit line to the distributions. Horizontal error bars show the range in *r* over which the line was fitted. The results for the box-counting method are blue and pair-correlation are green.

For Rum the minimum range the fractal dimension could be calculated over was one order of magnitude, for El Hierro it was two. The raw data for Rum (Figure 7.14a) shows a spread of results over the entire possible range of D=0 to D=1, however when the average is taken for each method, the values in Table 7.5 and illustration in Figure 7.14b, shows that $D_0 \neq D_2$ as the values do not overlap within error.

Table 7.5 - Summary of the fractal dimension from the box-counting (p<0.8) and the pair correlation methods for Rum and El Hierro. All box-counting values are averages. The pair-correlation value for Rum is an average but the two values for El Hierro are deemed to be the most reliable results.

	Box-counting		Pair-correlation	
	D_0	Error ±	D_2	Error ±
Rum	0.191	0.080	0.416	0.118
El Hierro 1D	0.478	0.087	0.339	0.018
El Hierro 2D	1.264	0.052	1.560	0.281

For El Hierro there are half as many raw data points on Figure 7.14 as Rum, due to only three magnitude thresholds being used. Again the raw data for El Hierro (Figure 7.14c) shows a spread of results over the majority of the possible range for each dimension, and when the average is taken for the box-counting method and compared to the most reliable pair-correlation result, the values in Table 7.5 and illustration in Figure 7.14d again show D_0 and D_2 do not overlap within error, therefore $D_0 \neq D_2$.

For the capacity dimension, in 1D the average for Rum is $D_0 = 0.191 \pm 0.080$ compared to $D_0 = 0.478 \pm 0.087$, these results do not agree within the error. However, importantly these results overlap in the scale of measurements and cover over 6 orders of magnitude from 1cm to 10,000 m scale. The results in 2D for El Hierro give $D_0 = 1.264 \pm 0.052$. Assuming a random transect through a self-similar set of objects, one might expect this to result in capacity dimensions $D_{1D} = D_{2D} - 1 =$

0.264 ± 0.052, where the inferred value is close to the value of $D_0 \approx 0.19$ of the 1D transect at Rum. This implies an almost identical degrees of clustering.

For the correlation dimension, in 1D the average for Rum is $D_2 = 0.416 \pm 0.118$ compared to $D_0 = 0.339 \pm 0.018$, these results do agree within the error. The results in 2D for El Hierro give $D_2 = 1.560 \pm 0.281$. Again assuming $D_{1D} = D_{2D} - 1 = 0.560 \pm 0.281$, which fall comfortably within error of the value at Rum where $D_2 \approx 0.42$. The correlation dimension shows a lesser degree of clustering than the correlation dimension, but for both we can imply identical degrees of clustering between the rum lineaments data in 1D and the El Hierro seismic data in 2D.

7.5.1 Interpretation

$D_0 = 0.191$ for Rum and $D_0 = 0.416$ for El Hierro both imply greater levels of clustering than a Cantor Set where $D = 0.6039$, where at each order two of three of the original segments are retained. Likewise in 2D, $D_2 = 1.264$ and $D_2 = 1.560$ show much greater clustering than a similar comparison of the Sierpinski Carpet where $D = 1.893$ (Section 2.4.1).

In Section 6.4 it was observed that, on the west side of the gulley, fractures were concentrated around fault zones with relatively little fracturing in between. Figure 7.15 shows the graphical representation of Transect 5 where we can clearly see several clusters of fractures with one predominant zone running though the centre of the transect. Although other transects in Figure 6.28 do not visually exhibit as high levels of fracturing, the consistency is shown by the values obtain by box-counting in Table 7.2, indicate this behaviour is characteristic of the fracture observed on Rum, ranging from a scale from 0.3 cm to 1 m. Above *r*=1 m the probability of sampling a fracture is 1, thus sampling at r>1 m would involve larger detailed transects of the observed fault zones and lineaments covered by the grassy gulleys.

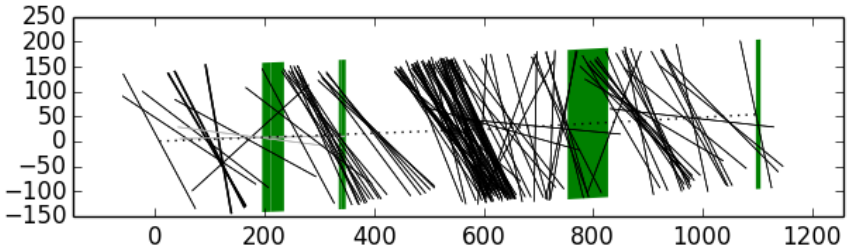

Figure 7.15 – Visual representation of fractures in Transect 5 showing high levels of clustering.

At El Hierro from 2011-15 we see several phases of seismic activity, including the eruption in 2011. In general the higher the magnitude threshold, the better the power-law fit. This makes sense as larger earthquakes happen less frequently through time as a considerable change in the local stress distribution may be needed to trigger them, e.g. mass migration of magma. For M_{min}=3.0 there are over an order of magnitude more events, and we see large variations in the pair-correlation function producing a non-linear trend. This means the events aren't correlated as a whole, they are likely to only be correlated to the event occurring in the same phase due to smaller more proximal changes in stress. Conversely the Rum fractures are the final cumulative deformation over all time, whereas the El Hierro data is just a two year 'snapshot'.

The fractures observed on Rum, assuming they have been offset laterally/vertically and are not just extensional cracks, would have likely produced 1.0-2.0M earthquakes (5-25m lateral offset), and the gulleys would have been on the order of 3. (~120 m lateral offset). This means the observations made on Rum are directly analogous to the analysis of the El Hierro seismic catalogue. From field observations it is concluded that the fractures and lineaments are associated with one magma chamber collapse event, with some of the larger structures potentially being reactivated, post-volcanic activity (Section 1.1.1). From observations of the El Hierro pair-correlation distribution we also conclude that for catalogues where M<4.0M, events are most highly correlated to other events in the concurrent phase of activity. In both cases (Rum and El Hierro data) the fractal dimension implies a high level of clustering or

localization of the deformation in both one and two dimensions, implying a high degree of stress concentration.

7.6 Conclusions

In order to compare the Rum fracture data to seismic data at active volcanoes a frequency-magnitude distribution is estimated for the deformation observed on satellite imagery at Rum. 405 events were sampled with 146 events in the complete catalogue ranging in magnitude from 2.90-3.82. The estimated $\tilde{b}$-value is 1.87 ± 0.40. This is considered a high b-value in line with other high values observed at volcanoes in Chapter 5.

Secondly, fractal analysis was performed comparing the Rum fracture data to El Hierro 2011-13 seismic catalogue. Three methods were used to calculate the fractal capacity and correlation dimensions of the Rum data using one dimensional data of the transects, and of the El Hierro catalogue by sampling in one, two, and three dimensions. For Rum $D_0 = 0.191$ and $D_2 = 1.264$, and at El Hierro $D_0 = 0.416$ and $D_2 = 1.560$. In both cases the 1D analysis produces significant differences between the capacity and correlation dimensions whereby $D_0 \neq D_2$, implying the set of rupture sources or mapped fault traces form a multifractal set. A newly developed method of sampling 1D transects randomly orientated in 2D space, and modelling each earthquake as a circle in 2D space, produced consistent but probably maximum-estimates of D. The calculated correlation dimension increases by one unit when the sampling dimension increases by one unit, implying the underlying distribution is an isotropic or self-similar multifractal set. The 2D fractal dimensions of the El Hierro catalogue is for both D_0 and D_2 are closely consistent with the 1D findings on Rum, if corrected for the sampling dimension. These values imply high levels of clustering likely to be associated with just one major phase of deformation in both cases. Broadly the scaling of fracture sets in an ancient volcano has similar properties to those observed in a modern volcano, except that the Rum data imply a greater absolute degree of spatial clustering of deformation than the modern data on El Hierro.

Chapter 8 – Discussion

8.1 Introduction

Chapters 3, 4 and 5 of this thesis primarily concern the improvement of standard practice and quantification of errors when calculating *b*-values for seismic catalogues, with specific application to volcanoes due to significance given to their reportedly high *b*-values discussed in Chapter 2. Chapter 6 describes the fieldwork undertaken at the exhumed extinct magma chamber of Rum, and the fault population data sets obtained at various scales. Chapter 7 compares the fault populations on Rum with the seismic catalogue of El Hierro, firstly by estimating a frequency-magnitude distribution of the lineaments of the Rum satellite data then by comparing the fractal dimensions of the two.

Firstly in this chapter, in Section 8.2 I discuss the implications of the results of this thesis and how they have answered the six research questions proposed in Section 2.5.1. Then following the analysis of the fault population in Chapter 7 in Section 8.3, I discuss how using focal mechanisms could be a third way to compare the Rum and El Hierro data sets, then explain how my models could be improved using seismic catalogue with known focal mechanisms (Mount Etna). Secondly, in Section 8.4 I discuss the *a priori* assumption that a power-law is the best fit for both the seismic frequency-magnitude and fractal distributions. Then in Section 8.5 I discuss the limitations in the completeness of the frequency-magnitude distribution at Rum and suggest how this completeness could be lowered using higher resolution analysis. Thirdly, in Section 8.6 I show preliminary results from my attempt at extending

analysis variations in the *b*-value from 1D sampling through time (i.e. the iterative sampling method in Chapter 4) to 2D sampling in space using my iterative Voronoi tessellation method. Finally, in Section 8.7 I propose some specific ideas for future work.

8.2 Implications of results

In Chapters 1 and 2 the current literature and conceptual framework was introduced and the key research questions were outlined (Section 2.5.1). Here I address the extent to which the results of this thesis answer these questions and what the implications are?

Question 1), "To what extent can we infer volcanic processes from properties of volcanic earthquakes?" is the broad, bigger-picture question addressed throughout the thesis. In short, this thesis has shown how direct observations from extinct volcanoes can be used to identify processes that are probably creating the earthquakes recorded today at active volcanoes. The methodologies used for *b*-value and fractal dimension analysis allow for high resolution analysis proposed here of changing characteristic of a seismic catalogue from which we can potentially infer the ongoing processes with greater understanding.

Chapters 3 and 4 address the second research question as to "whether the current methodology for calculating completeness magnitudes and *b*-values is adequate, and if not how can it be improved upon?" In Section 3.4 I synthesised the methods used in previous studies based on an extensive literature review, to calculate *Mc* and the resultant volcanic *b*-values. It was shown that there was no consistent method for calculating *Mc*. Following analysis of synthetic catalogues Figure 3.9 illustrates a workflow for calculating *Mc* that I recommend for all future analyses of seismic catalogues. Secondly, the source of error introduced by having to select *Mc* has been quantified for the first time, (Figure 3.11c). I also recommend this template is used for future analyses to obtain the total error in the estimated *b*-value. Thirdly, the new

iterative sampling method provides a less subjective and unbiased way to provide high-resolution near-real-time analysis of temporal *b*-value variations, and is able to highlight concurrent discrete clusters of events, from which it may be possible to infer the attributable volcanic process. There are still significant ways for improving the methodology, for example spatial sampling will be discussed in Section 8.6. However, in response to question 2) significant advances have been made to standardise and improve the currently methodology.

Question 3) fundamentally underpins Chapters 3-5, and indeed the title of the Roberts *et al.* (2015) paper, is "Are volcanic seismic *b*-values high, and if so when?" Using newly developed, more robust methodology, and higher resolution analysis, an in depth study of El Hierro and further case studies of eight other volcanic seismic catalogues has shown that we do indeed see high *b*-values (b>1.5) frequently, if not inherently, at volcanoes. In Chapter 5 I deliberately avoided detailed interpretation of the geological processes, in order to focus on the overall patterns in the *b*-value variations exhibited by the case studies as a whole. Therefore, the question still remains what is the cause of the high *b*-values?

Table 5.4 summarised the results from the case studies and it was concluded that although in some examples high event rates appear to be correlated with high $\tilde{b}_P$-values this is certainly not the case for every period of intense seismicity. At Bárðarbunga, Grímsvötn and Katla, high $\tilde{b}_P$-values arise from non-Gutenberg-Richter frequency-magnitude distributions. At El Hierro, Table 4.1 summarised the results from eight phases of activity with the highest $\tilde{b}_P$-values being attributed to inflation/deflation above both the upper and lower magma chambers, as well as values as high as $\tilde{b}_P$=1.5 for lateral magma intrusion. These observations suggest high *b*-values cannot be attributed to a specific volcanic process and so it is unlikely that high *b*-values can be used to 'predict' an eruption. However, in response to question 4), "How do *b*-value vary through time?", the 'mode-switching' behaviour observed using the iterative sampling method reveals changes in behaviour in the seismicity,

and so can be used to aid eruption forecasting in conjunction with further techniques, and perhaps provide additional evidence that can be considered during structured short-term hazard assessment.

Question 5), "Can studies of structural aspects of ancient volcanic systems provide insights into the processes controlling patterns of seismicity at active volcanoes?" is directly addressed in Chapter 6 using the field study area on Rum as a case study. Importantly, the fracturing structural data and field observations have allowed the timing of the deformation in the Long Loch area to be associated with a single deformation event, making the gathered lineament population directly comparable to the current seismicity observed at El Hierro. Mattsson *et al.* (2015) collected lineament orientations of the study area, however no previous structural data had been collected with the aim of constraining potential focal mechanisms or statistical measures of potential attributes of its past earthquake sources. For example, the distribution of rupture length and spatial correlations in the population at a similar resolution to the transect data collected here in Section 6.4. Rum provides a great showcase for an area that has been very well studied in the literature, and yet there are still major new observations and, particularly structurally, a lot of new data that can be used to make direct comparisons to processes occurring at active volcanoes. There are serval other volcanic centres just in the Hebridean Igneous Province (Figure 2.6), let alone worldwide, from which similar data could be collected.

Question 6), "Is it possible to compare fracture distributions at an ancient volcano to seismic frequency-magnitude distributions at an active volcano, using *b*-values and fractal dimensions?" is directly answered in Chapter 7 with the data coming from Chapter 6. In Chapter 7 it was shown using newly developed methods it is possible to infer a *b*-value from a lineament frequency-magnitude distribution and perform fractal clustering analysis, which produces results that are comparable to those calculated for similar analysis of seismic frequency-magnitude distributions at present-day active volcanoes. As will be discussed in Section 8.5, the resolution of the

field data limits the bandwidth of the results. Equally, as shown in Table 7.2, decreasing the minimum magnitude of the events used in the clustering analysis can have a significant effect of the resulting fractal dimensions.

One element of processing earthquake catalogues that has not yet been discussed is waveform relocation of hypocentres, resulting in more accurate maps of seismicity (Battaglia *et al.*, 2003; Hauksson *et al.*, 2012). The methodology used in Section 7.4 assumes no prior known orientation of events, or preferential sampling orientation of the transects. Section 8.3 introduces the potential for using focal mechanisms to improve the former. However, better earthquake locations may lead to denser clustering of events, if they occur in reality along a line, or plane. This may have major implications for the fractal dimensions obtained for the El Hierro data set as it would lower the fractal dimension. In Section 7.6 it was concluded that Rum had lower fractal dimensions than El Hierro implying a greater degree of localisation. However, with earthquake relocation (Rubin et al., 1998) this may put the results at El Hierro more directly in line with those at Rum.

Finally, question 7) is another big-picture outcome of the thesis. "Can improved understanding and analysis of FMDs lead to improved eruption forecasting?" Fundamentally this thesis has improved upon standard practice and introduced a new iterative sampling method last can provide near-real-time analysis of the most recent events, and identified a new characteristic behaviours of the *b*-value in 'mode-switching' and multi-modality that have never previously been observed. The key limitation to this, and all frequency-magnitude analysis, is the number of complete events in your catalogue, which can only be fundamentally improved upon by improving the monitoring itself to increase the completeness of the original catalogue.

There are two key strands of eruption forecasting to which this new methodology can be directly applied. Firstly, the completeness magnitude calculated through the iterative sampling method can be applied to event-rate based forecasting models. For example, Figure 8.1 (Bell et al., 2013) shows a catalogue with an increasing event rate,

with a forecast eruption time. As the increase in event rate is likely to raise the completeness magnitude (Section 2.2.2.2), current methods for calculating *Mc* are increasingly likely to be underestimate it. By calculating, then applying a continuous and varying *Mc*, the complete catalogue should be more accurately defined as the event rate increases.

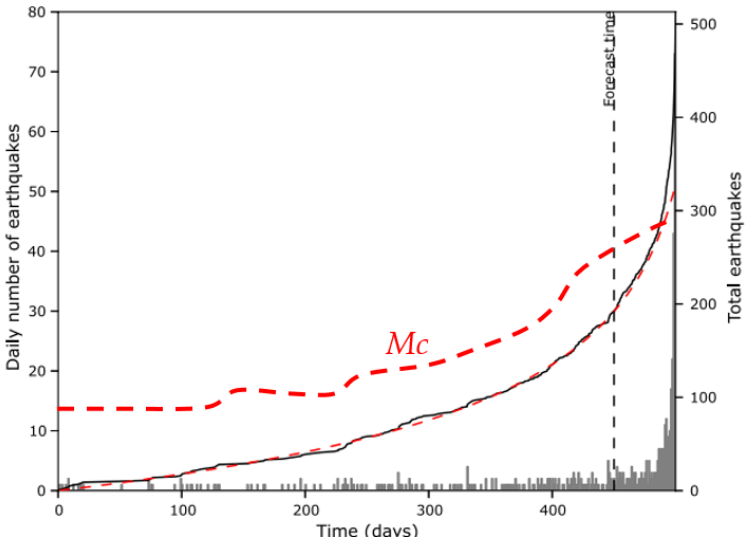

Figure 8.1 – Taken from figure 1 in Bell et al. 2013. Daily number of events (grey bars) and event rate (black line), used to forecast the eruption time. The dashed red line is a schematic illustration of the completeness magnitude *Mc*, showing how it may increase through time, as calculated using the iterative sampling technique.

Finally, the standardised workflow (Figure 3.9) and iterative sampling method can be introduced into a probability event tree used to estimate volcanic hazard (Martí et al., 2008; Marzocchi and Bebbington, 2012), as an improved method for fundamental analysis aiding decision around eruption forecasting. The operational significance of all of these improvements and suggestions is yet to be proven or otherwise.

8.3 Focal mechanisms

One of the significant omissions in Chapter 7 in comparing data from faults and fractures with earthquake catalogue data is the use of focal mechanisms. Seismic sources of earthquakes are related to local stress patterns and analysis of focal mechanisms can help understand the physical process of magma migration in active volcanic studies (Silva *et al.,* 2012; Del Fresno *et al.,* 2015). The focal mechanism of an earthquake describes the deformation in the source region in terms of areas of extensional or compressional strain. The focal mechanism is derived from a solution of the moment tensor, which is estimated from analysis of observed seismic waveforms. Knowing the focal mechanism of a specific seismic event allows us to infer the type of faulting that has caused it. Using dip and strike measurements of field exposure at extinct volcanoes (Rum) it is possible to plot stereoplot of the data from which the focal mechanism causing the deformation in that region can be calculated. By calculating focal mechanisms calculated from seismicity at active volcanoes and focal mechanisms from field observation it is possible to directly compare the two stress regimes.

8.3.1 Rum

At Rum there has not been any published data of the potential focal mechanisms that might have been associated with events around the right-lateral strike-slip fault (Long Loch Fault - LLF) assumed to have be acting as feeder for the Central Intrusion (CI) magma chamber. Mattsson *et al.* (2015) presented a stereoplot of the CI fault splay orientations identified in the field (Figure 8.2), however as the direction of displacement is not known the focal mechanism cannot be determined for this catalogue of faults.

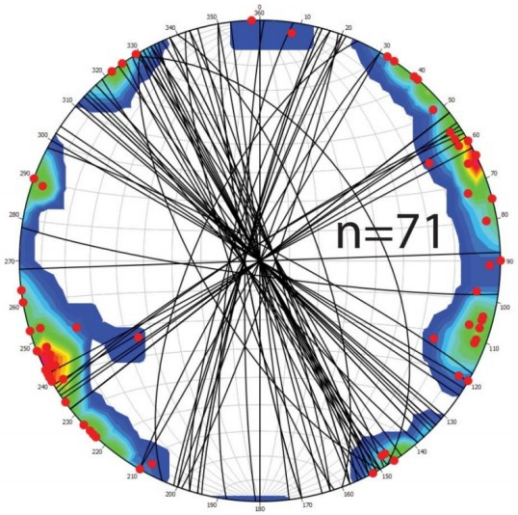

Figure 8.2 – Stereoplot of the Central Intrusion, Rum, fault splay orientations from figure 43b in Mattsson *et al.* (2015). (Equal area plot of the lower hemisphere).

In Sections 6.4 and 1.1 the results of fracture sampling and observations of lineaments in satellite imagery are presented respectively. The fractures were generally measured on a 2D horizontal surface so it was not possible to determine the dip of many of ~1000 fractures. When the dip was observable it was typically 80-90° and predominantly eastward towards the LLF. From Figure 6.31 when displacement was observed in 49 of 51 cases there was left-lateral displacement and/or vertical displacement downthrown to the east. From Figure 6.30 the average strike of the fractures was 339°.

Using these observations it is possible to estimate the associated focal mechanisms. The Long Loch Fault is assumed to be a vertically-dipping right-lateral strike-slip fault and so it would have a simple focal mechanisms as in Figure 8.3a. Figure 8.3b provides a similar plot for the left-lateral faults observed in the study area, with the average strike of 344° and an assumed vertical dip. Figure 8.3c shows the best estimate of the mapped faults with left-lateral slip combined with eastward extension and a dip of 80°.

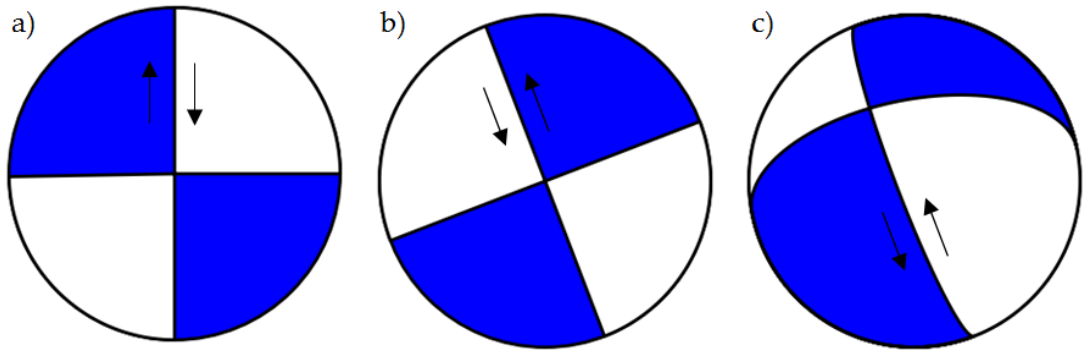

Figure 8.3 – Estimated focal mechanisms on Rum for a) The Long Loch Fault (strike = 000°, dip = 90°, rake = 180°), b) observed left-lateral strike-slip faults in the study area (strike = 339°, dip = 90°, rake = 0°), and c) transtensional faults with equal left-lateral and normal displacement, downthrow to the east with a dip of 80° (strike = 159°, dip = 80°, rake = -45°). Areas coloured blue represent those where compressional arrivals would have cut the lower focal hemisphere. Arrows indicate direction of slip and actual fault plane.

8.3.2 El Hierro

Del Fresno *et al.* (2015) have estimated the focal mechanisms for a M_w 4.0 earthquake (8 October 2011, pre-eruption) and its 34 foreshocks. The main shock (Figure 8.4b) is consistent with a pure double-couple mechanism of a strike-slip motion with a reverse component, indicating horizontal compression on a NNW-SSE direction, parallel to the southern ridge of the Island.

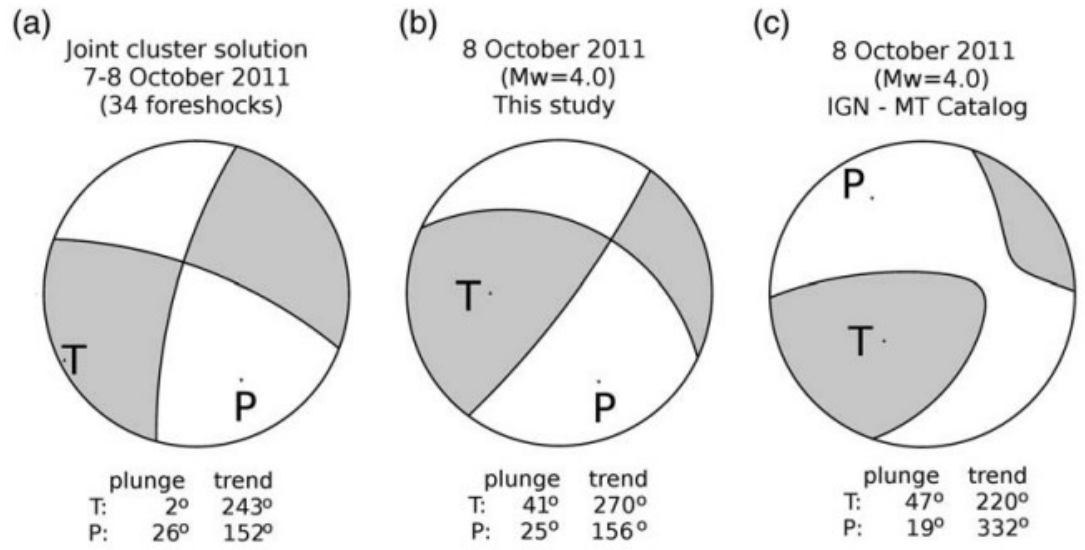

Figure 8.4 – Figure 6 from del Fresno *et al.* (2015) estimating focal mechaisms for a Mw 4.0 earthquake and its foreshocks. a) A comparison of the results obtained for the joint fault-plane solution of the whole cluster. b) The results of the M_w 4.0 obtained in their study through the amplitude spectra inversion. C) The automatic moment tensot (MT) solution of the M_w 4.0 earthquake of the real-time MT catalog of the Instituto Geografico Nacional. The annotated dots represent pressure (P-) and tension (T-) axes with the orientations described by their plunge and trend.

The focal mechanism of the foreshocks in Figure 8.4a is not generally applicable to the entire 2011-13 El Hierro catalogue as so few events are used, and as shown in Table 4.1 there is great variability in the inferred processes controlling the seismicity. The foreshock sequence occurs during Phase 2 (20/9/11 to 18/10/11 (Table 4.1)) and contains 2849 events. It would be reasonable to apply this focal mechanism to the 2D ruler sampling method in Section 7.4.1 in order to model the events as fault planes, rather than a circle/sphere in which the fault could be orientated, and then re-process the fractal dimension analysis in Section 1.1.

If the faults have a restricted case of orientation this should decrease the probability of a randomly orientated transect intersecting the fault plane, thus the fractal dimension should also decrease. This means the level of clustering may have been even greater than that previously inferred from the El Hierro data in Section 3.7.

8.3.3 Mt. Etna

Two extensive studies have been done on the focal mechanisms at Mount Etna (Scarfi *et al.*, 2013; Sicali *et al.*, 2015). Scarfi *et al.* (2015) calculated 300 focal mechanism solutions in Sicily and southern Calabria from 1999 to 2011. At Mount Etna they found different stress field at different depths due to a combination of the regional tectonics, the strong pressurization of the deep magmatic system, and the dynamics of the shallower portion of the volcano.

Sicali *et al.* (2015) studied the earthquake catalogue from November 2000 preceding the July 2001 eruption calculating 111 focal mechanism solutions. Again they showed no homogeneous kinematic pattern, although strike-slip solutions did outweigh the normal and reverse ones. The variations in the focal mechanisms may reflect spatial heterogeneity in the stress field or the presence of faults with different orientations subjected to a uniform stress field. This makes it very difficult to apply the findings directly to the 2D ruler sampling method (Section 7.4.1).

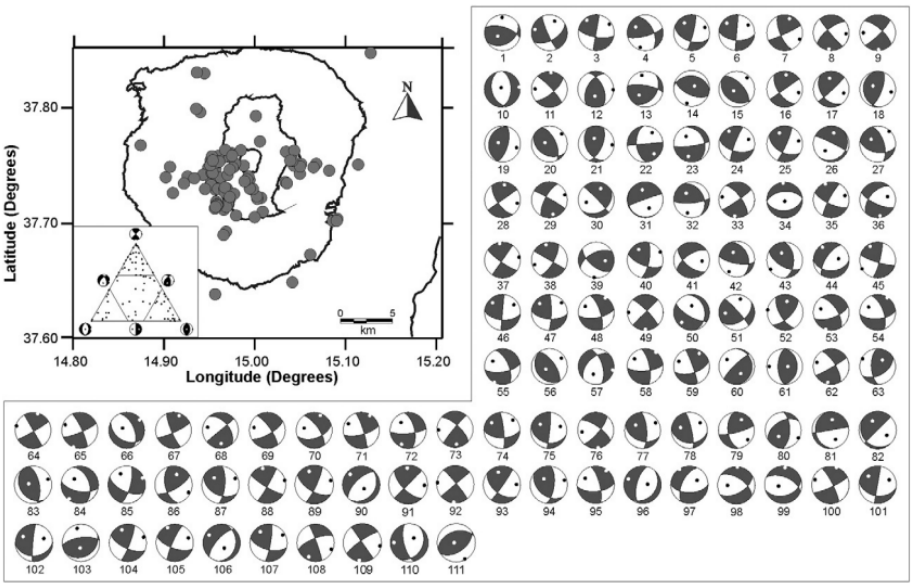

Figure 8.5 – Epicentral map distribution of the selected 111 focal mechanisms (lower hemisphere projection) and relative focal mechanisms. The inset displays the triangular diagram of focal mechanisms, where the vertices represent normal, thrust, and strike-slip focal mechanisms. The P and T axes are identified respectively by white and black dots. Figure 5 from Sicla *et al.* (2015).

However, from their findings they were also able to analyse the pressure (P-) and tension (T-) axes. They observed the P-axis pointed radially away from a unique source pressure located at the southwestern of the Central Craters, whereas the T-axis was tangential to this pressure centre. They also tested three seismogenic volumes and concluded the optimum strain tensor was a near W-E ε_1, a practically vertical ε_2, and a roughly N-S-orientated ε_3. These values are summarised in Table 8.1. Using these values is should be possible to develop a simplified model of fault orientations at Mount Etna that could in principle be applied to the fractal dimension analysis methods in future work to test their accuracy, and to correct for any bias identified above.

Table 8.1 –Dip and strike of the Maximum (σ_1 and ε_1), Intermediate (σ_2 and ε_2) and compressive (σ_3 and ε_3) stress and strain axes, at Mount Etna using data set B, from Table 2 in Sicali *et al.* (2015).

	Dip	Strike
σ_1	12	89
σ_2	65	206
σ_3	21	355
ε_1	1	87
ε_1	74	181
ε_1	16	356

8.3.4 Summary

As a general statement, the methodology for performing fractal dimension analysis in Section 1.1 could be refined and improved by introducing modelling of fault orientations using any available focal mechanism data. Insufficient data is currently available for Rum and El Hierro however it should be possible to develop a model at Mount Etna given the 111 focal mechanisms made available by Sicali *et al.* (2015)

8.4 Gutenberg-Richter law assumption

One of the main assumptions upon which nearly the entirety of this thesis is based (Chapters 3-5 and 7) is that a 'complete' seismic catalogue follows the Gutenberg-Richter (GR) relationship in Equation [1.1]. A gamma or exponential model is an alternative that fits a 'tapered'-GR model, or a characteristic 'bump' (Main, 1987) modelled by a Gaussian peak in inferred rupture length above a given magnitude threshold. Although both methods may provide a good fit, and indeed in some cases use of a Bayesian Information Criterion (Leonard *et al.*, 2001) shows the gamma fit is preferential (Main et al, 2011), it has been shown that globally (Main *et al.*, 2008) and at subduction zones (Naylor *et al.*, 2009). In this thesis (Chapters 3-5 and 7) there has not been sufficient bandwidth of data to test alternate hypotheses. For now, as is widely shown Section 5.4, the GR-law is applicable to the seismic data sets, at least as a null hypothesis that cannot be rejected.

Similarly in Chapter 7 a power law distribution is used *a priori* to determine the fractal dimension of the data sets. The influence of the finite size effect on larger values of the spacing increment r (e.g. Figure 7.4), is an example of where this distribution might not be the case. Potentially a gamma distribution would allow for the inclusion of greater values of r. This would need to be considered should further analysis of similar data sets be undertaken, although again a greater bandwidth of scales than available here would be needed to settle this question.

8.5 Fieldwork resolution limitations

In Section 7.2 the frequency-length distribution of the Rum satellite lineaments was used to approximate a frequency-magnitude distribution. The maximum estimate magnitude was 3.8 whilst the completeness magnitude was calculated as being 2.9. This is a magnitude range of 0.9, and for a high b-value of 1.9 this is very reasonable compared to results from real volcanic seismic catalogues with a similar magnitudes and bandwidths. However, using Equation [7.1] a magnitude 2.9 event corresponds

to a fault with a surface rupture length of ~100 m. The minimum length of the lineaments was 9m and in total 258 of the 404 lineaments were deemed to be below the completeness threshold. It should be possible to decrease the completeness threshold and increase the resolution at which the lineaments are sampled by higher-resolution image analysis.

One possible solution may be to use a digital elevation model (DEM) and extract lineaments from slope gradient maps (Abarca, 2006; Chen *et al.*, 2015). Using a 35 m grid size, Abarca (2006) used all lineaments down to 90 m. Chen at al. (2015) using 1 m resolution DEM to identify fine-detail in a 750 m long thrust fault. On Rum a 5 m resolution DEM is available so in theory lineaments <100 m in length should be identifiable with the implementation of effective methodology, i.e. quite compatible with the actual scale lengths of the bulk of events recorded in modern volcanic seismicity.

The satellite imagery used for Section 1.1 is 30 cm resolution and so again with the correct analytical methodology I would hope it may be possible to generate a catalogue complete to beneath 100 m in future work.

8.6 Spatial sampling of the *b*-value

The iterative sampling method developed in Chapter 4 is an improvement in the temporal sampling of the *b*-value compared to current literature. However it only gives an indication of spatial variations in *b* through multi-modality and mode-switching. Accordingly I began work on a solution to improved spatial sampling in the form of an iterative Voronoi sampling method, a short time before the results of a similar approach was published independently by Kamer and Hiemer (2015). I did not have time to fully develop and test a method that could be reliably applied to a real seismic catalogue, but the results obtained so far are presented in Appendix D as a pointer for potential future work.

The key difference between my approach and that of Kamer and Hiemer (2015) is the selection criteria. They calculated the *b*-value for the FMD of every Voronoi polygon in each iteration regardless of the number of events in the polygon, then they ranked the iterations using the BIC and stacked the best 100 or 1000 iterations. My proposed alternate method is to stack every iteration but to only include polygons that have greater than a given threshold number of incomplete events. This was done because of the importance of threshold as a source of potential bias and large amplification in uncertainty highlighted in the synthetic analysis of Figure 3.11. Figure 8.7 gives an example. Here the El Hierro seismic data set is divided into 20 sub-sets using Voronoi polygons.

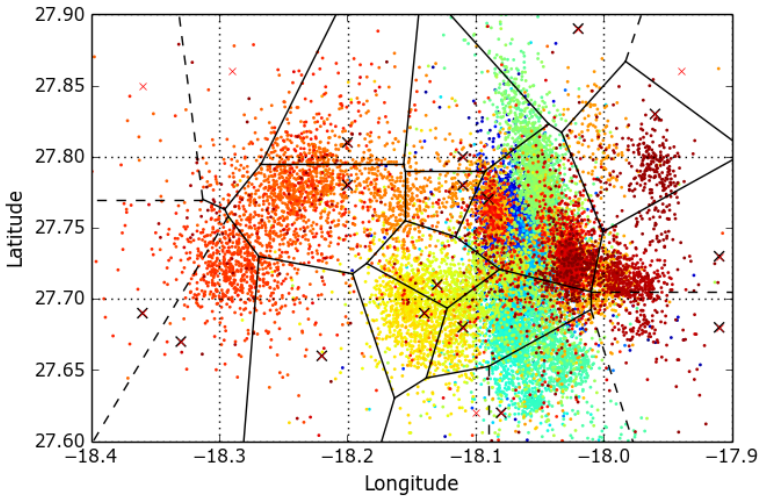

Figure 8.6 - Example of one iteration of the iterative Voronoi sampling method using 20 Voronoi polygons. Some 16 of the 20 polygons contain the minimum threshold of 100 events. The average catalogue sizes are *N*=1530 and *Nc*=236. This figure shows the position of the Voronoi polygons relative to the El Hierro seismic catalogue (coloured dots). The crosses show the randomly generated points controlling the polygons positions. Black crosses show polygons with >100 events, red crosses show rejected polygons with <100 events.

Figure 8.7 shows the results for 20 iterations of the iterative Voronoi sampling technique using a random number of polygon between 20 (Appendix D.4) and 200 (Appendix D.5). The average number of polygons created in each iteration is 114, this is in line with the expected number of 110 (i.e. $(20 + 200)/2$) through random

sampling. In total 634 polygons were accepted as they contained >100 events, meaning on average ~28% of the polygons were accepted. The average catalogue sizes are N=637, above the suggested 500 minimum, and Nc=125. Figure 8.7a shows the location of the 634 random points that defined accepted polygons. There are very few points outside the main clusters of the epicentres of the events. Figure 8.7b shows near complete data coverage except in the very NW corner of the dataset where they are nearly no events. This is a positive result as it shows the method is not spatially over-sampling the catalogue. Figure 8.7d shows the peak $P(\tilde{b}_P)$ value; after 20 iterations all of these peak values are relatively low (<0.08) compared with some of those seen after just one iteration.

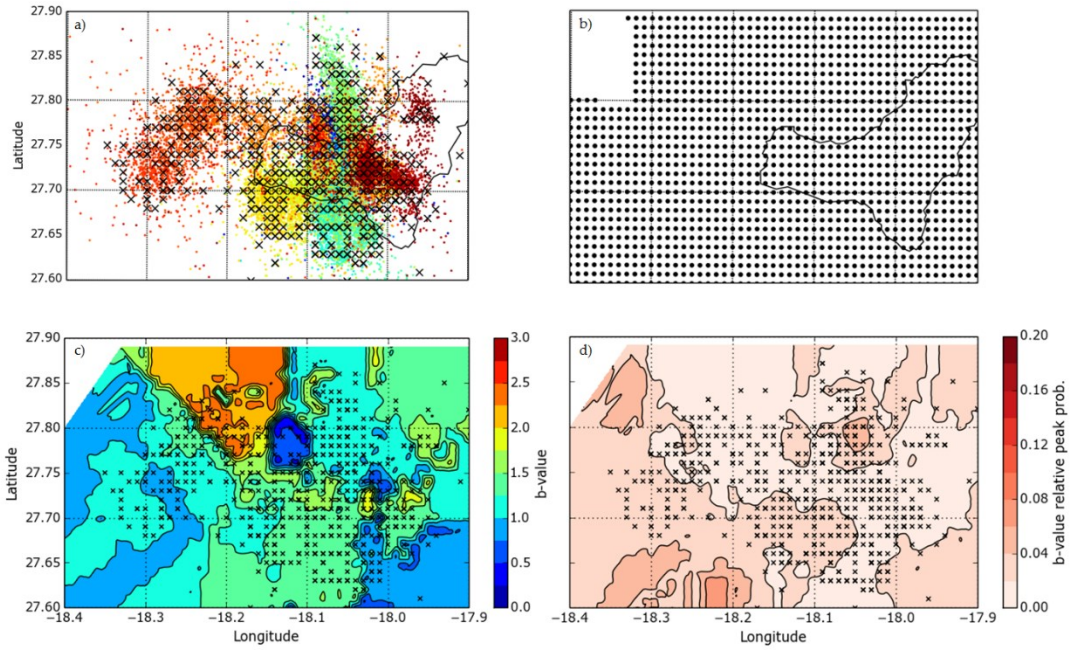

Figure 8.7 - Example of 20 iterations of the iterative Voronoi sampling method using 20-200 Voronoi polygons. In total 634 polygons were accepted. The average catalogue sizes are N=637 and Nc=125. a) Position of the Voronoi polygons relative to the El Hierro seismic catalogue (coloured dots). The crosses show the randomly generated points controlling the polygons positions. Black crosses show accepted polygons with >100 events, red crosses show rejected polygons. b) Data points within accepted polygons that have been assigned b-values. Resolution of 0.01 degrees

latitude/longitude. c) Contoured $\tilde{b}_P$-value using data points from b). d) Contoured peak $P(\tilde{b}_P)$ values using data points from b).

The next step would to be to develop a 3D iterative sampling method including variations with depth. Currently the catalogue is effectively sampled with a vertical prism with the end faces being defined by the Voronoi polygon. To extend the method to 3D, a third random point, depth, would simply be generated alongside a random longitude and latitude. The same process of attributing each event to its nearest random point, this time in 3D space rather than 2D, could then be performed. E.g. by using the computer code described in http://stackoverflow.com/questions/28267500/python-efficient-3d-voronoi-diagram-using-voxels. Such 'Voronoi Voxels' are already being used for animation in computer games (https://www.youtube.com/watch?v=_XOCjv4yF4U).

Although I have not presented any formal error analysis here due to time constraints, it would be possible to produce similar figures of the probability distribution, as in Figure 4.4 of Chapter 4, except for each spatial data point shown in Figure 8.7b, rather than for each polygon or point in time, or as depth 'slices'.

8.7 Ideas for future work

Several ideas arise naturally for future work, based on this discussion chapter and that in the main body of the thesis. A list of these tasks for recommended future work is given below, broken down into smaller elements where appropriate:

- Extend the fractal dimension analysis by:
    - Testing the effect on *D* of having randomly orientated or aligned faults in 2D space by using synthetically-generated fault populations.
    - Modelling fault orientations using focal mechanisms as described in Section 8.3 (Initially this should be achievable at Mount Etna).
- Extend the study by Schorlemmer *et al.* (2005) to data from volcanic settings (explicitly excluded in their study) using the new iterative sampling method

described in Section 4.3.2. The aim would be to see if such *b* values also vary systematically with respect to faulting style, and if so in the same systematic way, i.e. with normal faults having the highest *b*-values, thrust faults the lowest and strike-slip events with intermediate values. Such a study would require access to the focal mechanisms of volcanic seismic catalogues.

- Enhance the methods applied here and apply them to a greater range of settings by:
    - Time-frequency analysis - In catalogues such as at Katla and the Tjornes fracture zone where yearly stacking was processed as part of Section 5.4, it may be possible to take the Fourier-transform of the *b*-value time-series to ideally show there is a peak in the component frequencies at a yearly intervals.
    - Lab results – In this thesis the iterative testing method was tested on real seismic catalogues. A *b*-value analysis was also performed on the Rum field data set. No work has been done so far on application to lab results of microseismic experiments, such as those done by Main *et al.* 1996. It may also be possible to repeat the fractal clustering analysis on lab experiments to increase the range over which observations are made in Figure 7.14, in the comparison with the results obtained in Rum and El Hierro.
    - Sub-dividing the seismic catalogues by type of event: volcano-tectonic (high frequency or 'a'-type) associated with faulting due to magma propagation; Long period ('b'-type) believed to be associated with increased gas pressure in the volcanic plumbing system; harmonic tremor that results from pressurisation of magma; and explosive earthquakes that accompany many eruptions, often characterised by an air-shock phase. In my analysis through this thesis the entire catalogue has been used regardless of event type. Sub-dividing the catalogues may reveal different behaviour of the *b*-value through the progressive stages of an eruption.

- Continue developing the 2D and 3D iterative Voronoi sampling method discussed in Section 8.6. Other applications to improve the spatial sampling may be:
    - To apply the workflow for calculating the completeness magnitude in Figure 3.9 to the penalized-likelihood method proposed by Hamer and Kiemer (2014), and to compare the results to my un-penalised method with a finite threshold of events sampled.
    - Implement a partitioning algorithm using adaptive clustering (Scitovski and Scitovski, 2013; Morales-Esteban *et al.*, 2014), instead of random Voronoi sampling.
- Decrease the completeness magnitude of the estimated Rum frequency-magnitude distribution to beneath 100 m, using software to identify lineaments in 5m-resolution DEM and/or 30cm-resolution satellite imagery. This would help to show whether the high inferred *b*-value on Rum is real, or whether it is just an artefact of under-sampling.

Chapter 9 – Conclusions

9.1 New methodologies for calculating *b*-values

- A literature review of past studies of volcanic *b*-value revealed that sample sizes are commonly very small, and that there is no standard method of inferring the completeness magnitude, *Mc*.
- Of three common methods the *b*-value stability method was found to be the most reliable and accurate through synthetic catalogue analysis. A new workflow for calculating *Mc* was proposed to standardise current practice. A minimum incomplete catalogue size of 500 events, and a minimum complete size of 200 events was proposed.
- An error in calculating *Mc* was identified and quantified, having previously been assumed to be negligible. This new error always increases the total error with a greater effect when $\tilde{b}$ is high (>2), regardless of the catalogue size.
- In order to reduce bias from finite sampling of time windows a new iterative sampling method was developed. The method reveals a full net probability density function that is in general non-Gaussian and can be quite complex.

9.1 Application of methods to real catalogues

- The iterative sampling method confirms that $\tilde{b}$ at tectonic setting does equal 1.

- Although b-values as high as 3.3 are reported the modal $\tilde{b}_P$-value is often still 1.0. 'High' $\tilde{b}_P$-values (>1.5) are regularly reported in volcanic catalogues, although each volcano has its own unique character.
- At El Hierro we report high $\tilde{b}$-values of up to 3.25 before the main submarine eruption on 10th October 2011, followed by a relatively stable period when $\tilde{b}$=1. From August 2012 to March 2013 we observe strongly multi-modal behaviour with four significant local peaks, associated with spatially separate concurrent clusters of seismic activity. The observed high $\tilde{b}$-values are not inherently linked with a specific volcanic process.
- At several other volcanoes high $\tilde{b}_P$-values are also linked with non-Gutenberg-Richter frequency-magnitude distributions.
- We observe mode-switching of $\tilde{b}_P$ as it jumps between otherwise stationary values. As far as I am aware this observation has not previously been reported.

9.2 Field mapping on the Isle of Rum

- Field observations have helped identify structural features associated with a volcano-tectonic collapse event singular collapse event in the youngest major volcanic unit, the Central Intrusion.
- Quantitative measurements of fractures along six transects revealed offset was predominantly left-lateral and extensional, with near-vertical faults dipping eastward towards the right-lateral Long Loch fault. There were two families of faults identified; those parallel to a gulley striking at 347°, and to the west of the gulley a set of possible Riedel shears at 332°.
- Orientations of lineaments were measured on satellite imagery. The average strike was 344°, consistent with the fracture data. Therefore it was likely the observed structures could be up-scaled, and that these lineaments were formed under the same stress regime as the fractures.

9.3 Comparison of fault population data with modern volcanic seismic data

- Magnitudes of the Rum satellite lineament data were estimated to create an inferred frequency-magnitude distribution with a $\tilde{b}$-value of 1.87 ± 0.40, confirming b-values may have also been relatively high in the geological past.
- Three methods were used to calculate to fractal capacity and correlation dimensions (D_0 and D_2) of the Rum data along a one dimensional transect, and of the El Hierro catalogue in 1D transects and two dimensional planes. For Rum $D_0 = 0.191$ and $D_2 = 1.264$, and at El Hierro $D_0 = 0.416$ and $D_2 = 1.560$. In both cases the 1D analysis shows $D_0 \neq D_2$, implying the set of rupture sources or mapped fault traces form a multifractal set.
- These relatively low values of D imply relatively high levels of clustering associated with just one major phase of deformation.
- Broadly, the scaling of fracture sets (b, D_0 and D_2) in an ancient volcano has similar properties to those observed in a modern volcano, except that the Rum data imply a greater absolute degree of spatial clustering of deformation than the modern data on El Hierro.

Bibliography

Abarca, M.A.A., 2006. Lineament Extraction from Digital Terrain Models. Unpublished Masters Thesis, International Institute For Geo-Information Science and Earth Observation Enschede, The Netherlands.

Aki, K., 1965. Maximum Likelihood Estimate of *b* in the Formula log $N = a - bM$ and its confidence limits. Bulletin of the Earthquake Research Institute, 43: 237-239.

Aki, K., 1984. A probablistic synthesis of precursory phenomena. In: D.W. Simpson and P.G. Richards (Editors), Earthquake prediction. American Geophysical Union, Washington D.C., pp. 566-574.

Battaglia, J., Got, J.L. and Okubo, P., 2003. Location of long-period events below Kilauea Volcano using seismic amplitudes and accurate relative relocation. Journal of Geophysical Research: Solid Earth, 108(B12).

Becerril, L., Cappello, A., Galindo, I., Neri, M. and Del Negro, C., 2013. Spatial probability distribution of future volcanic eruptions at El Hierro Island (Canary Islands, Spain). Journal of Volcanology and Geothermal Research, 257: 21-30.

Bell, A., Naylor, M. and Main, I., 2013. Convergence of the frequency-size distribution of global earthquakes. Geophys. Res. Lett., 40: 1-5.

Ben-Zion, Y., Dahmen, K., Lyakhovsky, V., Ertas, D. and Agnon, A., 1999. Self-driven mode switching of earthquake activity on a fault system. Earth and Planetary Science Letters, 172: 11-21.

Bender, B., 1983. Maximum likelihood estimation of b values for magnitude grouped data. Bulletin of the Seismological Soceity of America, 73(3): 831-851.

Bing, 2015. Bing maps.

Bonnet, E., Bour, O., Odling, N.E., Davy, P., Main, I., Cowie, P. and Berkowitz, B., 2001. Scaling of fracture systems in geological media. Review of Geophysics, 29(3): 347-383.

Bridges, D.L. and Gao, S.S., 2006. Spatial variation of seismic b-values beneath Makushin Volcano, Unalaska Island, Alaska. Earth and Planetary Science Letters, 245: 408-415.

Bruno, B.C., Taylor, G.J., Rowland, S.K. and Baloga, S.M., 1994. Quantifying the effect of rheology on lava-flow margins using fractal geometry. Bull. Volcan., 56: 193-206.

Bruno, B.C., Taylor, G.J., Rowland, S.K., Lucey, P.G. and Self, S., 1992. Lava flows and fractals. Geophys. Res. Lett., 19: 305-308.

Cao, A. and Gao, S.S., 2002. Temporal variation of seismic b-values beneath northeastern Japan island arc. Geophysical Research Letters, 29(9): 1-3.

Caruso, F., Vinciguerra, S., Latora, V., Rapisarda, A. and Malone, S., 2006. Multifractal Analysis of Mount St. Helens Seismicity as aTool for Identifying Eurptive Activity. Fractals, 3: 179-186.

Centamore, C., Patane, G. and Tuve, T., 1999. Maximum entropy estimation of b values at Mt. Etna: comparison with conventional least squares and maximum likelihood results and correlation with volcanic activity. Annali Di Geofisica, 42(3): 515-528.

Chambers, L.M., Pringle, M.S. and Parrish, R.R., 2005. Rapid formation of the Small Isles Tertiary centre constrained by precise 40Ar/39Ar and U–Pb ages. Lithos, 79(3-4): 367-384.

Chen, R.F., Lin, C.W., Chen, Y.H., He, T.C. and Y., F.L., 2015. Detecting and Characterizing Active Thrust Fault and Deep-Seated Landslides in Dense Forest Areas of Southern Taiwan Using Airborne LiDAR DEM. Remote Sens., 7: 15443-15466.

Clark, C.D., Hughes, A.L.C., Greenwood, S.L., Jordan, C. and Sejrup, H.P., 2012. Pattern and timing of retreat of the last British-Irish Ice Sheet. Quaternary Science Reviews, 44: 112-146.

Clifton, A. and Einarsson, P., 2005. Styles of surface rupture accompanying the June 17 and 21, 2000 earthquakes in the South Icleand Seismic Zone. Tectonophysics, 296: 141-159.

Cowie, P.A., Sornette, D. and Vanneste, C., 1995. Multifractal scaling properties of a growing fault population. Geophys. J. Int., 122: 457-469.

Cowie, P.A., Vanneste, C. and Sornette, D., 1993. Statistical Physics Model for the Spatiotemporal Evolution of Faults. Journal of Geophysical Research, 98(B12): 809-821.

Del Fresno, C., Dominquez Cerdena, I., Cesca, S. and Buforn, E., 2015. The 8 October 2011 Earthquake at El Hierro (mw 4.0): Focal Mechanisms of the Mainshock and Its Foreshocks. Bulletin of the Seismological Soceity of America, 105(1).

Donaldson, C.H., Drever, H.I. and Johnston, R., 1973. Crystallisation of poikilomacro-spherulitic feldspar in a Rhum peridotite. Nature Physical Sciences, 243: 69-70.

Emeleus, C.H., 1994. Rum - Solid Geology Map. Scottish Natural Heritage.

Emeleus, C.H., 1997. Geology of Rum and the adjacent Islands. Memoir of the British Geological Survery, Scotland((Sheet 60)).

Emeleus, C.H., Cheadle, M.J., Hunter, R.H., Upton, B.G.J. and Wadsworth, W.J., 1996. The Rum Layered Suite. In: Cawthorn, R.G. (ed) Layered igneous rocks. Amsterdam: Elsevier,: 403-440.

Emeleus, C.H. and Troll, R.V., 2014. The Rum Igneous Centre, Scotland. Mineralogical Magazine, 78(4): 805-839.

Emeleus, C.H.B., B R., 2005a. The Palaeogene volcanic districts of Scotland. British Geological Survey, pp. 92-138.

Emeleus, C.H.B., B R., 2005b. The Palaeogene volcanic districts of Scotland. British Geological Survey, pp. 1-7.

Farrell, J., Husen, S. and Smith, R.B., 2009. Earthquake swarm and b-value characterization of the Yellowstone volcano-tectonic system. Journal of Volcanology and Geothermal Research, 188: 260-276.

Feder, J., 1988. Fractals. Plenum press, New York: 283.

Frolich, C. and Davis, S.D., 1993. Telesiesmic b values; Or, Much Ado About 1.0. Journal of Geophysical Research, 98(No. B1): 631-644.

Gaonach, H., Lovejoy, S. and J., S., 1992. Scale invariace of basaltic lava flows and their fractal dimensions. Geophys. Res. Lett., 19: 785-788.

García, A., Fernandez-Ros, A., Berrocoso, M., Marrero, J.M., Prates, G., De la Cruz-Reyna, S. and Ortiz, R., 2014. Magma displacements under insular volcanic fields, applications to eruption forecasting: El Hierro, Canary Islands, 2011–2013. Geophys. J. Int., 197(1): 322-334.

Ghosh, A., Newman, A.V., Thomas, A.M. and Farmer, G.T., 2008. Interface locking along the subduction megathrust from b-value mapping near Nicoya Peninsula, Costa Rica. Geophysical Research Letters, 35(L01301).

Godano, C., Alonzo, M.L. and Bottari, A., 1996. Multifractal analysis of the spatial distribution of earthquakes in southern Italy Geophys. J. Int., 125: 901-911.

Green, R.G., Greenfield, T. and White, R.S., 2015. Triggered earthquakes suppressed by an evolving stress shadow from a propagating dyke. Nature Geoscience, 8: 629-632.

Greenhough, J. and Main, I., 2008. A Poisson model for earthquake frequency uncertainties in seismic hazard analysis. Geophysical Research Letters, 35.

Gudmundsson, A., 1988. Formation of collapse calderas. Geology, 16: 808-810.

Gudmundsson, A., 1998. Formation and development of normal-fault calderas and the initiation of large explosive eruptions. Bull Volcanol, 60: 160-170.

Gudmundsson, A., 2007. Infrastructure and evolution of ocean-ridge discontinuities in Iceland. Journal of Geodynamics, 43: 6-29.

Gudmundsson, A., 2011a. Rock Fractures in Geological Processes. Cambridge University Press, pp. 255-287.

Gudmundsson, A., 2011b. Rock Fractures in Geological Processes. Cambridge University Press, pp. 288-318.

Gudmundsson, A., Lecoeur, N., Mohajeri, N. and Thordarson, T., 2014. Dike emplacement at Bardarbunga, Iceland, induces unusualstress changes, caldera deformation, and earthquakes. Bull Volcanol: 76:869.

Gudmundsson, A., Marti, J. and Turon, E., 1997. Stress fields generating ring faults in volcanoes. Geophys. Res. Lett., 24: 1559-1562.

Gutenberg, B. and Richter, C.F., 1954. Seismicity of the Earth, 2nd ed., 310.

Gutenberg, B. and Richter, C.F., 1956. Earthquake magnitude, intensity, energy, and acceleration (second paper). Bulletin of the Seismological Society of America, 46(2): 105-145.

GVP, 2015. Volcanoes of the World. In: E.e. v. 4.4.1 Venzke (Editor). Simithsonian Institution.

Hamilton, M.A., Pearson, D G., Thompson, R N., Kelly, S P., Emelues, C H., 1998. Rapid eruption of Skye lavas inferred from precise U-Pb and Ar-Ar dating of the Rum and Cullin plutonic complexes. Nature(394): 260-263.

Hanks, T.C. and Kanamori, H., 1979. A moment magnitude scale. Journal of Geophysical Research, 84(B5): 2348-2350.

Hauksson, E., Yang, W. and Shearer, P.M., 2012. Waveform relocated earthquake catalog for southern California (1981 to June 2011). Bulletin of the Seismological Society of America, 102(5): 2239-2244.

Henderson, J.R., Main, I.G., Maclean, C. and Norman, M.G., 1994. A Fracture-mechanical Cellular Automaton Model of Seismicity PAAGEOPH, 142(3/4).

Holness, M., Sides, R., Prior, D., Cheadle, M. and Upton, B., 2011. The peridotite plugs of Rum: crystal settling and fabric development in magma conduits. . 1-53.

Holohan, E., Holohan, E., Troll, R.V., Troll, R.V., Errington, M., Errington, M., Donaldson, C.H., Donaldson, C.H., Nicoll, G.R., Nicoll, G.R., Emeleus, C.H. and Emeleus, C.H., 2012. The Southern Mountains Zone, Isle of Rum, Scotland: volcanic and sedimentar y processes upon an uplifted and subsided magma chamber roof Geological Magazine, 146(03): 400-418.

Holschneider, M., Zoller, G., Clements, R. and Schorlemmer, D., 2014. Can we test for the maximum possible earthquake magnitude? J. Geophys. Res. Solid Earth, 199: 2019-2028.

Ibanez, J.M., De Angelis, S., Diaz-Moreno, A., Hernandez, P., Alguacil, G., Posdas, A. and Perez, N., 2012. Insights into the 2011-12 submarine eruption off the coast of El Hierro (Canary Islands, Spain) from statistical analyses of earthquake activity. Geophys. J. Int., 191: 659-670.

IGEPN, 2016. pp. Instituto Geofísico Escuela Politécnica Nacional - Tunguruhua LP seismic catalouge.

IGN, 2016. El Hierro seismic catalogue, pp. Instituto Geográfico Nacional, El Hierro seismic catalogue.

IMO, 2016. pp. Icelandic Met Office - Iceland seismic catalogue.

INGV, 2016. Mount Etna seismic catalogue, pp. Istituto Nazionale di Geofisica e Vulcanologia, Mount Enta seismic catalogue.

Jacobs, K.M. and McNutt, S.R., 2010. Using seismic b-values to interpret seismicity rates and physical processes during the preeruptive earthquake swarm at Augustine Volcano 2005-2006. USGS Professional Paper, 1769-3: 59-83.

Jolley, D.W., Clarke, B. and Kelly, S., 2003. Paleogene time scale miscalibration: Evidence from the dating of the North Atlantic igneous province: Comments and Replies. Geology, 31: 469-470.

Jolly, A.D. and McNutt, S.R., 1999. Seismicity at the volcanoes of Katmai National Park, Alaska; July 1995-December 1997. Journal of Volcanology and Geothermal Research, 93: 173-190.

Jónsdóttir, K., Roberts, R., Pohjola, V., Lund, B., Shomali, Z.H., Tryggvason, A. and Böðvarsson, R., 2009. Glacial long period seismic events at Katla volcano, Iceland. Geophysical Research Letters, 36(L11402).

Jónsdóttir, K., Tryggvason, A., Roberts, R., Lund, B., Soosalu, H. and Böðvarsson, R., 2007. Habits of a glacier-covered volcano: seismicity patterns and velocity structure of Katla volcano, Iceland. Annals of Glaciology, 45(1): 169-177.

Jordan, T.H., Chen, Y., Gasparini, P., Madariaga, R., Main, I., Marzocchi, W., Papadopoulos, G., Sobolev, G., Yamaoka, K. and Zschau, J., 2011. Operational Earthquake Forecasting: State of Knowledge and Guidelines for Utilization. Annals of Geophysics, 54(4).

Kagan, Y.Y. and Knopff, L., 1980. Spatial distribution of earthquakes: The two-point distribution problem. Geophys. J. Roy. Astron. Soc., 62: 303-320.

Kamer, Y. and Hiemer, S., 2015. Data-driven spatial *b* value estimation with applications to California seismicity: To *b* or not to *b*. J. Geophys. Res. Solid Earth(120).

Kanamori, H. and Anderson, L., 1975. Theoretical basis of some emperical relations in seismology. Bull. Seis. Soc. Am., 65: 1073-1095.

Katz, Y., Weinberger, R. and Aydin, A., 2004. Geometry and kinematic evolution of Riedel shear structures, Capitol Reef National Park, Utah. Journal of Structural Geology, 26: 491-501.

Klein, F., Koyanagi, R., Nakata, J. and Tanigawa, W., 1987. The seismicity of Kilauea's magma system. Volcanism in Hawaii, 2: 1019-1185.

Komuro, H., 1987. Experiments on cauldron formation fractures. Journal of Volcanology and Geothermal Research, 31: 139-149.

Komuro, H., Fujita, Y. and Kodama, K., 1984. Numerical and experimental models on the formation mechanism of collapse breccias during the Green Tuff Orogenesis, Japan. Bull Volcanol, 47: 649-666.

Lee, H.K. and Schwarz, H.P., 1995. Fractal clustering of fault activity in California. Geology, 23: 377-380.

Legrand, D., 2002. Fractal Dimensions of Small, Intermediate and Large Earthquakes. Bull. Seis. Soc. Am., 92(8): 3318-3320.

Leonard, T., Papasouliotis, O. and Main, I.G., 2001. A Poisson model for identifying characteristic size. Journal of Geophysical Research, 106(B7): 13,473-413,484.

López, C., Blanco, M.J., Abella, R., Brenes, B., Rodríguez, V.M.C., Casas, B., Cerdeña, I.D., Felpeto, A., Villalta, M.F., Del Fresno, C., García, O., García-Arias, M.J., García-Cañada, L., Moreno, A.G., Gonzalez-Alonso, E., Pérez, J.G., Iribarren, I., López-Díaz, R., Luengo-Oroz, N., Meletlidis, S., Moreno, M., Moure, D., Pablo, J.P., Rodero, C., Romero, E., Sainz-Maza, S., Domingo, M.A.S., Torres, P.A., Trigo, P., Villasante-Marcos, V., de Villalta, M.F. and de Pablo, J.P., 2012. Monitoring the volcanic unrest of El Hierro (Canary Islands) before the onset of the 2011–2012 submarine eruption. Geophysical Research Letters, 39(13).

López, c., Marti, J., Abella, R. and Tarraga, M., 2014. Applying Fractal Dimensions and EnergyBudget Analysis to Characterize Fracturing Processes During Magma Migration and Eruption: 2011–2012 El Hierro (Canary Islands) Submarine Eruption. Surveys in Geophysics.

Main, I., 1996. Statistical Physics, Seismogenesis, and Seismic Hazard. Review of Geophysics, 34(4): 433-462.

Main, I., 2000. Apparent Breaks in Scaling in the Earthquake Cumulative Frequency-Magnitude Distribution: Fact or Artifact? Bulletin of the Seismological Soceity of America, 90(1): 86-97.

Main, I.G., 1987. A characteristic earthquake model of the seismicity preceding the eruption of Mount St. Helens on 18 May 1980. Physics of the Earth and Planetary Interiors, 49: 283-293.

Main, I.G., Li. L, McCloskey, J. and Naylor, M., 2008. Effect of the Sumatran mega-earthquake on the global magnitude cut-off and event rate. Nature Geoscience, 1: 142.

Mandelbrot, B.B., 1967. How long is the coast of Britain? Statistical self-similarity and fractal dimension. Science, 156(636-8).

Marti, J., Ablay, G.J., Redshaw, L.T. and Sparks, R.S., 1994. Experimental studies of collapse calderas. J Geol Soc Lond, 151: 919-929.

Martí, J., Aspinall, W., Sobradelo, R., Felpeto, A., Geyer, A., Ortiz, R., Baxter, P., Cole, P., Pacheco, J. and Blanco, M., 2008. A long-term volcanic hazard event tree for Teide-Pico Viejo stratovolcanoes (Tenerife, Canary Islands). Journal of Volcanology and Geothermal Research, 178(3): 543-552.

Marti, J., Castro, A., Rodriguez, C., Costa, F., Carrasquilla, S., Pedreira, R. and Bolos, X., 2013a. Correlation of Magma Evolution and geophysical Monitroing during the 2011-2012 El Hierro (Canary Islands) Submarine Eruption. Journal of Petrology, 54(7): 1359-1373.

Marti, J., Pinel, V., Lopez, C., Geyer, A., Abella, R., Tarraga, M., Blanco, M.J., Castro, A. and Rodriguez, C., 2013b. Causes and mechanisms of El Hierro submarine eruption (2011-2012) (Canary Islands). JGR: 1-47.

Marzocchi, W. and Bebbington, M.S., 2012. Probabilistic eruption forecasting at short and long time scales. Bulletin of Volcanology, 74(8): 1777-1805.

Marzocchi, W. and Sandri, L., 2003. A review and new insights on the estimation of the b-value and its uncertainty. Annals of Geophysics, 46(6): 1271-1282.

Mattsson, T., Troll, R.V. and Burchardt, S., 2014. The Roots of a Magma Chamber, the Central Intrusion, Rum, NW-Scotland. Unpublished Masters Thesis, Uppsala universitet.

Mazzotti, S., Leonard, L.J., Cassidy, J.F., Rogers, G.C. and Halchuk, S., 2011. Seismic hazard in western Canada from GPS strain rates versus earthquake catalog. Journal of Geophysical Research, 116(B12310): 1-17.

McClurg, J.E., 1982. Petrology and evolution of the northern part of the Rhum ultrabasic complex. Unpublished PhD Thesis, University of Edinburgh.

McNutt, S.R., 1996. Seismic Monitoring and Eruption Forecasting of Volcanoes: A Review of the State-of-the-Art and Case Histories. 9-146.

McNutt, S.R., 2005. Volcanic Seismology. Annual Review of Earth and Planetary Sciences, 33(1): 461-491.

Meredith, P.G. and Atkinson, B.K., 1983. Stress corrosion and acoustic emission during tensile crack propagation in Whin Sill dolerite and other basic rocks. Geophys. J. R. astr. Soc., 75(1): 1-21.

Mignan, A. and Woessner, J., 2012. Estimating the magnitude of completeness for earthquake catalogs. Community Online Resource for Statistical Seismicity Analysis: 1-45.

Mogi, K., 1962. Magnitude frequency relations for elastic shocks accompanying fractures of various materials and some related problems in earthquakes. Bull. Earthquake Res. Inst. Univ. Tokyo, 40: 831-853.

Morales-Esteban, A., Martinez-Alvarez, F., Scitovski, S. and Scitovski, R., 2014. A fast partitioning algorithm using adaptive Mahalanobis clustering with application to seismic zoning. Computers and Geosciences, 73: 132-141.

Mori, J. and Abercrombie, R.E., 1997. Depth dependence of earthquake frequency-magnitude distributions in California: Implications for rupture initiation. Journal of Geophysical Research, 102: 15081-15090.

Murru, M., Console, R., Falcone, G., Montuori, C. and Sgroi, T., 2007. Spatial mapping of the *b* value at Mount Etna, Italy, using earthquake data recorded from 1999 to 2005. J. Geophys. Res., 112(B12303).

Murru, M., Montuori, C., Console, R. and Lisi, A., 2005. Mapping of the b value anomalies beneath Mt. Etna, Italy, during July-August 2001 lateral eruption. Geophysical Research Letters, 32(L05309).

Murru, M., Wyss, M. and Privitera, E., 1999. The locations of magma chambers at Mt. Etna, italy, mapped by b-values. Geophysical Research Letters, 26(16): 2553-1556.

Mussett, A.E., Dagley, P. and Skelhorn, R.R., 1988. Time and duration of activity in the British Tertiary Igneous Province. Geological Society, London, Special Publications, 39: 337-348.

Nakata, J.S. and Okubo, P.G., 2009. Hawaiian Volcano Observatory seismic data, January to December 2008. 2331-1258, US Geological Survey.

Naylor, M., Greenhough, J., McCloskey, J., Bell, A. and Main, I., 2009. Statistical evaluation of characteristic earthquakes in the frequency-magnitude distributions of Sumatra and other subduction zone regions. Geophysical Research Letters, 36(20).

Naylor, M., Orfanogiannaki, M. and Hart, D., 2010. Exploratory data analysis: magnitude, space, and time. Community Online Resource for Statistical Seismicity: 1-42.

Novelo-Casanova, D.A., Martinez-Bringas, A. and Valdes-Gonzalez, C., 2006. Temporal variations of Qc-1 and b-values associated to the December 2000–January 2001 volcanic activity at the Popocatepetl volcano, Mexico. Journal of Volcanology and Geothermal Research, 251: 347-358.

O'Driscoll, B., Donaldson, C.H., Troll, R.V., Jerram, D.A. and Emeleus, C.H., 2007. An origin for harrisitic and granular olivine in the Rum Layered Suite, NW Scotland: A Crystal Size Distribution study. Journal of Petrology, 48: 253-270.

Ouillon, G., Sornette, D. and Castaing, C., 1995. Organisation of joints and faults from 1 cm to 100 Km scales revealed by optimized anisotropic wavelet coefficient method and multifractal analysis. Nonlinear Process in Geophysics, 2: 158-177.

Patane, D., Caltabiano, T., Del Pezzo, E. and Gresta, S., 1992. Time variation of B and Qc at Mt. Etna (1981-87). Physics of the Earth and Planetary Interiors, 71: 137-140.

Pfeiffer, E. and Obert, M., 1989. Fractals: basic concepts and terminology, The Fractal Approach to Hetrogeneous Chemistry. Wiley New York, pp. 11-43.

Poliakov, A.N.B. and Herrmann, H.J., 1994. Self-organized criticality os plastic shear bands in rocks. Geophys. Res. Lett., 21: 2143-2146.

Power, J.A., Wyss, M. and Latchman, J.L., 1998. Spatial variations in the frequency-magnitude distribution of earthquakes at Soufriere Hills Volcano, Montserrat, West Indies Geophysical Research Letters, 29(19): 3652-3656.

Riedel, W., 1929. Zur Mechanik Geologischer Brucherscheinugen. Zentral-blatt fur Mineralogie, Geologie und Paleontologie B: 354-368.

Riel, B., Milillo, P., Simons, M., Lundgren, P., Kanamori, H. and Samsonov, S., 2015. The collapse of the Bardarbunga caldera, Iceland. Geophys. J. Int., 202: 446-453.

Roberts, A.M. and Holdsworth, R.E., 1999. Linking onshore and offshore structures: Mesozoic extension in the Scottish Highlands. Journal of the Geological Society, 156(6): 1061-1064.

Roberts, N.S., Bell, A.F. and Main, I.G., 2015. Are volcanic seismic b-values high, and if so when? Journal of Volcanology and Geothermal Research, 308: 127-141.

Robertson, M.C., Sammis, C.G., Sahimi, M. and Martin, A.J., 1995. Fractal analysis of three-dimensional spatial distribution patterns of earthquakes with a percolation interpretation. J. Geophys. Res., 100: 609-620.

Rubin, A.M., Gillard, D. and Got, J.L., 1998. A reinterpretation of seismicity associated with the January 1983 dike intrusion at Kilauea Volcano, Hawaii. Journal of Geophysical Research: Solid Earth, 103(B5): 10003-10015.

Rydelek, P.A. and Sacks, I.S., 1989. Testing the completeness of earthquake catalogs and hypothesis of self-similarity. Nature, 337: 251-253.

Sammonds, P.R., G., M.P. and Main, I.G., 1992. Role of pore fluids in the generation of seismic precursors to shear fracture. Nature, 359: 228-230.

Sanchez, J.J., Gomez, J.A., Torres, P.A., Calvache, M.L., Ortega, A., Ponce, A.P., Acevedo, A.P., Gil-Cruz, F., Londono, J.M., Rodriguez, S.P., Patino, J.D.J. and Bohoroquez, O.P., 2005. Spatial mapping of the b-value at Galeras volcano, Columbia, using earthquakes recorded from 1995 to 2002. Earth Sci. Res. J., 9(1): 30-36.

Sanchez, J.J., McNutt, S.R., Power, J.A. and Wyss, M., 2004. Spatial Variations in the Frequency-Magnitude Distribution of Earthquakes at Mount Pinatubo Volcano. Bullertin of Seismological Society of America, 94(2): 430-438.

Savage, J. and Cockerham, R., 1984. Earthquake swarm in Long Valley caldera, California, January 1983: Evidence for dike inflation. Journal of Geophysical Research: Solid Earth, 89(B10): 8315-8324.

Scarfi, L., Messina, A. and Cassisi, C., 2013. Sicily and the southern CAlabria focal mechanisms database: a vaulable tool for ocal and regional stress-field determination. Annals of Geophysics, 56(1): D0109.

Scholz, C.H., 1968. The frequency-magnitude relation of microfracturing in rock and its relation to earthquakes. BSSA, 58(1): 399-415.

Schorlemmer, D., Wiemer, S. and Wyss, M., 2005. Variations in earthquake-size distribution across different stress regimes. Nature, 437(7058): 539-542.

Schwarz, G., 1978. Estimating the dimension of a model. Ann. Stat., 6(2): 461-464.

Scitovski, R. and Scitovski, S., 2013. A fast partitioning algorithm and its application to earthquake investigation. Computers and Geosciences, 59: 141-131.

Shi, Y. and Bolt, B.A., 1982. The standard error of the magnitude-frequency b value. Bulletin of the Seismological Soceity of America, 72(5): 1677-1687.

Sicali, S., Barberi, G., Cocina, O., Musumeci, C. and Patane, D., 2015. Volcanic unrest leading to the July-August 2001 lateral eruption at Mt. Enta: Seismological constraints. Journal of Volcanology and Geothermal Research, 304: 11-23.

Sigmundsson, F., Hooper, A., Hreinsdottir, S., Vogfjord, K.S., O´feigsson, B.G., Heimisson, E.R., Dumont, S., Parks, M., Spaans, K., Gudmundsson, G.B., Drouin, V., Arnadottir, T., Jonsdottir, K., Gudmundsson, M.T., Hognadottir, T., Fridriksdottir, H.M., Hensch, M., Einarsson, P., Magnusson, E., Samsonov, S., Brandsdottir, B., White, R.S., Agustsdottir, T., Greenfield, T., Green, R.G., Hjartardo ´ttir, A.R., Pedersen, R., Bennett, R.A., Geirsson, H., La Femina, P.C., Bjornsson, H., Pa ´lsson, F., Sturkell, E., Bean, C.J., Mollhoff, M., Braiden, A.K. and Eibl, E.P.S., 2015. Segmented lateral dyke growth in a rifting event atBarðarbunga volcanic system, Iceland. Nature, 517: 191-195.

Silva, R., Havskov, C., Bean, C. and Wallenstein, N., 2012. Seismic swarms, fault plane solutions, and stress tensors for Sao Migeul Island central region (Azores). J. Seismol., 16: 389-407.

Smalley, R.F., Chatelain, J.L., Turcotte, D.L. and Pervot, R., 1987. A fractal approach to the clustering of earthquakes: Applications to the seismicity of the New Hebredes. Seis. Soc. Am. Bull., 77: 1368-1381.

Smith, K., 2012. The Fascadale Fault: A tectonic link between the Cenozoic volcanic centres of Rum and Ardnamurchan, Scotland, revealed by multibeam survey. Scottish Journal of Geology, 48: 91-102.

Soosalu, H., 2002. Unusually high seismic activity at the Katla volcano, south Iceland, European Seismological Commission workshop Seismic Phenomena Associated with volcanic activity, Montserrat, West Indies.

Thatcher, W. and Savage, J., 1982. Triggering of large earthquakes by magma-chamber inflation, Izu Peninsula, Japan. Geology, 10(12): 637-640.

Thompson, R.N., 1982. Magmatism of the British Tertiary Volcanic Province. Scottish Journal of Geology, 18: 49-107.

Tinti, S. and Mulargia, F., 1985. Effects of Magnitude Uncertainties on Estimating the Parameters in the Gutenberg-Richter Frequency-Magnitude Law. Bulletin of the Seismological Soceity of America, 75(6): 1681-1697.

Touati, S., Naylor, M., Main, I. and Christie, M., 2011. Masking of earthquake triggering behavior by a high background rate and implications for epidemic-type aftershock sequence inversions. Journal of Geophysical Research: Solid Earth, 116(B3).

Troll, R.V., Emeleus, C. and Donaldson, C., 2000. Caldera formation in the Rum Central Igneous Complex, Scotland. Bull Volcanol: 1-17.

Troll, R.V., Nicoll, G.R., Donaldson, C.H. and Emeleus, H.C., 2008. Dating the onset of volcanism at the Rum Igneous Centre, NW Scotland. Journal of the Geological Society, 165(3): 651-659.

Turcotte, D.L., 1997. Fractals and Chaos in Geology and Geophysics. Cambridge University Press.

Upton, B., Upton, B., Skovgaard, A., Skovgaard, A., McClurg, J., McClurg, J., Kirstein, L., Kirstein, L., Cheadle, M., Cheadle, M., Emeleus, C., Emeleus, C., Wadsworth, W., Wadsworth, W., Fallick, A. and Fallick, A., 2012. Picritic magmas and the Rum ultramafic complex, Scotland. Geological Magazine, 139(04): 437 - 452.

Vicsek, T., 1992. Fractal Growth Phenomena. World Scientific, Singapore, 19-23 pp.

Vinciguerra, S. and Day, S., 2013. Magma Intrusion as a Driving Mechanism for the Seismic Clustering Following the 9 May 1989 Earthquake Swarms at the Canary Islands Acta Geophysica, 61(6): 1626-1641.

Vinciguerra, S., Gresta, S., Barbano, M.S. and Disetfano, G., 2001. The two behaviours of Mt. Etna volcano before and after a large intrusive episode: evidences from b value and fractal dimension of seismicity. Geophysical Research Letters, 28(11): 2257-2260.

Volker, J.A., 1983. The geology of the Trallval area, Rhum, Inner Hebrides. Unpublished PhD thesis, University of Edinburgh.

Volker, J.A. and Upton, B.G.J., 1990. The structure and petrogenesis of the Trallval and Ruinsival areas of Rhum ultrabasic complex. Transactions of the Royal Society of Edinburgh: Earth Sciences, 81: 69-88.

Wadsworth, W.J., 1961. The layered ultrabasic rocks of south-west Rhum, Inner Hebrides. . Philosophical Transactions of the Royal Society, London, 244B: 21-64.

Wadsworth, W.J., 1992. Ultrabasic igneous breccias of the Long Loch area, Isle of Rum. Scottish Journal of Geology, 28(2): 103-113.

Walsh, J.J. and Watterson, J., 1993. Fractal analysis of fracture patterns using the standard box-counting technique: valid and invalid methodologies Journal of Structural Geology, 15(12): 1509-1512.

Wells, D.L. and Coppersmith, K.J., 1994. New Empirical Relationships among Magnitude, Rupture Length, Rupture Width, Rupture Area, and Surface Displacement. Bulletin of the Seismological Soceity of America, 84(4): 974-1002.

Wiemer, S., 2001. A software package to analyse seismicity: ZMAP. Seismological Research Letters, 72(2): 373-382.

Wiemer, S. and Benoit, J.P., 1996. Mapping the b-value anomaly at 100 km depth in the Alaska and New Zealand subduction zones. Geophysical Research Letters, 23(13): 1557-1560.

Wiemer, S. and McNutt, S.R., 1997. Variations in the frequency-magnitude distribution with depth in two volcanic areas: Mount St. Helens, Washington, and Mt. Spurr, Alaska. Geophysical Research Letters, 24(2): 189-192.

Wiemer, S., McNutt, S.R. and Wyss, M., 1998. Temporal and three-dimensional spatial analyses of the frequency–magnitude distribution near Long Valley Caldera, California. Geophys. J. I., 134: 409-421.

Wiemer, S. and Wyss, M., 2000. Minimum Magnitude of Completeness in Earthquake Catalogs: Examples from Alaska, the Western United States, and Japan. Bulletin of the Seismological Society of America, 90(4): 859-869.

Wiemer, S. and Wyss, M., 2002. Mapping spatial variability of the frequency-magnitude distribution of earthquakes. Advances in Geophysics, 45: 259-302.

Woessner, J. and Wiemer, S., 2005. Assessing the Quality of Earthquake Catalogues: Estimating the Magnitude of Completeness and Its Uncertainty. Bulletin of the Seismological Society of America, 95(2): 684-698.

Wyss, M., Klein, F., Nagamine, K. and Wiemer, S., 2001. Anomalously high b-values in the South Flank of Kilauea volcano,Hawaii: evidence for the distribution of magma below Kilauea's East rift zone. Journal of Volcanology and Geothermal Research, 106: 23-37.

Wyss, M., Shimazaki, K. and Wiemer, S., 1997. Mapping active magma chambers by b values beneath the off-Ito volcano, Japan. Journal of Geophysical Research, 102(B9): 20413-20422.

Zamani, A. and Agh-Atabi, M., 2011. Multifractal analysis of the spatial distribution of earthquake epicenters in the Zagros and Alborz-Kopeh Dagh regions of Iran Iranian Journal of Science & Technology, A1: 39-51.

Appendix A – Glossary and a list of figures and tables

A glossary of all abbreviations and acronyms used throughout the thesis (A.1), a table of figures (A.2), and a list of tables (A.3).

A.1 – Glossary of abbreviations and acronyms

These are separated into those used in chapters focussed on Seismicity (Chapters 2, 3, 4, 5 & 8), fractal dimensions (Chapters 2, 7 & 8), and the Isle of Rum (Chapters 2, 6, 7, & 8).

A.1.1. Seismicity abbreviations

a – 'a'-value, constant described by the Gutenberg-Richter relationship. It a measure of the seismicity rate of the region.

b – 'b'-value, constant described by the Gutenberg-Richter relationship. Represents the relative proportion of large and small events in a seismic catalogue.

b – Known b-value

$\tilde{b}$ – Estimated b-value

b_{min} – Minimum b-value

b_{max} – Maximum b-value

b_{typ} – Typical b-value

$\tilde{b}_P$ – b-value with peak probability, $P'(\tilde{b})$.

E_p - The number of events you wish have per data point.

it - Number of iterations

M – Magnitude

M_c – Completeness magnitude of a seismic catalogue.

$\bar{M}$ - Mean magnitude

ΔM - Magnitude bin size

M_{min} – Minimum magnitude

N – Original number of earthquakes

N_c – Number of earthquakes in the complete catalogue

$P(\tilde{b})$ – Probability density of the estimated b-value.

$P'(\tilde{b})$ – Peak probability density of the b-value.

R – Error multiplication factor

R_l – Surface rupture length

S_{min} – Minimum sample size

S_{max} - Maximum sample size

σ_1, σ_2, σ_3 – Maximum, intermediate and minimum stress axes

ε_1, ε_2, ε_3 – Maximum, intermediate and minimum strain axes

$\hat{\mu}$ - Average magnitude of the sample.

$\sigma_{\tilde{b}}$ – Random error in the estimated b-value.

$R\sigma_{\tilde{b}}$ – Total error in the estimated b-values once R has been applied.

A.1.2. Fractal dimension abbreviations

A – Rupture area

C – Constant of proportionality

$C(r)$ – Pair-correlation distribution

r – Spacing, inner radius

r′ – Outer radius

Δr – Distance between inner and out radius

N – Original number of points.

ρ – Density

α – Constant related to the fractal dimension.

D – Fractal dimension

D_0 – Capacity Dimension

D_2 – Correlation dimension

D_{mag} – Fractal dimension of the source rupture length

M – Seismic moment

m – Earthquake magnitude

P_i – Length of the object perimeter.

p_i – Probability

N_i – Number of objects (i.e. fragments) with a characteristic linear dimension r_i in the i^{th} order.

r_i – Characteristic dimension

c, d, β – Constants

A.1.3. Rum abbreviations

n – Number of fractures

A.1.4. Acronyms associated with seismicity

BIC – Bayesian information criterion

BVS – *b*-value stability method

EMR – Entire magnitude range method

FMD – Frequency magnitude distribution

GFT – Goodness-of-fit method

GR – Gutenberg-Richter

IGN - Instituto Geográfico Nacional

INGV - Istituto Nazionale di Geofisica e Volcanologia

LS – Least squares

MaxC – Maximum curvature method

PDF – Probability density function

SISZ – South Iceland seismic zone

WLS – Weighted least squares

A.1.5. Acronyms associated with fractal dimensions

1D, 2D, 3D – One, two and three dimensions respectively

A.1.6. Acronyms associated with Rum

BPIP - British Palaeogene Igneous Province

CI – Central Intrusion

DEM – Digital elevation model.

ELI - Eastern Layered Intrusion

HIP - Hebridean Igneous Province

LLF – Long Loch Fault

MRF - Main Ring Fault

MNZ - Northern Marginal Zone

SMZ - Southern Mountains Zone

T1 to T6 – Transects 1 to 6

WLI – Western Layered Intrusion

A.2 – List of Figures

Figure 2.1 – Ideal wall or surface displacements of a fracture are denoted by mode I, mode II, and mode III (Gudmundsson, 2011a). 10

Figure 2.2 – Two examples of a magma chamber, dyke and collapsed caldera. a) A feeder dyke (Mode I) in the centre of a collapsed caldera and the ring dyke/fault (Mode III) are best modelled as through cracks. All ring faults are dip-slip faults, here it is a reverse fault. b) A non-feeder dyke in the centre of a collapsed caldera. The dyke originates at the top of a shallow, fluid magma chamber and then extends partly up into the host rock. Here the ring fault of the collapsed caldera is a normal fault (Gudmundsson, 2011a). 10

Figure 2.3 – Schematic diagram of a stratovolcano showing the difference between a conduit, dyke, sill, and tip (Gudmundsson, 2011b). 11

Figure 2.4 – Ideal crack geometries for modelling fractures: a) a 'through' crack, b) a 'part-through' crack, and c) an' interior' crack (Gudmundsson, 2011a). 12

Figure 2.5 – a) A filtered synthetic frequency-magnitude distribution containing 500 events. The synthetic data have a known completeness magnitude of 1.0 and a known *b*-value of 1.0. The discrete frequency is shown by red circles and the cumulative frequency by green squares. b) Event magnitudes plotted in the order they were generated. The magnitude range is 0.0 to 3.6. c) A moving window containing 50 events moving in increments of 5 events is applied to the catalogue to generate a varying *b*-value against realisation number (which could be time or depth). The blue error bars show one standard deviation calculated using a best fit Equation [2.3]. The grey error bars are calculated using the modified error distribution proposed by Roberts *et al.* (2015) and in this thesis. 16

Figure 2.6 - Map showing the positions of the Palaeogene central complexes, lava fields, sill-complexes and dyke swarms in the BPIP (Emeleus, 2005a) 21

Figure 2.7 - Top: Schematic section from the Outer Hebrides to the Great Glen Fault showing how the elevated footwalls of Mesozoic faults are exposed above sea level (Roberts and Holdsworth, 1999) Bottom: Orientation of the section. 23

Figure 2.8 - Geological map of Rum (Emeleus, 1994) with key faults and units highlighted. The volcanic units forming the central complex are the Western Granite, Northern Marginal zone (NMZ), Southern Mountains zone (SMZ), Eastern Layered Intrusion (ELI), Western Layered Intrusion (WLI) and the Central Intrusion (CI). The study area is marked by the red box. 24

Figure 2.9 - Diagrams showing the possible evolution of the Rum caldera (Troll *et al.*, 2000). 26

Figure 2.10 – Taken from Figure 7 in Troll *et al.* (2008). The timeline shows the age of the Rum volcanic suites. 27

Figure 2.11 - Conceptual model of breccia formation from Mattsson et. al. (Figure 69, 2014) 1) Intrusion along cumulate bedding. 2) Hydraulic fracturing forming clasts supported braccia. 3) Megablocks sliding along planes lubricated by intrusive material. 4) Talus breccia forming at the base of faults. 5) Shearing occurs in intrusive planes. 6) Rotational collapse of clasts. 7) Large convection clouds of magma settling to form pebbly peridotite. Photos of hese units are described in Section 6.3. 30

Figure 2.12 – Illustration of a 1st and 2nd order a) Cantor Set, and b) Sierpinski Carpet. 33

Figure 2.13 – Example of fractal clustering and the calculation of fractal dimension, *D*, for 234 fractures on the Isle of Rum, Scotland, taken from Chapter 7. The circles gives the fraction of intervals *p*, of length *r*, that include a fracture. The solid line represents the best-fit Equation [2.9] with *D*=0.257. 35

Figure 2.14 - Example of the pair-correlation, $C(r)$, as a function of spacing, r, for a transect containing 238 fractures on the Isle of Rum, Scotland. The solid line is the best-fit correlation, described in Equation [2.14], for r, up to half the total transect length. 38

Figure 3.1 – Synthesis of b-value distributions compared to a) depth, b) magnitude, and c) the number of events in each catalogue, N_c. The errors bars show the minimum and maximum values of b from Table 1, and the range of depth/magnitude over which the catalogue was comprised. The blue dots show the typical b-values. The dotted line marks b=1. 52

Figure 3.2 – a) Discrete and cumulative frequency-magnitude distributions, demonstrating the Maximum Curvature Method (MaxC). The vertical dotted line represents the estimate of Mc at the highest discrete magnitude bin at (Mc=1.5). b) Residuals of the Goodness-of-Fit method (GFT) as a function of trial cut-off. Once the residual falls beneath 5% the completeness magnitude is selected, in this case Mc=2.5. c) b-value stability curve showing the b-values for each cut-off magnitude. The vertical dashed line indicates when successive b-values (green line) fall within error of the b-value. Here Mc=2.5. 56

Figure 3.3 – a) Example of a sharp-peaked frequency-magnitude distribution. b) Example of a broad-peaked frequency-magnitude distribution. Both catalogues have an Mc of 1.0 and a b-value of 1.0. Discrete distributions are in reds, cumulative distributions are in green. The dashed lines show the 95% confidence intervals representing the scatter in the synthetic data c) The probability filter applied to b). Above Mc=1.0 all generated events are kept in the catalogue. Beneath Mc=1.0 there is a constantly decreasing probability that that will remain in the catalogue, creating the broad peak in the filtered discrete FMD. 58

Figure 3.4 – Histograms for the estimated Mc and b-value for the MaxC (red), GFT (green), and BVS (blue) methods for different catalogue sizes (columns) and b-values (rows) for the sharp-peaked distribution. The known values of Mc=1.0 and b=1.0 are marked with vertical bold dashed lines. The median value calculated by each method is shown by the vertical dotted line. 60

Figure 3.5 – Histograms as in Figure 3.4 except for a broad-peaked distribution. 61

Figure 3.6 – Frequency-magnitude distributions for b=1 & 2, and N_c=50 & 5000 in the case of a broad-peaked distribution. Red shows discrete frequency and green the cumulative frequency. The solid red and green lines show the average values of the 100 catalogues. The dashed lines represent a 95% confidence window. The vertical dashed black lines show the known Mc of the catalogue, Mc=1.0, and the Mc's calculated by each method. 62

Figure 3.7 - Summary of histograms for broad-peaked distributions in Figure 3.5 for b=1. They show the spread of Mc's and b-value's against catalogue size, N, for each of the three methods. Error bars represent a 95% spread of the data, with dots representing the median value and x's the average. The known Mc=1.0 and b=1.0 are marked with a vertical dashed line. 64

Figure 3.8 - Summary graphs as in Figure 3.7 but for b=2. 66

Figure 3.9 - Proposed workflow for best practice based on synthetic analysis. 68

Figure 3.10 - b-value frequency plot for 100 synthetic catalogues when N_c=1000 and b=2. The blue (epistemic) error bar represents one standard deviation error in the data centred on the median b-value. The black error bars show the average aleatoric (Shi & Bolt b-value uncertainty) error for each bin. 69

Figure 3.11 – Contour plots showing a) the statistical error in b-value estimated from eq. (5) as a function of varying complete catalogue size, N_c, and b-value. b) The error in b-value associated with the uncertainty in calculating Mc, estimated as in the example given in Figure 3.10 as a blue horizontal error bar. c) The ratio of the error in (b) to the statistical error in (a). 71

Figure 3.12 – Top: b-value variation through time for the July 2011 to December 2013 El Hierro seismic catalogue using the proposed workflow. The eruption date is marked by the red dashed line. Bottom: Daily number of events (grey bars) and cumulative number of events (black line). The

phase divisions are marked by vertical grey dotted lines with the number of events in the complete catalogue of each phase noted at the top of the plot. 73

Figure 3.13 – Plots as in Figure 3.12 but for the 1999 - 2014 Mount Etna seismic catalogue. The initiation of the 2002 and 2004 flank eruptions are marked by the vertical dashed lines. 74

Figure 3.14 - *b*-value variation through time for a) the 2011-13 El Hierro catalogue, and b) the 1999 - 2014 Mount Etna seismic catalogue. Sample bias errors in are blue and estimated epistemic error are in grey. One standard deviation error is represented by the error bars and the grey dashed and blue dotted line respectively represent the 2 standard deviation error envelope. 75

Figure 4.1 - The synthetic catalogue has a parent Gutenberg-Richter distribution above Mc=1.0, with b=1 for the first and last 5000 events, and b=2 for the middle 5000. a) Each event is shown as a black dot. The red, blue and green lines show the boundaires of each catalogue in three succesive iterations. b) Cloud of data points produced by 100 iterations. c) The b-value probability density by event number. The dashed grey line shows the underlying known b-value. The dotted black line marks bP. 85

Figure 4.2 - Sensitivity testing of the size of the window used to create the b-value probability density function. a) Uses 10 data points, b) 20, c) 50, d) 100 and e) 200. 50 data points were chosen as a compromise between eliminating noise and over-smoothing the data. However, every window size shows the major steps in the modal b-value. 87

Figure 4.3 - The b-value probability density plotted by a) event number, and b) time, using the iterative sampling method described in the methods section. The dotted black line traces bP. The vertical dot-dashed black, red and blue lines mark the times of the events: i) Event 2020 on 9/8/2010, ii) Event 10800 on 2/11/2010, and iii) Event 15720 on 18/12/2011. Overlain is a comparison of results in Figure 3.14a using fixed, subjectively chosen windows. The error bars show the total b-value at one standard deviation, accounting for the error in Mc. The dashed lines show two standard deviations error (approximately 95% confidence limits). The bars with numbers 1-8 shows the phases in Table 4.1. The red line in phase 2 indicates the time of the eruption on 10/10/11. 89

Figure 4.4 – Cross-sections of the b-value probability density function marked in Figure 4.3, using a 50 data point window. Coloured error bars in iii) represent the b-values calculated for the clusters in Figure 4.5. 91

Figure 4.5 – Epicentral and hypocentral locations of earthquakes above magnitude 0.0 in phase 6 (Table 4.1). Each colour marks a separate cluster of events, A-D. All clusters ceased activity by 18/3/13. Cluster A started on 13/8/12. Clusters B and C started on 14/9/12. Cluster D began on 31/12/12. Events coloured grey were judged not to be part of any of the clusters of events. The coloured polylines show where the majority of events in phases 1-5, 7 and 8 are clustered. The black and grey ovals and lines in the cross section indicate the relative position of the magma chamber described in Marti *et al.* (2013a, 2013b). The direction of migration in phase 2 is marked with an arrow. 92

Figure 5.1 – The b-value probability density function at El Hierro from July 2011 to December 2013 containing ~21000 events. The dashed line shows the null hypothesis b=1 for reference, and the maximum likelihood value is indicated by the dotted line. 103

Figure 5.2 - The b-value probability density function at El Hierro for the first 6000 events of phase 1 containing multiple periods with high b-values. Plotted as in Figure 5.1. 103

Figure 5.3 – Daily event rate (grey bars) and cumulative number of events (black line) for El Hierro. 104

Figure 5.4 - The b-value probability density function at Mount Etna from August 1999 to February 2014 containing ~8000 events. Vertical dotted lines highlight the phase boundaries listed in Table 5.3. Plotted as in Figure 5.1. 106

Figure 5.5 – Event magnitude through time at Mount Etna, coloured by event number. Dashed line shows the completeness magnitude obtained through the iterative sampling method. 107

Figure 5.6 - The b-value probability density function at Kilauea from January 1959 to December 1984 containing ~11000 events. Plotted as in Figure 5.1. 108

Figure 5.7 - The b-value probability density function at Tungurahua from January 1999 to August 2015 containing ~165000 events. Plotted as in Figure 5.1. 110

Figure 5.8 - Event magnitude through time at Tungurahua. Coloured by event number. Dashed line shows the completeness magnitude obtained through the iterative sampling method. 110

Figure 5.9 – Hypocentres and epicentres of earthquakes surrounding the Bárðarbunga caldera, dyke emplacenment and fissure site between June 2014 and July 2015. Events are coloured blue to red, from oldest to most recent. The two dashed boxes incidate the two sub-catalouges used in Figure 5.10 to Figure 5.13. 111

Figure 5.10 - Event magnitude through time at Bárðarbunga caldera, coloured by event number. Dashed line shows the completeness magnitude obtained through the iterative sampling method. Vertical dashed red line shows the onset of the eruption. 112

Figure 5.11 – Top: discrete b-values calculated using the workflow in Figure 3.9 for each of the caldera, dyke and eruption sites at Bárðarbunga between June 2014 and July 2015. Bottom: daily event rate (grey bars) and cumulative number of events (solid black line) with the phase boundaries (dotted vertical grey lines) and eruption date (dashed vertical red line). 113

Figure 5.12 - The b-value probability density function at Bárðarbunga from June 2014 to Janurary 2015 containing ~16000 events. Plotted as in Figure 5.1. 114

Figure 5.13 - The b-value probability density function at Bárðarbunga caldera from June 2014 to Janurary 2015 containing ~8500 events. Plotted as in Figure 5.1. 114

Figure 5.14 – Frequency-magnitude distribution of the Bárðarbunga caldera between 10th June 2014 and 25th January 2015. a) The entire magnitude range with bi-modality in the discrete distribution (red); $b = 0.35 \pm 0.01$. b) The FMD for the first mode of magnitudes up to and including 2.9M; $b = 1.02 \pm 0.02$. c) The FMD for the second mode of magnitude from 3.0M upwards; $b = 1.19 \pm 0.15$ 115

Figure 5.15 – Conceptual model for the mechanics of the collapsing caldera (Riel *et al.*, 2015). 116

Figure 5.16 - The b-value probability density function at Bárðarbunga dyke intrusion from June 2014 to Janurary 2015 containing ~6000 events. Plotted as in Figure 5.1. 117

Figure 5.17 - Event magnitude through time at Bárðarbunga dyke, coloured by event number. The dashed line shows the completeness magnitude obtained through the iterative sampling method. Vertical dashed red line shows the onset of the eruption. 117

Figure 5.18 - Daily event rate (grey bars) and cumulative number of events (black line) for Grímsvötn. 118

Figure 5.19 - The b-value probability density function at Grímsvötn from January 2009 to August 2015 containing ~500 events. Plotted as in Figure 5.1. 119

Figure 5.20 – Frequency-magnitude distribution for Grímsvötn between 10th March 2011 and 1st September 2013 (event numbers 275 – 410). $b = 0.61 \pm 0.14$, however the discrete distribution (red circles) has a potentially bi-modal characteristic distribution rather than following the Gutenberg-Richter relationship. 120

Figure 5.21 - Event magnitude through time at Grímsvötn, coloured by event number. Vertical dashed red line shows the onset of the eruption. 120

Figure 5.22 - The b-value probability density function at Eyjafallajökull from January to May 2010 containing ~4000 events. Plotted as in Figure 5.1. 121

Figure 5.23 – Frequency-magnitude distribution for Eyjafallajökull from 15th – 18th March 2010 (event numbers 2459 - 3279). $b = 2.46 \pm 0.58$ 122

Figure 5.24 – a) Daily event rate (grey bars) and cumulative number of events (black line) for Eyjafallajökull. b) The b-value probability density function through time at Eyjafallajökull as plotted as in Figure 5.1. The red dashed line shows the start of the eruption.....122

Figure 5.25 - The b-value probability density function at Katla from January 1995 to August 2015 containing ~27000 events. Plotted as in Figure 5.1. 123

Figure 5.26 - Event magnitude through time at Katla, coloured by event number. Dashed line shows the completeness magnitude obtained through the iterative sampling method. 123

Figure 5.27 – Frequency-magnitude distributions at Katla show high bP-values for a) events 14570 to 14720 (20th September to 12th November 2006) where $b = 2.71 \pm 0.99$, and b) events 15480-15870 (17th September 2007 to 8th January 2008) where $b = 2.19 \pm 0.72$.....125

Figure 5.28 – Annual stacking of the Katla 2004 to 2009 catalogue. Top: raw data from iterative sampling technique. Bottom: contoured PDF with peak bP-value marked with the dotted line. Plotted as in Figure 5.1. 126

Figure 5.29 – Average number of event per month (grey bars) and average bP-value with one standard deviation error (blue error bars) for the Katla 2004 to 2009 catalgoue.....127

Figure 5.30 - Hypocentres and epicentres of earthquakes in the Tjörnes fracture zone from 1995 to 2015. Events are coloured blue to red from oldest to most recent. The dashed line indicates the split between the north-east and south-east sub-catalogues. 128

Figure 5.31 - The b-value probability density function for the NE cluster of the Tjörnes fracture zone from January 1995 to August 2015 containing ~37000 events. Plotted as in Figure 5.1. 129

Figure 5.32 - The b-value probability density function plotted by event number for the SW cluster of the Tjörnes fracture zone from January 1995 to August 2015 containing ~33000 events. Plotted as in Figure 5.1. 129

Figure 5.33 - The b-value probability density function plotted by timefor the SW cluster of the Tjörnes fracture zone from January 1995 to August 2015. Plotted as in Figure 5.1. 130

Figure 5.34 - The b-value probability density function showing the cyclical nature of the b-value, for a) the NE cluster of the Tjörnes fracture zone from January 2003 to January 2007, and b) the SW cluster of the Tjörnes fracture zone from January 2007 to January 2010. Plotted as in Figure 5.1. 130

Figure 5.35 - Average number of event per month (grey bars) and average bP-value with one standard deviation error (blue error bars) for a) the NE Tjörnes catalogue from 2003-2007, and b) the SW Tjörnes catalogue from 2007 to 20010. Average monthly minimum magnitude (light grey), completeness magnitude (green) and maximum magnitude (dark grey) for c) the NE Tjörnes catalogue from 2003-2007, and d) the SW Tjörnes catalogue from 2007 to 2010. 131

Figure 5.36 - Daily event rate (grey bars) and cumulative number of events (black line) for the SW Tjörnes catalogue. 132

Figure 5.37 - Annual stacking of for a) the NE cluster of the Tjörnes fracture zone from January 2003 to January 2007, and b) the SW cluster of the Tjörnes fracture zone from January 2007 to January 2010. It is a countoured contoured PDF with peak bP-value marked with the dotted line. As plotted in Figure 5.1. 133

Figure 5.38 - Annual stacking of the Tjörnes 1995 to 2015 catalogue for a) the NW catalogue and b) the SE catlouge. It is a countoured contoured PDF with peak bP-value marked with the dotted line. Plotted as in Figure 5.1. 134

Figure 5.39 - The b-value probability density function for the South Iceland seismic zone from January 2000 to August 2015 containing ~60000 events. Plotted as in Figure 5.1. 135

Figure 5.40 - The Annual stacking of the Southern Iceland seismic zone catalogue from 2000 to 2015. It is a countoured contoured PDF with peak bP-value marked with the dotted line. Plotted as in Figure 5.1. 135

Figure 5.41 - The b-value probability density function South California from January 1984 to December 2002 containing ~72000 events. Plotted as in Figure 5.1. 136

Figure 5.42 - Annual stacking of the Southern California catalogue from 1984 to 2002. It is a countoured PDF with peak bP-value marked with the dotted line. Plotted as in Figure 5.1. 136

Figure.6.1 - a) Satellite image (Bing, 2015) of the Long Loch area identifying linear features on a 5-200 m scale in the Central Intrusion. b) Photo from the slopes of Barkeval, looking west at the Central Intrusion. The linear features can be seen cutting the outcrop. 144

Figure 6.2 - a) Ultrabasic peridotite of the WLI. b) Harrisitic peridotite of the WLI. 1 m^2 quadrant for scale. 147

Figure 6.3 – Ultrabasic peridotite of the CI containing feldspathic intrusive material. Compass for scale. 147

Figure 6.4 – Troctolite found on the west side of the Long Loch Fault. 148

Figure 6.5 – Allivalite block displaying clear dipping cumulate layers. 148

Figure 6.6 – The visible grey layers are the troctolite that have acted as a low friction layers over which the orange peridotite megablock has moved. The basal facies is simialr in process to breccia type 5 shown below in Figure 2.11. Boulder in forground is 1 m across. 149

Figure 6.7 – Various examples of intrusive breccia: a) Pervasive intruding veins of feldspatchic peridotite at the CI-WLI boundary as in Figure 2.11.2. The clasts are not yet mobilised. b) A large heavily fractured allivalite clast with the mobilised intrusive breccia. c) Angular troctolite clasts that have been mobilised but over a short distance. Not talus deposits but similar to those shown in Figure 2.11.4. d) Very mobile breccia, the clasts appear to have rotataed and partially melted, as in Figure 2.11.5. 150

Figure 6.8 – Pebble breccia of the CI. Rounded peridotite clasts between 1 mm to 3 cm in size, within a feldspathic matrix. Pencil for scale. 151

Figure 6.9 - Map of the field study area. The Western Layered Intrusion and Central Intrusion are seperated by intrusive breccais and a layer of troctolite, with debris flows cascading down into the still active Central Intrusion within the magma chamber. Key localities are marked for orientation. Colour scheme based on the solid geology map compiled by Emeleus, 1994. 152

Figure 6.10 - Stratigraphic sequence of the igneous rocks in the study area. Thickness of the transitional peridotite unit, troctolite, allivalite and sliding basal unit all vary through the area. Combined thickness of those units may be ~20-50 m. 153

Figure 6.11 - West-east schematic (not to scale) cross-section through Loch Dornabac showing the stratigrahpy of the peridotite units and the relationship with the intrusive breccia. 154

Figure 6.12 – Localities A-G. 156

Figure 6.13 - Locality A. a) Heavy feldspathic veining within the WLI peridotite at the margin with the intrusive breccia. b) Intrusive matrix-supported breccia. Peridotite host rock is completely broken into clasts that have been disaggregated. 157

Figure 6.14 - View north at locality B. a) Breccia intruding vertically past the troctolite. b) Sketched boundaires shown in black and interpreted fault scarps in grey, mapped in Figure 6.9. 157

Figure 6.15 - Contact between the intrustive breccia and troctolite at locality B in Figure 6.13 At the margin the troctolite is partially melted and starting to be incorporated into the breccia matrix. Compass for scale. 158

Figure 6.16 - View to north at Locality C. Intrusive breccia flowing up and over underlying troctolite. The arrow shows the direction of flow. Note also the ~5 m right-lateral offset of the troctolite across the loch. Notebook for scale. 159

Figure 6.17 - View to north at Locality D. Intrusive breccia flowing over the top of the troctolite. The arrow shows the direction of flow. Notebook for scale. 159

Figure 6.18 - View to north at Locality E. Near sperical peridoite clast within the breccia flow. Troctolite bands flowing around the clast. The arrow shows the direction of flow. Compass for scale. 160

Figure 6.19 - View to north at Locality E. Heavily melted troctolite lobe rotating within the breccia flow. Melted troctolite is being incorporated into the matrix. The arrow shows the direction of flow. Compass for scale. 160

Figure 6.20 - Locality B. a) Heavily fractured troctolite. Looking east, bag for scale. b) Sheared troctolite breccia. looking NW, person for scale. 162

Figure 6.21 - View to north at Locality G. Pebble breccia onlapping onto a distal outcrop of the intrusive breccia. 163

Figure 6.22 - View to north at Locality F. Pebble breccia eroding into layered allivlite. A strip of allivalite can be seen being incorporated into the breccia. The clipboard provides a scale. 163

Figure 6.23 – Map of the faults allivalite in the SE of the field area. 164

Figure 6.24 – Hanging wall of a westerly dipping fault. Allivalite is being torn apart as it subsides, with a newly intruded matrix holding clasts in suspension. View to north, notebook for scale. 165

Figure 6.25 – Example of offset along fractures at transect 5. Individual fracture may have several centimetres of offset, but summed over the whole fracture zone this can add up to metres of offset. 167

Figure 6.26 – Rose diagrams for each of the sampled quadrants overlain on the map in Figure 6.9. They show fracture orientation and density for 37 quadrant sites. The size of the rose diagram is proportional to the peak number of fractures in one 10° bin. One grey square is 200 m. 168

Figure 6.27 – Location of the 6 transects within the WLI along the Central Ridge. Red lines show the transects, black lines are mapped fault zones. 170

Figure 6.28 – Visulisation of the data for the six transects. The dotted line shows the orientation of the transect. Solid black lines show the orientation of the fractures. Solid grey lines show the orientation of gabbro veins. Green polygons indicate there was no outcrop for this section. Scale in centimetres. 171

Figure 6.29 – Fracture density (fractures per metre) for each transect. Yellow coloured bins contain a mapped fault, red bins do not. 172

Figure 6.30 – Bi-directional rose diagram plots for all the transect data; three transects east and west of the gulley; and each of the individual 6 transects. For reference, the main gulley has a strike of 340°. 173

Figure 6.31 – Bi-directional rose diagram showing the strike of 49 fractures with observed left-lateral offset (blue), and 2 fractures with right lateral offset (red). 174

Figure 6.32 – a) Southward facing photo of exposure just to the north of transect 2. b) Faults are drawn in black, with a westward downthrown gabbro vein highlighted in grey. 176

Figure 6.33 - Troctolitic unit bounded by two faults. 177

Figure 6.34 – Sketch of mapped faults intersecting transect 2. Apparent left-lateral slip is visible on the top horizontal surface. Apparent vertical-slip is visible on the north-facing vertical exposure (Figure 6.32). Orange colour indicates peridotite, however, more feldspathic units (grey) are bounded by some of the faults. 177

Figure 6.35 - Sattelite imagery (Bing, 2015) with 405 highlighted lineaments. The study area has been divided east and west, then the west side has been divided in 3 sub-areas; Central, Ridge, Southern Ridge and An Dornabac. Rose diagrams for these areas are shown in Figure 6.37. 179

Figure 6.36 – Results from Mattsson et. al. (2014) of satellite image analysis. a) Satellite image analysis of lineaments assumed to represent fractures and faults with Rose diagram showing the strikes of the lineaments. b) Fault traces identified in the field projected onto a stereoplot. 180

Figure 6.37 - Bi-directional rose diagram plots for all the lineament traces data, east and west divisions either side of the Long Loch Fault, three divisions in the west: Central ridge, Southern ridge and An Dornabac. 181

Figure 6.38 – Bi-directions rose diagrams for a) all of the fractures data from the six transects, b) all the mapped faults in Figure 6.27, and c) the Central ridge zone lineaments. 182

Figure 6.39 - a) Sketch of the orientation and diretion of offset of the lineaments and fractures in Figure 6.27 relative to the Long Loch Fault. The observations do not correspond to Riedel Shears of a right-lateral strike-slip fault.b) Basic Riedel shear strutcutres forming right-lateral conjugate shear zones. R and R′ and synthetic and antithetic shear bands. Φ is the angle of internal friction (Katz *et al.*, 2004). b) Horse-tail splay termination at the end of a right-lateral strike-slip fault. d) Extensional duplex or negative flower-structure form where there is an offset in the plane of the main strike-slip fault. 185

Figure 6.40 – Simplified solid geology map of west of Long Loch with key structural features. 187

Figure 6.41 – Schematic 2D diagrams of the formation fo the intrusive breccia and peridotite siding block at the base of the active magma chamber. a) eastward dipping layered peridotite (orange) with troctolite layer (grey). b) Subsidence in the east due to magma evacuation. Intrusive breccia intrudes vertically. c) Peridotite block slides along lubricated troctolite layer. Breccia flows down over the top of the peridotite to the north. 189

Figure 7.1 – Frequency-length distributions of the Rum lineament data. Containg 405 measurements from Figure 6.35. a) Frequency-length distribution with 25 m bin size. b) Frequency-$\log_{10}$(length) distribution with 0.1 bin size. 196

Figure 7.2 – Frequency-magnitude distribution of the estimated magnitudes of the Rum lineaments dataset in Figure 6.35. Discrete frequency is plotted in red, and cumulaltive frequency in green. The workflow in Figure 3.9 is used to calculate the completenss magnitude (vertical dashed line). The maximum likelihood estimation of b (red and green lines) is $b = 1.87 \pm 0.40$. $Nc = 146$. 198

Figure 7.3 – 1D box-counting analysis of the 6 Rum transects (Section 6.4.2). The circles plot the fraction of intervals, p, of length r, that include at least one fracture. The solid line is the best-fit to a power-law distribution Equation [2.9]. In this case the fractal dimension D is the capacity dimension D_0. 200

Figure 7.4 – Plots as in Figure 7.3 but with a maximum cut-off in r defined by $p \leq 0.8$ instead of $p < 1.0$. 202

Figure 7.5 – The pair-correlation distribution, $C(r)$, as a function of spacing, r, for the 6 Rum transects. The solid line is the best fit correlation, described in Equation [2.14] for r up to half the total transect length. (vertical dashed line to the right on both diagrams). 203

Figure 7.6 - The near neaighbour distribution, $C(r)$, as a function of spacing, r, for the six Rum transects. The solid line is the best fit correlation. 205

Figure 7.7 – Schematic diagrams demonstrating how the 2D ruler method is used. a) an event with a known magntude but unknown focal mechanism is represented in 2D space as a circle. The randomly orientated transect (green line) cuts the circle. b) for the same event, if the focal mechansm was known the event could be represented as a line/fault plane (red line) rather than a circle; in this example the transect would not interset the line. 209

Figure 7.8 - 2D ruler method sampling of the 2011-2015 El Hierro data set. Circles represent one event with the diameter being equal to the rupture length calculated using Equation [7.1]. The minimum magnitude here is 3.0M. The lines are the randomly orientated transect lines, *r*, varying in length from 100-17783 m. There are 50 samples of each length.....210

Figure 7.9 - 2D ruler method sampling of the 2011-2015 El Hierro data set. The lines are the randomly orientated transect lines, r, varying in length from 100-17783 m. There are 1000 samples of each length. This shows complete sampling of the possible fault planes. 210

Figure 7.10 – Fraction of transects, *p*, of length *r*, that intersect an event for the 2011-15 El Hierro seismic catalogue. The circles represent the data and the solid line is the best-fit power law function described in the 'box-counting' method in Section 2.4.3. a) A mimimum magnitude of 2.0M with a minimum sampling length of *r*=18 m b) A mimimum magnitude of 3.0M with a minimum sampling length of *r*=100 m. c) A mimimum magnitude of 4.0M with a minimum sampling length of *r*=316 m. In all cases the maximum box length is 18000 m. The fractal dimensions *D* here are the capacity dimension D_0.....212

Figure 7.11 - The pair-correlation distribution, *C(r)*, as a function of spacing, *r*, for the 2011-15 El Hierro seismic catalgoue. 1D,2D and 3D distributions for M_{min}=3.0 and 4.0. The solid line is the best fit correlation function, described in Equation [2.14].....214

Figure 7.12 - The near neaighbour distribution, *C(r)*, as a function of spacing, *r*, for the 2011-15 El Hierro seismic catalogue. 1D, 2D and 3D distributions for M_{min}=3.0 and 4.0 The solid line is the best fit correlation.....215

Figure 7.13 – 2D box-counting plots for the 2011-15 El Hierro seismic catlogue. The circles given the fraction of transects, *p*, of length *r*, that intersect an event. The solid line is the best-fit correlation function described in Equation [2.9]. A, b and c) with sampling thresholds as in Figure 7.10. ...217

Figure 7.14 – a & c) Graphic representation of the Raw data from Table 7.1, Table 7.2 & Table 7.4 for the Rum transect data and El Hierro seismic catalogues. b & d) Average or selected values from these tables, previosuly highlighted in bold. Vertical error bars are the error calculated with the best-fit line to the distributions. Horizontal error bars show the range in *r* over which the line was fitted. The results for the box-counting method are blue and pair-correlation are green. 219

Figure 7.15 – Visual representation of fractures in Transect 5 showing high levels of clustering. 222

Figure 8.1 – Taken from figure 1 in Bell et al. 2013. Daily number of events (grey bars) and event rate (black line), used to forecast the eruption time. The dashed red line is a schematic illustration of the completeness magnitude *Mc*, showing how it may increase through time, as calculated using the iterative sampling technique. 230

Figure 8.2 – Stereoplot of the Central Intrusion, Rum, fault splay orientations from figure 43b in Mattsson *et al.* (2015). (Equal area plot of the lower hemisphere). 232

Figure 8.3 – Estimated focal mechanisms on Rum for a) The Long Loch Fault (strike = 000°, dip = 90°, rake = 180°), b) observed left-lateral strike-slip faults in the study area (strike = 339°, dip = 90°, rake = 0°), and c) transtensional faults with equal left-lateral and normal displacement, downthrow to the east with a dip of 80° (strike = 159°, dip = 80°, rake = -45°). Areas coloured blue represent those where compressional arrivals would have cut the lower focal hemisphere. Arrows indicate direction of slip and actual fault plane. 233

Figure 8.4 – Figure 6 from del Fresno *et al.* (2015) estimating focal mechaisms for a Mw 4.0 earthquake and its foreshocks. a) A comparison of the results obtained for the joint fault-plane solution of the whole cluster. b) The results of the M_w 4.0 obtained in their study through the amplitude spectra inversion. C) The automatic moment tensot (MT) solution of the M_w 4.0 earthquake of the real-time MT catalog of the Instituto Geografico Nacional. The annotated dots represent pressure (P-) and tension (T-) axes with the orientations described by their plunge and trend. 234

Figure 8.5 – Epicentral map distribution of the selected 111 focal mechanisms (lower hemisphere projection) and relative focal mechanisms. The inset displays the triangular diagram of focal mechanisms, where the vertices represent normal, thrust, and strike-slip focal mechanisms. The P and T axes are identified respectively by white and black dots. Figure 5 from Sicla *et al.* (2015). 235

Figure 8.6 - Example of one iteration of the iterative Voronoi sampling method using 20 Voronoi polygons. Some 16 of the 20 polygons contain the minimum threshold of 100 events. The average catalogue sizes are N=1530 and Nc=236. This figure shows the position of the Voronoi polygons relative to the El Hierro seismic catalogue (coloured dots). The crosses show the randomly generated points controlling the polygons positions. Black crosses show polygons with >100 events, red crosses show rejected polygons with <100 events. 239

Figure 8.7 - Example of 20 iterations of the iterative Voronoi sampling method using 20-200 Voronoi polygons. In total 634 polygons were accepted. The average catalogue sizes are N=637 and Nc=125. a) Position of the Voronoi polygons relative to the El Hierro seismic catalogue (coloured dots). The crosses show the randomly generated points controlling the polygons positions. Black crosses show accepted polygons with >100 events, red crosses show rejected polygons. b) Data points within accepted polygons that have been assigned b-values. Resolution of 0.01 degrees latitude/longitude. c) Contoured bP-value using data points from b). d) Contoured peak PbP values using data points from b). 240

A.3 – List of Tables

Table 2.1 – The relationship between seismic moment *M*, and earthquake magnitude *m*, (Equation [2.20]) to calculate the constant, *c*, in order to relate the fractal dimension *D*, and seismic *b-value b*, using Equation [2.24] (Legrand, 2002).....3939

Table 3.1 - Compilation of *b-values* and range of magnitudes for volcanic seismic catalogues.....50

Table 4.1 – Phases of seismic activity at El Hierro from July 2011 to Dec 2013 (Figure 4.5). A description of the inferred process of the events are given, the time and event ranges are stated. Phases 1-3 have been previously defined by (Ibanez *et al.*, 2012). Modal $\tilde{b}_P$ and appriximate 95% $\tilde{b}$ range are all identifed using Figure 4.3. The $\tilde{b}$-values given in the final column are from Figure 3.12 and shown in Figure 4.3b for comparison. *95% range estimated from PDF producing multi-modal errors in Figure 4.4iii.....95

Table 5.1 – Original parameters used for the random sampling method.....100

Table 5.2 – Sub-phases of El Hierro. Phase 1 containing high *b-values* identified in Figure 5.2. $\tilde{b}$ is the discrete value calculated using the workflow in Figure 3.9. $\tilde{b}_P$ is an estimate of the modal *b-value* during the sub-phase from Figure 5.2...104

Table 5.3 – 10 phases for the Mount Etna 1999-2014 seismic catalogue as defined in Section 3.7 and depicted in Figure 5.4. $\tilde{b}$ is the discrete value calculated using the workflow in Figure 3.9. $\tilde{b}_P$ is an estimate of the modal *b-value* during the sub-phase from Figure 5.4.....107

Table 5.4 – Summary of results from the application of the random sampling methodology to the eight volcanic seismic and two tectonic seismic catalogues.....139

Table 6.1 – Summary of the modal bin of the strikes, and mean fracture density for each transect and fractures with offset, in comparison to the strike of the main gulley.....178

Table 6.2 – Summary of observations for each of the three scales of measurement…172

Table 7.1 - Summary of the fractal dimensions calculated for each of the six Rum transects, using the 1D box-counting method to calculate *D0*; the 1D pair collection and 1D nearest neighbour methods to calculate *D2*.....207

Table 7.2 - Summary of the fractal dimensions calculated the El Hierro seismic catalogue for minimum magnitude thresholds of 2.0, 3.0 and 4.0M. The 1D box-

counting method was used to calculate *D0*; the 1D pair collection and 1D nearest neighbour methods to calculate *D2.* Italicised values are not used in the average.....216

Table 7.3 – Summary or 2D and 3D pair correlation results from Figure 7.11 showing with *D2* being exactly 1 greater in 3D due to the extra dimension of sampling.....217
217

Table 7.4 - Summary of the fractal dimensions calculated the El Hierro seismic catalogue for minimum magnitude thresholds of 2.0, 3.0 and 4.0M. The 2D box-counting method was used to calculate D0; *the* 2D pair collection and 2D & 3D nearest neighbour methods calculated D2. Italicised values are not used in the average.....218

Table 7.5 - Summary of the fractal dimension from the box-counting ($p<0.8$) and the pair correlation methods for Rum and El Hierro. All box-counting values are averages. The pair-correlation value for Rum is an average but the two values for El Hierro are deemed to be the most reliable results.....220

Table 8.1 –Dip and strike of the Maximum ($\sigma1$ and $\varepsilon1$), Intermediate ($\sigma2$ and $\varepsilon2$) and compressive ($\sigma3$ and $\varepsilon3$) stress and strain axes, at Mount Etna using data set B, from Table 2 in Sicali *et al.* (2015).....236

Appendix B – Spatio-Temporal Evolution of Seismicity for Seismic Catalogues in Chapter 5

Here two figures are presented for each of the 11 catalogues in Chapter 5. In Chapter 5 the $\tilde{b}$-value probability density function is presented by event number; here in the first figure the results are instead plotted by time for a) the magnitude of events and completeness magnitude, b) the daily and cumulative event rates, and c) the $\tilde{b}$-value probability density function. In the second figure the hypocentre and epicentres of every event in the sampled catalogue are plotted.

B.1 – El Hierro

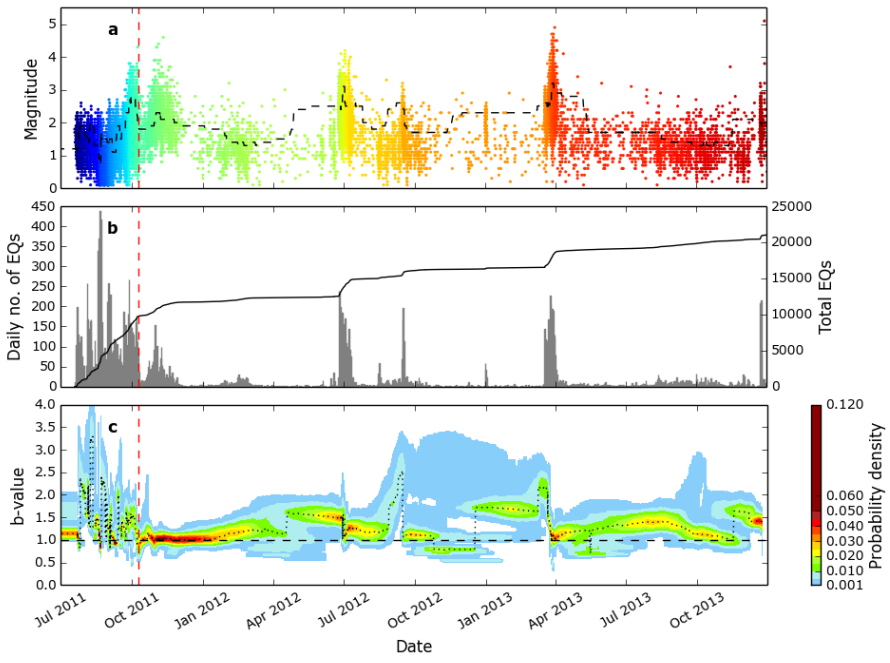

Appendix B.1 – El Hierro 2011-2013 catalogue showing: a) magnitude of events through time. The completeness magnitude is marked with the dashed black line. b) Daily event rate and cumulative number of events. c) $\tilde{b}$-value probability density function plotted by date. The dotted black line shows peak $\tilde{b}_P$. For all the vertical red dashed line shows the date of the eruption.

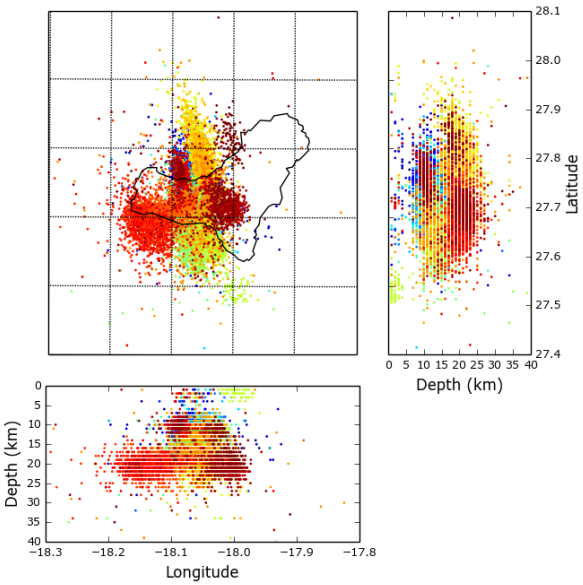

Appendix B.2 - Hypocentres and epicentres of earthquakes at El Hierro from 2011-2013. Events are coloured blue to red from oldest to most recent.

B.2 – Mt. Etna

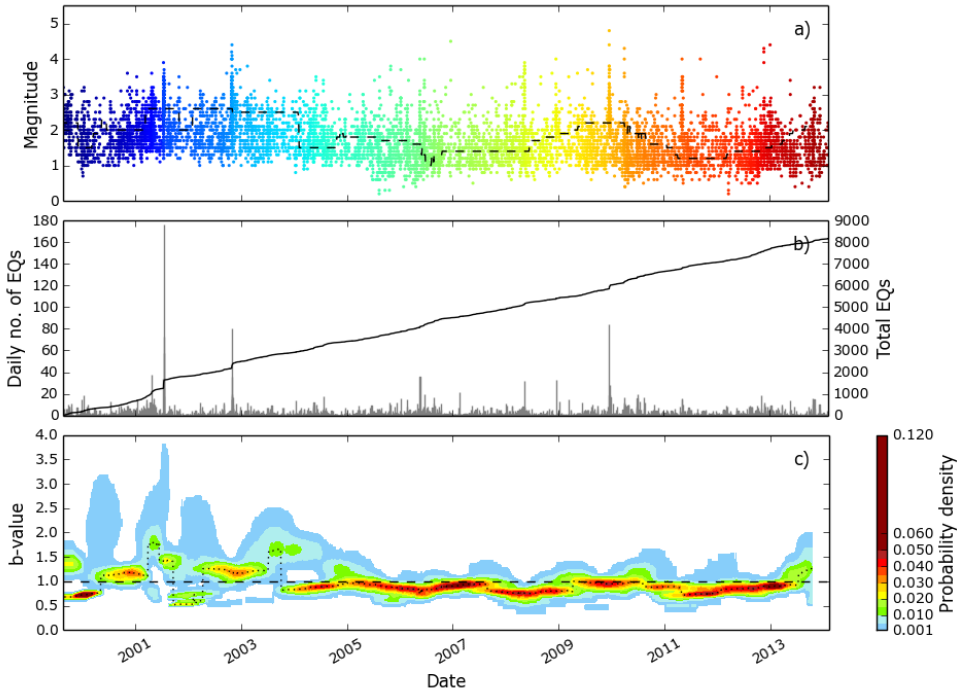

Appendix B.3 – Mount Etna 1999-2014 catalogue showing: a) magnitude of events through time. The completeness magnitude is marked with the dashed black line. b) Daily event rate and cumulative number of events. c) $\tilde{b}$-value probability density function plotted by date. The dotted black line shows peak $\tilde{b}_P$.

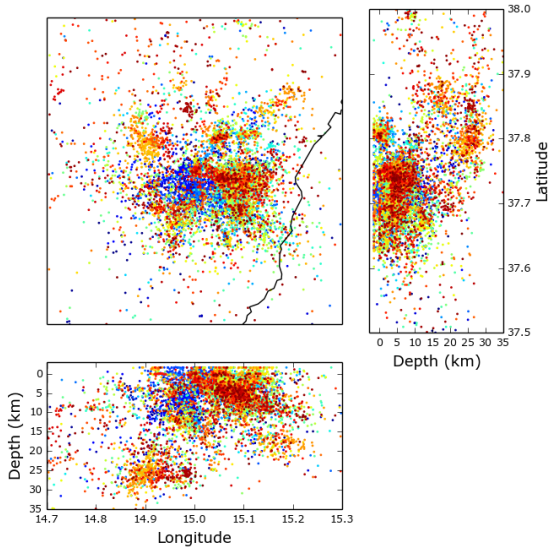

Appendix B.4 - Hypocentres and epicentres of earthquakes at Mount Etna from 1994-2014. Events are coloured blue to red from oldest to most recent.

B.3 - Kilauea

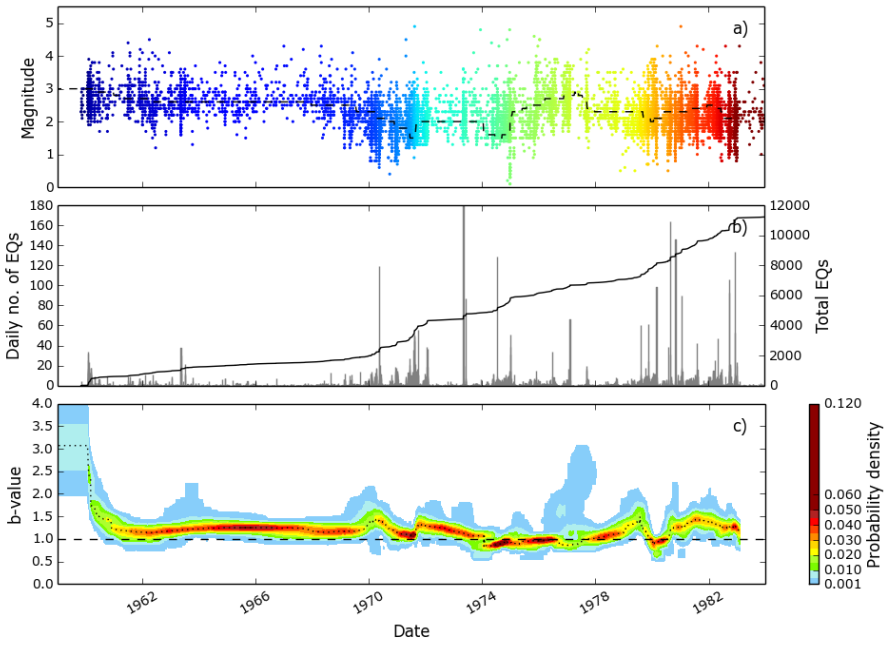

Appendix B.5 - Kilauea 1959-1984 catalogue showing: a) magnitude of events through time. The completeness magnitude is marked with the dashed black line. b) Daily event rate and cumulative number of events. c) $\tilde{b}$-value probability density function plotted by date. The dotted black line shows peak $\tilde{b}_P$.

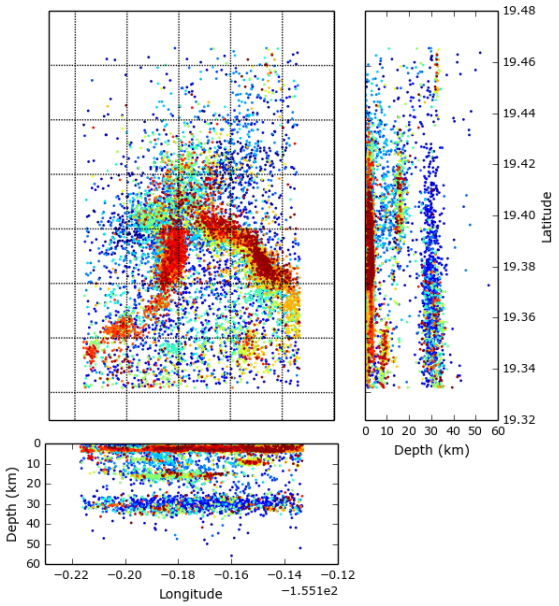

Appendix B.6 - Hypocentres and epicentres of earthquakes at Kilauea caldera from 1959-1984. Events are coloured blue to red from oldest to most recent.

B.4 - Tungurahua

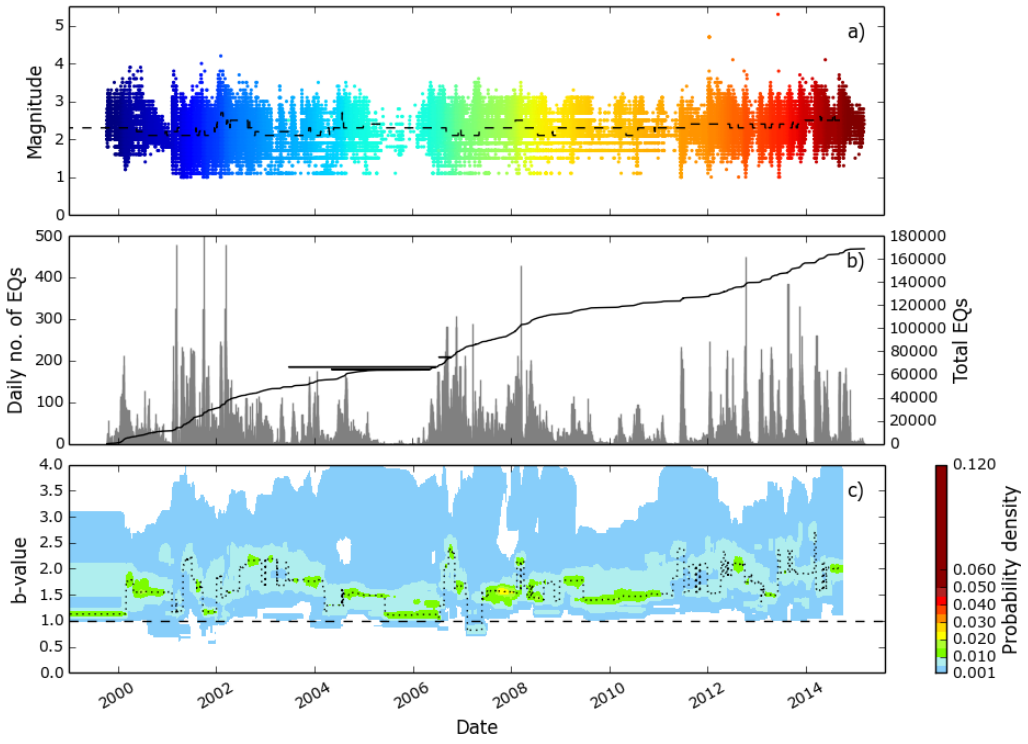

Appendix B.7 - Tungurahua 1999-2013 catalogue showing: a) magnitude of events through time. The completeness magnitude is marked with the dashed black line. b) Daily event rate and cumulative number of events. c) $\tilde{b}$-value probability density function plotted by date. The dotted black line shows peak $\tilde{b}_P$.

B.5 - Bárðarbunga

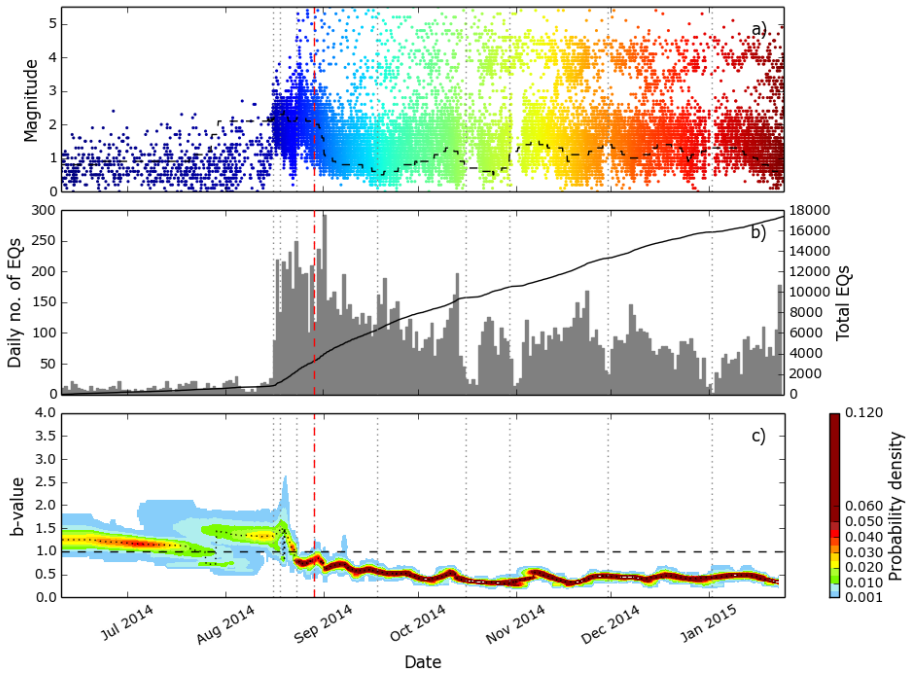

Appendix B.8 – Entire Bárðarbunga June 2014 to January 2015 catalogue showing: a) magnitude of events through time. The completeness magnitude is marked with the dashed black line. b) Daily event rate and cumulative number of events. c) $\tilde{b}$-value probability density function plotted by date. The dotted black line shows peak $\tilde{b}_P$. For all the vertical red dashed line shows the date of the eruption.

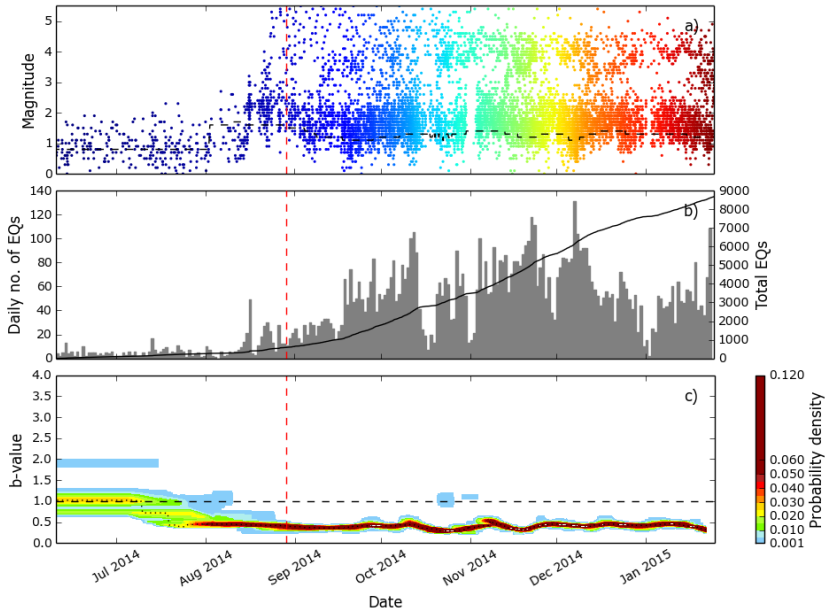

Appendix B.9 – Bárðarbunga caldera catalogue from June 2014 to January 2015 showing: a) magnitude of events through time. The completeness magnitude is marked with the dashed black line. b) Daily event rate and cumulative number of events. c) $\tilde{b}$-value probability density function plotted by date. The dotted black line shows peak $\tilde{b}_P$. For all the vertical red dashed line shows the date of the eruption.

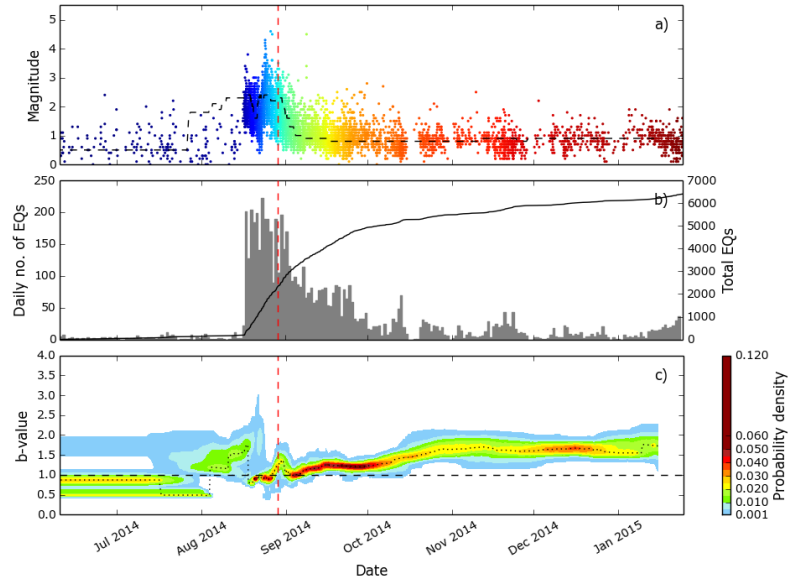

Appendix B.10 - Bárðarbunga dyke catalogue from June 2014 to January 2015 showing: a) magnitude of events through time. The completeness magnitude is marked with the dashed black line. b) Daily event rate and cumulative number of events. c) $\tilde{b}$-value probability density function plotted by date. The dotted black line shows peak $\tilde{b}_P$. For all the vertical red dashed line shows the date of the eruption.

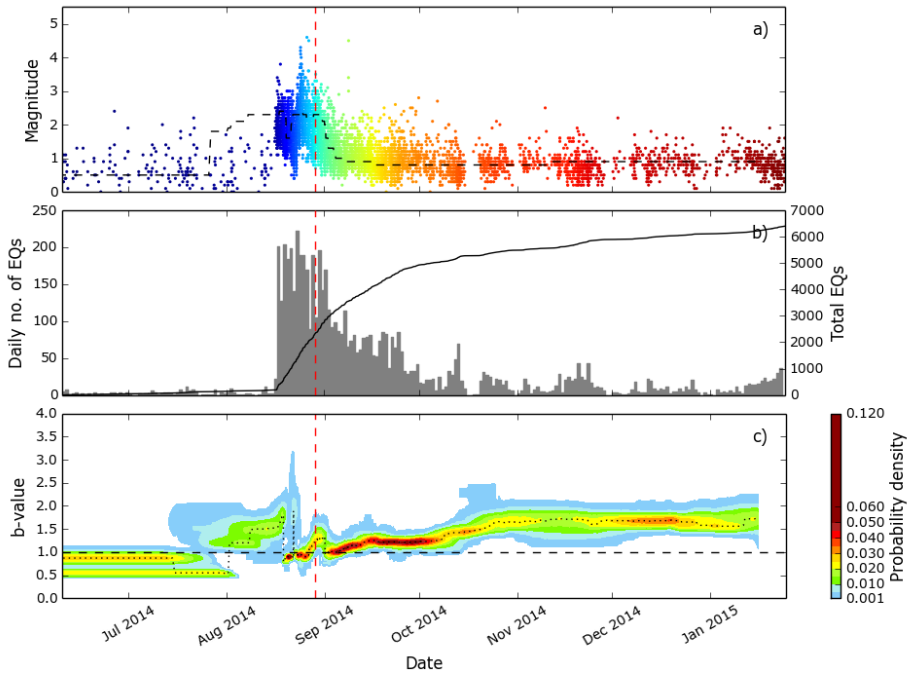

Appendix B.11 - Bárðarbunga eruption catalogue from June 2014 to January 2015 showing: a) magnitude of events through time. The completeness magnitude is marked with the dashed black line. b) Daily event rate and cumulative number of events. c) $\tilde{b}$-value probability density function plotted by date. The dotted black line shows peak $\tilde{b}_P$. For all the vertical red dashed line shows the date of the eruption.

B.6 - Grímsvötn

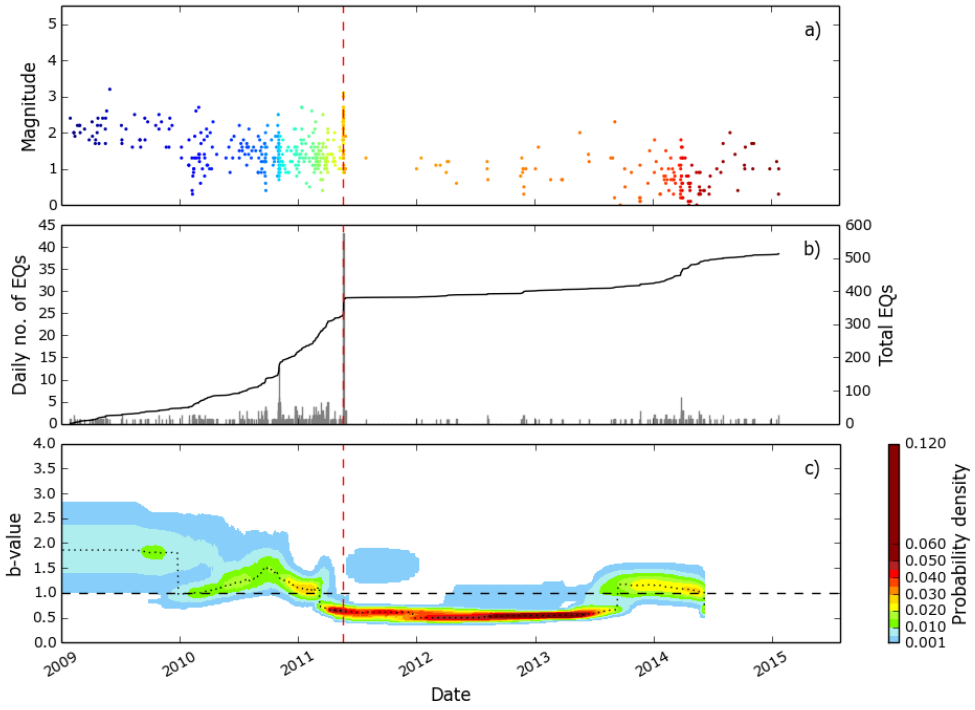

Appendix B.12 - Grímsvötn 2009-2015 catalogue showing: a) magnitude of events through time. The completeness magnitude is marked with the dashed black line. b) Daily event rate and cumulative number of events. c) $\tilde{b}$-value probability density function plotted by date. The dotted black line shows peak $\tilde{b}_P$. For all the vertical red dashed line shows the date of the eruption.

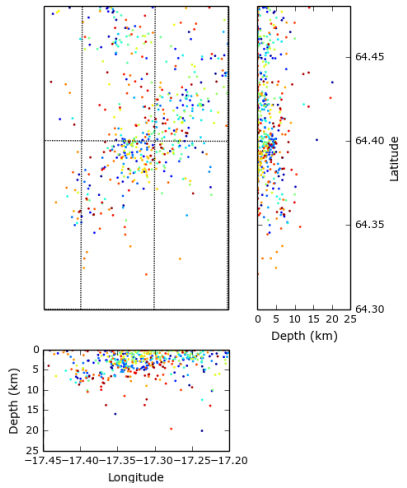

Appendix B.13 - Hypocentres and epicentres of earthquakes at Grímsvötn from 2009-2015. Events are coloured blue to red from oldest to most recent.

B.7 Eyjafallajökull

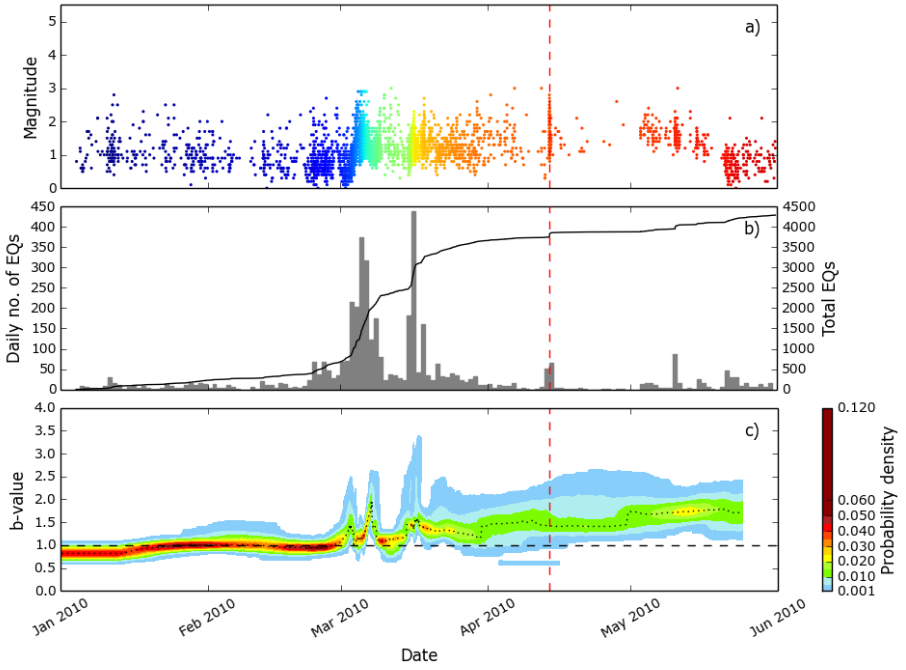

Appendix B.14 - Eyjafallajökull catalogue from January to June 2010 showing: a) magnitude of events through time. The completeness magnitude is marked with the dashed black line. b) Daily event rate and cumulative number of events. c) $\tilde{b}$-value probability density function plotted by date. The dotted black line shows peak $\tilde{b}_P$. For all the vertical red dashed line shows the date of the eruption.

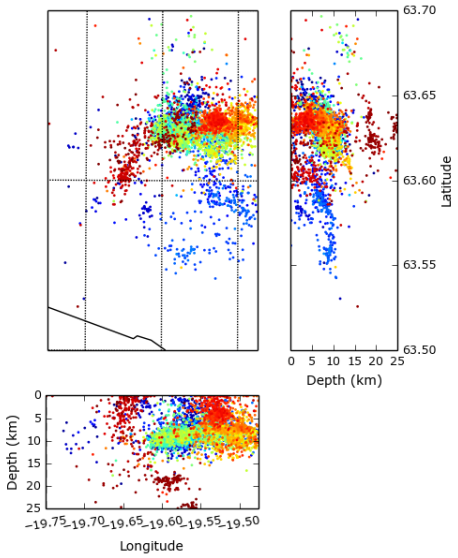

Appendix B.15 - Hypocentres and epicentres of earthquakes at Eyjafallajökull from 2009-2015. Events are coloured blue to red from oldest to most recent.

B.8 - Katla

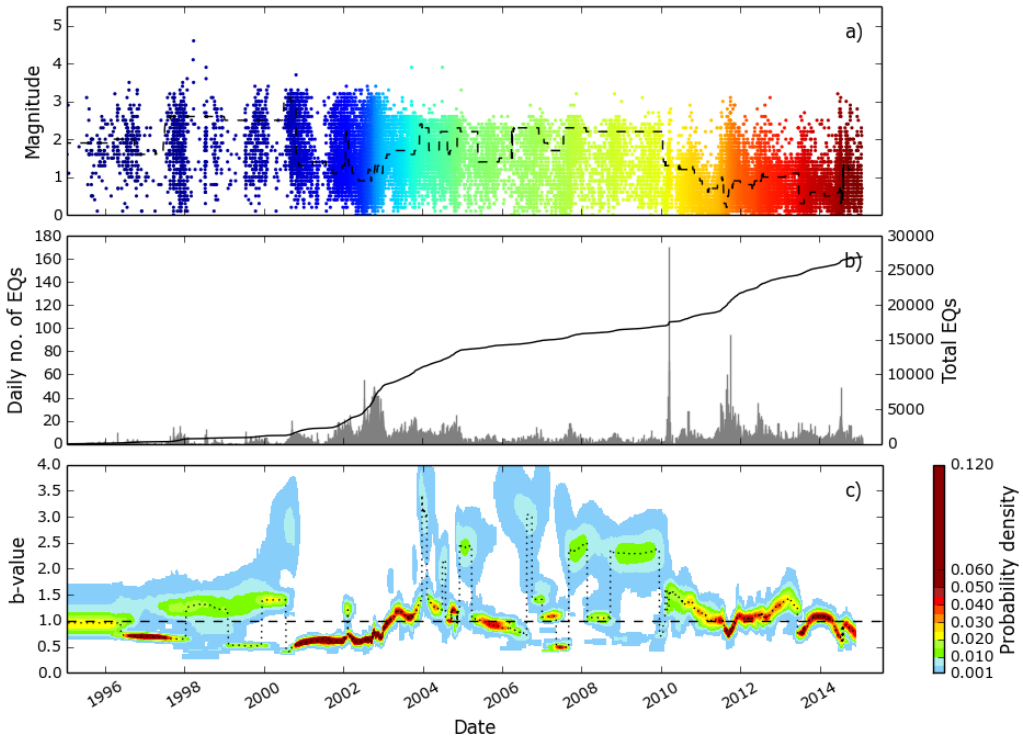

Appendix B.16 – Katla 1995 to 2015 catalogue showing: a) magnitude of events through time. The completeness magnitude is marked with the dashed black line. b) Daily event rate and cumulative number of events. c) $\tilde{b}$-value probability density function plotted by date. The dotted black line shows peak $\tilde{b}_P$.

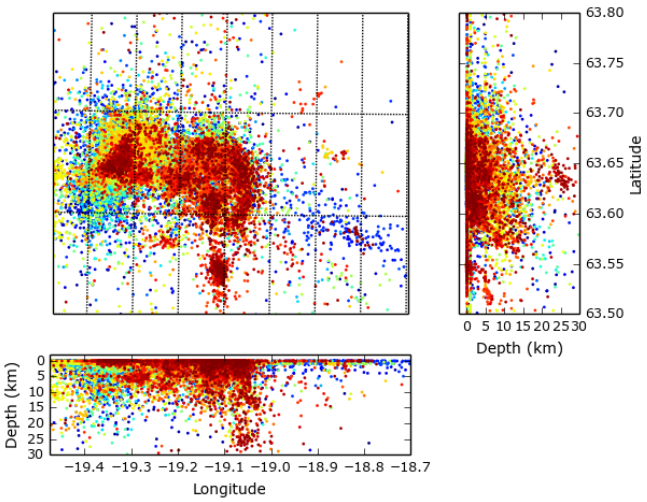

Appendix B.17 - Hypocentres and epicentres of earthquakes at Katla from 1995-2015. Events are coloured blue to red from oldest to most recent.

B.9 - Tjörnes Fracture Zone

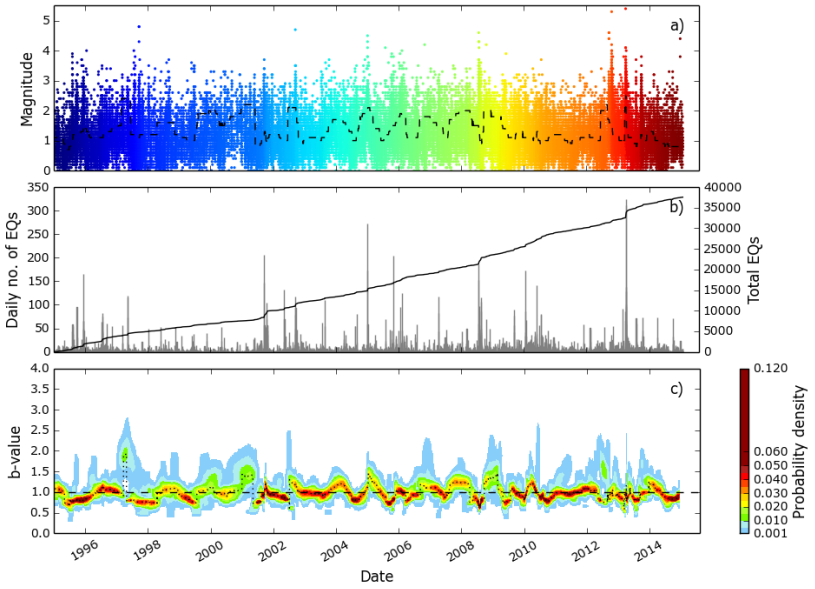

Appendix B.18 – North-east Tjörnes Fracture Zone 1995 to 2015 catalogue showing: a) magnitude of events through time. The completeness magnitude is marked with the dashed black line. b) Daily event rate and cumulative number of events. c) $\tilde{b}$-value probability density function plotted by date. The dotted black line shows peak $\tilde{b}_P$.

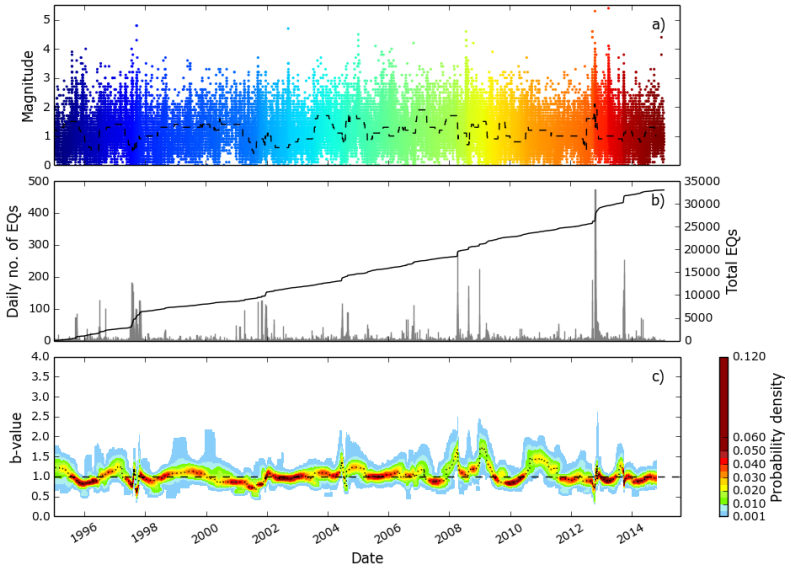

Appendix B.19 – South-west Tjörnes Fracture Zone 1995 to 2015 catalogue showing: a) magnitude of events through time. The completeness magnitude is marked with the dashed black line. b) Daily event rate and cumulative number of events. c) $\tilde{b}$-value probability density function plotted by date. The dotted black line shows peak $\tilde{b}_P$

B.10 – South Iceland Seismic Zone

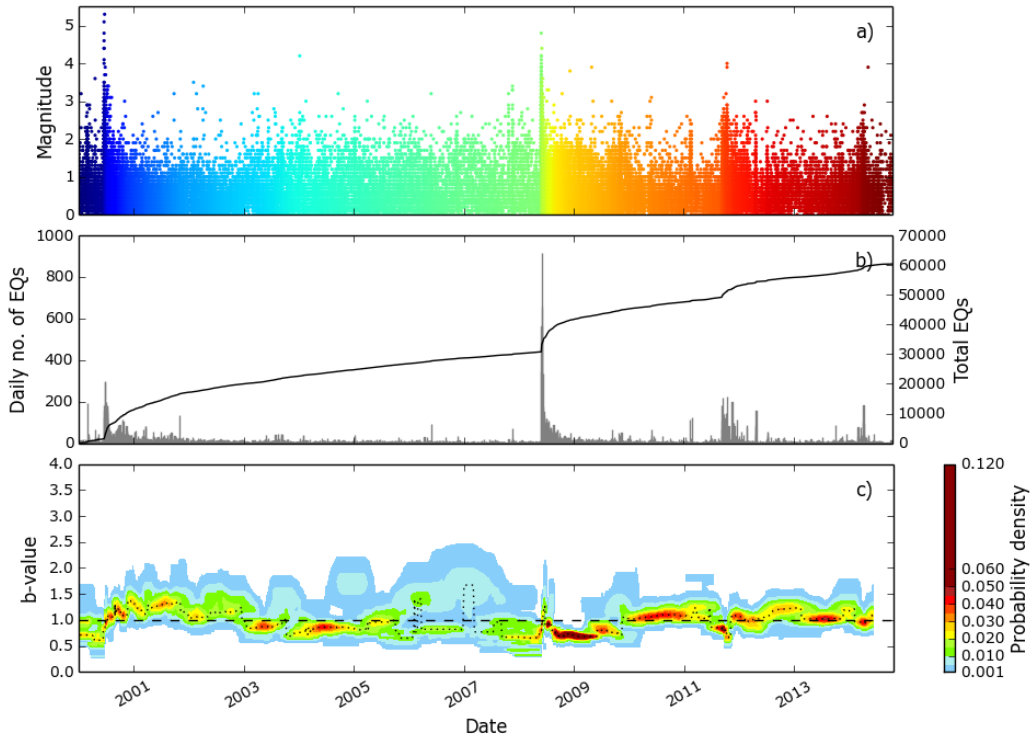

Appendix B.20 – South Iceland Seismic Zone 2000 to 2015 catalogue showing: a) magnitude of events through time. The completeness magnitude is marked with the dashed black line. b) Daily event rate and cumulative number of events. c) $\tilde{b}$-value probability density function plotted by date. The dotted black line shows peak $\tilde{b}_P$.

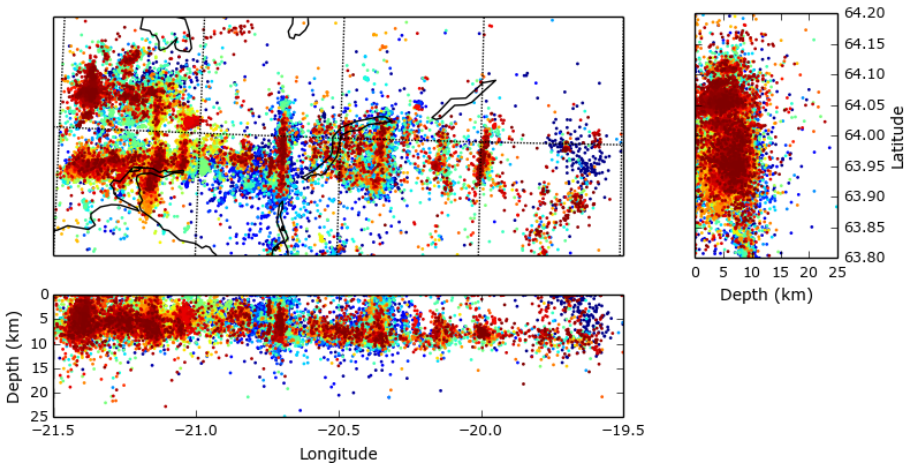

Appendix B.21 - Hypocentres and epicentres of earthquakes at the South Iceland Seismic Zone from 2000-2015. Events are coloured blue to red from oldest to most recent.

B.11 - Southern California

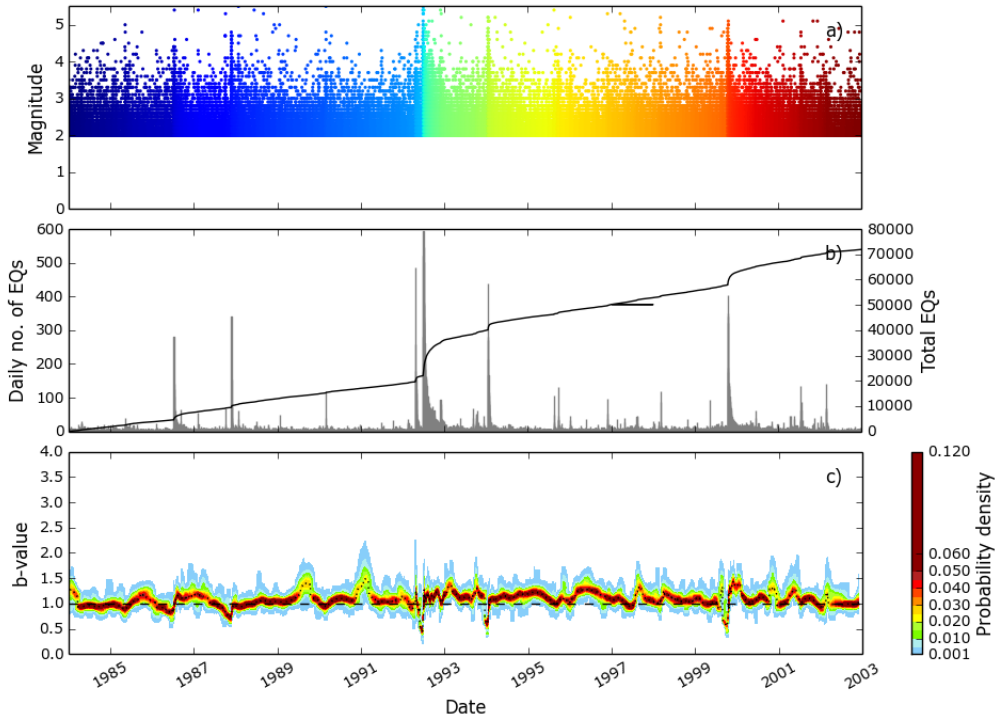

Appendix B.22 – Southern California 1984 - 2002 catalogue showing: a) magnitude of events through time. The completeness magnitude is marked with the dashed black line. b) Daily event rate and cumulative number of events. c) $\tilde{b}$-value probability density function plotted by date. The dotted black line shows peak $\tilde{b}_P$.

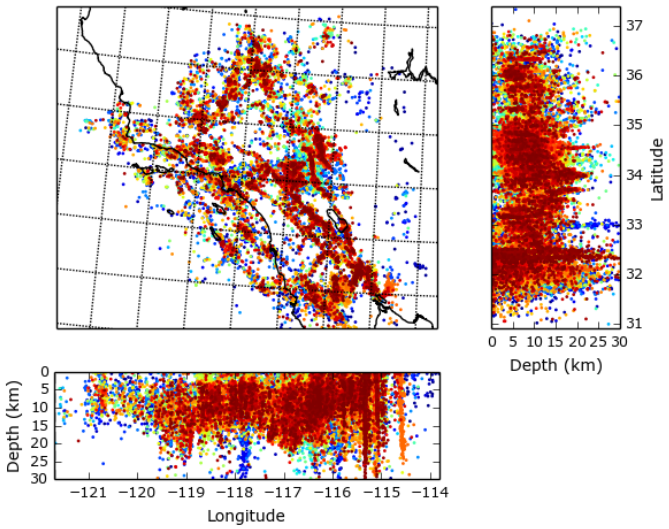

Appendix B.23 - Hypocentres and epicentres of earthquakes in Southern California from 1984-2002. Events are coloured blue to red from oldest to most recent.

Appendix C – Rum transect data

The following sections (B.1 – B.6) contain the raw data from the six Rum transects used in section 6.4. The column headings are as follows:

1 Fracture number/°
2 Type of fracture: v- vein, gv - gabbro vein, wv – white vein. 'Grass' means no outcrop, FZ – fault zone.
3 Strike/°
4 Spacing from previous fracture/ cm
5 Cumulative spacing/ m
6 Transect strike/°
7 Fracture count per metre
8 Fracture density per metre
9 Dip/°
10 Dip direction/°
11 Fracture width/ mm
12 Horizontal offset minimum/ mm
13 Horizontal offset maximum/ mm
14 Horizontal offset direction
15 Vertical offset minimum/ mm
16 Vertical offset maximum/ mm
17 Vertical offset direction

C.1 – Transect 1

1	2	3	4	5	6	7	8	9	10	11
1	v	320	45	0.45	38					
2	v	323	20	0.65						
3	v	314	0.9	0.659						
4	v	85	6.3	0.722						
5	v	0	0.5	0.727		5	5.0			
6	v	284	57	1.297						
7	v	307	1	1.307		2	2.0			
8	v	314	89	2.197	52					
9	v	309	17	2.367						
10	v	328	6	2.427						
11	v	349	10	2.527						
12	v	5	0.5	2.532						
13	v	358	32	2.852						
14	v	345	14	2.992		7	7.0			
15	v	2	5	3.042						
16	wv	338	12.5	3.167						1
	GRASS		15	3.317						
17	v	327	26	3.577						
18	v	26	20.5	3.782						
19	v	331	18	3.962		5	6.2			
	GRASS		7	4.032	65					
20	v	278	46	4.492						
21	v	353	2.4	4.516						
22	v	346	1.8	4.534						
23	v	354	8	4.614						
24	gv	346	1.3	4.627				8	E	3
25	v	341	26	4.887						
26	v	321	6.5	4.952						
27	v	335	1.2	4.964		8	8.3			2
28	v	328	10	5.064						
29	v	331	1.7	5.081						
30	v	328	8.5	5.166						
			18	5.346						
	GRASS		12	5.466						
31	v	307	16	5.626				70	E	
32	v	349	8	5.706						
33	v	322	15	5.856						
34	v	327	1.8	5.874		7	8.0			
35	v	12	15	6.024						
	GRASS		16	6.184						
36	v	332	8	6.264						
37	v	329	7.5	6.339						
38	v	343	4	6.379						
39	v	300	14.5	6.524						
40	v	299	0.8	6.532						
41	v	311	15	6.682				71	W	
42	v	1	1	6.692						
43	v	27	8.5	6.777						
44	v	275	11	6.887		10	11.9			
45	v	15	12	7.007						

1	2	3	4	5	6	7	8	9	10	11
46	v	288	4.5	7.052						
			26	7.312						
	GRASS		28	7.592						
47	v	324	5.5	7.647	38					
48	v	310	24	7.887						
49	v	316	9.3	7.98		5	6.9			
50	v	315	10	8.08						
51	v	337	18.5	8.265						
52	v	342	2.1	8.286						
53	v	313	17	8.456						
54	v	315	3.8	8.494						
56	v	311	32	8.814						
57	v	309	9	8.904		7	7.7			
	GRASS		25	9.154						
58	v	347	7	9.224						
59	v	346	2.3	9.247						
60	v	342	8	9.327						
	GRASS		13	9.457						
61	v	289	0	9.457						
62	v	315	16	9.617						
63	v	316	10	9.717						
64	v	278	6.5	9.782						
65	v	317	3.5	9.817		8	11.2			
66	v	312	21	10.03						
67	v	266	6.7	10.09						
	GRASS		73	10.82						
68	v	267	4.1	10.87						
69	v	249	0.9	10.87						
70	v	280	4	10.91						
			8	10.99		5	18.9			
	GRASS		66	11.65						
71	v	313	2.7	11.68						
72	v	359	1.8	11.7						
73	v	280	12	11.82						
74	v	291	4	11.86		4	11.6			
75	v	315	32	12.18						
76	gv	229	4	12.22						
77	gv	343	4	12.26				65	SE	2
78	v	241	1.5	12.27				32	E	4
79	v	221	5.3	12.33				45	N	
80	v	225	1.3	12.34				63	S	
81	v	276	21	12.55						
82	v	283	31	12.86						
83	v	329	3.3	12.89		7	7.0			
84	v	332	12.5	13.02						
85	wv	337	39	13.41						1
			26	13.67		2	3.0			
	GRASS		58	14.25						
86	v	270	0	14.25						
87	v	292	16.5	14.41						
88	v	300	0.1	14.41						
89	v	302	0.3	14.42						
90	wv	323	4.4	14.46						

1	2	3	4	5	6	7	8	9	10	11
91	v	343	7.2	14.53				77	E	1
92	v	266	32	14.85						
			14	14.99		7	9.4			
	GRASS		680	21.79	43					
93	v	18	12	21.91						
94	v	4	0.8	21.92	35	2	9.7			
			16	22.08						
	GRASS		53	22.61						
95	v	24	16	22.77						
96	v	295	4.2	22.81						
97	v	295	7.3	22.89						
98	gv	46	8	22.97		3	6.4			
99	v	295	22	23.19				72	S	2
100	v	307	5.3	23.24						
101	v	242	30	23.54						
102	v	0	19	23.73						
103	v	313	3	23.76						
104	v	46	8	23.84						
105	v	330	4.8	23.89		7	7.0			
106	v	299	50	24.39						
107	v	304	1.5	24.4						
108	v	301	22	24.62						
109	v	56	9.5	24.72						
110	v	300	6.9	24.79						
111	v	315	0.7	24.79						
112	v	318	10	24.89						
113	v	60	7.6	24.97		8	8.0			
114	v	298	15	25.12						
115	v	61	1.8	25.14						
116	v	298	36	25.5						
117	v	61	20	25.7						
118	v	59	12	25.82	27					
119	v	301	5	25.87						
120	v	303	4.5	25.91						
121	v	312	1.8	25.93						
122	v	333	4.1	25.97		9	9.0			
123	v	334	10	26.07						
124	v	301	1.3	26.08						
125	v	55	19.5	26.28						
126	v	301	5.2	26.33						
127	v	323	7.5	26.41						
128	v	53	4	26.45						
129	v	67	29	26.74						
130	v	305	10	26.84		8	8.0			
131	v	346	55	27.39						
132	v	295	6.6	27.45						
133	v	265	3.3	27.49						
134	v	345	14	27.63						
135	v	289	18	27.81						
136	v	291	6.5	27.87						
136	v	268	2.7	27.9		7	7.0			
137	v	280	15	28.05						
138	v	262	8	28.13						

1	2	3	4	5	6	7	8	9	10	11
139	v	47	18	28.31					1	
140	wv	337	7	28.38					3	
141	wv	51	2.5	28.4						
142	v	317	16	28.56						
143	v	320	17	28.73						
144	v	304	12	28.85		8	8.0			
145	v	50	16	29.01						
146	v	294	4	29.05						
147	v	54	14	29.19						
148	v	323	19	29.38						
149	v	327	16	29.54						
150	wv	56	4.9	29.59					1	
151	v	321	7.5	29.67						
152	v	300	6.6	29.73						
153	v	326	11.5	29.85		9	9.0			
154	v	324	20	30.05						
155	v	302	29.5	30.34	53					
156	v	32	20	30.54						
157	v	319	4	30.58						
158	v	327	2.8	30.61						
159	v	262	5.8	30.67						
160	v	298	2.5	30.69						
161	v	25	10	30.79						
162	v	23	10	30.89						
163	v	347	4.5	30.94						
164	v	335	2.2	30.96						
165	v	337	0.8	30.97						
166	v	328	2.8	31		13	13.0			
167	wv	320	3.6	31.03						
168	v	21	95	31.98		2	2.0			
169	Wv	301	20	32.18						
170	v	33	29	32.47						
171	v	312	20	32.67						
172	v	336	8	32.75		4	4.0			
173	v	317	36	33.11						
174	wv	294	36	33.47					2	
175	v	320	20.5	33.68						
176	v	348	11	33.79						
177	v	343	0.4	33.79						
178	v	1	8.8	33.88		6	6.0			
179	v	311	15	34.03						
	GRASS		55	34.58						
180	v	299	4	34.62						
181	v	289	5.5	34.67						
182	v	0	6	34.73						
183	v	273	18	34.91		5	11.1			
184	v	238	9.5	35.01						
			5	35.06						
	GRASS	FAULT	68	35.74						
185	v	317	1.5	35.75	48					
186	v	356	1.7	35.77						
187	v	347	1.5	35.79						
188	v	246	2.7	35.81						

1	2	3	4	5	6	7	8	9	10	11
189	v	347	0.3	35.82						
190	v	342	2.4	35.84					3	
192	v	359	2.5	35.87						
193	v	349	7	35.94		8	25.0			
194	v	305	13	36.07						
195	wv	342	2	36.09						
196	v	0	12	36.21						
197	v	295	11	36.32						
198	v	281	19	36.51						
199	v	270	17	36.68						
200	v	277	14	36.82						
201	v	306	1.8	36.83						
202	v	4	13	36.96		9	9.0			
203	wv	331	21	37.17						
204	v	313	6.5	37.24					1	
			6	37.3						
	GRASS		16	37.46						
205	v	343	4	37.5						
206	v	326	11	37.61						
207	v	271	5	37.66						
208	v	308	4.7	37.71						
209	v	36	8	37.79		7	8.3			
210	v	307	32	38.11						
211	v	295	2.6	38.13						
212	wv	54	8	38.21		3	14.2			

C.2 – Transect 2

1	2	3	4	5	6	7	8	9	10	11	12	13	14	15	16	17
213	v	354	43	0.430	46					1						
214		322	6.7	0.497												
215		295	2	0.517						2	0	22	R			E down
216		332	6	0.577						1						
217		294	5.5	0.632												
218		304	6	0.692												
219		298	0.3	0.695												
220		281	7	0.765		8	8.04			1						
			23	0.995												
	GRASS		24	1.235												
221		9	3	1.265												
222		19	2.7	1.292												
223		347	2	1.312												
224		9	4.1	1.353												
225		14	4	1.393												
226		323	5.5	1.448												
F1	FZ	336	2.1					82	E	220						
227		338	2.1	1.469												
228		15	2.2	1.491												
229		316	4	1.531							170	170	L			E down
230		322	1.7	1.548												
231		308	0.5	1.553												
232		303	1.4	1.567												
233		284	1.3	1.580												
234		314	1.3	1.593												
235		358	2	1.613												
236		327	0.6	1.619						3						
237		343	0.8	1.627						1						
238		265	1.6	1.643												
239		321	2.2	1.665												
240		324	1.1	1.676												
241		329	1.6	1.692												
242		336	0.4	1.696						6						
243		342	3.2	1.728												
244		260	1.9	1.747		24	31.4									
245		10	47	2.217												
##		11	5.5	2.272												
##		331	5.5	2.327												
249		9	6.3	2.390												
			8	2.470												
	GRASS		13	2.600												
250		255	0	2.600												
251		352	3.8	2.638												
252		333	2.7	2.665												
253		304	10	2.765												
254		332	1.3	2.778		9	13.9									

1	2	3	4	5	6	7	8	9	10	11	12	13	14	15	16	17
			0	2.778												
	GRASS		43	3.208												
255		333	0													
F2	FZ	333	18	3.388	7764S			71E		750						
256		331	18	3.568						4						
257		342	2	3.588												
258		270	3.4	3.622												
259		343	3	3.652												
			0	3.652												
	GRASS		11													
260		295	2.6	3.678												
261		265	5.2	3.730												
262		343	5	3.780												
263		356	9.2	3.872												
264		262	0.8	3.880						4						
265		331	4	3.920		11	16.1			3	42	56	L	19	52	E down
266		336	12	4.040												
267		353	15	4.190												
268		336	0.5	4.195										16	22	E down
269	GV	341	2.6	4.221						8						
270		338	1.4	4.235												
271		340	1.5	4.250												
272		334	6.9	4.319												
273		335	27	4.589		7	7									
			92	5.509												
	GRASS		16	5.669												
274		333	21	5.879												
F3	FZ	326	4					87E		210						
275		339	4	5.919						11						
276		336	0.6	5.925												
277		335	0.4	5.929						1						
278		354	0.2	5.931												
279		322	4.3	5.974		6	7.14									
280		332	5.1	6.025						13						
281		338	1	6.035												
282		344	0.8	6.043												
283		338	5	6.093												
284		320	4	6.133												
285		325	3	6.163												
286		275	7	6.233												
287		277	3	6.263												
288		328	11.5	6.378												
289		325	4.1	6.419												
290		287	4	6.459												
291	GV	323	3	6.489						2						
292		346	25	6.739												
293		331	14	6.879												
			0	6.879		15	17.1									
	Grass		39	7.269												

1	2	3	4	5	6	7	8	9	10	11	12	13	14	15	16	17
294	WV	5	0	7.269	85											
295	WV	356	6.5	7.334												
296	WV	23	6.5	7.399												
297	WV	22	45	7.849												
298	WV	35	2	7.869												
299	WV	25	6.8	7.937												
300	WV	32	3.4	7.971												
301	WV	35	1	7.981												
302	WV	30	0.9	7.990		9	12.3									
303		21	30	8.290												
304	304	327	29	8.580		2	2			6						
305	305	56	66	9.240						4						
			64	9.880		1	1.14									
	Grass		20	10.080												
306		61	18	10.260												
307	GV	324	13	10.390						1						
			52	10.910		2	2.41									
	Grass		19	11.100												
308		336	33	11.430												
309	GV	274	26	11.690		1	1.11	38	S	7						
310		289	36	12.050												
			9	12.140												
	GRASS		76	12.900		1	4.17									
			52	13.420												
	GRASS		13	13.550												
311	WV	344	3	13.580												
312	WV	1	29	13.870		2	2.3			1						
313	WV	335	141	15.280						1						
314		268	63	15.910		2	2									
315		41	17	16.080		1	1									
316		63	143	17.510		1	1									
			82	18.330												
	GRASS		34	18.670												
F4	FZ	340	23					86	E	690	36	81	L			
317		332	23	18.900						5						
318		340	4	18.940												
319		344	1.5	18.955		3	4.55									
320		2	16	19.115												
321		66	5	19.165												
322		26	3.5	19.200												
323		1	1.8	19.218												
324		346	1.3	19.231												
325		345	1.7	19.248												
326		40	3	19.278												
327		332	4.7	19.325												
328		21	5.3	19.378												
329		346	0.5	19.383												
330		358	2	19.403												

1	2	3	4	5	6	7	8	9	10	11	12	13	14	15	16	17
331		9	2.3	19.426												
332		11	0.5	19.431												
333		7	1.8	19.449												
334		11	2.6	19.475												
335		355	2.1	19.496												
336		12	2	19.516												
337		4	2.1	19.537												
338		359	1.6	19.553						7	36	81	L			
339		7	2.2	19.575												
340		354	1.1	19.586												
341		253	5.5	19.641												
342		4	5.1	19.692												
343		355	4.9	19.741												
344		257	11	19.851												
345		250	9.5	19.946		26	27.5									

C.3 – Transect 3

1	2	3	4	5	6	7	8	11	12	13	14
714	WV	321	8.7	0.087	55						
715	WV	305	12.5	0.212							
716		270	32	0.532		3	3.0				
717		256	47	1.002							
			6	1.062							
	GRASS		44	1.502							
718		324	6.5	1.567							
719		332	3.7	1.604							
720		333	0.2	1.606							
721		331	7	1.676				1			
722		331	4.5	1.721							
723		335	21.5	1.936							
724		328	2	1.956							
725		357	4.1	1.997		9	16.1				
726		289	1	2.007							
727		267	2.1	2.028							
728		259	1.1	2.039							
F14		332	17.5	2.214				12	35	65	L
729		330	17.5	2.214					35	65	L
730		333	1.2	2.226							
731		335	5.2	2.278							
732		332	4.3	2.321							
733		249	12	2.441							
734		249	11	2.551		9	9.0				
			16								
	GRASS		27	2.821							
736		325	19.3	3.014							
737		332	3	3.044							
738		309	5.2	3.096							
739		334	4	3.136							
740		268	0.7	3.143							
741		285	19.5	3.338							
742		273	36	3.698		7	9.6				
			15	3.848							
	GRASS		8	3.928							
743		283	65	4.578							
744		331	6	4.638		2	3.1				
			2	4.658							
	GRASS		126	5.918							
745		286	45	6.368							
			6	6.428							
	GRASS		42	6.848							
746		261	10	6.948		2	3.8				
			21	7.158							
	GRASS	332	720	14.358							
747		336	31.5	14.673	50						
748		336	2.6	14.699							
749		334	4.8	14.747							
750		341	25	14.997		4	6.2				
751		33	4	15.037							

1	2	3	4	5	6	7	8	11	12	13	14
752		17	9.5	15.132							
753	GV	13	9	15.222				7			
754		292	1.1	15.233							
755		9	5	15.283							
756		1	9	15.373							
757		348	15	15.523							
758		321	4.5	15.568							
759		2	12	15.688							
760		16	7.5	15.763							
761		16	7	15.833							
762		9	6	15.893							
763		2	9	15.983		12	12.0				
764		353	8	16.063							
765		351	9.5	16.158							
766		351	5	16.208							
767		0	6.7	16.275				9			L
768		299	2.6	16.301							
769		321	5.6	16.357							
770		304	5	16.407							
771		13	3.8	16.445							
772		358	38	16.825							
773		355	11.5	16.940							
774		6	3	16.970		11	11.0				
F15		339	7	17.010				100			L
775		333	7	17.080							
776		319	2.1	17.101							
777		336	1	17.111				7			
778		321	4	17.151							
779		342	2.4	17.175							
780		353	1	17.185							
781		351	4.8	17.233							
782		353	5	17.283							
783		277	15	17.433							
784		342	0.3	17.436							
785		6	5.2	17.488							
786		13	5	17.538							
787		329	17.5	17.713							
788		334	0.3	17.716							
789		339	4.2	17.758							
790		339	16	17.918		16	16.0				
791		3	18	18.098							
792		325	21	18.308							
793		334	10.3	18.411							
794		334	2	18.431							
795		266	3	18.461							
796		325	13.5	18.596					10	50	L
797		321	1.5	18.611							
798		39	10.5	18.716							
799		317	19.5	18.911							
800		335	8.1	18.992		10	10.0		11	24	L
801		326	8.2	19.074					40	70	L
802		340	2.5	19.099				1	30	80	L
803		328	0.9	19.108				1			

1	2	3	4	5	6	7	8	11	12	13	14
804		331	3	19.138							
F16		330	23	19.368				160			L
805		333	23	19.368							L
806		339	0.8	19.376							
807		325	5.1	19.427					8	18	L
808		329	1.5	19.442							
809		335	2.8	19.470				2			L
810		333	0.9	19.479							
811		340	5.5	19.534							
			0	19.534							
	GRASS		10	19.634							
812		311	5.5	19.689	72						
813		338	9.2	19.781							
814		343	2.7	19.808							
815		335	5.1	19.859							
816		260	2.1	19.880		16	17.8				
817		207	16	20.040							
818		303	18	20.220							
819		306	30	20.520							
820		313	5	20.570							
821		334	5	20.620		5	5.0				
			13	20.750							
	GRASS		64	21.390							
822		324	4.3	21.433	57						
823		43	10	21.533							
824		11	16	21.693							
825		23	8	21.773							
826		331	4.1	21.814							
827		310	11.5	21.929							
828		305	1.4	21.943		7	11.5				
829		279	9.1	22.034							
F17		328	4	22.074				11	860		L
##		337	4	22.074					860		L
##		332	1.1	22.085				2			
838		344	7	22.155							
839		327	6.3	22.218							
840		347	44	22.658							
841		260	5.3	22.711		7	7.1				
			27	22.981							
	GRASS		83	23.811							
842		342	6.5	23.876		1	5.3				
843		335	18.5	24.061							
844		319	20	24.261							
845		338	16	24.421							
			8	24.501							
	GRASS		26	24.761							
846		301	3.8	24.799							
847		302	20	24.999		5	6.8				
848		316	2.9	25.028							
849		301	8	25.108							
850		280	17	25.278							
851		334	10	25.378							
852		331	1.9	25.397							

1	2	3	4	5	6	7	8	11	12	13	14
853		325	4.8	25.445							
854		330	11.3	25.558							
856		324	4	25.598							
F18		326	5.1	25.649				39	670		L
857		326	5.1	25.700					670		L
858		323	0.5	25.705							
859		325	2.9	25.734							
860		320	0.4	25.738							
861		320	6	25.798					0	9	L
862		298	0.8	25.806							
863		323	7	25.876					50	60	L
864		303	0.6	25.882							
865		306	3.5	25.917							
866		323	4	25.957		18	18.0		0	15	L
867		328	5.3	26.010					15	40	L
868		322	16	26.170							
869		320	6.4	26.234							
870		323	4	26.274				1	15	80	L
871		316	2.6	26.300							
872		336	17	26.470							
873		312	2.7	26.497							
874		250	14	26.637							
875		317	3.1	26.668							
876		267	2.5	26.693							
877		340	9.6	26.789							
878		336	0.9	26.798							
879		339	2.3	26.821							
880		332	2.8	26.849							
881		271	4.2	26.891		15	15.8				
			6	26.951							

C.4 – Transect 4

1	2	3	4	5	6	7	8	11	12	13	14	15	16	17
870		327	2.8	0.028	75									
871		335	4	0.068										
F19		346	10	0.168								150	-	E
872		346	10	0.168								150	-	E
873		343	5.5	0.223										
874		348	19	0.413										
875		338	15	0.563										
			15	0.713										
	GRASS		13	0.843										
877		343	15.5	0.998		7	8.2							
878		335	1	1.008										
879		334	15	1.158										
880		337	5.2	1.210										
881		11	9.5	1.305										
882		303	4	1.345										
883		16	0.7	1.352										
F20		347	18	1.525					15	-	L			E
884		347	18	1.532										
885		323	7	1.602										
886		347	0.5	1.607										
887		339	20.5	1.812										
888		351	2	1.832										
889		314	2.8	1.860										
890		19	7	1.930										
891		357	1.7	1.947		14	14.5							
			2	1.967										
	GRASS		13	2.097										
892		21	0	2.097										
893		16	2	2.117										
894		283	43	2.547										
895		289	2.2	2.569										
896		327	17	2.739										
897		345	12	2.859										
898		347	1.5	2.874		7	8.7							
			0	2.874										
	GRASS		10	2.974										
899		347	3	3.004										
900		13	2.1	3.025										
901		9	1.7	3.042										
##		335	6	3.102										
904		328	19	3.292										
905		336	0.7	3.299										
906		347	0.9	3.308										
907		10	13.3	3.441										
908		55	6.2	3.503										
909		277	23	3.733										
910		262	0.6	3.739										
911		273	6.3	3.802										
			0	3.802										
	GRASS		15	3.952										

1	2	3	4	5	6	7	8	11	12	13	14	15	16	17
912	GV	26	3.8	3.990										
913		346	0.4	3.994		14	16.5							
914		342	2	4.014										
915		330	0.6	4.020										
916		340	18	4.200										
917		342	5	4.250										
918		340	3.1	4.281										
919		358	3.5	4.316										
920		345	1.2	4.328										
921		338	2.5	4.353										
##		4	6.5	4.418										
924		26	1	4.428		10	10.0	1						
925		35	59	5.018										
926		330	17	5.188										
927		44	5	5.238										
928		336	8.5	5.323										
929		334	9.5	5.418										
930		341	6	5.478										
931		325	27	5.748		7	7.0							
932		355	39	6.138										
933		355	19	6.328										
934		330	3.5	6.363										
935		270	2	6.383										
936		8	22	6.603										
937		330	6.5	6.668		6	6.0							
F21		342	31	6.913				280						E
938		338	31	7.223										
939		316	4.9	7.272										
940		47	0.1	7.273										
941		357	6.2	7.335										
942		4	1.1	7.346										
943		349	1.5	7.361										
944		298	5	7.411										
945		330	1.7	7.428										
946		337	1.6	7.444										
947		348	0.9	7.453										
948		327	2.2	7.475										
949		329	2	7.495										
950		338	7.5	7.570										
951		331	1.5	7.585										
952		331	4	7.625										
953		337	4.5	7.670										
954		349	1.2	7.682										
955		353	4	7.722										
			1	7.732										
	GRASS		7	7.802										
956		348	13	7.932										
957		323	3	7.962		20	21.5							
958		343	11	8.072										
959		12	16	8.232										
960		334	8.8	8.320										
961		342	5.7	8.377										
962		299	10	8.477										

1	2	3	4	5	6	7	8	11	12	13	14	15	16	17
963		328	2.5	8.502										
964		359	1	8.512										
##		334	0.9	8.521										
##		309	3	8.551										
968		344	33	8.741										
969		338	19	8.851										
970		317	11	8.951										
971		270	10	8.971										
F22		345	2	8.971				140						E
972		348	2	8.991		14	14.0							
973		327	1.3	9.004										
974		356	4.3	9.047										
975		6	0.9	9.056										
##		328	4.8	9.104				9						
##		323	23	9.334										
979		310	3	9.361										
980		357	2.7	9.413										
981		347	5.2	9.423										
982		322	1	9.623										
983	GV	44	20	9.893		9	9.0	7						
984		5	27	10.283										
985		25	39	10.373		2	4.7							
			9	11.423		0	0.0							
	GRASS		105	12.473										
986		329	2.1	12.494	74									
987		5	1.7	12.511										
988		351	6	12.571										
989		2	8.5	12.656										
990		352	3	12.686										
991		351	0.6	12.692										
992		330	5	12.742										
993		347	6.7	12.809										
994		316	5	12.859										
995		358	2.9	12.888										
996		357	1.5	12.903										
997		355	1.8	12.921										
998		334	1.6	12.937										
999		338	1.6	12.953										
F23		342	1.5	12.952				55						E
1000		333	1.5	12.967										
1001		338	0.7	12.974		16	30.4	3						
1002		18	8	13.054										
1003		328	14	13.194										
1004		275	11	13.304		3	5.1							
			28	13.584										

C.5 – Transect 5

1	2	3	4	5	6	7	8	9	10	11	12	13	14	15	16	17
346		334	8	0.080	68											
347		306	59	0.670												
348		310	32	0.990		3	3.0									
F5		346	2.6					88	E	260						
349		332	2.6	1.016						6						
350		335	5.5	1.071						5						
351		351	17.5	1.246						3						
352		301	53	1.776												
353		45	10	1.876		5	5.0									
354	WV	278	18	2.056												
355	WV	269	5.2	2.108												
			17	2.278												
	GRASS		26	2.538												
356		334	28	2.818		3	4.1									
357		310	21	3.028												
358		338	24	3.268												
359		332	2.5	3.293										0	75	E down
360		328	6.6	3.359										0	22	E down
361		337	0.8	3.367												
362		338	4.5	3.412												
363		334	4.6	3.458												
364		329	0.4	3.462												
365		336	0.9	3.471												
366		328	7	3.541												
367		323	4.8	3.589												
368		329	2.7	3.616												
			5.3	3.669		12	13.1									
	GRASS		8.5	3.754												
369		326	37	4.124										0	480	E down
F6		323	18					87	E	90				120	170	E down
370		325	18	4.304												
371		323	4.5	4.349												
372		319	0.3	4.352												
373		315	0.5	4.357												
374		317	4	4.397		7	7.0									
375		340	110	5.497												
376		329	7	5.567												
F7		334	10					88	E	830	780	>780	Left	700	>700	E down
377		329	10	5.667										210	>210	E down
378		323	3	5.697												
379		325	1.3	5.710												
380		325	0.9	5.719												
381		326	0.6	5.725												
382		339	1.2	5.737												
383		321	0.5	5.742												
384		323	2.9	5.771												

1	2	3	4	5	6	7	8	9	10	11	12	13	14	15	16	17
385		348	1.2	5.783				12								
386		335	2.2	5.805												
387		332	0.7	5.812												
388		334	1.9	5.831							60	80	L	30	45	E down
389		332	0.4	5.835												
390		339	2.1	5.856												
391		337	2.6	5.882												
392		331	2.1	5.903							30	36	L	30	5	E down
393		325	2	5.923							0	2	L	0	1	E down
394		331	3	5.953												
395		326	1.1	5.964												
396		327	0.4	5.968												
397		338	3	5.998		23	23.0				0	3	L	0	3	E down
398		338	0.6	6.004												
399		313	1	6.014							0	51	R	0	29	W down
400		344	5.5	6.069												
401		335	0.5	6.074												
402		333	0.7	6.081												
403		331	1	6.091												
404		346	3.4	6.125							0	8	L	0	29	E down
405		342	0.5	6.130												
406		331	1	6.140												
407		343	1.2	6.152							140	280	L	52	16	E down
408		342	1	6.162												
409		331	1.5	6.177												
410		339	2	6.197												
411		337	0.9	6.206												
412		335	0.6	6.212												
413		331	5.8	6.270												
414		332	2.8	6.298												
415		331	3	6.328							200	270	L	120	230	E down
416		337	1.5	6.343												
417		334	0.8	6.351												
418		339	0.7	6.358												
419		343	0.6	6.364							70	100	L	30	100	E down
420		337	2.7	6.391												
421		340	0.5	6.396												
422		337	2.5	6.421							50	60	L	45	55	E down
423		339	0.5	6.426												
424		3	2	6.446												
425		337	1	6.456						10	260	>260	L	170	>170	E down
426		335	16	6.616	59											
427		336	15	6.766							40	70	L	10	30	E down
428		287	8	6.846												
429		322	7.5	6.921												
430		349	4	6.961		33	33.0									

1	2	3	4	5	6	7	8	9	10	11	12	13	14	15	16	17
431		18	6.5	7.026												
432		338	6	7.086												
433		325	8.8	7.174												
434		26	3.2	7.206												
435		346	20	7.406												
436		1	17	7.576												
437		276	6.5	7.641												
438		2	29	7.931		8	8.0									
439		11	20	8.131												
440		341	0.5	8.136												
441		9	3.1	8.167												
442		347	3.8	8.205												
443		335	3.4	8.239												
444		345	1.6	8.255		6	21.8									
			2	8.275												
	GRASS		85	9.125												
445		19	13	9.255												
446		332	15	9.405							40	160	L	40	100	E down
447		317	32	9.725												
448		338	1.1	9.736												
F8		325	3.5								920	1870	L	470	>470	E down
449		321	3.5	9.771							950	>950	L			
450		350	1.8	9.789												
451		323	0.4	9.793							150	>150	L	80	>80	E down
452		328	2.7	9.820							100	110	L	60	70	E down
453		325	3.8	9.858							50	60	L	40	50	E down
454		317	3.2	9.890												
455		323	1.5	9.905		11	12.6									
456		338	18	10.085												
457		333	0.7	10.092												
458		303	1.4	10.106												
459		342	4.5	10.151							270	420	L	160	170	E down
460		337	1.5	10.166												
461		312	60	10.766												
462		333	7.7	10.843												
463		277	7	10.913												
464		349	0.5	10.918												
465		336	4.8	10.966		10	10.0				60	200	L	60	120	E down
466		335	6.2	11.028												
467		312	52	11.548												
468		318	2.8	11.576		3	3.0									
469		349	70	12.276		1	2.7				16	50	L	7	40	E down
	GRASS		10	12.376												

C.6 – Transect 6

1	2	3	4	5	6	7	8	11	15	16	17
F9		347	0		62			470			
470		343	0	0.000							
471		41	3	0.030							
472		331	17	0.200							
473		359	6	0.260							
474		335	6.5	0.325							
475		342	2	0.345							
476		352	3.5	0.380							
477		349	6	0.440							
478		297	8	0.520							
479		325	8	0.600							
480		18	11.7	0.717		11	11.0				
481		357	62	1.337							
482		313	28	1.617							
483		319	3	1.647		3	3.0				
484		40	58	2.227							
485		15	11	2.337							
486		339	9	2.427							
487		341	6.8	2.495							
488		352	7	2.565							
489		302	1.6	2.581							
490		309	4	2.621							
491		0	0.6	2.627		8	10.2				
			16	2.787							
	GRASS		44	3.227							
F10		347	0					960			
492		332	0	3.227							
493		343	4.5	3.272							
494		344	2.4	3.296							
495		346	1.9	3.315							
496		359	2.8	3.343							
497		354	1.8	3.361							
498		11	2.6	3.387							
499		345	0.4	3.391							
500		4	1.8	3.409							
501		356	3.3	3.442							
502		8	3	3.472							
503		9	1.9	3.491							
504		341	5.3	3.544							
505		354	3.5	3.579							
506		341	4	3.619							
507		343	2.5	3.644							
508		352	16.5	3.809							
509		19	3.6	3.845							
510		351	3.8	3.883							
511		2	1.5	3.898							
512		338	1.9	3.917							
513		355	3.9	3.956							
514		334	3.4	3.990		23	29.8				
515		14	2.6	4.016							

1	2	3	4	5	6	7	8	11	15	16	17
516		343	3.4	4.050							
517		347	13	4.180							
518		304	9.5	4.275							
519		336	1.3	4.288							
520		9	0.2	4.290							
521		11	3.5	4.325							
522		358	5.4	4.379							
523		327	1.2	4.391							
524		351	1.6	4.407							
525		10	3.8	4.445							
526		341	1.8	4.463							
527		359	1.5	4.478							
528		246	15	4.628							
529		48	14	4.768							
530		331	3.5	4.803							
531		278	12	4.923							
532		353	1	4.933							
533		47	2.3	4.956		19	19.0				
534		85	16	5.116							
535		83	1.3	5.129							
536		348	4.2	5.171							
537		271	5.3	5.224							
538		269	2.8	5.252							
539		341	1.1	5.263							
540		303	6.5	5.328							
541		37	0.2	5.330							
542		34	20.5	5.535							
543		39	8.2	5.617							
544		35	5	5.667							
545		10	0.9	5.676							
546		7	1	5.686							
547		19	1.5	5.701							
548		3	12	5.821							
549		352	1.1	5.832							
550		355	1	5.842							
551		356	2.9	5.871							
552		9	6.5	5.936		19	19.0				
553		10	9	6.026							
554		329	14.5	6.171				8			
555		20	0.8	6.179							
556		7	0.7	6.186							
557		2	2.5	6.211							
558		336	2	6.231							
559		15	2	6.251							
560		14	5.5	6.306							
561		15	1.4	6.320							
562		292	5	6.370							
563		9	10	6.470							
564		340	8	6.550							
565		347	2.8	6.578							
566		35	12	6.698							
567		325	3	6.728							
568		326	9.6	6.824							

1	2	3	4	5	6	7	8	11	15	16	17
569		335	6.2	6.886							
570		358	7.8	6.964							
571		319	3	6.994		19	19.0				
572		262	3.4	7.028							
573		2	4.5	7.073							
574		331	2	7.093							
575		245	3	7.123							
576		357	4.2	7.165							
577		342	1	7.175							
578		346	0.6	7.181							
579		10	5.9	7.240							
580		22	2.1	7.261							
581		2	2.9	7.290							
582		10	2.6	7.316							
583		9	6.4	7.380							
584		12	7	7.450							
585		16	2.2	7.472							
586		9	2	7.492							
587		265	9	7.582							
588		26	2.2	7.604							
589		32	0.9	7.613							
##		5	1	7.623							
##		26	7.1	7.694							
593		8	10.7	7.801							
594		336	15	7.951		22	22.0				
595		323	4.9	8.000							
596		337	2.4	8.024							
597		307	1.6	8.040							
598		343	1.3	8.053							
599		27	1	8.063							
600		334	2.3	8.086							
601		356	0.6	8.092							
602		257	3.5	8.127							
F11		340	0.8					78			
603		353	0.8	8.135							
604		338	4	8.175							
605		345	3.8	8.213				4			
			25	8.463							
	GRASS		9	8.553							
606		59	26	8.813	55						
607		332	7	8.883							
608		16	10	8.983		14	15.4				
609		328	1.8	9.001							
610		347	13	9.131							
611		341	18	9.311							
612		343	1.7	9.328							
613		253	9.6	9.424							
614		320	14	9.564							
615		338	3.2	9.596							
F12		341	39					24	960	1650	L
616		342	39	9.986							
617		339	1.1	9.997		9	9.0				
618		336	1	10.007							

1	2	3	4	5	6	7	8	11	15	16	17
619		333	1.3	10.020							
620		346	1.2	10.032							
621		342	1	10.042							
622		332	0.9	10.051							
623		331	0.9	10.060							
624		338	1.6	10.076							
625		338	1	10.086							
626		359	3	10.116							
627		5	7.6	10.192							
628		342	2	10.212				5			
629		329	1.2	10.224							
630		346	14.6	10.370							
631		9	6	10.430							
			0	10.430							
	GRASS		10	10.530							
632		353	13	10.660							
633		348	0.7	10.667							
634		337	1.4	10.681							
635		340	0.6	10.687							
636		354	5	10.737							
637		340	2.6	10.763		20	25.6				
			6	10.823							
	GRASS		12	10.943							
638		352	7	11.013							
639		355	3.5	11.048							
640		7	7	11.118							
641		355	10	11.218							
642		359	16	11.378							
643		347	4	11.418							
644		11	2.8	11.446							
645		315	6	11.506							
646		347	2.3	11.529							
647		345	1.5	11.544							
648		349	1.3	11.557							
649		343	0.3	11.560							
650		343	3.4	11.594							
651		352	0.6	11.600							
			1.7	11.617							
	GRASS		8	11.697							
652		313	5	11.747							
653		331	7.3	11.820							
654		353	4.9	11.869							
655		352	2	11.889							
656		348	1.8	11.907							
657		353	3.6	11.943		20	21.7				
F13		353	8					105			L
658		346	8	12.023							
659		348	0.7	12.030				2			
660		346	5.5	12.085							
661		349	2	12.105							
662		25	2.1	12.126							
663		353	4.6	12.172							
664		9	1.7	12.189							

1	2	3	4	5	6	7	8	11	15	16	17
665		26	2	12.209							
666		45	10	12.309							
667		282	0.5	12.314							
668		329	5.6	12.370							L
669		328	1.9	12.389							
670		308	0.9	12.398							
671		323	1.2	12.410							
672		331	1.7	12.427							
673		23	5.5	12.482							
674		28	2.6	12.508							
675		22	6.3	12.571							
676		328	19	12.761		19	23.7				
			4	12.801							
	GRASS		28	13.081							
677		349	1	13.091	51						
678		327	2	13.111							
679		311	7.6	13.187							
680		0	0.4	13.191							
681		357	2	13.211							
682		330	0.7	13.218							
683		347	1.9	13.237							
684		326	1.5	13.252							
685		18	10	13.352							
686		353	4.8	13.400							
687		5	3.5	13.435							
688		6	1.6	13.451							
689		349	3	13.481							
690		353	7.5	13.556							
691		335	5.2	13.608							
692		347	11.5	13.723							
693		262	8	13.803							
694		66	8.5	13.888							
695		350	0.5	13.893							
696		1	9.5	13.988							
697		340	0.7	13.995		21	22.9				
698		309	17	14.165							
699		296	2	14.185							
700		271	18	14.365							
701		266	2.2	14.387							
702		18	0.1	14.388							
703		269	3.6	14.424							
704		25	9	14.514							
705		287	13	14.644							
706		310	21	14.854		9	9.0				
707		28	17	15.024							
708		281	11	15.134							
709		273	4.1	15.175							
710		238	13	15.305							
711		344	2.7	15.332							
712		330	1.9	15.351							
713		284	8.5	15.436		7	12.4				
			12	15.556							

Appendix D – Spatial sampling of the *b*-value using Voronoi polygons

Here are the preliminary results of the Voronoi spatial sampling methodology I have developed as discussed in Section 8.6.

D.1 Current literature

In order to calculate a spatial *b*-value you must either select a specific area of the dataset to perform iterative sampling on, or simply calculate a discrete *b*-value for the desired area of the catalogue, neither of which as ideal solutions as they vastly reduce the catalogue size. The ZMAP method (Wiemer, 2001) (Section 2.2.2.3) is currently the best 2D and 3D spatial sampling method used in the literature. It uses overlapping circles/spheres of fixed area/volume or number of events to create a dense spatial grid of data points. However as previously noted the sample sizes used are typically 100-200 total events. The suggested minimum total from the synthetic analysis in Chapter 3 (Roberts *et al.*, 2015) is $N \geq 500$.

The key trade-off with all spatial sampling techniques is between spatial resolution and the sample size, in this case the number of events. The main problem with ZMAP's methodology is that to maintain high spatial resolution the sampling area/size if fixed. This introduces an inherent flaw in the methodology as if a cluster of related events is much larger than the sample size, it will never be completely sampled. The results are also heavily correlated due to the greatly overlapping samples.

More recently Kamer and Hiemer (2015) have proposed a penalised likelihood-based method to try and address these limitations (Section 2.2.2.4). It is a parameter-free

method based on optimal partitioning using Voronoi tessellation, penalized likelihood and wisdom of the crowd philosophy. The results when selecting the best 100 and 1000 solutions (Appendix B.1d,e) are impressive when compared to simply using the nearest 150 and 1000 events (Appendix B.1b,c) for a synthetic checkerboard catalogue (Appendix B.1a). However, the method fails to calculate the correct *b*-value of a synthetic catalogue with a known *b*-value so may be fundamental flawed. The catalogue is composed of two synthetic distribution, one with a known *b*-value (b_{bkg}) and the second with an anomalous *b*-value (b_{ano}), the ratio of which is noted. The method performs better with a higher b_{bkg}/b_{ano} ratio however in both examples in Appendix B.2(a, b) when $b>1$ the $\tilde{b}$-value is systematically underestimated regardless of the size of the catalogue. The results of testing the MaxC method on synthetic catalogues were presented in this thesis in chapter 2 with the key plots highlights here in Appendix B.3. For both $b=1$ and $b=2$ the MaxC dramatically underestimates the known *b*-value.

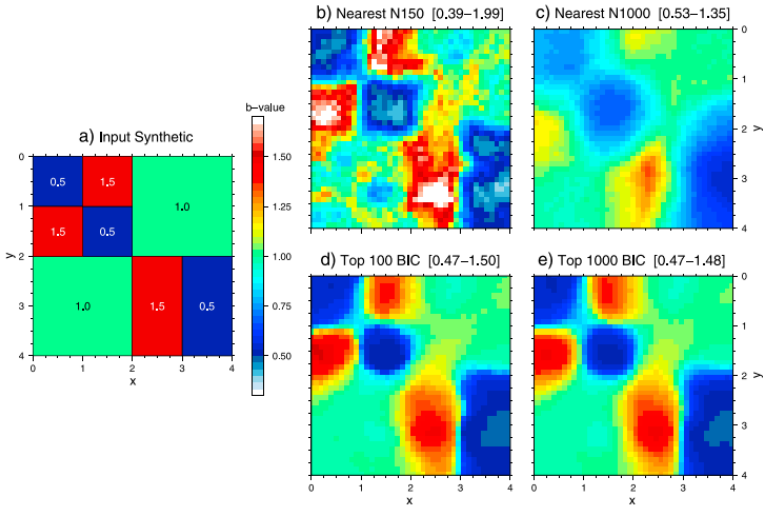

Appendix B.1 - Figure 1 from Kamer and Heimer (2015). (a) Underlying spatial *b*-value distribution for the generation of synthetic magnitudes for 8000 uniformly distributed events. (b and c) Resulting *b*-value maps using the classical nearest neighbour mapping method for Nmin= 150 and Nmin= 1000, respectively. (d and e) Resulting *b*-value maps based on the penalized likelihood approach for 50,000 randomly generated models in the complexity range of 1–100 Voronoi nodes (showing the median of the 100 and 1000 best performing models, respectively). Ranges of resulting *b*-values are given in the title of each subplot.

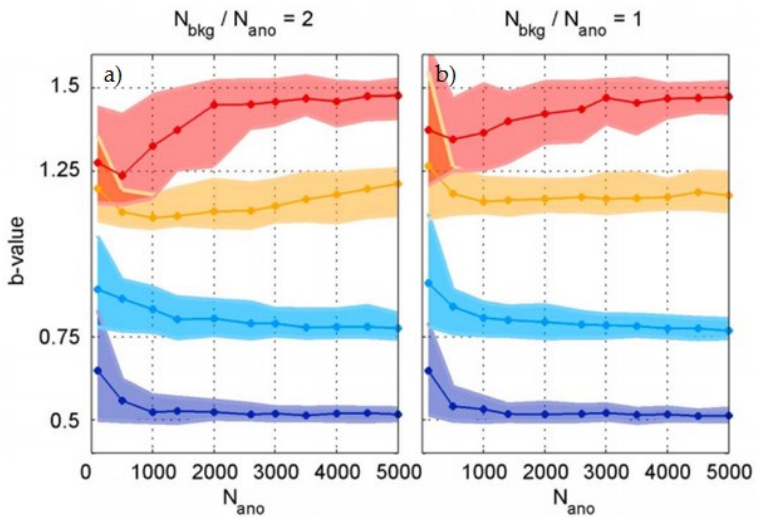

Appendix B.2 - Figure 4 from Kamer and Heimer (2015). Convergence of the method for four different *b*-value anomalies (0.5, 0.75, 1.25, and 1.5) with varying sample sizes (from 100 to 5000). The three panels show results for different sample size ratios with respect to the surrounding events. The synthetic catalogue is composed of two separate frequency-magnitude distribution with a given number of background events (N_{bkg}) and anomalous b-value events (N_{ano}). Solid lines and shaded areas denote the corresponding median *b*-value and 0.16–0.84 quantiles, respectively.

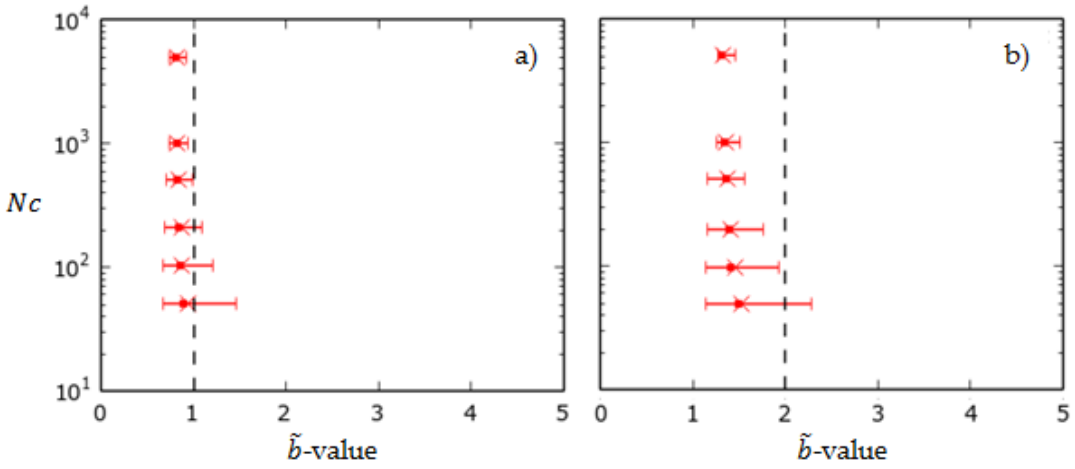

Appendix B.3 – Taken from Figure 3.7 and Figure 3.8 in this thesis (Roberts *et al.*, 2015). $\tilde{b}$-values for varying *Nc* using the maximum curvature method to calculate a known *Mc*, when a) *b*=1 and b) *b*=2. Error bars show 95% confidence with dots representing the median value and x's the average.

This analysis implies the inferred *b*-values in Kamer and Hiemer (2015) are systematically low. Despite the residual bias the Voronoi tessellation and Bayesian

Information Criteria (BIC) selected methodology is still a valuable improvement on spatial sampling. The proposed method could simply be rectified be applying the *Mc* workflow proposed in Figure 3.9 when fully tested.

D.2 Iterative 2D Voronoi tessellation

After developing the iterative sampling method in Section 4.3.2 I had started developing my own spatial sampling methodology based on iterative Voronoi sampling before the Kamer and Hiemer paper was published. The key difference is in the selection criteria: Kamer and Hiemer (2015) calculated the *b*-value for the FMD of every Voronoi polygon in each iteration regardless of the number of events in the polygon, then they ranked the iterations using the BIC and stacked the best 100 (Appendix B.1d) or 1000 (Appendix B.1e) iterations. My proposed alternate method is to stack every iteration but only include polygons that have greater than a threshold number of incomplete events. As with the iterative sampling method the polygons are applied before any frequency-magnitude analysis is performed, so the minimum suggested incomplete catalogue size of $N \geq 500$ is used. It is not feasible to apply this strictly and achieve the sought-after resolution; therefore we try and set the minimum threshold so the average incomplete catalogue size is above 500. After synthetic testing a minimum of $N=100$ was found to be sufficiently low.

Appendix E.8 details a step-by-step methodology of my iterative Voronoi sampling technique. For each iteration the number of polygons is randomly generated. The minimum and maximum values are chosen to be 20 (Appendix B.4) and 200 (Appendix B.5). A minimum of 20 polygons gives good spatial coverage without including too many phases of events. Appendix B.4a shows the area of coverage is a similar size to each of the phases identified in Figure 4.5. In this examples 16 of 20 polygons contain the minimum 100 events required. The average incomplete catalogue size is 1530, well above the suggested minimum; and the average complete size is 236, also above the recommendation. Although polygons clearly capture multiple phases this is the nature of randomly sampling in space illustrating why

stacking multiple iterations is very important. The plotting resolution is set to 0.01 degrees; every data point within a polygon is assigned the same *b*-value. Appendix B.4b shows ~80% coverage of points assigned a given *b*-value fin one iteration. However when compared to the distribution of events in Appendix B.4a it is clear there is spatial over-sampling; as this is the minimum number of polygons that would be used this is a desirable outcome. Appendix B.4c shows a contoured plot of the $\tilde{b}_P$-value distribution and Appendix B.4d shows the peak $P(\tilde{b}_P)$ value. As there is just one iteration the contouring shows the well-defined distinct values for each polygon.

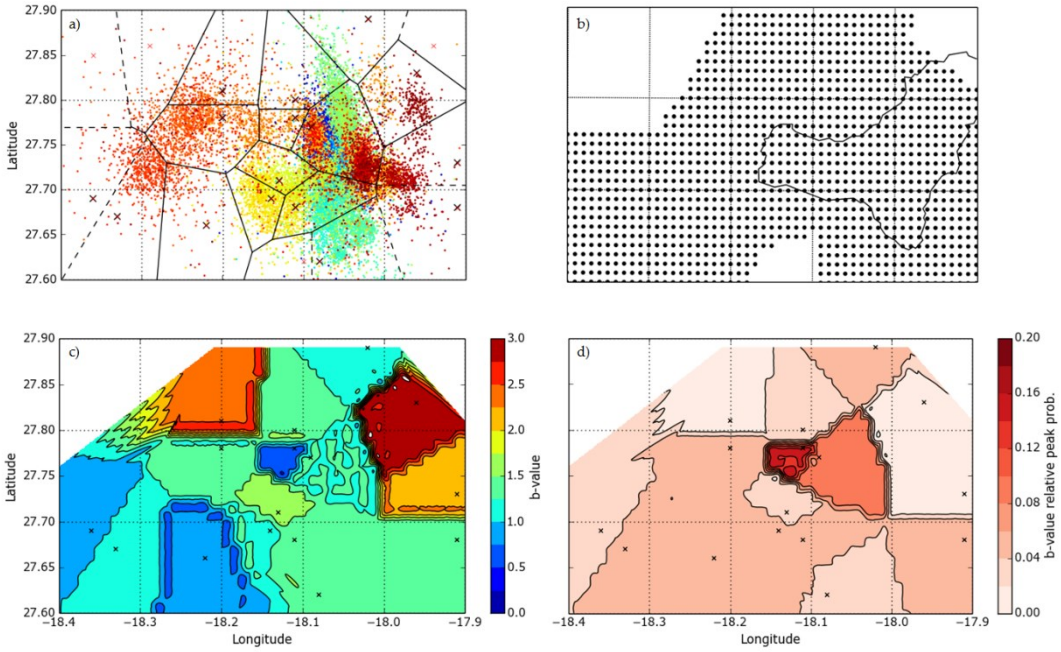

Appendix B.4 - Example of one iteration of the iterative Voronoi sampling method using 20 Voronoi polygons. 16 of the 20 polygons contain the minimum 100 events. The average catalogue sizes are *N*=1530 and *Nc*=236. a) Position of the Voronoi polygons relative to the El Hierro seismic catalogue (coloured dots). The crosses show the randomly generated points controlling the polygons positions. Black crosses show polygons with >100 events, red crosses show rejected polygons with <100 events. b) Data points within accepted polygons that have been assigned *b*-values. Resolution of 0.01 degrees latitude/longitude. c) Contoured $\tilde{b}_P$-value using data points from b). d) Contoured peak $P(\tilde{b}_P)$ values using data points from b).

Appendix B.5 shows one iteration for the maximum sampling size of 200 polygons. Appendix B.5a shows the area of the polygons is now significantly less than the

clusters of event meaning each phase would be under-sampled, however smaller sub-phases such as 6a-d (Figure 4.5) will be sampled more effectively. In this example 38 of 200 polygons contain the minimum 100 events required. The average total catalogue size is 505 (including incomplete events), essentially equal to the minimum suggested catalogue size. The average complete size is 113; less than the recommended 200 events but still above 100, a typical value used in the current literature. Appendix B.5b shows the coverage of points assigned a *b*-value for one iteration. There is now only ~25% coverage; however when compared to the distribution of events in Appendix B.4a it is clear there is under-sampling; as this is the maximum number of polygons that would be used. This is again a desirable outcome. Appendix B.5a and b show the contoured $\tilde{b}_P$-value and peak $P(\tilde{b}_P)$ value. The highly increased resolution is much clearer than with only 20 polygons and the segmentation of each sampled polygon is less apparent.

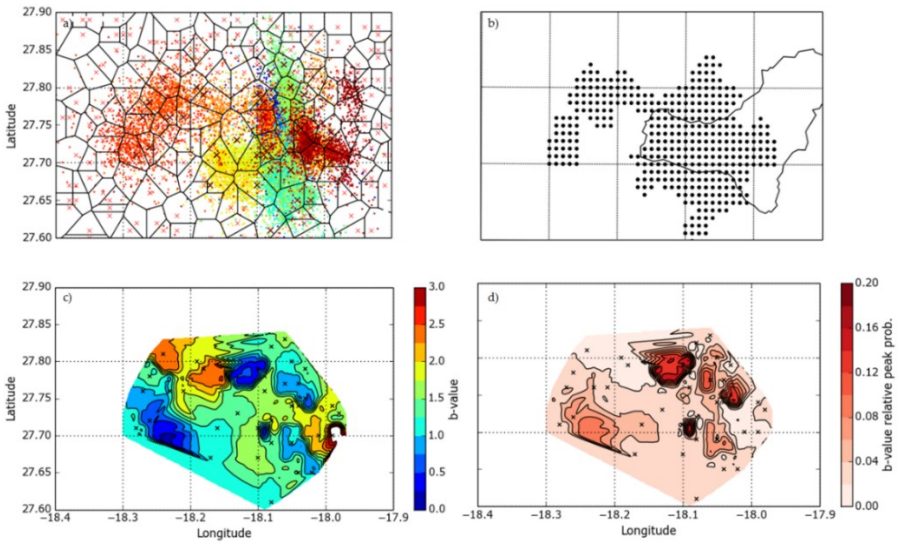

Appendix B.5 – Example of 1 iteration of the iterative Voronoi sampling method using 200 Voronoi polygons. 38 of the 200 polygons contain the minimum 100 events. The average catalogue sizes are *N*=505 and *Nc*=113. a) Position of the Voronoi polygons relative to the El Hierro seismic catalogue (coloured dots). The crosses show the randomly generated points controlling the polygons positions. Black crosses show accepted polygons with >100 events, red crosses show rejected polygons. b) Data points within accepted polygons that have been assigned *b*-values. Resolution of 0.01 degrees latitude/longitude. c) Contoured $\tilde{b}_P$-value using data points from b). d) Contoured peak $P(\tilde{b}_P)$ values using data points from b).

Appendix B.6 shows the results for 20 iterations of the iterative Voronoi sampling technique using a random number of polygon between 20 (Appendix B.4) and 200 (Appendix B.5). The average number of polygons created in each iteration is 114, this is in line with the expected number of 110 through random sampling. In total 634 polygons were accepted as they contained >100 events, meaning on average ~28% of the polygons were accepted. The average catalogues sizes are *N*=637, above the suggested 500 minimum, and *Nc*=125. Appendix B.6a shows the location of the 634 random points that defined accepted polygons. There are very few points outside the main clusters of the epicentres of the events. Appendix B.6b shows near complete data coverage except in the very NW corner of the dataset where they are nearly no events. This is a positive result as it shows the method is not spatially over-sampling the catalogue. Appendix B.6d shows the peak $P(\tilde{b}_P)$ value; after 20 iterations all values are relatively low (<0.08) compared with some of the peak values seen from just one iteration.

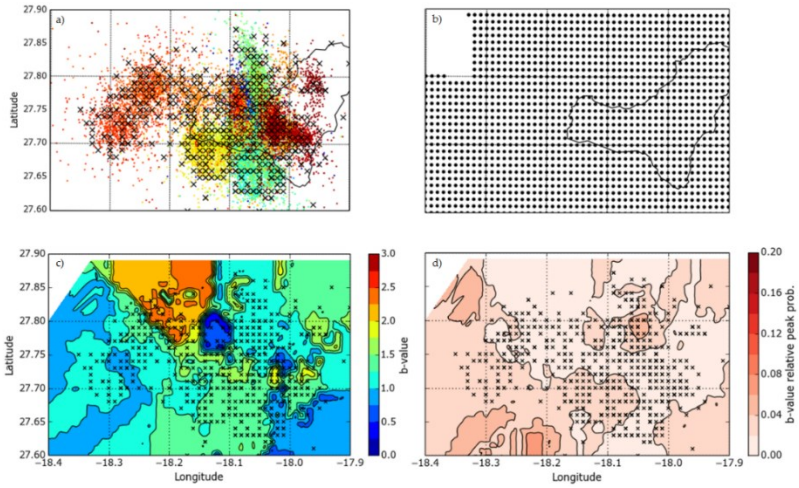

Appendix B.6 – Example of 20 iterations of the iterative Voronoi sampling method using 20-200 Voronoi polygons. In total 634 polygons were accepted. The average catalogue sizes are *N*=637 and *Nc*=125. a) Position of the Voronoi polygons relative to the El Hierro seismic catalogue (coloured dots). The crosses show the randomly generated points controlling the polygons positions. Black crosses show accepted polygons with >100 events, red crosses show rejected polygons. b) Data points within accepted polygons that have been assigned *b*-values. Resolution of 0.01 degrees latitude/longitude. c) Contoured $\tilde{b}_P$-value using data points from b). d) Contoured peak $P(\tilde{b}_P)$ values using data points from b).

D.2.1. El Hierro Voronoi interpretation

Although Appendix B.6 just shows preliminary results from the iterative Voronoi sampling method it is very clear there are areas of typical ($0.75 \geq b \geq 1.25$), low ($0.75 \leq b$) and high ($b \geq 1.25$) b-values. The background b-value does appear to be in the typical range with lower values in the very south-eastern corner and very high values to the north. This northern high b ranges between 2.0-2.5. Spatially it is just offshore to the north-west of El Hierro Island and forms the earliest part of phase 7 (Figure 4.5). Phase 7 is a westward propagating cluster of events, but the high b-value does not continue through the whole cluster. In Section 1.1.1 the modal b-values reported within the phase (Table 5.4), were 1.1 and 2.0; therefore it appears these two modal groups are controlled by their spatial distribution.

Immediately to the east of this high-b zone is are the lowest reported values in the dataset of $b<0.5$. This is spatially a relative seismically inactive gap in the dataset. Between phases 1, 5 and 7. Most of the phases 'fill in' an area that has been previously inactive and this the key area that has not had a cluster of actively, therefore the catalogue comprising this low b-value zone may just contain outliers from each of the other cluster and so the events may not be correlated. There are other smaller clusters with anomalous b-values that could be analysed in further detail.

D.3 Further improvement of method

The next step would to be to develop 3D iterative sampling that can output variations with depth. Currently the catalogue is effectively sampled with a vertical prism with the end faces being defined by the Voronoi polygon. To upscale the method to 3D, a third random point, depth, would simply be generated alongside a random longitude and latitude. The same process of attributing each event to its nearest random point, this time in 3D space rather than 2D, could then be performed.

Running time of the code is one of the key parameters controlling the usefulness of the method. Currently in 2D one iteration takes between 15/20 minutes to run,

therefore in order to run multiple iterations and stack a large data set it takes many hours to produce one set of results. Even just sampling at 1km depth resolution this will greatly increase the runtime of the code. This needs to be minimised to make the method more easily applicable.

Although I have not presented any formal error analysis here due to time constraints, it is possible to produce similar figures of the probability distribution, as in Figure 4.4, except for each spatial data point shown in Appendix B.6b, rather than for each polygon or point in time. Overcoming how to visually communicate more than 3 parameters on what is effectively a 2D graph is a key challenge in many complex models.

Appendix E - Code

This appendix contains Python codes used in the research: Sections E.1 to E.9 present both self-contained functions and sections of code used is Chapters 3, 4, and 5.

E.1 Imported packages

Some or all of the following packages are required to be imported at the start of any script:

```
import numpy as np
import collections
import matplotlib.pyplot as plt
import matplotlib as mpl
import matplotlib.dates as mdates
import matplotlib.gridspec as gridspec
import datetime as dt
import fMags as mags
from scipy import stats
from scipy.stats import nanmean
from operator import itemgetter, attrgetter
from scipy.interpolate import griddata
from scipy.optimize import curve_fit
from scipy.optimize import leastsq
from mpl_toolkits.basemap import Basemap
```

E.2 Parameters

These are the parameters used to define the size of the original seismic catalogue, the extent of the map when the data is plotted, then the parameters controlling the iterative sampling process. All values given here are for the El Hierro 2011-2013 catalogue

```
# define the bounds of the catalogue in space and time
z_max = 40.0 #Specify maximum depth
m_min = 0.1 #Specify minimum magnitude (e.g. remove 0.0s)
t_start = mdates.date2num(dt.date(2011,7,1)) #start time
t_end = mdates.date2num(dt.date(2013,12,31)) #finish time
mbin = 0.1 # Specify magnitude data precision

## Data extent
```

```
data_lon_min = -18.5
data_lon_max = -17.8
data_z_min = 0
data_z_max = 40

##Map extent
lat_min = 27.4
lat_max = 28.1
lon_min = -18.5
lon_max = -17.8

#Start & end dates of entire colour catalogue, used when plotted all data points against a smaller
phase
col_t_start = mdates.date2num(dt.date(2011,7,1))
col_t_end = mdates.date2num(dt.date(2015,7,31))

#parameters used for the random sampling method
min_samp = 50 #minimum random sample size
max_samp = 1000 # maximum random sample size
samp_it = 100 #number of random catalogue sampling iterations, min of 20
mov_av = 50 #number of point in moving average calculation
```

E.3 Importing the catalogue

This section imports the .txt file and split the columns into the desired arrays. Again this is specific to the IGN El Hierro catalogue. Column 0 is the time/date. 1 is the latitude. 2 is the longitude. 3 is the depth. 4 is the magnitude:

```
#Import catalogue in IGN fixed width text file format
columns = [slice(5,12), slice(17,27), slice(34,42), slice(50,57), slice(64,75), slice(85,87), slice(114,117)]
output = []

myfile = open('XXXXX/XXXXX.txt') #Hiero_260314.txt
for line in myfile:
fields = [line[column].strip() for column in columns]
output.append(fields)
Cat1 = np.array(output) #Cat1 is the array containing all the data
Cat1[Cat1==''] = 999
y=Cat1[1:,3:].astype(np.float)
# y is [lattitude,longitude]
x=Cat1[1:,1:3]
# x is [Date,time]

dates =[]
times = []
for line in x:
datevalues = mdates.date2num(dt.datetime.strptime(line[0], "%d/%m/%Y"))
timevalues = mdates.date2num(dt.datetime.strptime(line[1], "%H:%M:%S"))-
(mdates.date2num(dt.date(1900,01,01)))
dates.append(datevalues)
times.append(timevalues)
```

```
datetimes = np.add(dates,times)
datetimes = datetimes.reshape(len(dates),1)
Cat1 = np.concatenate((datetimes,y), axis=1)
Cat1 = Cat1[Cat1[:,0].argsort()]
#print 'cat1 =', Cat1

CatCol = Cat1 #CatCol is the entire catalogue for figures when event are plotted in colour
```

If the .txt. file already comes in the desired format you simply need to import the file:

```
Cat1 = np.array(np.loadtxt('XXXXX/XXXXX.txt'))
```

E.4 Filtering the catalogue

This reduces the size of the catalogue using the parameters defined in E.2:

```
#Filter catalogue
#1. By Latitude
Cat1 = Cat1[np.logical_and(Cat1[:,1]>=lat_min, Cat1[:,1]<lat_max),:]
#2. By Longitude
Cat1 = Cat1[np.logical_and(Cat1[:,2]>=data_lon_min, Cat1[:,2]<data_lon_max),:]
#3. By depth
Cat1 = Cat1[np.logical_and(Cat1[:,3]>=data_z_min, Cat1[:,3]<=data_z_max),:]
#4. By time
Cat1 = Cat1[np.logical_and(Cat1[:,0]>=t_start, Cat1[:,0]<t_end),:]
#5. By magnitude
Cat1 = Cat1[Cat1[:,4]>=m_min,:]
Cat1[:,4] = (np.round((Cat1[:,4]+0.00001)/mbin))*mbin
#round to required no. dp
#Added small value is to avoid rounding down at e.g. 1.45
NCat1 = (len(Cat1[:,0])) # given the size of the filtered catalogue
```

Filter the coloured catalogue containing all the events:

```
#Filter catalogue
CatCol = CatCol[np.logical_and(CatCol[:,1]>=lat_min, CatCol[:,1]<lat_max),:]
CatCol = CatCol[np.logical_and(CatCol[:,2]>=data_lon_min, CatCol[:,2]<data_lon_max),:]
CatCol = CatCol[np.logical_and(CatCol[:,3]>=data_z_min, CatCol[:,3]<=data_z_max),:]
CatCol = CatCol[np.logical_and(CatCol[:,0]>=col_t_start, CatCol[:,0]<col_t_end),:]
CatCol = CatCol[CatCol[:,4]>=m_min,:]
CatCol[:,4] = (np.round((CatCol[:,4]+0.00001)/mbin))*mbin

#Create catalogue up to the start of the sampled time window
CatCol_start = CatCol1[np.logical_and(CatCol1[:,0]>=col_t_start, CatCol1[:,0]<t_start),:]
#Create catalogue up to and including the start of the sampled time window
CatCol_end = CatCol2[np.logical_and(CatCol2[:,0]>=col_t_start, CatCol2[:,0]<t_end),:]
```

E.5 Functions

E.5.1. Daily number of events rates

Simply calculates the daily number of events then stores it to be plotted as a histogram:

```
days = np.floor(Cat1[:,0])
day_bins = np.arange(days.min(), days.max()+1)
DER, DER_bes = np.histogram(days, day_bins)
```

E.5.2. Frequency-magnitude distribution function

Defines the function that turns the catalogue of events into a discrete and cumulative binned frequency-magnitude distribution. Uses the magnitude catalogue (mags) and the magnitude bin resolution (mbin). Returns the number of events in the catalogue (nmags) the boundaries of the bins used (m_bins), the discrete number of events in each bin (dis_mf) and the cumulative number of events in each bin (cum_mf):

```
def fmd(mags, mbin):
        nmags = len(mags)
        minmag = np.min(mags)
        maxmag = np.max(mags)
        m_bins = np.arange(minmag, maxmag+0.8, mbin) #+0.8 to extend best fit dis/cum lines
        nbins = len(m_bins)
        dis_mf = np.zeros(nbins)
        cum_mf = np.zeros(nbins)
        for i in range(nbins):
                cum_mf[i] = len(mags[mags>m_bins[i]-mbin/2])
        dis_mf = np.absolute(np.diff(np.concatenate((cum_mf, [0]), axis=0)))
        Fmd = collections.namedtuple('Fmd', ['nmags','m_bins','dis_mf','cum_mf'])
        fmd = Fmd(nmags,m_bins,dis_mf,cum_mf)
        return fmd
```

E.5.3. Maximum Curvature function – completeness magnitude

Defines a function calculation the completeness magnitude of a frequency-magnitude distribution using the Maximum Curvature method (MaxC) (Wiemer and Wyss, 2002). Uses the magnitude catalogue (mags) and the magnitude bin size (mbin). Returns the completeness magnitude (mc):

```
def maxc(mags, mbin):
```

```
    FMD = fmd(mags, mbin)
    mc = FMD.m_bins[FMD.dis_mf==np.max(FMD.dis_mf)]
    return mc
```

E.5.4. Goodness-of-Fit function – completeness magnitude

Defines a function calculation the completeness magnitude of a frequency-magnitude distribution using the Goodness-of_fit method (GFT) (Wiemer and Wyss, 2002). Uses the magnitude catalogue (mags) and the magnitude bin size (mbin). Returns the completeness magnitude (Mc_GFT), the best-fit outcome: 95% fit, 90% fit or the MaxC method (best). It also returns all the tested completeness magnitudes (Mco) and the corresponding for percentages (R).

```
def GFT(mags, mbin):
    FMD = fmd(mags, mbin)
    maxmag = np.max(mags)
    maxc_mc = maxc(mags, mbin)
    maxc_mc = maxc_mc[0]
    Mco = maxc_mc+np.arange(-0.7,3.0,mbin)
    n_R = len(Mco)
    R = np.zeros(n_R)
    for i in range(n_R):
        mags_sel = mags[mags>Mco[i]-mbin/2]
        GR_paras = GR_mle(mags_sel, Mco[i], mbin)
        cum_model = GR_dist(FMD.m_bins, GR_paras.a_mle, GR_paras.b_mle)
        R[i] = np.sum(np.abs(FMD.cum_mf[FMD.m_bins>=Mco[i]]-
        cum_model.GR_cum[FMD.m_bins>=Mco[i]]))/np.sum(FMD.cum_mf[FMD.m_bins>=M
        co[i]])*100
    logic_GFT = R<=5
    if np.any(logic_GFT):
        Mco_sel = Mco[logic_GFT]
        Mc_GFT = Mco_sel[0]
        best = '95%'
    else:
        logic_GFT = R<=10
        if np.any(logic_GFT):
            Mco_sel = Mco[logic_GFT]
            Mc_GFT = Mco_sel[0]
            best = '90%'
        else:
            Mc_GFT = maxc_mc
            best = 'Maxc'
    GFT = collections.namedtuple('GFT', ['Mc_GFT','best', 'Mco', 'R'])
    gft = GFT(Mc_GFT,best,Mco,R)
    return gft
```

E.5.5. *b*-value stability function – completeness magnitude

Defines a function calculation the completeness magnitude of a frequency-magnitude distribution using the *b*-value stability (BVS) (Cao and Gao, 2002). Uses the magnitude catalogue (mags) and the magnitude bin size (mbin). Returns the completeness magnitude (mc). Returns the completeness magnitude (Mc_mbs), all the tested completeness magnitudes (Mco), the *b*-value for all tested Mco's (bi), the error in *b* for all the tested Mco's (unc) and the 5-point moving average of *b* (bave):

```
def mbs(mags, mbin):
	maxmag = np.max(mags)
	maxc_mc = maxc(mags, mbin)
	maxc_mc = maxc_mc[0]
	Mco = maxc_mc+np.arange(-0.7,3.0,mbin)
	n_bs = len(Mco)
	bi = np.zeros(n_bs)
	unc = np.zeros(n_bs)
	for i in range(n_bs):
		mags_sel = mags[mags>Mco[i]-mbin/2]
		n_mags_sel = len(mags_sel)
		GR_paras = GR_mle(mags_sel, Mco[i], mbin)
		bi[i] = GR_paras.b_mle
		unc[i] = GR_paras.b_unc
	bave = np.zeros(n_bs-5)
	for i in range(n_bs-5):
		bave[i] = np.mean(bi[i:i+5])
	dbi = np.abs(bave-bi[0:n_bs-5])
	logic_dbi = dbi<=unc[0:n_bs-5]
	Mco_sel = Mco[logic_dbi]
	if len(Mco_sel) == 0:
		Mc_mbs = maxc_mc
	else:
		Mc_mbs = Mco_sel[0]
	MBS = collections.namedtuple('MBS', ['Mc_mbs', 'Mco', 'bi', 'unc', 'bave'])
	mbs = MBS(Mc_mbs,Mco,bi,unc,bave)
	return mbs
```

E.5.6. Maximum-likelihood estimation of the Gutenberg-Richter distribution function

Defines the function that calculate the Gutenberg-Richter parameters of the frequency-magnitude distribution created in E.5.3. Uses the magnitude catalogue (mags), the completeness magnitude (mco) and the magnitude bin size (mbin). Returns the maximum likelihood estimation of the *b*-value (b_mle) as defined by

Bender (1983) in Equation [3.3], the error in *b* as defined by Shi and Bolt (1982) in Equation [3.5], and the *a*-value:

```
def GR_mle(mags, mco, mbin):
        nbev = len(mags)
        b_mle = np.log10(np.exp(1))/(np.mean(mags)-(mco-mbin/2))
        b_unc = (2.3*b_mle**2)*np.sqrt(np.sum((mags-np.mean(mags))**2)/(nbev*(nbev-1)))
        a_mle = np.log10(nbev) + b_mle*mco
        GR_paras = collections.namedtuple('GR_paras', ['b_mle','b_unc','a_mle'])
        gr_paras = GR_paras(b_mle,b_unc,a_mle)
        return gr_paras
```

E.5.7. Estimated Gutenberg-Richter distribution function

Defines the function that uses the parameters calculated in E.5.3 to estimate the Log-linear Gutenberg-Richter relationship. Uses the magnitude bin size (m_bins), the a-value (*a*_value) and *b*-value (b_value). Returns the estimated cumulative (GR_cum) and discrete (GR_dis) Gutenberg-Richter distributions:

```
def GR_dist(m_bins, a_value, b_value):
        GR_cum = 10**(a_value-b_value*m_bins)
        GR_dis = np.absolute(np.diff(np.concatenate((GR_cum, [0]), axis=0)))
        GR_dist = collections.namedtuple('GR_dist', ['GR_cum','GR_dis'])
        gr_dist = GR_dist(GR_cum,GR_dis)
        return gr_dist
```

E.5.8. Error modification

The data for the modified *b*-value errors shown in Figure 3.11c.

```
N1=[50,70,100,150,200,300,400,500,700,1000,1500,2000,3000,4000,5000,
50,70,100,150,200,300,400,500,700,1000,1500,2000,3000,4000,5000,
50,70,100,150,200,300,400,500,700,1000,1500,2000,3000,4000,5000,
50,70,100,150,200,300,400,500,700,1000,1500,2000,3000,4000,5000,
50,70,100,150,200,300,400,500,700,1000,1500,2000,3000,4000,5000,
50,70,100,150,200,300,400,500,700,1000,1500,2000,3000,4000,5000,]
b1=[0.5,0.5,0.5,0.5,0.5,0.5,0.5,0.5,0.5,0.5,0.5,0.5,0.5,0.5,0.5,
1,1,1,1,1,1,1,1,1,1,1,1,1,1,1,
1.5,1.5,1.5,1.5,1.5,1.5,1.5,1.5,1.5,1.5,1.5,1.5,1.5,1.5,1.5,
2,2,2,2,2,2,2,2,2,2,2,2,2,2,2,
2.5,2.5,2.5,2.5,2.5,2.5,2.5,2.5,2.5,2.5,2.5,2.5,2.5,2.5,2.5,
3,3,3,3,3,3,3,3,3,3,3,3,3,3,3,]
values=[2.626,2.168,1.832,1.629,1.543,1.448,1.380,1.375,1.290,1.288,1.270,1.250,1.171,1.120,1.100,
3.030,2.700,2.405,2.360,2.327,2.199,1.886,1.760,1.540,1.536,1.555,1.322,1.370,1.324,1.333,
2.554,2.769,3.058,2.503,2.767,2.850,2.940,3.030,2.902,2.786,2.378,2.627,2.348,2.218,1.972,
2.155,2.425,3.008,3.316,3.573,3.198,3.303,3.555,3.600,3.757,3.813,3.802,4.052,4.106,4.314,
```

```
1.877,2.210,2.639,3.223,3.910,4.809,4.870,5.084,4.814,4.484,4.398,4.400,4.592,4.594,4.859,
1.819,1.951,2.161,3.129,3.440,4.633,5.427,6.446,8.112,8.279,13.624,14.216,8.021,5.957,5.444]
xs,ys = np.mgrid[100:10000:500j,0.5:3:500j]
resampled_errors = griddata((N1,b1), values, (xs, ys), method='cubic')
```

E.5.9. Iterative sampling method

Defines the function that performs the iterative sampling method described in Section 4.3.2. Uses the magnitude catalogue (mags), the magnitude bin size (mbin), the minimum (min_samp) and maximum sample sizes parameters (max_samp), the number of required iterations (samp_it), and the dates catalogue (dates). Returns a collection of all the 13 calculate outputs(b_sampled), the total number of catalogues sampled through all the iterations (R),and the calculated probability density function (PDF):

```
b_sampled = np.zeros((samp_it*J,12)) # create empty array to store empty parameters
def rand_cat(mags,mbin,min_samp,max_samp,samp_it,dates):
        it=0
        R=0
        N=len(mags)
        PDF = np.empty((samp_it*1000,402))
        PDF[:] = np.NaN
        while it in range(0, samp_it):
                ##### If N is greater than the maximum sample size
                if N >= max_samp:
                        rand = np.random.randint(min_samp,max_samp)
                        magsS = mags[N-rand:N]
                        Nhalf = N - np.round(rand/2)
                        datesS = dates[N-rand:N]
                        days_length = dates[N-1]-dates[N-rand-1]
                        event_rate = np.round((rand/days_length),1)
                        Dmean = np.mean(datesS)
                        max_magS = np.amax(magsS)
                        FMD_all = fmd(magsS, mbin)
                        ##### Perform MaxC analysis
                        maxc_mcS = maxc(magsS, mbin)
                        Mc_plotS1 = maxc_mcS[0]
                        mags_plotS1 = magsS[magsS>(Mc_plotS1-mbin/2)]
                        Nc1 = len(mags_plotS1)
                        GR_paras_allS1 = GR_mle(mags_plotS1, Mc_plotS1, mbin)
                        FMD_sel_binsS1 = FMD_all.m_bins[FMD_all.m_bins>=Mc_plotS1]
                        GR_MLE_fitS1 = GR_dist(FMD_sel_binsS1, GR_paras_allS1.a_mle,
                        GR_paras_allS1.b_mle)
                        ##### perform BVS analysis
                        mbs_mcS = mbs(magsS, mbin)
                        Mc_plotS2 = mbs_mcS.Mc_mbs
                        mags_plotS2 = magsS[magsS>(Mc_plotS2-mbin/2)]
                        Nc2 = len(mags_plotS2)
```

```
GR_paras_allS2 = GR_mle(mags_plotS2, Mc_plotS2, mbin)
FMD_sel_binsS2 = FMD_all.m_bins[FMD_all.m_bins>=Mc_plotS2]
GR_MLE_fitS2 = GR_dist(FMD_sel_binsS2, GR_paras_allS2.a_mle,
GR_paras_allS2.b_mle)
##### perform GFT analysis
GFT_mcS = GFT(magsS, mbin)
Mc_plotS3 = GFT_mcS.Mc_GFT
mags_plotS3 = magsS[magsS>(Mc_plotS3-mbin/2)]
Nc3 = len(mags_plotS3)
GR_paras_allS3 = GR_mle(mags_plotS3, Mc_plotS3, mbin)
FMD_sel_binsS3 = FMD_all.m_bins[FMD_all.m_bins>=Mc_plotS3]
GR_MLE_fitS3 = GR_dist(FMD_sel_binsS3, GR_paras_allS3.a_mle,
GR_paras_allS3.b_mle)
##### choose which method to use
        if (np.absolute(Mc_plotS1-Mc_plotS2) < 0.15) and
        (np.absolute(Mc_plotS1-Mc_plotS3) < 0.15):
        GR_paras_allS = GR_paras_allS1
        Mc_plotS = Mc_plotS1
        Nc = Nc1
        Method = 1 # maxc
else:
        if (GR_paras_allS2.b_mle > 0.25) and (GR_paras_allS3.b_mle <=
0.25):
                GR_paras_allS = GR_paras_allS3
                Mc_plotS = Mc_plotS3
                Nc = Nc3
                Method = 3 # GFT
        else:
                GR_paras_allS = GR_paras_allS2
                Mc_plotS = Mc_plotS2
                Method = 2 # BVS
                Nc = Nc2
#print 'Method = ',Method
Bandwidth = max_magS - Mc_plotS
######################
#Error modification using E.5.8
idx = find_nearest(xs[:,0],Nc)
idy = find_nearest(ys[0,:],GR_paras_allS.b_mle)
b_unc_mod = GR_paras_allS.b_unc*resampled_errors[idx,idy]
######################
###gather all the paramteres
b_sampled[R,0]=Nhalf
b_sampled[R,1]=GR_paras_allS.b_mle
b_sampled[R,2]=GR_paras_allS.b_unc
b_sampled[R,3]=Dmean
b_sampled[R,4]=GR_paras_allS.a_mle
b_sampled[R,5]=Mc_plotS
b_sampled[R,6]=event_rate
b_sampled[R,7]=max_magS
b_sampled[R,8]=Bandwidth
b_sampled[R,9]=Method
b_sampled[R,10]=b_unc_mod #modified b error
b_sampled[R,11]=Nc #no. events in complete catalogue
mew = b_sampled[R,1]
sigma = b_sampled[R,2]
```

```
            PDF[R,0] = Nhalf
            R=R+1
            N=N-rand
            ####################
##### If N is less than the maximum sample size
elif min_samp <= N < max_samp:
            rand = np.random.randint(min_samp,max_samp)
            if rand > N:
                        rand = N
            magsS = mags[N-rand:N]
            Nhalf = N - np.round(rand/2)
            datesS = dates[N-rand:N]
            days_length = dates[N]-dates[N-rand]
            event_rate = np.round((rand/days_length),1)
            Dmean = np.mean(datesS)
            max_magS = np.amax(magsS)
            FMD_all = fmd(magsS, mbin)
            ##### Perform MaxC analysis
            maxc_mcS = maxc(magsS, mbin)
            Mc_plotS1 = maxc_mcS[0]
            mags_plotS1 = magsS[magsS>(Mc_plotS1-mbin/2)]
            Nc1 = len(mags_plotS1)
            GR_paras_allS1 = GR_mle(mags_plotS1, Mc_plotS1, mbin)
            FMD_sel_binsS1 = FMD_all.m_bins[FMD_all.m_bins>=Mc_plotS1]
            GR_MLE_fitS1 = GR_dist(FMD_sel_binsS1, GR_paras_allS1.a_mle,
            GR_paras_allS1.b_mle)
            ##### Perform bvs analysis
            mbs_mcS = mbs(magsS, mbin)
            Mc_plotS2 = mbs_mcS.Mc_mbs
            mags_plotS2 = magsS[magsS>(Mc_plotS2-mbin/2)]
            Nc2 = len(mags_plotS2)
            GR_paras_allS2 = GR_mle(mags_plotS2, Mc_plotS2, mbin)
            FMD_sel_binsS2 = FMD_all.m_bins[FMD_all.m_bins>=Mc_plotS2]
            GR_MLE_fitS2 = GR_dist(FMD_sel_binsS2, GR_paras_allS2.a_mle,
            GR_paras_allS2.b_mle)
            GFT_mcS = GFT(magsS, mbin)
            ##### Perform GFT analysis
            Mc_plotS3 = GFT_mcS.Mc_GFT
            mags_plotS3 = magsS[magsS>(Mc_plotS3-mbin/2)]
            Nc3 = len(mags_plotS3)
            GR_paras_allS3 = GR_mle(mags_plotS3, Mc_plotS3, mbin)
            FMD_sel_binsS3 = FMD_all.m_bins[FMD_all.m_bins>=Mc_plotS3]
            GR_MLE_fitS3 = GR_dist(FMD_sel_binsS3, GR_paras_allS3.a_mle,
            GR_paras_allS3.b_mle)
            #####choose which method to use
            if (np.absolute(Mc_plotS1-Mc_plotS2) < 0.15) and (np.absolute(Mc_plotS1-
            Mc_plotS3) < 0.15):
                        GR_paras_allS = GR_paras_allS1
                        Mc_plotS = Mc_plotS1
                        Nc = Nc1
                        Method = 1 # maxc
            else:
                        if (GR_paras_allS2.b_mle > 0.25) and (GR_paras_allS3.b_mle <=
            0.25):
                                    GR_paras_allS = GR_paras_allS3
```

```
                                        Mc_plotS = Mc_plotS3
                                        Nc = Nc2
                                        Method = 3 # GFT
                                else:
                                        GR_paras_allS = GR_paras_allS2
                                        Mc_plotS = Mc_plotS2
                                        Nc = Nc3
                                        Method = 2 # BVS
                        Bandwidth = max_magS - Mc_plotS
                        ##################
                        #Error modification
                        idx = find_nearest(xs[:,0],Nc)
                        idy = find_nearest(ys[0,:],GR_paras_allS.b_mle)
                        b_unc_mod = GR_paras_allS.b_unc*resampled_errors[idx,idy]
                        ###################
                        b_sampled[R,0]=Nhalf
                        b_sampled[R,1]=GR_paras_allS.b_mle
                        b_sampled[R,2]=GR_paras_allS.b_unc
                        b_sampled[R,3]=Dmean
                        b_sampled[R,4]=GR_paras_allS.a_mle
                        b_sampled[R,5]=Mc_plotS
                        b_sampled[R,6]=event_rate
                        b_sampled[R,7]=max_magS
                        b_sampled[R,8]=Bandwidth
                        b_sampled[R,9]=Method
                        b_sampled[R,10]=b_unc_mod #modified b error
                        b_sampled[R,11]=Nc #no. events in complete catalogue
                        mew = b_sampled[R,1]
                        sigma = b_sampled[R,2]
                        PDF[R,0] = Nhalf
                        R=R+1
                        N=N-rand
                elif N < min_samp:
                        N=len(mags)
                        it=it+1
                ##### generate probability density function using mean and s.d.
                b_inc=0
                for b_inc in range(0,401):
                        B_INC=b_inc*0.01
                        pdf = e** ( -1* ((B_INC-mew)**2) / (2*(sigma**2)) ) / (sigma*np.sqrt(2*pi))
                        PDF[R-1,b_inc+1] = pdf
                #print 'R = ',R
print''
PDF = PDF[0:R,:]
Rand_cat = collections.namedtuple('Rand_cat', ['b_sampled','R','PDF'])
Rand_cat = Rand_cat(b_sampled,R,PDF)
return Rand_cat
```

E.6 Run analysis

Sections of code that uses the functions defined in Section E.5 to perform analysis of the frequency-magnitude distribution:

```
#Define the mags catalogue from 'Cat1' along with dates and min and max magnitudes.
mags = Cat1[:,4]
len_mags = len(Cat1[:,4])
event_no=range(len_mags)
dates = Cat1[:,0]
min_mag = min(mags)
max_mag = np.amax(mags)
```

Perform the iterative (random) sampling analysis:

```
#random catalogue sampling
RAND_CAT = rand_cat(mags, mbin, min_samp, max_samp, samp_it,dates)
Rand_cat = RAND_CAT.b_sampled
R = RAND_CAT.R
PDF = RAND_CAT.PDF

#sort catalouge by middle event number then find moving averages
Rand_cat = Rand_cat[Rand_cat[:,0].argsort()]
Rand_cat = Rand_cat[((samp_it*J)-R-1):,:]
PDF = PDF[PDF[:,0].argsort()]   #Probability density function

#Sum the PDF's
S=0
sum_PDF=np.zeros((R))
for S in range (0,R):
sum_PDF[S] = np.nansum(PDF[S,1:])
```

Smooth the results from the iterative sampling (Rand_cat) using a moving window (mov_av) as defined in the parameters in Section E.2:

```
#Calculate (mov_av) point moving averages
#Create null arrays
Rand_cat_av5 = np.zeros((R-mov_av+1,27))
PDF_av5 = np.zeros((R-mov_av+1,403))
maxb5 = np.zeros(R-mov_av+1)

X=0
for X in range (0,R-mov_av5+1):
Rand_cat_av[X,0] = np.mean(Rand_cat[X:(X+mov_av-1),0]) #average event number
Rand_cat_av[X,1] = np.mean(Rand_cat[X:(X+mov_av-1),1]) #average b
Rand_cat_av[X,2] = np.mean(Rand_cat[X:(X+mov_av-1),2]) #average b_unc
Rand_cat_av[X,3] = np.mean(Rand_cat[X:(X+mov_av-1),3]) #average date
Rand_cat_av[X,4] = np.median(Rand_cat[X:(X+mov_av-1),1]) #median b
Rand_cat_av[X,5] = np.median((Rand_cat[X:(X+mov_av-1),1])+(Rand_cat[X:(X+mov_av-1),2])) #median
b+unc
Rand_cat_av[X,6] = np.median((Rand_cat[X:(X+mov_av-1),1])-(Rand_cat[X:(X+mov_av-1),2])) #median b-
unc
Rand_cat_av[X,7] = np.median(Rand_cat[X:(X+mov_av-1),4]) #median a-value
Rand_cat_av[X,8] = np.percentile(Rand_cat[X:(X+mov_av-1),4],84.1) #median a-value + 1sd
Rand_cat_av[X,9] = np.percentile(Rand_cat[X:(X+mov_av-1),4],15.9) #median a-value - 1sd
Rand_cat_av[X,10] = np.median(Rand_cat[X:(X+mov_av-1),5]) #median Mc
Rand_cat_av[X,11] = np.percentile(Rand_cat[X:(X+mov_av-1),5],84.1) #median Mc + 1sd
```

```
Rand_cat_av[X,12] = np.percentile(Rand_cat[X:(X+mov_av-1),5],15.9) #median Mc - 1sd
Rand_cat_av[X,13] = np.median(Rand_cat[X:(X+mov_av-1),6]) #median event rate
Rand_cat_av[X,14] = np.percentile(Rand_cat[X:(X+mov_av-1),6],84.1) #median event rate + 1sd
Rand_cat_av[X,15] = np.percentile(Rand_cat[X:(X+mov_av-1),6],15.9) #median event rate - 1sd
Rand_cat_av[X,16] = np.median(Rand_cat[X:(X+mov_av-1),7]) #median max mag
Rand_cat_av[X,17] = np.percentile(Rand_cat[X:(X+mov_av-1),7],84.1) #median max mag + 1sd
Rand_cat_av[X,18] = np.percentile(Rand_cat[X:(X+mov_av-1),7],15.9) #median max mag - 1sd
Rand_cat_av[X,19] = np.median(Rand_cat[X:(X+mov_av-1),8]) #median bandwidth
Rand_cat_av[X,20] = np.percentile(Rand_cat[X:(X+mov_av-1),8],84.1) #median bandwidth + 1sd
Rand_cat_av[X,21] = np.percentile(Rand_cat[X:(X+mov_av-1),8],15.9) #median bandwidth - 1sd
Rand_cat_av[X,22] = np.median(Rand_cat[X:(X+mov_av-1),2]) #median b_unc
Rand_cat_av[X,23] = Rand_cat[X,0] #minimum event for error
Rand_cat_av[X,24] = Rand_cat[(X+mov_av-1),0] #maximum event for error
Rand_cat_av[X,25] = Rand_cat[X,3] #minimum date for error
Rand_cat_av[X,26] = Rand_cat[(X+mov_av-1),3] #maximum date for error

#sum the PDFs within the moving window
P=0
for P in range (0,402):
        PDF_av[X,P] = np.nansum(PDF[X:(X+mov_a5),P]) #generate probability for each 0.01 increment
of b
total_pdf = np.nansum(PDF_av[X,2:]) #sum probaility for curve
PDF_av[X,2:] = PDF_av[X,2:]/total_pdf5 #normalise probability to 1
PDF_av[X,0] = PDF_av[X,0]/mov_av #event number / no points
PDF_av[X,1] = Rand_cat_av[X,3] #Date / no points
maxb[X] = 0.01*np.ndarray.argmax(PDF_av[X,2:400]) #total probability for summed curve
```

Select an event number or date of interest through which to create a cross-section through the PDF:

```
###PDFs of interest
#Select event number
#here the chosen event number of interest is 2020
idx1 = find_nearest(PDF_av20[:,0],2020)
event1 = PDF_av20[idx1,0]
event1_min = Rand_cat_av20[idx1,23]
event1_max = Rand_cat_av20[idx1,24]
PDF1 = PDF_av20[idx1,2:]
event1date = PDF_av20[idx1,1]

#Select date
#here the chosen event number of interest is (19,7,2011)
date1 = mdates.date2num(dt.date(2011,7,19))
id1 = find_nearest(PDF_av20[:,1],date1)
date1 = PDF_av20[id1,1]
date1_min = Rand_cat_av20[id1,23]
date1_max = Rand_cat_av20[id1,24]
pdf1 = PDF_av20[id1,2:]
```

E.7 Print outputs

Print various key pieces of information:

```
#print the number of sample iterations
Print 'it = ', it
#print the size of the Cat1 catalogue
print ' NCat1 = ', NCat1
#print the size of the coloured catalogue
print ' Ncatcol = ', Ncatcol
#print the maximum magnitude in the catalogue
print 'max_mag = ', max_mag
#print the total number of sampled catalogues
print 'Total sampled catalogues = ',R

#print the event number plus errors for the selected cross-section through the PDF
print 'pdf1(mov_av) event no. = ', np.round(event1,0), ' + ', event1_max-np.round(event1,0), ' - ',
np.round(event1,0)-event1_min
#print the date for the selected cross-section through the PDF
print 'pdf1(20) date = ', mdates.num2date(date1)
```

E.8 Plotting figures

Here is the code for key plots of the spatial and temporal evolution of the frequency-magnitude distribution and *b*-value PDF's.

E.8.1. **Frequency-magnitude related plots**

- Plot of earthquake epicentres and hypocentres as in Appendix A.

```
mpl.rcParams['figure.subplot.left'] = 0.08
mpl.rcParams['figure.subplot.right'] = 0.90
mpl.rcParams['figure.subplot.top'] =0.97
mpl.rcParams['figure.subplot.bottom'] = 0.1
mpl.rcParams['xtick.labelsize'] = 9
mpl.rcParams['ytick.labelsize'] = 9

fig = plt.figure(figsize=(6, 4)) #figure size and gridspec bleow will need to be adjusted individually for
each catalogue
gs = gridspec.GridSpec(3, 5)
ax1 = fig4.add_subplot(gs[:2, :4])
cm = mpl.cm.get_cmap('summer')
m = Basemap(llcrnrlon=lon_min, llcrnrlat=lat_min, urcrnrlon=lon_max, urcrnrlat=lat_max,
resolution='h',projection='tmerc',lon_0=lon_max +(lon_max-lon_min)/2.,lat_0=lat_max +(lat_max-
lat_min)/2.)
m.drawcoastlines()
x,y = m(Cat1[:,2],Cat1[:,1])
m.scatter(x,y,s=4, c=range(NCat1), norm=plt.Normalize(vmin=0, vmax=Ncatcol), marker='o',
edgecolor='none')
m.drawparallels(np.arange(64.0,66.5,0.2),labels=[0,0,0,0])
m.drawmeridians(np.arange(-18,-16,0.2),labels=[0,0,0,0])
```

```
ax2 = plt.subplot(gs[:-1,4])
ax2.scatter(Cat1[:,3],Cat1[:,1],s=4, c=range(NCat1), norm=plt.Normalize(vmin=0, vmax=Ncatcol),
marker='o', edgecolor='none')
ax2.set_xlim(0,z_max)
ax2.set_xlabel('Depth (km)')
ax2.set_ylim(lat_min,lat_max)
ax2.set_yticklabels([])
ax4 = ax2.twinx()
ax4.set_ylabel('Latitude')
ax4.set_ylim(lat_min,lat_max)

ax3 = plt.subplot(gs[2,:-1])
ax3.scatter(Cat1[:,2],Cat1[:,3],s=4, c=range(NCat1), norm=plt.Normalize(vmin=0, vmax=Ncatcol),
marker='o', edgecolor='none')
ax3.set_xlim(lon_min,lon_max)
ax3.set_ylim(z_max,0)
ax3.set_xlabel('Longitude')
ax3.set_ylabel('Depth (km)')
```

- Plot latitude, longitude, depth, magnitude and daily event rate versus time.

```
mpl.rc('font', *{'sans-serif':'Verdana','family':'sans-serif','size':7})
mpl.rcParams['xtick.labelsize'] = 7
mpl.rcParams['ytick.labelsize'] = 7
mpl.rcParams['figure.subplot.left'] = 0.10
mpl.rcParams['figure.subplot.right'] = 0.95
mpl.rcParams['figure.subplot.top'] =0.98
mpl.rcParams['figure.subplot.bottom'] = 0.07
mpl.rcParams['lines.markersize'] = 3 # fig 1

fig = plt.figure(2, figsize=(8, 10))

#plot lattitude
ax1 = fig2.add_subplot(511)
ax1.scatter(mdates.num2date(CatCol[:,0]),CatCol[:,1],s=5,c=range(Ncatcol),
norm=plt.Normalize(vmin=0, vmax=Ncatcol), marker='o', edgecolor='none')
ax1.set_ylim(lat_min, lat_max)
ax1.set_ylabel('Latitude')
ax1.set_xlim(mdates.num2date(t_start), mdates.num2date(t_end))

#plot longitude
plt.subplot(512)
ax2 = fig2.add_subplot(512)
ax2.scatter(mdates.num2date(CatCol[:,0]),CatCol[:,2],s=5,c=range(Ncatcol),
norm=plt.Normalize(vmin=0, vmax=Ncatcol), marker='o', edgecolor='none')
ax2.set_ylim(lon_min,lon_max)
ax2.set_ylabel('Longitude')
ax2.set_xlim(mdates.num2date(t_start), mdates.num2date(t_end))

#plot depth
plt.subplot(513)
ax3 = fig2.add_subplot(513)
ax3.scatter(mdates.num2date(CatCol[:,0]),CatCol[:,3],s=5,c=range(Ncatcol),
norm=plt.Normalize(vmin=0, vmax=Ncatcol), marker='o', edgecolor='none')
```

```
ax3.set_ylim(z_max,0)
ax3.set_ylabel('Depth')
ax3.set_xlim(mdates.num2date(t_start), mdates.num2date(t_end))

#plot magnitude
plt.subplot(514)
ax4 = fig2.add_subplot(514)
ax4.scatter(mdates.num2date(CatCol[:,0]),CatCol[:,4],s=5,c=range(Ncatcol),
norm=plt.Normalize(vmin=0, vmax=Ncatcol), marker='o', edgecolor='none')
ax4.set_ylim(0,6)
ax4.set_ylabel('Magnitude')
ax4.set_xlim(mdates.num2date(t_start), mdates.num2date(t_end))

#daily and total rate plot
plt.subplot(515)
ax5 = fig2.add_subplot(515)
ax5.bar(mdates.num2date(day_bins[:-1]), DER, color='grey', edgecolor='grey')
ax5.set_ylabel('Daily no. of EQs')
ax5.set_xlim(mdates.num2date(t_start), mdates.num2date(t_end))

ax6 = ax5.twinx()
ax6.plot(mdates.num2date(Cat1[:,0]), np.arange(len(Cat1[:,0]))+1, 'k')
ax6.set_ylabel('Total EQs')
ax6.set_xlim(mdates.num2date(t_start), mdates.num2date(t_end))
if t_start <= phase1 and t_end > phase2 :
plt.axvline(x=phase2, color='k', linestyle='--')

plt.subplots_adjust(hspace=0.3)
plt.subplots_adjust(wspace = 0.5)

#for any of the subplots, to plot a vertical dashed line showing a phase boundary use
if t_start <= phase1 and t_end > phase2 :
    plt.axvline(x=phase2, color='k', linestyle='--')
```

- Plot the frequency-magnitude distribution. In this example the b-value stability method is used to calculate the *Mc* shown by (GR_MLE_fit_mbs). This can be modified to use the best selected method in Section E.5.9.

```
mpl.rcParams['xtick.labelsize'] = 11
mpl.rcParams['ytick.labelsize'] = 11
mpl.rc('font', **{'sans-serif':'Verdana','family':'sans-serif','size':12})
mpl.rcParams['figure.subplot.left'] = 0.18
mpl.rcParams['figure.subplot.right'] = 0.96
mpl.rcParams['figure.subplot.top'] =0.96
mpl.rcParams['figure.subplot.bottom'] = 0.15

fig = plt.figure(figsize=(4, 3))
plt.semilogy(FMD_sel_bins_mbs, GR_MLE_fit_mbs.GR_dis, 'r')
plt.semilogy(FMD_sel_bins_mbs, GR_MLE_fit_mbs.GR_cum, 'g')
plt.semilogy(FMD_all.m_bins, FMD_all.dis_mf, 'or', markersize = 3, markeredgecolor='none')
plt.semilogy(FMD_all.m_bins, FMD_all.cum_mf, 'sg', markersize = 3, markeredgecolor='none')
plt.axvline(x=mbs_mc.Mc_mbs, color='k', linestyle='--', label='b-value stability')
```

```
plt.xlim(0,6)
plt.ylim(0.9,10000)
plt.xlabel('Magnitude')
plt.ylabel('Frequency')
```

- Visually shows the three methods used in the new workflow for selecting *Mc* (Figure 3.9).

```
mpl.rcParams['xtick.labelsize'] = 9
mpl.rcParams['ytick.labelsize'] = 9
mpl.rc('font', **{'sans-serif':'Verdana','family':'sans-serif','size':10})
mpl.rcParams['figure.subplot.left'] = 0.06
mpl.rcParams['figure.subplot.right'] = 0.98
mpl.rcParams['figure.subplot.top'] =0.92
mpl.rcParams['figure.subplot.bottom'] = 0.135

fig = plt.figure(figsize=(10, 3.5))

#Maximum curvature method
ax1 = fig.add_subplot(131)
plt.semilogy(FMD_all.m_bins, FMD_all.dis_mf, 'or', markersize = 3, markeredgecolor='none',
label='Discrete')
plt.semilogy(FMD_all.m_bins, FMD_all.cum_mf, 'sg', markersize =
3,markeredgecolor='none',label='Cumulative')
plt.axvline(x=maxc_mc, color='k', linestyle=':')
plt.xlim(0,6)
plt.ylim(0.9,10000)
plt.xlabel('Magnitude')
plt.ylabel('Frequency')
plt.figtext(0.17,0.94,'A) MaxC')
plt.legend(bbox_to_anchor=(0.55,1),loc=2,fontsize=8)

#Goodness-of-fit method
ax2 = fig.add_subplot(132)
plt.plot(gft_mc.Mco, gft_mc.R, 'o',markersize = 3,markeredgecolor='none')
plt.axhline(y=10, color='0.5', linestyle=':')
plt.axhline(y=5, color='0.5', linestyle=':')
plt.axvline(x=gft_mc.Mc_GFT, color='k', linestyle='-.', label='95% GFT')
plt.xlabel('Mco')
plt.ylabel('Residuals (%)')
plt.xlim(0,6)
plt.ylim(0,25)
plt.figtext(0.50,0.94,'B) GFT')

#b-value stability method
plt.subplot(133)
plt.errorbar(mbs_mc.Mco, mbs_mc.bi, mbs_mc.unc, marker='o', markersize = 2)
plt.plot(mbs_mc.Mco[0:len(mbs_mc.bave)], mbs_mc.bave)
plt.axvline(x=mbs_mc.Mc_mbs, color='k', linestyle='--', label='b-value stability')
plt.axhline(y=GR_paras_all_mbs.b_mle, color='k', linestyle=':')
plt.axhline(y=1.0, color='0.5', linestyle=':')
plt.xlabel('Mco')
plt.ylabel('b-value')
```

```
plt.xlim(0,6)
plt.ylim(0.5,3.0)
plt.figtext(0.82,0.94,'C) BVS')
```

E.8.2. *b*-value probability density related plots

- Time v magnitude, event rate and *b*-value probability density as in the figures in Appendix A.

```
# plot parameters
mpl.rcParams['xtick.labelsize'] = 10
mpl.rcParams['ytick.labelsize'] = 10
mpl.rc('font', **{'sans-serif':'Verdana','family':'sans-serif','size':10})
mpl.rcParams['figure.subplot.left'] = 0.07
mpl.rcParams['figure.subplot.right'] = 1
mpl.rcParams['figure.subplot.top'] =0.98
mpl.rcParams['figure.subplot.bottom'] = 0.11

fig = plt.figure(figsize=(10, 7))
gs = gridspec.GridSpec(3, 120)

#plot magnitudes
ax1 = fig.add_subplot(gs[0:1, :96])
ax1.scatter(mdates.num2date(CatCol[:,0]),CatCol[:,4],s=5,c=range(Ncatcol),
norm=plt.Normalize(vmin=0, vmax=Ncatcol), marker='o', edgecolor='none')
ax1.plot(PDF_av[:,1],Rand_cat_av[:,10],marker='',linestyle='--',color='k')
ax1.set_ylim(0,5.5)
ax1.set_ylabel('Magnitude')
ax1.set_xlim(mdates.num2date(t_start), mdates.num2date(t_end))
plt.setp(ax1.get_xticklabels(), visible=False)
#plt.figtext(0.78,0.94,'a)',fontsize=12)
plt.figtext(0.12,0.94,'a',fontsize=12,fontweight='bold')
#ax1.axvline(x=eruption, color='r', linestyle='--') #date of eruption

#daily and cumulative rate plot
ax2 = fig.add_subplot(gs[1:2, :96])
ax2.bar(mdates.num2date(day_bins[:-1]), DER, color='grey', edgecolor='grey')
ax2.set_ylabel('Daily no. of EQs')
ax2.set_xlim(mdates.num2date(t_start), mdates.num2date(t_end))
plt.setp(ax2.get_xticklabels(), visible=False)

ax3 = ax2.twinx()
ax3.plot(mdates.num2date(Cat1[:,0]), np.arange(len(Cat1[:,0]))+1, 'k')
ax3.set_ylabel('Total EQs')
ax3.set_xlim(mdates.num2date(t_start), mdates.num2date(t_end))
plt.setp(ax3.get_xticklabels(), visible=False)
plt.figtext(0.12,0.64,'b',fontsize=12,fontweight='bold')

# b-value probability density plot
ax4 = fig.add_subplot(gs[2:3, :120])
CS1 = plt.contourf(PDF_av[:,1],bs,PDF_av[:,2:].T,interpolation='bicubic',origin='upper',levels=levels,
colors = colors)
```

```
plt.plot(PDF_av[:,1],maxb,marker='',linestyle=':',color='k')
plt.axhline(y=1.0, color='k', linestyle='--')
cb =colorbar(CS1, spacing='proportional')
cb.set_label('Probability density')
plt.ylim(0,4)
plt.xlim(mdates.num2date(t_start),mdates.num2date(t_end))
plt.ylabel('b-value',fontsize=12)
plt.xlabel('Date',fontsize=12)
plt.xticks(rotation=30)
plt.figtext(0.12,0.34,'c',fontsize=12,fontweight='bold')

#adjust subplot spacing
plt.subplots_adjust(hspace=0.1)
plt.subplots_adjust(wspace = 0.5)
```

- *b*-value probability density by event number:

```
mpl.rc('font', **{'sans-serif':'Verdana','family':'sans-serif','size':12})
mpl.rcParams['ytick.labelsize'] = 12
mpl.rcParams['xtick.labelsize'] = 12
mpl.rcParams['figure.subplot.left'] = 0.05
mpl.rcParams['figure.subplot.right'] = 1
mpl.rcParams['figure.subplot.top'] =0.97
mpl.rcParams['figure.subplot.bottom'] = 0.13

bs = np.linspace(0,4,401)
levels = [0.001,0.005,0.01,0.015,0.02,0.025,0.03,0.035,0.04,0.045,0.05,0.055,0.06,0.09,0.12]
#levels = [0.005,0.01,0.015,0.002,0.03,0.04,0.05,0.075,0.1,0.125,0.15,0.2,0.25,0.3,0.4,0.5,0.6]
colors =
('LightSkyBlue','PaleTurquoise','LawnGreen','GreenYellow','Yellow','Gold','DarkOrange','OrangeRed','Red'
,'FireBrick','DarkRed','DarkRed','DarkRed','DarkRed')

fig = plt.figure(figsize=(12, 4))
#plot filled contours

CS1 = plt.contourf(PDF_av20[:,0],bs,PDF_av20[:,2:].T,interpolation='bicubic',origin='upper',levels=levels,
colors = colors)
plt.plot(PDF_av20[:,0],maxb20,marker='',linestyle=':',color='k')
plt.axhline(y=1.0, color='k', linestyle='--')
cb =colorbar(CS1,spacing='proportional')
cb.set_label('Probability density',fontsize=12)
plt.clabel(CS1, inline=0, fontsize=0)
plt.ylim(0,4)
plt.xlim(0,len_mags)
plt.ylabel('b-value',fontsize=12)
plt.xlabel('Event number',fontsize=12)
```

- Plot the stacked *b*-value PDF through the cross-section of interest.

```
mpl.rc('font', **{'sans-serif':'Verdana','family':'sans-serif','size':12})
mpl.rcParams['figure.subplot.left'] = 0.08
mpl.rcParams['figure.subplot.right'] = 0.97
mpl.rcParams['figure.subplot.top'] =0.97
```

```
mpl.rcParams['figure.subplot.bottom'] = 0.2

fig = plt.figure(figsize=(2.5, 3))
plt.plot(PDF1,bs,marker='',linestyle='-',color='k')
plt.axhline(y=1.0, color='k', linestyle='--')
plt.xlim(0,0.02)
plt.ylim(0,4)
plt.xlabel('P(b)',fontsize=12)
plt.ylabel('b-value',fontsize=12)
plt.xticks(rotation=30)
```

- Plot showing the cloud of data for all the sampled catalogues compared to the *b*-value probability density distribution they create – by event.

```
mpl.rc('font', **{'sans-serif':'Verdana','family':'sans-serif','size':10})
mpl.rcParams['ytick.labelsize'] = 10
mpl.rcParams['figure.subplot.left'] = 0.11
mpl.rcParams['figure.subplot.right'] = 0.96
mpl.rcParams['figure.subplot.top'] =0.99
mpl.rcParams['figure.subplot.bottom'] = 0.05
mpl.rcParams['lines.markersize'] = 3 # fig 8

levels = [0.002,0.004,0.006,0.008,0.01,0.015,0.02,0.025,0.03,0.035,0.04,0.045,0.05,0.055,0.12]
colors =
('LightSkyBlue','PaleTurquoise','LawnGreen','GreenYellow','Yellow','Gold','DarkOrange','OrangeRed','Red'
,'FireBrick','DarkRed','DarkRed','DarkRed','DarkRed')

fig = plt.figure(figsize=(6, 10))
gs = gridspec.GridSpec(3, 120)
ax1 = fig3.add_subplot(gs[0:1, :97])
plt.errorbar(b_sampled[:,0], b_sampled[:,1], yerr=b_sampled[:,2], marker='.',linestyle='', color='r',
label='1sd')
plt.axhline(y=1, color='0.3', linestyle='--')
plt.ylim(0,4)
plt.xlim(0,len_mags)

ax2 = fig.add_subplot(gs[1:2, :120])
CS1 = plt.contourf(PDF_av[:,0],bs,PDF_av[:,2:].T,interpolation='bicubic',origin='upper',levels=levels,
colors = colors)
plt.plot(PDF_av[:,0],maxb,marker='',linestyle=':',color='k')
plt.axhline(y=1.0, color='k', linestyle='--')
plt.axvline(x=event1, color='r', linestyle='--') #plot the position of the event of interest
cb =colorbar(CS1, spacing='proportional')
cb.set_label('Probability density')
plt.ylim(0,4)
plt.xlim(0,len_mags)
plt.ylabel('b-value',fontsize=12)
```

- Plot showing the cloud of data for all the sampled catalogues compared to the *b*-value probability density distribution they create – by date.

```
mpl.rc('font', **{'sans-serif':'Verdana','family':'sans-serif','size':10})
mpl.rcParams['ytick.labelsize'] = 10
mpl.rcParams['figure.subplot.left'] = 0.11
mpl.rcParams['figure.subplot.right'] = 0.96
mpl.rcParams['figure.subplot.top'] =0.99
mpl.rcParams['figure.subplot.bottom'] = 0.05

levels = [0.002,0.004,0.006,0.008,0.01,0.015,0.02,0.025,0.03,0.035,0.04,0.045,0.05,0.055,0.12]
colors =
('LightSkyBlue','PaleTurquoise','LawnGreen','GreenYellow','Yellow','Gold','DarkOrange','OrangeRed','Red'
,'FireBrick','DarkRed','DarkRed','DarkRed','DarkRed')

fig = plt.figure(figsize=(6, 10))
gs = gridspec.GridSpec(3, 120)
ax1 = fig.add_subplot(gs[0:1, :97])
plt.errorbar(b_sampled[:,3], b_sampled[:,1], yerr=b_sampled[:,2], marker='.',linestyle='', color='r',
label='1sd')
plt.axhline(y=1, color='0.3', linestyle='--')
plt.ylim(0,4)
plt.xlim(mdates.num2date(t_start),mdates.num2date(t_end))

ax2 = fig.add_subplot(gs[1:2, :120])
CS1 = plt.contourf(PDF_av20[:,1],bs,PDF_av20[:,2:].T,interpolation='bicubic',origin='upper',levels=levels,
colors = colors)
plt.plot(PDF_av20[:,1],maxb20,marker='',linestyle=':',color='k')
plt.axhline(y=1.0, color='k', linestyle='--')
plt.axvline(x=Rand_cat[R,3], color='k', linestyle='--')
plt.axvline(x=event1, color='r', linestyle='--')
cb =colorbar(CS1, spacing='proportional')
cb.set_label('Probability density')
plt.ylim(0,4)
plt.xlim(mdates.num2date(t_start),mdates.num2date(t_end))
plt.ylabel('b-value',fontsize=12)
```

E.9 Voronoi polygons

E.9.1. Description

This is a description of the loops involved in performing the iterative sampling technique. The bracketed values indicate the size of the arrays.

Parameters:

- It – number of iterations
- Nvor – number of Voronoi polygons
- E – Total number of events in catalogue
- R – Number of points with events above minimum threshold

- Res – resolution of data points, typically 0.01°

1) Iteration loop (it)
   a) Generate random locations loop, (Nvor)
   b) For each event (E):
      i) Calculate nearest point (Nvor)
   c) For each random location (Nvor):
      i) Assign/don't assign each event (E)
      ii) If catalogue has enough events (>500/100) perform FM analysis (~Nvor/4)
2) For each random point (R):
   a) Calculate P(b) (401)
3) For each longitude sample (6/res):
   a) For each latitude sample (4/res):
      i) For each random point (R):
         (1) Decide if it is in the lat/long box, if so assign PDF(b)
      ii) If there are points in the lat/long box:
         *(1) Sum PDF's (401*Q points)*

E.9.2. **Voronoi sampling code**

Extra parameters to those in Section E.2:

```
#Number of Voronoi polygons
Vor_min = 20
Vor_max = 200

#Minimum catalogue size
Cat_min = 100

#number of sample iterations
samp_it = 3 #number of random catalogue sampling iterations

#resolution pf pdf squares
res = 0.01
```

Import and filter the catalogue as in Sections E.3 and E.4.

Generate Voronoi polygons, perform frequency-magnitude analysis and iterate.

```
#Genreate voronoi polygons and iterate

NVors = np.zeros((samp_it))
b_sampled = np.zeros((samp_it*100,13))
no_lon = np.int((lon_max-lon_min)/res)+1
no_lat = np.int((lat_max-lat_min)/res)+1
PDF_point=np.zeros((no_lon*no_lat,404))
R=0 # number of random points with data
it=0

while it in range (0,samp_it):
	NVor= np.random.randint(Vor_min,Vor_max) #no. of Vor. Polygons randomly generated
	between predefined max and min
	print 'NVor = ',NVor
	NVors[it] = NVor
	randloc = np.zeros((NVor,2))
	point_accepted=np.zeros((NVor))
	b_allpoints = np.zeros((samp_it*Vor_max,13))

	#Generate NVor random lat/long coordinates
	N=0
		while N in range (0,NVor):
		randloc[N,0] = (np.random.randint(lon_min*100,lon_max*100))
		randloc[N,0] = randloc[N,0]/100
		randloc[N,1] = (np.random.randint(lat_min*100,lat_max*100))
		randloc[N,1] = randloc[N,1]/100
		N=N+1
	vor = Voronoi(randloc)
	##########################################
	#for each event calculate nearest random point
	points = np.zeros((len(Cat1),1))
	Cat2 = np.concatenate((Cat1,points), axis=1)
	E=0
	while E in range (0,len(Cat2)):
		dis = np.zeros((NVor,2))
		N=0
		while N in range (0,NVor):
			dis[N,0] = np.sqrt(((Cat2[E,1]-randloc[N,1])**2)+((Cat2[E,2]-randloc[N,0])**2))
			dis[N,1] = N+1 #point reference
			N=N+1
		dis = dis[dis[:,0].argsort()]
		Cat2[E,5]= dis[0,1]
		E=E+1
	print ' Calculated nearest points ', it+1
	##########################################
	#sort event catalogue by Voronoi point reference
	Cat2 =Cat2[Cat2[:,5].argsort()]
	#Create catalogue for each Vor. point
	N=1
	#Create catalogue for each Vor. point
	while N in range (1,NVor+1):
		E=0
```

```
CatS = np.zeros((len(Cat2),6))
Count = 0
while E in range (0,len(Cat1)):
        if Cat2[E,5] == N:
                CatS[E,:] = Cat2[E,:]
                Count = Count+1
        E=E+1
#If count>cat minimum then perform FM analysis
if Count >= Cat_min:
        CatS = CatS[CatS[:,5].argsort()]
        CatS = CatS[len(CatS)-Count:,:]
        max_magS = np.amax(CatS[:,4])
        FMD_all = fmd(CatS[:,4], mbin)
        maxc_mcS = maxc(CatS[:,4], mbin)
        Mc_plotS1 = maxc_mcS[0]
        mags_plotS1 = CatS[CatS[:,4]>(Mc_plotS1-mbin/2),4]
        GR_paras_allS1 = GR_mle(mags_plotS1, Mc_plotS1, mbin)
        FMD_sel_binsS1 = FMD_all.m_bins[FMD_all.m_bins>=Mc_plotS1]
        GR_MLE_fitS1 = GR_dist(FMD_sel_binsS1, GR_paras_allS1.a_mle,
        GR_paras_allS1.b_mle)
        mbs_mcS = mbs(CatS[:,4], mbin)
        Mc_plotS2 = mbs_mcS.Mc_mbs
        mags_plotS2 = CatS[CatS[:,4]>(Mc_plotS2-mbin/2),4]
        GR_paras_allS2 = GR_mle(mags_plotS2, Mc_plotS2, mbin)
        FMD_sel_binsS2 = FMD_all.m_bins[FMD_all.m_bins>=Mc_plotS2]
        GR_MLE_fitS2 = GR_dist(FMD_sel_binsS2, GR_paras_allS2.a_mle,
        GR_paras_allS2.b_mle)
        GFT_mcS = GFT(CatS[:,4], mbin)
        Mc_plotS3 = GFT_mcS.Mc_GFT
        mags_plotS3 = CatS[CatS[:,4]>(Mc_plotS3-mbin/2),4]
        GR_paras_allS3 = GR_mle(mags_plotS3, Mc_plotS3, mbin)
        FMD_sel_binsS3 = FMD_all.m_bins[FMD_all.m_bins>=Mc_plotS3]
        GR_MLE_fitS3 = GR_dist(FMD_sel_binsS3, GR_paras_allS3.a_mle,
        GR_paras_allS3.b_mle)
        #choose which method to use
        if (np.absolute(Mc_plotS1-Mc_plotS2) < 0.15) and (np.absolute(Mc_plotS1-
        Mc_plotS3) < 0.15):
                GR_paras_allS = GR_paras_allS1
                Mc_plotS = Mc_plotS1
                CountComp = len(mags_plotS1)
                Method = 1 # maxc
        else:
                if (GR_paras_allS2.b_mle > 0.25) and (GR_paras_allS3.b_mle <=
                0.25):
                        GR_paras_allS = GR_paras_allS3
                        Mc_plotS = Mc_plotS3
                        CountComp = len(mags_plotS3)
                        Method = 3 # GFT
                else:
                        GR_paras_allS = GR_paras_allS2
                        Mc_plotS = Mc_plotS2
                        CountComp = len(mags_plotS2)
                        Method = 2 # BVS
        Bandwidth = max_magS - Mc_plotS
        ########################################################
```

```
#Error modification
idx = find_nearest(xs[:,0],Count)
idy = find_nearest(ys[0,:],GR_paras_allS.b_mle)
b_unc_mod = GR_paras_allS.b_unc*resampled_errors[idx,idy]
#########################################################
b_sampled[R,0]=Count #number of events
b_sampled[R,1]=GR_paras_allS.b_mle # b-value
b_sampled[R,2]=GR_paras_allS.b_unc # b-value error
b_sampled[R,3]=GR_paras_allS.a_mle # a-value
b_sampled[R,4]=Mc_plotS #completeness magnitude
b_sampled[R,5]=randloc[N-1,1] #latitude of random point
b_sampled[R,6]=randloc[N-1,0] #longitude of random point
b_sampled[R,7]=max_magS # max mag
b_sampled[R,8]=Bandwidth # Max mag - Mc
b_sampled[R,9]=Method # MaxC, BVS or GFT
b_sampled[R,10]=b_unc_mod #modified b error
b_sampled[R,11]=R # row reference
b_sampled[R,12]=CountComp #number of complete events
point_accepted[N-1] = 1
b_allpoints[N,0]=Count #number of events
b_allpoints[N,1]=GR_paras_allS.b_mle # b-value
b_allpoints[N,2]=GR_paras_allS.b_unc # b-value error
b_allpoints[N,3]=GR_paras_allS.a_mle # a-value
b_allpoints[N,4]=Mc_plotS #completeness magnitude
b_allpoints[N,5]=randloc[N-1,1] #latitude of random point
b_allpoints[N,6]=randloc[N-1,0] #longitude of random point
b_allpoints[N,7]=max_magS # max mag
b_allpoints[N,8]=Bandwidth # Max mag - Mc
b_allpoints[N,9]=Method # MaxC, BVS or GFT
b_allpoints[N,10]=b_unc_mod #modified b error
b_allpoints[N,11]=N # row reference
b_allpoints[N,12]=CountComp #number of complete events
########################################
#give PDF to each point on the grid given its nearest random point
lon=0
lat=0
p=0
for lon in range(0,no_lon):
        for lat in range (0,no_lat):
                r=0
                dis = np.zeros((NVor,2))
                n=0
                while n in range (0,NVor):
                        dis[n,0] = np.sqrt(((lat_min+(res*lat)-
                        randloc[n,1])**2)+(((lon_min+(res*lon)-
                        randloc[n,0])**2)))
                        dis[n,1] = n #point reference
                n=n+1
                dis = dis[dis[:,0].argsort()]
                if dis[0,1]+1 == N:
                        idn = dis[0,1]+1
                        PDF_point[p,0] = lon_min+(res*lon)
                        PDF_point[p,1] = lat_min+(res*lat)
                        mew = b_allpoints[idn,1]
                        sigma = b_allpoints[idn,2]
```

```
                                                b_inc=0
                                                for b_inc in range(0,401):
                                                        B_INC=b_inc*0.01
                                                        PDF_point[p,b_inc+2] =
                                                        PDF_point[p,b_inc+2] + (e** ( -1*
                                                        ((B_INC-mew)**2) / (2*(sigma**2)) ) /
                                                        (sigma*np.sqrt(2*pi)))
                                        p=p+1
                R=R+1
        else:
                point_accepted[N-1] = 0
        N=N+1

        print 'it = ',it+1
        print ' No. points = ',R
        it = it+1

point_count=0
for p in range (0,no_lat*no_lon):
if PDF_point[p,1] < lat_min:
PDF_point[p,:] = np.nan
else:
point_count=point_count+1

PDF_point = PDF_point[PDF_point[:,1].argsort()]
PDF_point = PDF_point[0:point_count,:]

b_sampled = b_sampled[0:R,:]

print 'av. cat. size = ',np.average(b_sampled[:,0])
print 'av. complete cat. size = ',np.average(b_sampled[:,12])
print 'NVor av = ',np.average(NVors)

######################################################################
#Normalise PDFs
maxb = np.zeros((point_count,4))
maxb[:] = np.nan

lon=0
lat=0
X=0
while X in range(0,point_count):
total_pdf = np.nansum(PDF_point[X,2:]) #sum probaility for curve
PDF_point[X,2:] = PDF_point[X,2:]/total_pdf #normalise probability to 1
maxb[X,0] = PDF_point[X,0]
maxb[X,1] = PDF_point[X,1]
maxb[X,2] = 0.01*np.ndarray.argmax(PDF_point[X,2:403]) #b value with maximum probability
maxb[X,3] = np.max(PDF_point[X,2:403]) # relative probability
X=X+1
```

E.9.3. Plotting figures

- Plot the event epicentres overlain by the random sampling points and associated Voronoi polygons, as in Figure 8.6.

```
mpl.rc('font', **{'sans-serif':'Verdana','family':'sans-serif','size':12})
mpl.rcParams['xtick.labelsize'] = 11
mpl.rcParams['ytick.labelsize'] = 11
mpl.rcParams['figure.subplot.left'] = 0.13
mpl.rcParams['figure.subplot.right'] = 0.93
mpl.rcParams['figure.subplot.top'] =0.97
mpl.rcParams['figure.subplot.bottom'] = 0.10
mpl.rcParams['lines.markersize'] = 3 # fig 1

fig = plt.figure(figsize=(6, 4))
ax = fig.add_subplot(111)
plt.scatter(Cat1[:,2],Cat1[:,1],s=4, c=range(NCat1), norm=plt.Normalize(vmin=0, vmax=Ncatcol),
marker='o', edgecolor='none')
plt.ylim(lat_min,lat_max)
plt.xlim(lon_min,lon_max)
plt.xlabel('Longitude')
plt.ylabel('Latitude')

#plot voronoi polygons
plt.plot(vor.points[:,0], vor.points[:,1], 'x', c='r', markersize=5)
plt.scatter(b_sampled[:,6],b_sampled[:,5],s=40,marker='x',color='black')

for simplex in vor.ridge_vertices:
simplex = np.asarray(simplex)
if np.all(simplex >= 0):
plt.plot(vor.vertices[simplex,0], vor.vertices[simplex,1], 'k-')

ptp_bound = vor.points.ptp(axis=0)

center = vor.points.mean(axis=0)
for pointidx, simplex in zip(vor.ridge_points, vor.ridge_vertices):
        simplex = np.asarray(simplex)
        if np.any(simplex < 0):
                i = simplex[simplex >= 0][0] # finite end Voronoi vertex
                t = vor.points[pointidx[1]] - vor.points[pointidx[0]] # tangent
                t /= np.linalg.norm(t)
                n = np.array([-t[1], t[0]]) # normal

                midpoint = vor.points[pointidx].mean(axis=0)
                direction = np.sign(np.dot(midpoint - center, n)) * n
                far_point = vor.vertices[i] + direction * ptp_bound.max()

                plt.plot([vor.vertices[i,0], far_point[0]],
                [vor.vertices[i,1], far_point[1]], 'k--')
                plt.axvline(x=-18.3,linestyle=':',color='k')
#Plot any lines of latitude or longitude you want. For example:
plt.axvline(x=-18.2,linestyle=':',color='k') #longitude
```

```
plt.axhline(y=27.6,linestyle=':',color='k') #lattitude
```

- Plot the event epicentres on a basemap overlain by the random sampling points, as in Figure 8.7a.

```
mpl.rc('font', **{'sans-serif':'Verdana','family':'sans-serif','size':12})
mpl.rcParams['xtick.labelsize'] = 11
mpl.rcParams['ytick.labelsize'] = 11
mpl.rcParams['figure.subplot.left'] = 0.13
mpl.rcParams['figure.subplot.right'] = 0.93
mpl.rcParams['figure.subplot.top'] =0.97
mpl.rcParams['figure.subplot.bottom'] = 0.10
mpl.rcParams['lines.markersize'] = 3 # fig 1

fig = plt.figure(figsize=(6, 5))
ax = fig.add_subplot(111)
m.drawcoastlines()
m.scatter(x,y,s=4, c=range(NCat1), norm=plt.Normalize(vmin=0, vmax=Ncatcol), marker='o',
edgecolor='none')
m.scatter(X,Y,s=40,marker='x',color='black')
m.drawparallels(np.arange(27.4,28.1,0.1),labels=[1,0,0,0])
m.drawmeridians(np.arange(-18.5,-17.8,0.1),labels=[1,0,0,1])
```

- Data points within accepted polygons that have been assigned b-values. Resolution of 0.01 degrees latitude/longitude, as in Figure 8.7b.

```
mpl.rc('font', **{'sans-serif':'Verdana','family':'sans-serif','size':12})
mpl.rcParams['xtick.labelsize'] = 11
mpl.rcParams['ytick.labelsize'] = 11
mpl.rcParams['figure.subplot.left'] = 0.14
mpl.rcParams['figure.subplot.right'] = 0.94
mpl.rcParams['figure.subplot.top'] =0.97
mpl.rcParams['figure.subplot.bottom'] = 0.10
mpl.rcParams['lines.markersize'] = 3 # fig 1

fig = plt.figure(figsize=(6, 4.5))
ax = fig.add_subplot(111)

m.drawcoastlines()
m.scatter(X,Y,s=40,marker='x',color='black')
m.drawparallels(np.arange(27.4,28.1,0.1),labels=[1,0,0,0])
m.drawmeridians(np.arange(-18.5,-17.8,0.1),labels=[1,0,0,1])
```

- Contoured $\tilde{b}_P$-value using data points from above, as in Figure 8.7c.

```
mpl.rc('font', **{'sans-serif':'Verdana','family':'sans-serif','size':12})
mpl.rcParams['xtick.labelsize'] = 11
mpl.rcParams['ytick.labelsize'] = 11
mpl.rcParams['figure.subplot.left'] = 0.12
mpl.rcParams['figure.subplot.right'] = 0.98
```

```
mpl.rcParams['figure.subplot.top'] =0.97
mpl.rcParams['figure.subplot.bottom'] = 0.13
mpl.rcParams['lines.markersize'] = 3 # fig 1

resampled_maxb_b = griddata((maxb[:,0], maxb[:,1]), maxb[:,2], (xs, ys), method='cubic')
v=[0,0.25,0.5,0.75,1,1.25,1.5,1.75,2,2.25,2.5,2.75,3]

fig = plt.figure(figsize=(7.5, 5))
CS4 = plt.contourf(xs,ys,resampled_maxb_b, v,
extent=(lon_min,lon_max,lat_min,lat_max),interpolation='bicubic',origin='upper')
plt.contour(xs,ys,resampled_maxb_b, v,
extent=(lon_min,lon_max,lat_min,lat_max),interpolation='bicubic',origin='upper',colors='k')
cb =colorbar(CS4, spacing='proportional')
plt.scatter(b_sampled[:,6],b_sampled[:,5],s=10,marker='.',color='black')
cb.set_label('b-value')

plt.ylim(lat_min,lat_max)
plt.xlim(lon_min,lon_max)
plt.xlabel('Longitude')
plt.ylabel('Latitude')
```

- Contoured peak $P(\tilde{b}_P)$ values using data points from above, as in Figure 8.7d.

```
mpl.rc('font', **{'sans-serif':'Verdana','family':'sans-serif','size':12})
mpl.rcParams['xtick.labelsize'] = 11
mpl.rcParams['ytick.labelsize'] = 11
mpl.rcParams['figure.subplot.left'] = 0.12
mpl.rcParams['figure.subplot.right'] = 0.98
mpl.rcParams['figure.subplot.top'] =0.97
mpl.rcParams['figure.subplot.bottom'] = 0.13
mpl.rcParams['lines.markersize'] = 3 # fig 1

prob_levels=[0,0.02,0.04,0.06,0.08,0.1,0.12,0.14,0.16,0.18,0.2]

fig = plt.figure(figsize=(7.5, 5))
resampled_maxb_p = griddata((maxb[:,0], maxb[:,1]), maxb[:,3], (xs, ys), method='cubic')
CS5 = plt.contourf(xs,ys, resampled_maxb_p, prob_levels,
extent=(lon_min,lon_max,lat_min,lat_max),interpolation='bicubic',origin='upper',cmap='Reds')
plt.contour(xs,ys, resampled_maxb_p, prob_levels,
extent=(lon_min,lon_max,lat_min,lat_max),interpolation='bicubic',origin='upper',colors='k')
cb =colorbar(CS5, spacing='proportional')
plt.scatter(b_sampled[:,6],b_sampled[:,5],s=10,marker='.',color='black')
cb.set_label('b-value relative peak prob.')

plt.ylim(lat_min,lat_max)
plt.xlim(lon_min,lon_max)
plt.xlabel('Longitude')
plt.ylabel('Latitude')
```